THE ROLE OF INTERMETALLIC PHASES IN THE CORROSION OF MAGNESIUM-RARE EARTH ALLOYS

Vom Promotionsausschuss der
Technischen Universität Hamburg-Harburg
zur Erlangung des akademischen Grades

Doktor-Ingenieurin (Dr.-Ing.)
genehmigte Dissertation

von
Maria del Rosario Silva Campos

aus
Mexico, Distrito Federal

2016

Gutachtern der Dissertation:

1. Gutachter: Prof. Dr.-Ing. habil. Karl Ulrich Kainer

2. Gutachter: Prof. Dr.-Ing. habil. Bodo Fiedler

Vorsitzender des Prüfungsauschusses:

Prof. Dr.-Ing. Wolfgang Hintze

Tag der mündlichen Prüfung:

25th July 2016

Acknowledgemt

I would like to thank Prof. Dr.-Ing. Karl Ulrich Kainer, head of the Magnesium Innovation Centre (MagIC) for giving me the opportunity to work at the institute as well as for his valuable guidance, expertise and support in bringing this work to its completion. I also would like to thank Prof. Dr.-Ing. Bodo Fiedler, head of the Polymer Composites Institute at the Hamburg University of Technology for being my second academic supervisor and for his valuable suggestions to the dissertation. Special thanks also go to Prof. Dr.-Ing. Wolfgang Hintze, head of the Production Management Institute and Technology at the Hamburg University of Technology for being the Chairman of my thesis defence.

I am very grateful to Prof. Dr. Mikhail Zheludkevich head of the Corrosion and Surface Technology (WZK) department for his guidance and helpful contributions to my work.

Special thanks go to Dr. Wolfgang Dietzel, for his guidance, support, motivation and for always creating a nice and friendly work environment.

I would like express my sincere respect and acknowledgment to Dr. Carsten Blawert for his support, encouragement, motivation, guidance and training he provided during the course of my PhD.

My deep gratitude and admiration to Dr. Chamini L. Mendis firstly, for her valuable help during the writing and the corrections of this manuscript, TEM evaluations, scientific expertise and suggestions, which contributed greatly to accomplish this work. Secondly, for being an extraordinary person and a great support.

I warmly thank my colleagues: Dr. Marta Mohedano Sanchez, Dr. Sviatlana Lamaka, Dr. Maria Serdechnova, Dr Nico Scharnagl, Dr. Daniel Höche, for their valuable scientific contributions. Mr.Volker Heitmann, Mr. Ulrich Burmester, Mr. Gert Wiese, Mrs. Petra Fischer, Mrs. Sabine Schrader, Mrs. Sabine Schubert, Mr. Volker Kree, Mr. Willi Punessen and Mr. Günter Meister for their technical assistance.

My friends that made my long PhD years very cheerful, Enrique Meza, Hoa Tran Nhu, Rodolfo González, Gurutze Arruebarrena, Emma Morales, Francesca Garesci, Israel Martínez, Carlos Rugerio, Verónica Alvarado, Heidi Pérez, Ligia Nascimento, Orley Milagres, Thiago Conceição, Andrea Kirst, Sangbong Yi, Yukyung Shin, Juliano Soyama, Rafael Paiotti, Karina Suarez, Carmen Gutiérrez, Morelia Vázquez, Dirk Schnubel, Josephin Enz, Henry Ovri, Nathamar Dudamell, Jonathan Inzunza, Lilian Rayas, Javier Trinidad, Mario Salgado, Paula de Oliveira, Ricardo Peniche, José Victoria, Jazmin González, Björn Wiese, Domonkos Tolnai, Gabor Szakacs, Luis Melo, Luis Ibarra, Jorge Domínguez, Roy López, Alexandra Amherd, Jorge González, Damla Keskin, Anissa Bouali, Xiaopeng Lu, Ricardo Buzolin, Yan Chen, Junjie Yang, Bahram Vaghefinazari, Eduardo Silva, Anna-Lisa Chaudhary, Maria Moreno. It has been a great pleasure working in such a friendly environment.

The financial support from the Mexican Council of Science and Technology (CONACyT) and the German Academic Exchange Service (DAAD) are acknowledged for providing me the opportunity to do this work.

A big thank to the german family, Heiner, Biggi, Elke, Erich, Phillip and the two angels Christa and Mario, for their support, love and making me feel at home.

I am also deeply and forever indebted to my family in Mexico, especially to my mother and father, for their love, support and prayers during these years. To the best siblings of this world: Mónica, Jesús, Ignacio, Andrés, Agustin, Carolina as well as Maricela, Norma, Tania and Verónica for being always by my side. My lovely nieces and nephews, Andrea, Mónica, Alejandra, Fernanda, Gabriela, Ximena, Luis, Rebeca, Andrés, Ana, Moisés, Sebastián and Sofía for their love and energy. All my aunts, uncles, cousins and all the good friends that I have in México and around the world, without their support I could never have accomplished this work.

Special thanks also to my dear Oliver for his love, unfailing support and encouragement during these years.

This work is dedicated to my son Pablo who is the most important person in my life. Te amo mi niño lindo!

Lastly but most importantly, I express my profound thanks to the almighty God for his mercies and blessings upon my life.

Muchísimas Gracias!

Summary

The role of intermetallic phases in the corrosion of Mg-RE alloys

A new concept to develop a RE based Mg alloy with improved corrosion resistance was followed in the current work. Based on subsequent characterisation steps to eliminate less suitable RE elements the best microstructure for improved corrosion resistance was identified.

At first, the corrosion properties of selected RE elements were determined. Based on these results RE elements that have a potential to enhance the corrosion resistance of Mg-RE alloys were selected. Two aspects of RE elements were important for the selection: the electrochemical properties and the solid solubility in Mg. If the solubility limit of RE elements in the Mg matrix is exceeded, they form intermetallic phases with Mg. By performing galvanic coupling measurements the compatibility between Mg matrix and intermetallic phases were estimated.

At that point three binary Mg-RE alloys systems remained (Mg-Ce, Mg-La, and Mg-Gd). To evaluate the influence of composition (amount of intermetallic phases) on the corrosion behaviour, four concentrations were cast with 1, 5, 10 and 15 wt. % of RE. Ce and La have a lower solid solubility in Mg matrix generating higher volume fraction of the secondary phases, thus higher dissolution rates in the binary Mg-RE alloys. While Gd with higher solid solubility shows a different behaviour. Additions of up to 10 wt. % Gd resulted in similar behaviour compared to 1 wt. % Gd addition.

The most promising results were obtained for the Mg-Gd system with 10 wt. % Gd. Thus, the microstructure of this alloy was further modified by heat treatments to understand the influence of microstructural changes on corrosion behaviour. A ternary element was used to attempt further optimisation of the corrosion performance. Additions of Al, Zn, Ga and Y did not show any improvement in the corrosion resistance of Mg10Gd. This is due to increasing volume fractions of critical more noble phases and the microstructure dominated by eutectic phase formation. Thus galvanic effects became much stronger due to the increased amount of cathodic phases in the eutectic regions. Mn was the only suitable ternary alloying element as it did not lead to the formation of Mn-rich intermetallics. It was found in solid solution in the intermetallics and to a lesser extent in the matrix without modifying the microstructure but increasing the corrosion resistance. The results of this work allow the design of new corrosion resistant Mg-Gd-Mn alloys by electrochemical evaluation and understanding of the basic corrosion mechanisms and interactions of the different phases. Better performance was predicted for reduced Gd contents and was finally experimentally verified.

Zusammenfassung

Die Rolle von intermetallischen Phasen in der Korrosion von Mg-SE-Legierungen

In der vorliegenden Arbeit wurde ein neues Konzept verfolgt, um eine SE-basierte Mg-Legierung mit verbesserter Korrosionsbeständigkeit zu entwickeln. Anhand von nachfolgenden Charakterisierungsschritten wurden Gefüge und Korrosionseigenschaften korreliert und dabei weniger geeignete SE-Elemente schrittweise eliminiert.

Zuerst wurden die Korrosionseigenschaften von ausgewählten reinen SE-Elementen bestimmt. Basierend auf diesen Ergebnissen wurden SE-Elemente ausgewählt, die ein Potential vermuten lassen, Mg-SE-Legierungen mit guten Korrosionseigenschaften zu ermöglichen. Dabei waren zwei Aspekte für die Auswahl der SE-Elemente wesentlich: die elektrochemischen Eigenschaften und die Löslichkeit im Magnesium. Ist die Löslichkeitsgrenze von SE-Elementen in der Mg-Matrix überschritten, bilden sich intermetallische Phasen mit Mg, die über Lokalelementbildung maßgeblich die Korrosionseigenschaften beeinflussen. Im nächsten Schritt wurden deshalb anhand von Polarisations- und Kontaktkorrosionsmessungen (intermetallische Phase/Matrix) die intermetallischen Phasen identifiziert, die eine gute elektrochemische Kompatibilität mit der Magnesiummatrix und hohe Eigenkorrosionsbeständigkeit aufweisen.

An diesem Punkt blieben drei binäre Mg-SE-Systeme von Interesse übrig (Mg-Ce, Mg-La und Mg-Gd). Um den Einfluss der Zusammensetzung (Menge an intermetallischen Phasen) auf das Korrosionsverhalten zu bewerten, wurden je vier Legierungen mit Konzentrationen von 1, 5, 10 und 15 Gew.% der jeweiligen SE-Elemente gegossen. Ce und La haben eine geringere Löslichkeit im festen Zustand in der Mg-Matrix, so dass ein mit der Legierungskonzentration zunehmender Volumenanteil der intermetallischen Phasen vorliegt, der mit höheren Auflösungsraten der binären Mg-RE-Legierungen korreliert werden kann. Gd mit einer deutlich höheren Löslichkeit im festen Zustand zeigt diese Konzentrationsabhängigkeit der Korrosionsrate bis 10 Gew. % Gd nicht und das Gefüge kann wegen der hohen Löslichkeit einfach modifiziert werden.

Insgesamt zeigte das Mg-Gd-System mit 10 Gew. % Gd im Gusszustand schon vielversprechende Korrosionseigenschaften, die durch weitere Modifikationen optimiert werden sollten. Im ersten Optimierungsschritt wurden unterschiedliche Wärmebehandlungen durchgeführt, um den Einfluss von Gefügeänderungen auf das Korrosionsverhalten zu verstehen. Fein verteilte Phasen hatten einen positiven Einfluss auf die Korrosionsbeständigkeit. Im zweiten Schritt wurde ein weiteres Legierungselement zu legiert, um die intermetallische Phase zu modifizieren. Zusätze von Al, Zn, Ga und Y zeigten jedoch eine Abnahme der Korrosionsbeständigkeit im Vergleich zu Mg10Gd. Dieses Verhalten konnte auf steigende Volumenanteile der kritischen edleren intermetallischen Phasen und eine verstärkte eutektische Phasenbildung zurückgeführt werden. Die lokalen galvanischen Effekte verstärkten sich sowohl durch die erhöhte Menge der kathodischen Phasen und deren kritische

Anordnung in den eutektischen Regionen. Mn erwies sich als das einzige geeignete ternäre Legierungselement, da es nicht zur Bildung von neuen Mn-reichen intermetallischen Verbindungen führte und die Korrosionsbeständigkeit erhöhte. Es löste sich sowohl in der intermetallischen Mg5Gd-Phase als auch in der Matrix, ohne das Gefüge zu beeinflussen. Die negativen Einflüsse der intermetallischen Phase wurden durch die Mn-Zugabe reduziert, die Korrosionsbeständigkeit der Matrix und die Passivierbarkeit der Legierung verbessert.

Zusammenfassend ermöglichen die Ergebnisse dieser Arbeit die Entwicklung neuer korrosionsbeständigerer Mg-Gd-Mn-Legierungen durch das Verständnis der grundlegenden Korrosionsmechanismen und der Korrelation von Gefüge (Rolle der intermetallischen Phasen) und der Korrosionseigenschaften. Abschließend wurden aufgrund der Ergebnisse deutlich bessere Korrosionseigenschaften für reduzierte Gd-Gehalte bei gleichbleibenden Mn-Gehalten vorhergesagt und experimentell verifiziert.

Table of Contents

List of abbreviations and symbols

γ	Activity coefficient
A	Exposed area
AC	Alternating current
AE	Auxiliary electrode
AMS	Aerospace material specification
ASTM	American society for testing and materials
BSE	Back scattered electrons
C_{dl}	Capacitance of the double layer
Ce	Cerium
C_{Oxi}	Capacitance of the oxide
CPE	Constant phase element
CR	Corrosion rate
DC	Direct current
Dy	Dysprosium
E	Potential
E_{corr}	Corrosion potential
EDS	Energy dispersive X-ray spectroscopy
EEC	Electrical equivalent circuit
EFV	Expeditionary fighting vehicle
EIS	Electrochemical impedance spectroscopy
E_{pit}	Pitting potential
F	As-cast condition
Gd	Gadolinium
HER	Hydrogen evolution reaction
HP	High purity
I	Current
i_{corr}	Corrosion current density
La	Lanthanum
LPSO	Lamellar long period stacking ordered
MBED	Micro-beam electron diffraction
Mg	Magnesium
MMPDS	Metallic materials properties development standardization
Nd	Neodymium
NDE	Negative difference effect
NHE	Normal hydrogen electrode
NSF	Neutral salt fog method
OCP	Open circuit potential
OM	Optical microscopy
PBR	Pilling-Bedworth ratio
PEO	Plasma electrolytic oxidation
R	Resistance
R_{Ct}	Charge transfer resistance
RE	Rare earth metals
RE	Reference electrode
R_{Oxi}	Resistance of the oxide
R_S	Resistance of the electrolyte
SAE	Society of automobile engineers
SAED	Selected area electron diffraction
SCC	Stress corrosion cracking
SE	Secondary electrons
SEM	Scanning electronic microscopy
SHE	Standard hydrogen electrode
SKPFM	Scanning Kelvin probe force microscopy
SSSS	Supersaturated solid solution
T4	Solution treatment
T6	Ageing treatment
TEM	Transmission electron microscopy
V_{β}	Volume of ß-phase
V_{α}	Volume of α-Mg
WE	Working electrode
XPS	X-ray photoelectron spectroscopy
XRD	X-ray diffraction
XRF	X-ray fluorescence
Y	Yttrium
Z	Impedance
Δg	Weight change
ΔH_f	Enthalpy of formation
ρ	Density of the material
ω	Frequency

1. Introduction

The poor corrosion resistance of many Mg alloys is due to two general reasons: *i)* the internal galvanic corrosion caused by impurities or second phases [1] and *ii)* the quasi-passive hydroxide film on Mg is less stable than the passive films which form on other metals such as aluminium and stainless steels [2]. Important improvements have been achieved during the last decade such as reducing the heavy metal impurity content, using diverse alloying elements and heat treatments to increase the resistance of magnesium alloys against corrosion in various environments. These advances can be understood partly in terms of increased passivity of the metal surface by incorporation of component which stabilizes the oxide formation on Mg alloys [3-11]. In NaCl solutions the Mg dissolution rate is higher, because chlorides can interfere with the formation and maintenance of the protective layer of corrosion products which decrease the severity of the attack [12]. Previous studies show that rare earth elements (RE) have a significant positive influence on the corrosion resistance of Mg alloys [13-23]. The rare earth elements improve the tendency of magnesium to passivation and decrease the micro-galvanic influence of the secondary phases [6, 12, 23, 24]. The RE elements and Mg are electrochemically active metals, the standard potentials for RE/RE^{3+} systems are between -2.6 to -2.0 V(SHE) [25, 26] while it is -2.4 V(SHE) for Mg/Mg^{2+} [1, 25] in aqueous solutions. However, RE elements have less active open circuit potential values compared with pure Mg in NaCl solution. This suggests the formation of an oxide layer on the surface [26, 27] which is more stable than the oxide on pure Mg, e.g. Gd and Dy. However, the layers on the surface of the other rare earth elements (e.g. La, Y and Ce) do not provide sufficient protection in solutions containing chloride ions as they show very high corrosion rates [28, 29]. As described above the second reason of the low corrosion resistance of the Mg alloys is due to the internal galvanic corrosion caused by second phases.

Due to different electrochemical properties and the formation of localised galvanic cells the presence of intermetallics can influence the overall corrosion resistance of Mg alloys. Such galvanic couples generate due to the inhomogeneity inherent in these alloys: rich phases in Mg coexisting with intermetallic phases rich in more noble elements. The composition of each phase and its volume fraction in an alloy, influence the level of galvanic interaction. Identifying the noncritical intermetallic phases, understanding the mechanisms to reduce the internal galvanic effects are essential tools to enhance the corrosion performance of Mg alloys. Thus the present work focuses on production and characterisation of a new Mg-RE alloy and optimisation of its corrosion resistance. Starting with a broad selection of RE elements the number of suitable RE were reduced in a sequence of basic studies ending finally with a new ternary Mg alloy. The following steps were performed:

1. Evaluation of electrochemical properties from proposed pure RE metals (Ce, Dy, Gd, La, Nd, and Y).

2. Production of isolated Mg-RE-intermetallics (Ce, Gd, La, Nd and Y) to determine their electrochemical properties and measurement of the galvanic current between the different phases and Mg matrix.
3. Analysis of the behaviour of selected intermetallics in the matrix (Ce, Gd, La) influence of composition, size, amount and distribution of intermetallic phases on the corrosion behaviour.
4. Development of corrosion minimisation strategies (Gd): a) heat treatments to minimise internal galvanic effects. b) Effects of additional ternary alloying elements. The selected elements are on the one hand typical commercial for Mg alloys e.g. Al, Mn, Y, Zn, or on the other hand more unusual e.g. Ga and c) determination of corrosion mechanisms.

The alloys fabricated were characterised not only with electrochemical techniques but also with XRD, SEM, TEM, EDX and XPS to obtain correlations between microstructures, intermetallic phases, passive films formation and corrosion properties.

2. Fundamentals

2.1 Magnesium and its alloys

Magnesium is considered as one of the lightest metals; this property makes it attractive for a number of applications where weight reduction is of importance. Magnesium alloys offer high stiffness/weight ratios, excellent machinability and high damping capacity [3, 30]. Moreover magnesium alloys possess, high thermal and electrical conductivity, good vibration and shock adsorption ability without toxic hazard [3, 31]. However, there are aspects concerning magnesium alloys which limit their usage for critical applications. The low ductility of some of the alloys is one problem, and the galvanic corrosion of magnesium in contact with other materials is another big issue. This could be further improved by appropriate processing and additional treatments of magnesium alloys, and thus these alloys have a great potential for many applications in the automotive and aeronautic industries [32].

2.2 Corrosion of magnesium

Magnesium alloys have relatively poor corrosion resistance which has been one of the reasons for lack of the widespread application of these alloys. One of the major challenges in the use of Mg alloys is their high susceptibility to corrosion attack [33]. There are three main factors that contribute to the poor corrosion resistance of magnesium alloys:

a) Magnesium is the most active metal used in engineering applications [34]. Thermodynamically, magnesium should react completely with oxygen and with water [35].

b) Susceptibility to internal galvanic attack caused by alloying or impurity elements and conditions which impede the stability of the protective film [36].

c) The oxide/hydroxide passive film on magnesium is much less stable than passive films formed on other metals such as iron or aluminium. This film has poor pitting resistance [37].

In a corrosive environment, pitting or other forms of local corrosion occurs as a result of film breakdown [35]. So magnesium is less resistant to acidic or saline environments. Since the corrosion resistance of magnesium alloys depends both on the concentration of critical chloride ions and the pH of the medium. So the corrosion rate increases for example with the concentration of chloride ions for any value of pH [38]. Sulphates, phosphates and nitrates attack magnesium but not to the same extent as chlorides [4]. Corrosion of magnesium alloys in the presence of chloride ions usually starts with the formation of irregular pits extendendly occupying the entire surface [4]. However this mechanism is different from the autocatalytic pitting observed in stainless steels, where there is a tendency to the formation of deep pits [39, 40]. This effect is not observed in the magnesium base materials probably due to the increase of pH caused by the formation of hydroxide layer on the surface of magnesium alloys [39, 41-43]. Generally, the corrosion rate is not significant in alkaline media at pH values above 10.5, fulfilling thermodynamics as shown in the Pourbaix diagram [25, 44].

2.2.1 Electrochemical basis of magnesium corrosion

The electrochemical reaction of magnesium in aqueous environments produces magnesium hydroxide and hydrogen gas. Consequently magnesium corrosion is relatively insensitive to the oxygen concentration, although the oxygen concentration is an important factor in atmospheric corrosion [4]. The corrosion attack in aqueous environments often involves micro-galvanic coupling between cathodic and anodic areas. The overall reaction for the corrosion of magnesium could be expressed as follow:

$$Mg + 2H_2O \rightarrow Mg(OH)_2 + H_2 \qquad (1)$$

This total reaction could be divided into two partial reactions according to reactions (2) and (3). The anodic partial reaction of Mg dissolution, reaction (2) may involve intermediate steps which produce the monovalent magnesium ion (Mg^+), with short lifetime [2]. The reduction process of hydrogen ions, reaction (3), and the hydrogen overvoltage of the cathodic phase play an important role in the corrosion of Mg. Low overvoltage cathodes such as Fe, Ni, Co, or Cu facilitate hydrogen evolution, causing a substantial corrosion rate [45]. Furthermore $Mg(OH)_2$ can form if the solubility limit is exceeds. The reaction product formation is described in reaction (4) [4].

$$2H^+ + 2e^- \rightarrow H_2 \qquad (cathodic\ partial\ reaction) \qquad (2)$$

$$2Mg \rightarrow 2Mg^+ + 2e^- \qquad (anodic\ partial\ reaction) \qquad (3)$$

$$Mg^{2+} + 2OH^- \rightarrow Mg(OH)_2 \qquad (corrosion\ product\ formation) \qquad (4)$$

The corrosion potential of Mg is approximately -2.37 V_{NHE}[1] [46] in aqueous solutions at 25°C. Mg forms magnesium hydroxide film, which can provide some protection over a wide pH range. Assuming that the protective film on Mg is $Mg(OH)_2$, the thermodynamics that govern the formation of this film are described by the Pourbaix diagram (Figure 2.1), which shows that Mg^{2+} is stable in most aqueous solutions up to ~ pH=10, above which $Mg(OH)_2$ is stable.

---

[1] The standard electrode is the *normal hydrogen electrode* (NHE) or *standard hydrogen electrode* (SHE) realized by bubbling hydrogen gas over a platinum surface, which has all components at unit activity. The reaction is $2H^+[1N] + 2e^- \rightarrow H_2[1\ atm]$. Potentials are often measured and quoted with respect to reference electrodes other than the NHE.

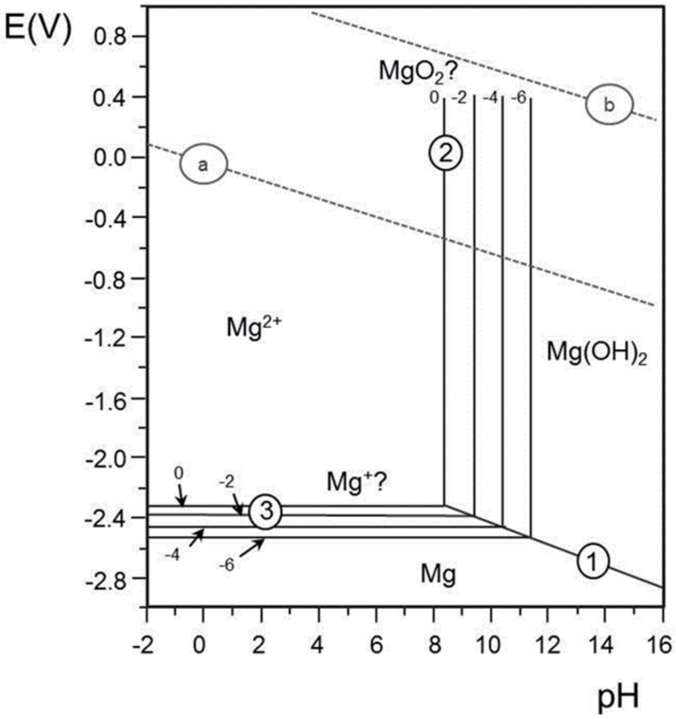

Figure 2.1 Pourbaix diagram for the Mg-H_2O system at 25 °C [25] .

In Figure 2.1 the region of water stability lies between the dashed lines marked a) and b). The different regions are separated by the following reactions:

(1) $Mg + 2H_2O \rightarrow Mg(OH)_2+H_2$

(2) $Mg^{2+} + H_2O \rightarrow MgO + 2H^+$ and

(3) $Mg \rightarrow Mg^{2+}+ 2e^-$

The magnesium peroxide (MgO_2) is marked in the Figure 2.1 as a guide but it was not taken into account in establish the equilibrium diagram because MgO_2 has not been prepared in the pure state. To obtained this is only by the action of hydrogen peroxide (H_2O_2) on Mg, on MgO or on the $Mg(OH)_2$. The lines marked as 10^0, 10^{-2}, 10^{-4}, and 10^{-6} represent the activity[2] [47] of the species. [4].

Several studies of magnesium suggested that the corrosion of magnesium and magnesium alloys initiates due to localized corrosion, and sometimes the localized corrosion is shallow and extended. Nevertheless the corrosion morphology of magnesium and its alloys depends on the alloy composition and the environmental exposure.

Table 2.1 details the different types of corrosion that occur in magnesium and magnesium alloys [3].

---

[2] Activity (a_i) is the effective concentration that takes into account the deviation from ideal behaviour, with the activity of an ideal solution equal to one. The activity value is affected by the concentration, temperature and pressure and normally is determined using an activity coefficient (γ_i) to convert from the solute's mole fraction x_i (as a unit concentration) to activity a_i using the following formula: $a_i=\gamma_i x_i$. For ideal solutions, pure and solid substances $a_i=x_i$ thus $\gamma_i=1$.

Table 2.1 Types of corrosion on Mg alloys and their features [3]

Corrosion type	***Special features***
Galvanic corrosion	▪ Localized corrosion of the magnesium adjacent to the cathode. ▪ External cathodes, as other metals in contact with magnesium (galvanic corrosion external). ▪ Internal cathodes, as second or impurity phases (galvanic corrosion internal). ▪ Highly susceptible to impurities such as Ni, Fe, Cu. ▪ The galvanic corrosion rate is increased by: highly conductive medium, large potential difference between anode and cathode, low polarisability of anode and cathode, large area ratio between cathode to anode, and short distance from anode to cathode [44].
Intergranular corrosion	▪ Slightly susceptible. ▪ Corrosion is normally concentrated in the area adjoining the grain boundary until eventually the grain may be undercut [2, 30].
Localized corrosion	▪ Highly susceptible when exposed to chloride ions and in a non-oxidizing medium [48]. ▪ Typically occur as pitting in neutral or alkaline salt solutions [49]. ▪ Heavy metal impurities promote general pitting attack [50]. ▪ In Mg-Al alloys: the pits form by selective attack around the cathodic areas [51]. ▪ Filiform corrosion due to an active corrosion cell moving across the alloys surface, where the head is the anode and the tail the cathode [52].
Stress corrosion cracking (SCC)	▪ In Mg alloys SCC is mainly transgranular however intergranular SCC occurs when $Mg_{17}Al_{12}$ precipitates along the grain boundaries (Mg-Al-Zn alloys) [2]. ▪ Alloying elements such as Al or Zn promote SCC [53], but additions of Zr protect against SCC [54]. ▪ Mg is resistant to SCC in alkaline media above pH 10.2, fluoride solutions and neutral solutions containing chlorides [44].
Corrosion fatigue	▪ Cracks propagate in a mixed transgranular-intergranular mode [55].
Corrosion at elevated temperatures	▪ The oxidation rate of Mg is a linear function of the time indicating a non-protective oxide on the magnesium surface [44]. ▪ Alloying elements such as Al and Zn promote a higher oxidation rate [44]. ▪ Ce and La additions show a lower oxidation rate compared to pure Mg [44].

2.3 Negative Difference Effect (NDE)

Gas evolution plays an important role in the overall process of material dissolution. For instance, under certain circumstances, the rate of hydrogen evolution on pure Mg increased with increasing potential [56]. This phenomenon is known as the *negative difference effect (NDE)*. Normally in electrochemistry, the corrosion reactions are classified as cathodic or anodic processes. In the majority of metals an anodic process increases with an applied more noble potential or current density generating an increase of the anodic dissolution rate and simultaneously a decrease in the cathodic hydrogen evolution rate. However, in magnesium the hydrogen evolution behaviour is quite different from iron, steels etc. Its behaviour is seen as contrary to that established with common electrochemical rules [3]. Figure 2.2 shows schematically the experimental representation of the *NDE* [5].

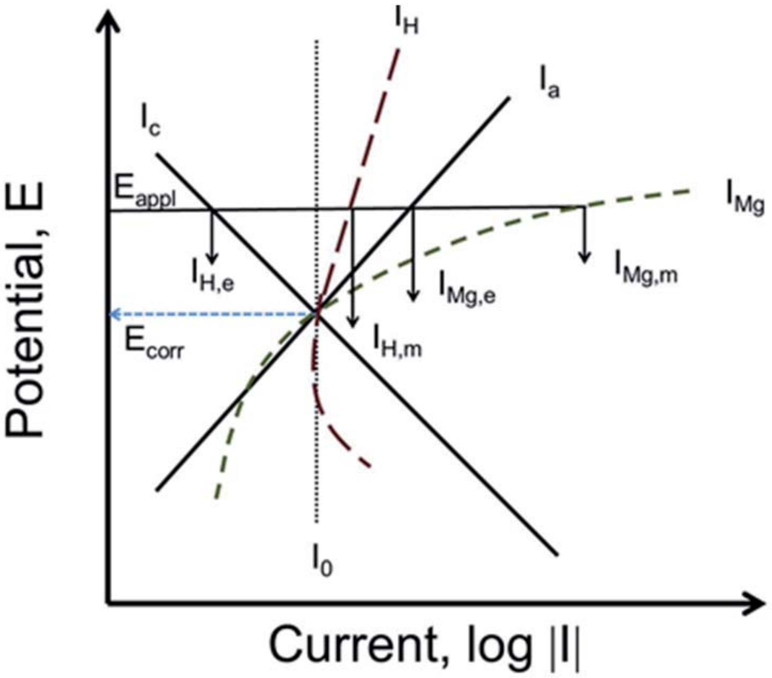

Figure 2.2 The Negative Difference Effect (NDE) of magnesium and its alloys [5]

In Figure 2.2 the solid lines correspond to the normal anodic partial reaction (marked as I_a[3]) and cathodic partial reaction (marked as I_c[4]), respectively, based on the Tafel kinetics[5]. The intersection of the two lines corresponds to I_0 at the corrosion potential E_{corr}. If the potential E_{appl} is more positive, then the rate of the anodic partial reaction would be expected to increase along

---

[3] In the anodic partial reaction (I_a) the metal atom loses n electrons and becomes n^+ ion. This is the oxidation reaction: $M \rightarrow M^{n+} + ne^-$ for Mg alloys is expressed as follow: $Mg \rightarrow Mg^{2+} + 2e^-$

[4] In the cathodic partial reaction (I_c) the electrons produced in the oxidation reaction are used up in the reduction reaction: $H^+ \rightarrow e^- + \frac{1}{2} H_2$

[5] Tafel kinetics is based on the oxidation or reduction reactions. The anodic linear section and the cathodic linear section are extrapolated to find the intersection at E_{corr} and i_{corr}. The anodic and cathodic currents are the same at E_{corr} - where the curves intersect. This results in a measured current difference approaching zero.

the curve marked as I_a to $I_{Mg,e}$ and simultaneously the cathodic reaction would be expected to decrease along the curve I_c to the value $I_{H,e}$ [5]. However, experimentally with Mg the hydrogen evolution reaction (HER) rate increased rather than decrease with increased potential [3-5]. As the potential is increased to more positive values:

- The hydrogen evolution reaction increased as shown by the dashed line marked as I_H. Thus for an applied potential E_{appl}, the actual HER corresponds to the value $I_{H,m}$, which represents a HER current significantly greater than the expected current $I_{H,e}$. For this condition there is a negative difference effect; the quantity Δ is negative because $I_{H,m}$ is greater than I_0.
- The second experimental observation is that the anodic dissolution current of magnesium increase faster than expected from the polarisation curve. This is shown by the dashed curve marked as I_{Mg}. Thus for an applied potential E_{appl}, the actual dissolution rate corresponds to the $I_{Mg,m}$; which represents a corrosion current significantly greater than the expected current corresponding to $I_{Mg,e}$, which does not follow the Faraday's Law.

For decades, investigators have been trying to explain the *NDE* phenomenon with electrochemical reaction mechanisms and five different mechanisms have been proposed for magnesium and its alloys. All five mechanisms succeed in explaining some part of the phenomenon, and fail to deal with other aspects. However, it is important to clarify the actual mechanism which operates in magnesium as an understanding of the *NDE* is required for understanding the electrochemical corrosion of magnesium alloys [3].

Mechanism I. Partially protective film

This mechanism attributes the *NDE* to the breakdown of the partially protective film on the magnesium surface during anodic dissolution [48, 57, 58]. The film is increasingly disrupted as the external current density or potential increased. The detection of $Mg(OH)_2$ and MgO on the magnesium surface by ex-situ techniques support this model [36, 59, 60]. However, there is no direct evidence that the film is partially protective. Parrault et al. [61] criticised this mechanism as it could not explain the corrosion potential of magnesium in neutral or acidic solutions.

Mechanism II. Undermined particles

NDE is explained in terms of the undermining and removal of second phase particles during corrosion, especially at a higher anodic current density or potential [37, 61, 62] . Most second phase particles, for example $Mg_{12}Al_{17}$ or the iron-rich impurity phase Al_3Fe, are cathodic to the surrounding magnesium matrix which undergo accelerated local corrosion at the particle boundary by local galvanic corrosion. It is common for a particle to be undermined by the corrosion of the adjacent magnesium matrix and fall out subsequently, resulting in a mass loss higher than that due to electrochemical dissolution. To support this mechanism, Kruger et al.

[37] provided SEM photomicrographs which showed a particle which had been partially undermined.

Mechanism III. Monovalent Mg ion

Monovalent magnesium ions may be involved as an intermediate species in the anodic dissolution process as the calculated valence of dissolved magnesium was reported in the range from 1.33 to 1.66 [61, 63-65]. Monovalent ion, Mg^+, is produced electrochemical according to:

$$Mg \rightarrow Mg^{+} + e^{-} \qquad (5)$$

The monovalent Mg^+ is assumed to exist as an intermediate species and react chemically to evolve hydrogen by means of:

$$2Mg^{+} + 2H^{+} \rightarrow 2Mg^{2+} + H_2 \qquad (6)$$

This provides a chemical rather than an electrochemical mean of hydrogen production.

Mechanism IV. MgH_2 formation

Magnesium can be reduced to hydride by the following electrochemical reaction:

$$Mg + 2H^{+} + 2e^{-} \rightarrow MgH_2 \qquad (7)$$

The MgH_2 is not stable in contact with water and reacts chemically to from hydrogen:

$$MgH_2 + 2H_2O \rightarrow Mg^{2+} + 2OH^{-} + 2H_2 \qquad (8)$$

The mechanism is based on thermodynamic data which predicts the stability of MgH_2. Strong evidence for the existence of MgH_2 comes from X-ray diffraction of material scraped from a magnesium electrode surface [57, 61, 66, 67].

Mechanism V. Re-deposition of the iron impurities based on Heyrovsky mechanism

Recently, Hoeche et al. [68] proposed how iron impurities influence the hydrogen evolution reaction (HER) during global anodic polarisation of magnesium based on two mechanisms. Firstly, a cathodic surface activity caused exposition to the impurities (Fe). This process act as kind of alkaline electrolysis electrodes based on Heyrovsky reactions (9 and (10) [69]. The electrochemical desorption process has much faster kinetics than the chemical desorption described by Tafel mechanism [68].

$$H_2O + e^{-} \leftrightarrow H_{(a)} + OH^{-} \qquad (Volmer) \qquad (9)$$

$$2H_2O + H_{(a)} + e^{-} \leftrightarrow H_{2(g)} + OH^{-} \qquad (Heyrovsky) \qquad (10)$$

At the beginning the area fraction between Mg and the active impurity surface is large (A_{Mg} /A_{imp} <<1) and the mixed electrolyte potential is close to that of Mg. Since Mg presents a faster anodic dissolution process, extensive negative overpotentials occur at the cathodic surface sites. The cathodic process is controlled by Heyrovsky reaction. Subsequently initiates the Mg^{2+} ions formation due to Mg dissolution [68].

Secondly, with the increase cathodic current influenced by the corrosion process itself forming a bilayer composed by $MgO/Mg(OH)_2$ with some Fe enrichment (dark film). This film is a result of impurity self-corrosion at the corrosion forefront. Additionally the re-deposition of the impurities (Fe) which accelerates HER and act as dominant process after the initial period. With corrosion progress of the dark zone fresh metallic Fe areas are newly deposited at the corrosion forefront in combination with increased H_2 generation. It is likely, that Mg dissolution and undermining mechanism around freshly re-deposited Fe film leads to its detachment followed by dissolution, reduction from solution and another re-deposition process [68].

2.4 Effect of alloy composition

The poor corrosion performance of Mg alloys depends on their metallurgy and external environmental factors. Magnesium metallurgy includes alloying and impurity elements, phase components and microstructure. Manipulation of phases present and composition help to improve the corrosion resistance of magnesium alloys [3].

2.4.1 Impurities

Due to the high reactivity of magnesium, alloying elements may have a detrimental effect on corrosion resistance of the magnesium alloy. Hanawalt et al. [36] evaluated the corrosion rate of fourteen magnesium binary alloys in salt water, and found that concentrations of up to 0. 2 wt. % of Fe, Ni, Cu and Co generated a high increment in the corrosion rate. Ag, Ca and Zn showed moderate negative influence for concentrations between 0.5 to 5 wt. %. Al, Sn, Cd, Mn, Si and Na exhibited relatively small influence on the corrosion rate for concentrations up to 5 wt.%. Other studies have confirmed that the most critical factor for the corrosion behaviour is the metal purity [31, 70]. Hillis et al. [71] reported that the corrosion rates are accelerated by a factor between 10 and 100 when the concentrations of impurity elements Ni, Cu and Fe increased beyond certain tolerance levels. These heavy metals form galvanic cells and enhance the corrosion rate and the effect of these impurities on the corrosion rate is illustrated in Figure 2.3 [70]. The tolerance limit depends on the alloys composition, for pure magnesium, the tolerable limits for Cu, Fe and Ni are 0.1 %, 0.005, and 0.0005 wt. % respectively. While or example, AZ91 alloy has tolerance limits of 20 ppm Fe, 12 ppm Ni and 900 ppm Cu [36]. The impurities arise from various sources; the iron from the melting crucibles and tools, copper comes from impure aluminium, while nickel is coming from containing stainless steel crucibles or traces may be contained in magnesium [54]. Once these impurities are within tolerable limits, a substantial improvement in the corrosion resistance of magnesium alloys could be seen [72]. Magnesium alloys in which the total of these impurities is restricted to “ppm” levels are referred to as high purity (HP) alloys, and these alloys can compete with aluminium alloys in terms of corrosion resistance [70]. Fe, Cu and Ni are extremely deleterious to corrosion resistance due to their low solid-solubility limits and formation of active cathodic sites [52, 73]. When the same concentration is used, the detrimental effect of these elements is as follows: Ni > Fe > Cu [74]. Additionally the surface contamination is important; producers of magnesium have demonstrated the importance of high-purity alloys for structural applications. However, surface contamination from handling and mechanical treatment can destroy the corrosion resistance of high-purity alloys, e.g., ceramic blasting media containing iron oxide can be just as harmful to the corrosion properties of magnesium as steel grit [73].

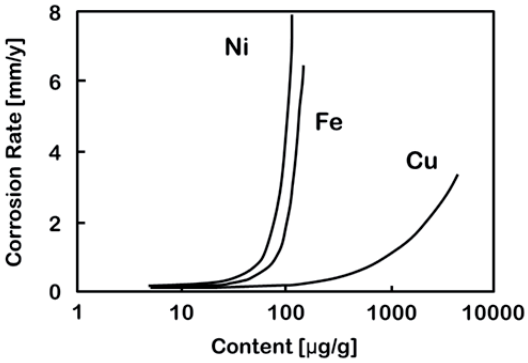

Figure 2.3 Effect of the impurities on the corrosion rate of magnesium alloys AZ91 [70]

2.4.2 Common alloying additions

The micro galvanic effects, as well as the formation of passive layer to minimize the corrosion can be influenced by additions of specific alloying elements. Table 2.2 shows the most common alloying elements for magnesium [32, 75]. The effect on corrosion behaviour of some of these elements is described below.

Table 2.2 Most commonly used alloying elements, and their respective notation letter [32, 75, 76]

Abbreviation letter	Alloying element	Abbreviation letter	Alloying element
A	Aluminium	**N**	Nickel
B	Bismuth	**P**	Lead
C	Copper	**Q**	Silver
D	Cadmium	**R**	Chromium
E	Rare earths	**S**	Silicon
F	Iron	**T**	Tin
H	Thorium	**W**	Yttrium
K	Zirconium	**Y**	Antimony
L	Lithium	**Z**	Zinc
M	Manganese		

a) Aluminium (Al)

Aluminium is one of the most important alloying elements for increasing the tensile yield strength of magnesium alloys by forming the intermetallic phase $Mg_{17}Al_{12}$. In addition to the improvements in mechanical properties, a higher amount of Al also significantly increases the castability. This is the main reason why most technical alloys, specially casting alloys, contain Al. However, the disadvantage is that a higher tendency to micro-porosity is observed as the aluminium content is increased [77]. Aluminium also improves the corrosion resistance in magnesium alloys when the alloying addition is increased from 2 to 9 wt. %. The benefit is twofold; first, the precipitation of the ß- $Mg_{17}Al_{12}$ forms a favourable corrosion resistant network along the grain boundaries, and second, the incorporation of aluminium oxide into the $Mg(OH)_2$ layer improves the stability of the passive layer on the surface and thus enhances the corrosion resistance [78-80]. Due to superior passive layer formation on the surface in aluminium containing magnesium alloys, a special form of corrosion can be observed. The so called filiform corrosion, is normally observed only underneath thin coatings [32]. Aluminium can also have a bad influence on corrosion due to reduction of the iron tolerance limit from 170 ppm to 20 ppm [54]. It was reported that the tolerance limit of iron decreases almost linearly with increasing aluminium content and allows the formation of a passive iron-manganese-aluminium intermetallic phase on solidification [81].

b) Zinc (Zn)

Zinc is another important alloying element for magnesium. This element behaves similarly to Al in terms of strengthening and castability. By adding up to 3 wt.% Zn to magnesium, shrinkage can be reduced and tensile yield strength is increased [82]. In addition to the improvements in mechanical properties, recent studies in binary Mg-Zn alloys by Meza et al. [82] showed that Zn is an important alloying element which contributes to grain refinement. The grain refinement mechanism is controlled by the Zn solute content and is associated with under-cooling of the melt. The grain refinement in the casting process also will influence strongly the deformation behaviour during thermo-mechanical processes like rolling and extrusion. In combination with other elements such as zirconium and/or thorium, Zn positively influences the mechanical properties. Additionally Zn improves the corrosion resistance of Mg alloys [32]. The presence of zinc in either binary or ternary alloys affect the surface film characteristics [3]. Zinc increases the tolerance limits and reduces the effect of impurities on corrosion once the tolerance limit has been exceeded [70]. In Mg-Al alloys, zinc improves the tolerance limits for Fe, Cu and Ni, but Zn addition is limited to 1-3 wt.% due to increased hot tearing susceptibility [50]. Additions of 3 wt.% Zn raises the tolerance limit to 30 ppm Fe and reduces the corrosion rate for iron concentrations of up to 180 ppm for the Mg-Al-Mn alloy [44]. For Mg-Al-Mn-Ni alloys, 3 wt.% Zn shifts the tolerance limit of Ni from 10 to 20 ppm and reduces the corrosion rate at higher concentrations of nickel [44]. Filiform corrosion in AZ alloys increases as the amount of zinc increased in the range of 0-3 wt.% [51]. Lunder et. al. [83] evaluated the influence of composition on various phases found in Mg-Zn alloys. They concluded that zinc render both α and β more noble. Zinc has an anomalous effect on the corrosion behaviour of magnesium produced by rapid solidification. The maximum corrosion rate occurs at 18.6 wt.% Zn, and additions of 4.8 wt.% and 27.5 wt.% Zn resulted in a corrosion rate slightly higher than that of pure magnesium [37].

c) Manganese (Mn)

In Mg alloys with rare earths metals the Mn addition improves their strength [84]. The small increase of the strength from Mn addition was confirmed for Mg-Nd alloys [84]. At room temperature the highest strengthening effect was observed at a Mn content of 1.60 wt. %. Manganese also improved the strength of the Mg-Nd alloys during creep at elevated temperatures [84]. The plasticity of the Mg-Nd alloys was unchanged when Mn was added [84]. Similar results were obtained with Mn addition to Mg-10Gd alloys [84]. The study was carried out using hot extruded rods. The alloy Mg10Gd was used as the base for addition of up to 1.5 wt. %. Unlike for mishmetal and neodymium containing alloys Mn additions was accompanied by significant decrease of plasticity [84]. According to the ternary phase diagrams of the Mg-RE-Mn systems there are no intermetallic phases with RE and Mn expected in Mg-rich alloys. Manganese did not actually change the solubility of the rare earth metals in Mg.

Manganese improves corrosion resistance of Mg alloys, particularly in the AZ series alloys [37]. Manganese itself does not improve the corrosion resistance, but it reduces the effect of impurities [2, 50]. In Mg-Al alloys, manganese increases tolerance limit of Ni [2], and Fe [54]. The critical iron content depend on the Mn content and the ratio Fe/Mn has been found to be a critical factor for corrosion resistance [81, 85]. Alloys with high ratio of Fe/Mn have a high corrosion rate regardless of the surface condition, heat treatment and grain size, whereas alloys with low Fe/Mn ratio and low Ni and Cu concentration show good corrosion performance [6]. There are two possible reasons for the reduced corrosion rate due to Mn. Firstly, Mn combines with the iron in the molten magnesium and forms an intermetallic compound which settles in the bottom of the crucible thereby decreasing the iron content of the alloy [74, 86, 87]. Secondly, Mn encapsulates the remaining iron particles during solidification, making them less active as local cathodic sites [87-89].

d) Zirconium (Zr)

In magnesium alloys zirconium is used as a grain refiner, in alloys that do not contain Al, Sn or contaminants such as C, N, O or H. Zirconium prevents grain growth during heat treatments [32]. Normally Zr alloys have good corrosion resistance in salt solutions and are relatively insensitive to Fe and Ni. Additions of zirconium in Mg alloys form insoluble particles [54]. In the alloys where zirconium is used as grain refiner, Fe and Ni contents are reduced as they are forming intermetallics in the melt [90].

e) Rare earths (RE)

Rare earth elements, gadolinium, cerium, neodymium, lanthanum, and yttrium, have been added to magnesium either individually or in the form of mishmetals. Despite the substantial differences in constitution and properties, magnesium alloys with rare earths additions show similar features [84]. All rare earth metals lead to improvements in strength when they are added to magnesium. Grain refinement and increased ductility are observed with even small additions of RE. These alloys show good casting properties and reduced weld cracking, mainly due to their narrow freezing range (this tends to suppress porosity). The strength, in particular, high temperature creep resistance and thermal stability [82], make them attractive for commercial applications.

- *Gadolinium (Gd)*

Due to the large solubility of Gd in Mg, it contributes to solid solution strengthening. Above 10 wt. % Gd additions improve strength due to precipitation hardening. The large solubility of Gd with increasing temperature also makes the Mg–Gd system suitable for heat treatments to adjust the mechanical properties in accordance with the requirements of the property profile of an application. By adjusting the concentration of Gd and the heat treatments, the mechanical properties and corrosion behaviour of these Mg–Gd alloys can be varied over a wide range [14]. The addition of gadolinium to AM50 and AZ91D alloys has modified the microstructure of the these alloys resulting in the formation of Al_2Gd and Al-Mn-Gd intermetallic compounds and consequently reduced the fraction of ß-$Mg_{17}Al_{12}$ phase [91, 92]. The corrosion rate of AM50 and AZ91D alloys decreased with additions of 0.7 and 1.0 wt.% gadolinium by 85% and 93%. This effect was associated mainly with the decrease in the cathodic reaction kinetics due to the suppression of micro-galvanic corrosion between primary and secondary phases [91]. In another study of Mg-Al alloys in humid environments, gadolinium reduced the effect of micro-galvanic couples and, consequently, the corrosion rate [92]. Arrabal et al. [93] studied the influence of Gd additions on the high temperature oxidation behaviour of AZ91D magnesium alloy. They found that Gd promotes the precipitation of Al_2Gd and Al-Mn-Gd intermetallic compounds in the AZ91D alloy, resulting in a reduction of the ß-phase fraction ($Mg_{17}Al_{12}$). The corrosion resistance increased due to improved surface passivity and suppression of micro-galvanic couples [94]. The changes results in a reduction of corrosion rates between 72-81% compared to AZ91D alloy without gadolinium additions.

- *Lanthanum (La)*

Lanthanum has a relatively low solubility in Mg compared with other rare earth elements [84]. Lanthanum is an abundant rare earth element. It has been considered as a substitute for other precious rare earth elements such as praseodymium (Pr) and neodymium (Nd) [95]. La provides excellent strengthening and enhance creep resistance due to the ability to form solid solutions in Mg and the formation of La-rich disperse phase precipitates [84], and has been widely used in AZ alloys [96]. Zang et al. [97] established that Mg alloys with Al and La additions consisted of various phases such as $Al_{11}La_3$ and Al_2La, depending on the concentrations of alloying elements. Both $Al_{11}La_3$ and Al_2La phases were distributed along the grain boundaries and these phases occupied a large area of the grain boundary, simultaneously blocking grain boundary sliding and dislocation motion in the vicinity of the grain boundary, and thus leading to the improvement of the tensile property of Mg-Al-La alloys. The alloys present also have good corrosion resistance, which is partly related to the presence of compact corrosion product film containing Al and Ce/La. Yamasaki et al. [98] found a $Mg_{17}La_{12}$ phase that formed in Mg-Zn-La alloys. This phase disperses in the Mg matrix homogeneously during solidification, which resulted in a fine microstructure, leading to uniform and mild corrosion of the Mg alloys. In addition, La containing Mg alloys showed a protective layer containing $Mg(OH)_2$ and La oxide, which enhanced the corrosion resistance [97, 98]. Birbilis et al. [15] studied the corrosion behaviour of the Mg-RE binary alloys. They suggested that the micro-galvanic corrosion occurs between the electrode pair composed of magnesium matrix phase and the only cathode phase, $Mg_{12}La$ for Mg-La alloys. As the amount of RE element increases, the effective surface area of the cathode phase increases leading to higher corrosion rates.

- *Cerium (Ce)*

The addition of Ce is generally considered to have a beneficial effect on the corrosion of Mg alloys [84, 99, 100], particularly for commercial Mg–Zn–Zr alloys (ZK alloys) [101] and Mg–Al–Zn (AZ) alloys [102-104]. In the case of ZK alloys with Ce, $Mg_{12}Ce$ and $Mg_{17}Ce_2$ phases form along grain boundaries, and thus decrease the grain size effectively. In Mg–Al–Ce alloys, Ce particles aggregate at the solid–liquid interface during solidification, leading to a reduction in the diffusion and grain growth is inhibited [105]. The Al–Ce phases show a pronounced effect on the corrosion of Mg–Al–Ce alloys. When the alloy contains a high concentration of Ce, $Al_{11}Ce_3$ needle-shaped particles act as a micro-galvanic cathode relative to the Mg matrix. They can form a network surrounding the Mg matrix, and delay the corrosion of Mg alloys [95]. In this micro-galvanic system, the potential difference between the Al–Ce phase and Mg matrix is relatively small, and the Al–Ce phase shows passivation in a wide range of pH values, which slows down the corrosion of Mg alloys. Liu et. al. [105, 106] suggested that the decreased corrosion rate of Mg alloys with Ce addition may be due to the reduced micro-galvanic corrosion in AZ91Ce. Birbilis et al. [15] observed the individual corrosion behaviour of the intermetallic phases of the Mg-RE binary alloys using the micro-capillary electrochemical method. They found that the corrosion potential of the $Mg_{12}Ce$ phase is -1.5V corresponding a difference of 145 mV compared to the magnesium electrode potential. They suggested that the micro-galvanic corrosion occurs between the electrode pair composed of magnesium matrix phase and the only cathode phase, $Mg_{12}La$ for Mg-La alloys. As the amount of RE element increases, the effective surface area of the cathode phase increases leading to higher corrosion rates [15].

- *Yttrium (Y)*

Yttrium is a particularly interesting alloying element for Mg alloys because it has similar electrochemical potential -2.372 V vs NHE compared to pure Mg -2.363 V vs NHE. Yttrium also exhibits a hexagonal close packed (hcp) lattice, the same as Mg [107]. For that reason it can act as a nuclei during the solidification of Mg-Y, resulting in substantial grain refinement, [98, 108] and thus enhancing the tensile yield strength [108-110]. The corrosion behaviour of binary Mg–xY alloys, where x= 0.25, 2.5, 5, 8 and 15 wt. % Y was investigated. The corrosion resistance was improved with Y addition, for Y contents below 2.5 wt. %. The corrosion mechanism altered to pitting corrosion with any further increase in Y due to the discontinuous distribution of the $Mg_{24}Y_5$ phases along the grain boundaries. $Mg_{24}Y_5$ phases caused galvanic cells to be set up. Further increasing the Y content to 15 wt.%, results in a continuous network of $Mg_{24}Y_5$ along the grain boundaries, resulting in improved corrosion resistance for Mg15Y [108, 111]. Furthermore Liu et al. [16] studied the corrosion behaviour of binary Mg–xY (where, x= 2, 3, 4, 5, 5.5, 6 and 7wt. %) in 0.1 M NaCl and 0.1 M Na_2SO_4 and found that the Mg–Y alloys show different corrosion behaviour. In 0.1 M NaCl, the Cl^- ions deteriorated the surface layer, and the matrix was easily exposed to the NaCl solution. The average corrosion rate of the Mg–Y alloys increased with increasing Y content in the range of 2-7 wt. % Y. Due to the volume fraction of intermetallic phases increased with Y addition, which deteriorated the corrosion resistance due to the accelerated micro-galvanic effect. While in 0.1 M Na_2SO_4 solution, the corrosion rate decreased when the Y content increased in the range between 3-7 wt. %, which was attributed to a Y-containing protective surface layer. Hänzi et al. [112] tried different heat treatments on an Mg–Y–RE alloy (WE43:Y content 3.7–4.3 wt. %) to obtain different surface conditions and studied the influence of different surfaces on the in vitro degradation behaviour of the Mg alloy. They suggested that solution heat-treated WE43 reveals improved degradation resistance reflected by a comparably low degradation rate. On the other hand, thermally oxidized at 500°C WE43 showed a decreased initial degradation rate that was attributed to the protective nature of the surface film consisting of oxides of MgO and Y_2O_3. Once the surface film was penetrated or removed, degradation accelerated until the deposition of corrosion products slowed down the degradation again.

- *Mixture of RE elements*

Additions of two or more rare elements are used to improve the mechanical and corrosion properties of Mg-RE alloys. Some examples will mention as following:

Elektron 21 (E21, EV31A) is recently developed advanced magnesium based alloy, which contains additions of Nd (2.6-3.1 %), Gd (1.0-1.7 %), Zinc (0.2-0.5 %) and Zr (saturated). According to the manufacturer [113] E21 alloy presents high corrosion resistance in chloride solution, excellent mechanical properties and light weight. The alloy was developed for motorsport and aerospace applications and designed to provide superior mechanical properties and improved corrosion resistance together with good castability. As listed in its specifications [113]. Elektron 21 alloy is the first magnesium alloy to achieve full design handbook entry in the Metallic Materials Properties Development and Standardization (MMPDS) and has achieved the Aerospace Material Specification (AMS4429) in the Society of Automobile Engineers (SAE) [114]. E21 showed superior corrosion resistance with 10-30 mpy in the salt spray test according with ASTM B117 [113]. E21 alloy was used in the complex transmission casings in the General Dynamics, the latest military amphibious vehicle for the U.S. Marines, the Expeditionary Fighting Vehicle (EFV). Due to this alloy combines castability, corrosion performance and the ability to operate a high temperatures [115]. Placzankis et al. [116] observed that E21 alloy shows low mass loss but deep localized damaged in the neutral salt fog method (NSF). This suggests the possible presence of tramp elements such as, Fe, Ni, or Cu, or intermetallic phases that act either local cathodes or anodes. However they considered that E21 alloy exhibits good balance of corrosion resistance and mechanical properties. Hamdy et al. [117] proposed a surface treatment with vanadium containing solutions to improve the corrosion resistance of E21 alloy. After one week immersion in 3.5 % NaCl, E21 alloy showed less pitting and crevice corrosion compared with the coated samples. Due to a formation of multi oxide layer of vanadia with the alloying elements of the E21, this promotes the micro-galvanic corrosion. Tekin et al. [118] investigated the electrochemical behaviour of bare and PEO-coated E21, WE43 and AZ31B alloys in 3.5% NaCl solution. They observed that bare E21 and WE43 alloys presented higher corrosion resistance than bare AZ31B. This is due to the formation of a more compact corrosion product layer on RE containing alloys, which avoid the ion exchange across this layer at longer immersion times. They improved the corrosion resistance of the three PEO-coated samples. However for longer immersion periods E21 and WE43 alloys showed better corrosion resistance that AZ31B alloy.

Elektron WE54 or WE54 is a magnesium based alloy, its chemical composition consists on Y (4.5-5.5%), Nd (1.5-2.0%), heavy rare earths (1.0-2.0% mainly Yb, Er, Dy and Gd) and Zr (0.4% min). According to the manufacturer, additions of yttrium contribute to the excellent corrosion resistance to the extent that it is of a similar order to aluminium casting alloys under salt spray conditions [119]. Kazum et al. [120] suggested that the rare earth contents in the WE54 alloy enhanced its passivation tendency, thus improving its the pitting corrosion resistance and decreased the corrosion current by 30% compared to pure magnesium in 0.5 wt.% NaCl solution. Luo et al. [76] reported that WE54 alloy retains its mechanical properties at high temperatures for up 1000 h. Another investigation reported that long-term exposure (1000-2000 h) at 200°C led to a reduction in ductility (below 2% elongation) [121]. For that reason WE54 alloy is no longer being considered for aerospace applications but is expected to be used in applications where high strength is critical, either for the short term or where ductility is less important (e.g. motor racing) [121]. According with the ASTM B 177-90 salt-spay test, the corrosion rate of WE54 alloy was between 0.1-0.2 mgcm^{-2}day^{-1} [122]. However, the higher cost of yttrium restricts application of the alloys [74]. Coy et al. reported that WE alloys have tightly packed crystals and blurred grain boundaries. Therefore the corrosion at the boundaries is reduced ensuring good anticorrosion properties of the WE alloys. However, there are unavoidably some Y-rich and Zr-rich particles in the alloy, which act as strong cathode phases and thus weaken anticorrosion capability [123, 124].

ZE41 magnesium alloy, has a composition based on Zn (3.5-5.0 %), rare earths (0.8-1.7 %), and Zr (0.4-1.0 %) [125]. Neil et al. [126] proposed a corrosion process for the ZE41 alloy. The initiation and propagation of the corrosion process involves pitting initially adjacent to the T-phase, followed by the deep attack at the Zr-rich regions, and pitting within the α-Mg phase. The observations of deep attack at the Zr-rich regions do not follow the theory that Zr additions enhanced corrosion protection [127, 128]. Kannan et al. [129] investigated the corrosion behaviour of ZE41 alloy, and compared with AZ80 alloy in 0.5 wt. % NaCl solution. They found that ZE 41 alloy showed extensive corrosion of the grains (pitting and intergranular corrosion), while AZ80 alloy possess better corrosion resistance. However they considered that rare-addition to magnesium enhances the passivation tendency of the alloy, as reported by Nordlien et al. [130] and Krishnamurthy et al. [131]. Coy et al. [123] suggested a corrosion process based on the electrode potential data of the matrix and second phase determined by scanning Kelvin probe force microscopy (SKPFM). Compared to the matrix potential, the potential at grain boundary is 80 mV lower and that of the T-phase at the boundary is 100 mV higher. Therefore, this alloy c presented a strong micro-galvanic corrosion due to the presence of the cathodic Zr_4Zn rich precipitates, as well as the combined effect of the cathodic T-phase (Mg_7Zn_3RE) and the depleted anodic areas, both present at the grain boundaries. Magnesium Elektron Ltd [132] proposed the Elektron RZ5/ZE41 alloy for applications operating up to 150°C due to its excellent castability and good mechanical properties. It is specified on many helicopters including the Agusta Westland AW101, NH Industries NH90, and Airbus Helicopters AS332 Super Puma. For superior mechanical properties and durability that enables longer intervals between overhauls and improved corrosion performance. Civil applications include intermediate casings for the Rolls Royce RB183 Tay engines and gearboxes (Elektron®RZ5/ZE41), as well as the Rolls Royce BR710 (Elektron®RZ5/ZE41).

2.4.3 Novel alloying additions

a) Gallium (Ga)

Additions of gallium to Mg based alloys was investigated by Macdonald [133]. He studied Mg-Ga-Mn ternary alloys, which can be made to a rolled sheet with sufficient degree of ductility, while having good tensile and yield strengths. He found that 1% gallium and 3% manganese gave the most desirable combination of properties. Mg-Ga anode materials were studied because gallium can enhance the electrochemical activity of magnesium anode and it can produce uniform dissolution of Mg in environments containing aggressive ions [134, 135] [134, 135] and has a high hydrogen over-potential [136]. Feng et al. [137] found that solid solution of Ga in Mg alloys can decrease the Faradaic impedance of double electric layer of Mg and enhance the current efficiency. Recent studies of Mg-Ga alloys were performed by Liu et al. [138] showing that Mg-2Ga alloy has a good elongation and aging treatments improved efficiently its yield tensile strength due to the tiny rod-shaped Mg_5Ga_2 precipitates distributed homogeneously in the Mg matrix. Additions of Ga were also studied in biodegradable metallic implants of Mg based alloys [139]. Kubásek et al. [140] found that low additions of Ga (around 1 wt.%) improve the mechanical properties of Mg-Ga alloys. Thereby Ga has lowest toxicity level compared to Sn or In. But at higher concentrations of Ga are detrimental for the corrosion resistance due to galvanic effects of the secondary phases Mg_5Gd_2.

b) Lithium (Li)

Lithium is used in large quantities in order to reduce the density of magnesium. Increase in Li content beyond 11% leads to a change in the crystal structure from hexagonal close packed to body centred cubic structure, enhancing deformability due to activation of more independent slip systems, but with a strength reduction. Further, the problems of burning occur while melting in the presence of higher levels of lithium [32]. Lithium was used in the bio applications area, as lithium decreases corrosion resistance at concentration below 9% in Mg [141]. Witte et al. [142] did in vivo corrosion experiments of LAE442 magnesium alloy as potential degradable implant material, and found that the extruded LAE442 magnesium alloy corroded in vivo without the appearance of subcutaneous gas cavities, which was illustrated by daily examination and post-operative X-ray investigations. Mg-Li alloys are of great interest in the fields of aerospace and military due to their super light-weight [143]. Song et al. [141] demonstrated that higher Li additions significantly accelerate the corrosion rates due to the presence of dual phase α and β structure, resulting in localized corrosion (micro-galvanic couple), which initiates in the boundary of α and β phase at the very early stage of corrosion. Then filiform corrosion was observed for longer immersion time.

2.4.4 Effect of the microstructure and secondary phases

Most of the alloying elements used in magnesium alloys have limited solid solubility and therefore secondary intermetallic phases are formed [73]. These phases have a pronounced influence on the corrosion of magnesium, due to differences in electrochemical potentials. Generally, these phases are more noble (i.e., have a higher redox potential) than the Mg matrix. Their influence on salt water corrosion depends on their potential relative to Mg matrix and their efficiency as cathodic sites, i.e., the ease at which they liberate hydrogen gas (over voltage)

[38]. The elements generally present in commercial magnesium alloys that influence saltwater corrosion can be classified as:

a) Generally benign or beneficial; e.g.: aluminium, beryllium, manganese, rare earths, silicon, zinc, and zirconium.

b) Moderately deleterious e.g.: silver

c) Severely deleterious e.g.: nickel, cobalt, iron, and copper [84].

The size and distribution of the cathodic phases play an important role in corrosion; and are influenced by process parameters and heat treatment. Homogenized and artificially aged specimens of AZ91E (T6) show considerably lower corrosion than as-cast (F) and homogenized (T4) specimens [83]. In particular for Mg-Al-Zn alloys the investigations focus on the corrosion behaviour of the β-phase ($Mg_{17}Al_{12}$) and the magnesium matrix. Song et al. [7] suggested that the β-phase ($Mg_{17}Al_{12}$) is cathodic respect to the Mg matrix and its effect on corrosion depends on the volume fraction of β-phase in the microstructure defined by the expression $f = V_ß/V_\alpha$, where $V_ß$ is the volume of β-phase and V_α is the volume of α-Mg phase. If f is low, then β-phase acts as a cathode, accelerating corrosion of the α-Mg matrix. If f is high, then β-phase acts as a partial barrier inhibiting the corrosion. Raman et al. [144] suggested that an increase in the relative size of the ß-phase and surrounding α-phase results in an increase in the localized corrosion. However, Al containing α-phase shows an independent electrochemical identity, depending on its composition and thermal history. Contradictory results have been shown in this study, as it did not consider the influence of the solidification rate that directly depends on the distribution and morphology of β-phase, which eventually affects the corrosion resistance of the Mg-Al-Zn alloys. Heat treatment influences the distribution of intermetallic ß-phase ($Mg_{17}Al_{12}$). Aging to T6 temper causes precipitation of ß phase as an almost continuous network of secondary particles along the grain boundaries. Following T4 heat treatment the ß-phase is fully dissolved in Mg matrix. In the cast AZ91 most important impurity elements (iron, copper, and nickel) are influenced by the cooling rate and the amount of manganese present [70, 145, 146]. In early stages of corrosion, filiform attack develops from a initiating pit adjacent to intermetallic particles, and the role of $Mg_{17}Al_{12}$ concentrated in grain boundaries is clearly illustrated. Cold working of magnesium alloys (e.g., by stretching or bending) has no appreciable effect on corrosion rate of these alloys [74].

3. Experimental procedures

3.1 Materials preparation

The raw materials used in this work do all have commercial purity. Magnesium (Mg) was delivered by Magnesium Elektron ®. Cerium (Ce), dysprosium (Dy), gadolinium (Gd), lanthanum (La), neodymium (Nd), yttrium (Y), and gallium (Ga) are obtained from Grirem Advanced Materials Co. Ltd. The aluminium (Al) came from Hydro Aluminium High Purity GmbH, while zinc (Zn) provided from Wilhelm Grillo Handelsgesellschaft GmbH. These materials have a commercial purity. Their chemical composition and purity is given in Table 3.1. The experimental alloys manufactured for this work are shown in Table 3.2. The alloys are divided in three different groups. The first group contains the Mg-RE-Intermetallics and include a high concentration of rare earth elements. The dilute binary alloys belong to the second group, where various compositions are produced to observe the influence on corrosion resistance. For the third group some extra alloying elements are considered based on the typical alloying elements for Mg alloys in order to improve the corrosion resistance of the Mg-RE alloys. All alloys were produced by gravity casting using an electrical resistance furnace (see Figure 3.1), under a protective atmosphere composed of Argon-0.3 % SF6. Alloying elements were added to the molten magnesium in the crucible at temperatures between 680 °C and 800 °C, depending on the alloy. The melt was stirred for 10 minutes to make sure that the alloying elements were homogeneously dissolved. The alloys were casted into a cylindrical steel mould of 18 mm diameter and 150 mm length. A schematic sketch is shown in Figure 3.2. The chemical compositions of each cast bar were measured at top and bottom positions in order to ensure the composition homogeneity in the whole specimen using X-ray fluorescence (XRF) (see Table 3.3).

Table 3.1 Chemical composition of the commercially pure elements

	Pure elements										
Impurities ↓	**Mg**	**Ce**	**Dy**	**Gd**	**La**	**Nd**	**Y**	**Al**	**Ga**	**Zn**	**Mg2Mn**
Ag											<0.0001
Al	0.0046		0.0036		0.0320	0.017	0.0170	**99.9966**		<0.0010	0.0137
Be											0.000036
Bi									0.0009		
C			0.0330			0.0340	0.0300				
Ca		0.0100	0.0042	0.0012	0.0020	0.0020	0.0230		0.0300		0.00071
Cd										<0.0030	
Ce		**99.000**	0.0065	0.0005			0.0005				0.00317
Co									0.0050		
Cu	0.0042		0.0214		0.0002	0.0002		0.0005		<0.0010	0.0025
Dy			**99.500**	0.0015			0.0180				
Er			0.0010	0.0003			0.001				
Eu		0.001	0.0010	0.0001			0.0003				
Fe	0.0021	0.1100	0.0405	0.0034	0.1700	0.1500	0.0360	0.0010	0.0211	<0.0020	0.00165
Ga									**99.900**		
Gd			0.0017	**99.000**			0.0032				
Ho			0.0010	0.0003			0.0012				
La		0.001	0.0005	0.0016	**99.000**		0.0007				0.00026
Lu			0.0020	0.0001			0.0001				
Mg	**99.965**		0.0001		0.0080	0.0045	0.0030	0.0001	0.0050		**97.7400**
Mn	0.0160				0.0020	0.0030			0.0090		**2.2200**
Mo					0.0260						
Nd		0.0283	0.0002	0.0025		**99.000**	0.0010				
Ni	0.0006				0.0005	0.0005					0.00163
O			0.1400			0.0280	0.700				
Pb										<0.0030	
Pr		0.0050	0.0045	0.0001			0.0003				
Sb									0.0200		
Si	0.0073	0.0100	0.0202	0.0016	0.0150	0.0240	0.0130	0.0018	0.0090		0.00771
Sm		0.0014	0.0054				0.0008				
Sn										<0.0010	<0.0005
Tb			0.0240	0.0073			0.0028				
Tm			0.0007	0.0001			0.0001				
W					0.0250						
Y			0.0020	0.0003			**99.000**				
Yb			0.0010	0.0001			0.0001				
Zn										**99.995**	0.0057
Zr											0.0050
Others	0.0002	0.8333	0.1855	0.9790	0.6933	0.7368	0.1479				

Table 3.2 Composition and casting parameters of experimental Mg alloys

Mg-RE-Intermetallic	**Wt. %**		**Balance**	**$T_{melting}$ (°C)**	**$T_{casting}$ (°C)**
Mg33Ce	33 Ce		Mg	760	730
Mg57Gd	57 Gd		Mg	800	800
Mg40La	40 La		Mg	760	730
Mg38Nd	38 Nd		Mg	785	730
Mg40Y	40 Y		Mg	730	700
Mg57Gd1Mn	57 Gd	1 Mn	Mg	730	730
Mg57Gd2Mn	57 Gd	2 Mn	Mg	730	730
Dilute binary alloys	**Wt. %**		**Balance**	**$T_{melting}$ (°C)**	**$T_{casting}$ (°C)**
Mg1Ce	1 Ce		Mg	680	650
Mg5Ce	5 Ce		Mg	700	660
Mg10Ce	10 Ce		Mg	700	660
Mg15Ce	15 Ce		Mg	770	720
Mg1Gd	1 Gd		Mg	700	660
Mg5Gd	5 Gd		Mg	700	660
Mg10Gd	10 Gd		Mg	700	660
Mg15Gd	15 Gd		Mg	700	660
Mg1La	1 La		Mg	700	700
Mg5La	5 La		Mg	700	700
Mg10La	10 La		Mg	700	700
Mg15La	15 La		Mg	700	700
Ternary alloys	**Wt. %**	**Wt. %**	**Balance**	**$T_{melting}$ (°C)**	**$T_{casting}$ (°C)**
Mg10Gd5Al	10 Gd	5 Al	Mg	720	700
Mg10Gd5Ga	10 Gd	5 Ga	Mg	720	660
Mg10Gd1Mn	10 Gd	1 Mn	Mg	720	700
Mg10Gd5Y	10 Gd	5 Y	Mg	720	700
Mg10Gd5Zn	10 Gd	5 Zn	Mg	720	700
Mg5Gd1Mn	5 Gd	1 Mn	Mg	710	710
Mg5Gd2Mn	5 Gd	2 Mn	Mg	720	720

Figure 3.1 Electrical resistance furnace

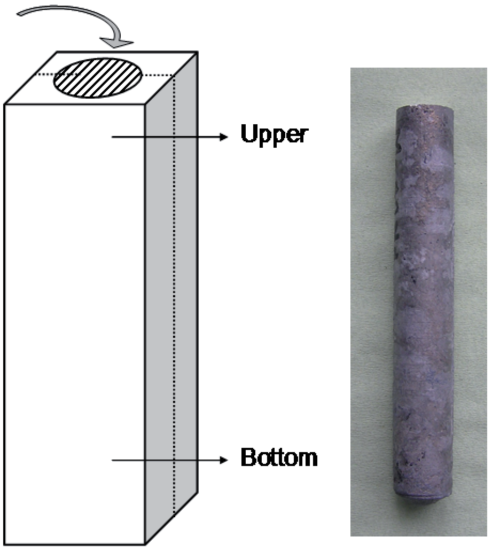

Figure 3.2 Cast mould and example of a casted ingot

Table 3.3 Chemical analysis of the experimental Mg alloys

Alloy	Element		Upper (wt. %)		Bottom (wt. %)		Balance
Mg33Ce	Ce		35.0		35.1		Mg
Mg57Gd	Gd		63.0		62.8		Mg
Mg40La	La		39.0		38.9		Mg
Mg38Nd	Nd		36.4		37		Mg
Mg40Y	Y		39.1		38.7		Mg
Mg57Gd1Mn	Gd	Mn	64.13	0.29	62.53	0.28	Mg
Mg57Gd2Mn	Gd	Mn	57.53	0.55	56.63	0.54	Mg
Mg1Ce	Ce		0.78		0.95		Mg
Mg5Ce	Ce		4.08		4.10		Mg
Mg10Ce	Ce		7.78		8.44		Mg
Mg15Ce	Ce		9.07		9.75		Mg
Mg1Gd	Gd		0.96		1.14		Mg
Mg5Gd	Gd		4.52		4.28		Mg
Mg10Gd	Gd		9.05		8.97		Mg
Mg15Gd	Gd		12.8		13.1		Mg
Mg1La	La		0.82		0.99		Mg
Mg5La	La		3.54		3.67		Mg
Mg10La	La		8.62		8.97		Mg
Mg15La	La		14.3		14.4		Mg
Mg10Gd5Al	Gd	Al	5.18	2.55	1.70	1.98	Mg
Mg10Gd5Ga	Gd	Ga	8.78	4.03	8.83	4.22	Mg
Mg10Gd1Mn	Gd	Mn	9.16	1.13	9.50	1.09	Mg
Mg10Gd5Y	Gd	Y	8.68	4.37	8.63	4.34	Mg
Mg10Gd5Zn	Gd	Zn	7.3	3.83	7.2	3.93	Mg
Mg5Gd1Mn	Gd	Mn	3.94	1.04	3.47	1.05	Mg
Mg5Gd2Mn	Gd	Mn	5.83	0.48	3.95	0.47	Mg

3.2 Heat treatment

Heat treatments (T6) were carried out to investigate the influence of the microstructure on the corrosion behaviour of the binary Mg10Gd alloy. First the cast material was subjected to solution treatment at 540°C for 24 h and quenched in water bath at room temperature. Subsequently some samples were aged at 200°C, 300°C and 400°C for 24 h and cooled by quenching in cold water bath (~ 8 °C) to freeze the microstructure developed at that condition. Figure 3.3 shows schematically the T6 process.

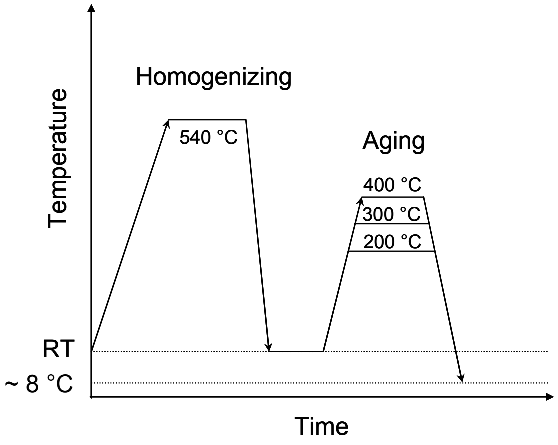

Figure 3.3 T6 heat treatment procedure

3.3 Microstructural characterization

3.3.1 Specimen preparation

Firstly the samples were cut and embedded in epoxy resin (Demotec 30). Then the specimens were ground with 800, 1200 and 2500 grit SiC paper using water as cooling fluid and between grinding steps the samples were rinsed with ethanol. After grinding the samples were mechanically polished using a porous cloth of neoprene (MD-Chem Struers) with 0.05 µm OPS (Struers) ™, suspension and soapy deionised water for 10 minutes to avoid oxidation. Finally the samples were rinsed with ethanol and dried with hot air. The polished samples were chemically etched for ~ 7 seconds with a solution of picric acid (140 ml of ethanol, 40 ml distilled water, 7 ml acetic acid, 3-4 g picric acid). Afterwards the samples were immediately rinsed with ethylic alcohol and dried with hot air.

3.3.2 Optical microscopy (OM)

After chemical etching the microstructure of the samples was evaluated using a Leica™ DMLM light optical microscope with magnifications between 1.6 to 1000X combined with a Colour View camera DC500. Subsequently the micrographs were viewed using image processing software “analySIS pro” version 5.0.

3.3.3 Scanning electronic microscopy (SEM)

Two scanning electron microscopes (SEM) were used. The Cambridge Stereoscan 200 with an acceleration voltages ranging from 5-10 keV was used to examine the surface appearance of the specimens before and after corrosion tests and ZEISS Ultra 55 with an acceleration voltages ranging from 8-20 keV and equipped with energy-dispersive X-ray analysis systems (EDX) for chemical microanalysis on selected areas or punctual analysis. Images were recorded using secondary electrons (SE) and back scattered electrons (BSE).

3.3.4 Transmission electron microscopy (TEM)

Analyses of precipitate microstructures were conducted in a Phillips CM200 transmission electron microscope operating at 200 kV. The samples for TEM analysis were prepared by electric discharge machining 3 mm discs from alloy specimens that were ~ 200 mm in thickness and twin jet electropolishing using a solution of 1.5% perchloric acid in methanol at a polishing temperature of ~-45°C with a current of ~0.8-1.2mA and a voltage of 50V. Upon perforation the specimens were washed in ethanol to remove any trace of acid. The investigations were carried out in the bright field imaging mode, while selected area electron diffraction (SAED) patterns were also recorded from areas of interest. Micro-beam electron diffraction (MBED) patterns were recorded, with a nominal beam diameter of approximately 7.5 or 10 nm, and a nominal condenser aperture diameter of 30 mm, from primary intermetallic phases and solid-state precipitates.

3.3.5 X-Ray Diffraction (XRD)

The presence of the different phases in the proposed alloys was evaluated by X-ray diffraction (XRD) analysis using a Siemens D5000 X-ray Powder Diffractometer with Cu Kα radiation. A current of 40 mA at a voltage of 40 kV was used during the measurements. The samples were scanned over a range of 10° to 90° at a step size of 0.010° with 7 sec/step and rotation speed of 30 rpm.

3.3.6 X-Ray photoelectron spectroscopy (XPS)

The surface treated samples were investigated by X-ray photoelectron spectroscopy (XPS) using a Kratos DLD Ultra Spectrometer with an Al-Kα X-ray source (monochromator) as anode. For the survey spectra a pass-energy (PE) of 160 eV was used while for the region scans PE was 40 eV. For all samples charge neutralization was necessary. Depth profiling was carried out by using argon sputtering with energy of 3.8 keV and a current density of 125 μA/cm^2. The etching rate was calibrated to 12 nm/min by using Ta_2O_5.

3.4 Corrosion characterization

3.4.1 Electrochemical analysis

The entire electrochemical evaluations of the samples were performed using a typical three electrode acrylic cell (330 ml electrolyte) as shown in the set-up in Figure 3.4. In this cell the sample is the working electrode (WE) with a ~0.5 cm^2 exposed area, while reference (RE) and auxiliary (AE) electrodes were Ag/AgCl, and Pt grid respectively. The electrolyte used was an aerated solution of 0.5 wt. % NaCl. The cell was connected to a Gill AC Potentiostat from ACM Instruments. The experiments were carried out with stirring at 21.5 ± 0.5 °C.

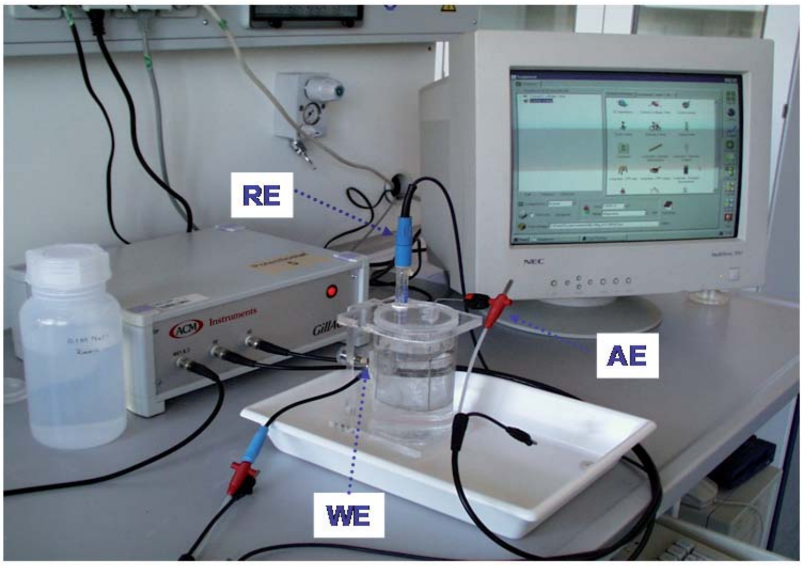

Figure 3.4 Experimental set-up for electrochemical evaluations, where RE is the reference electrode, AE is the auxiliary electrode and WE is the working electrode

Specimens with the following dimensions 20 x 15 x 10 mm^3 and 15 mm diameter x 15 mm thickness were cut from the cast ingot. For corrosion testing the samples were grounded in the same way as described in 3.3.1 but only up to grit 1200. Following electrochemical techniques were used:

Open circuit potential measurements (OCP)

The open circuit potential (also referred to as the equilibrium potential, the rest potential, open circuit voltage) is the potential at which there is no external current. OCP is simply a technique that measures the potential difference between the working and reference electrodes when there is no current or potential existing in the cell. The OCP measurements were recorded for 5 (EIS), 30 (Polarisation) minutes immersion to reach potential stabilization before starting the specific test. Recording of OCP only was done for 2 hours for the pure elements. Figure 3.5

shows an example of OCP of a specimen recorded after 1800 s of exposure in 0.5 wt. % NaCl solution.

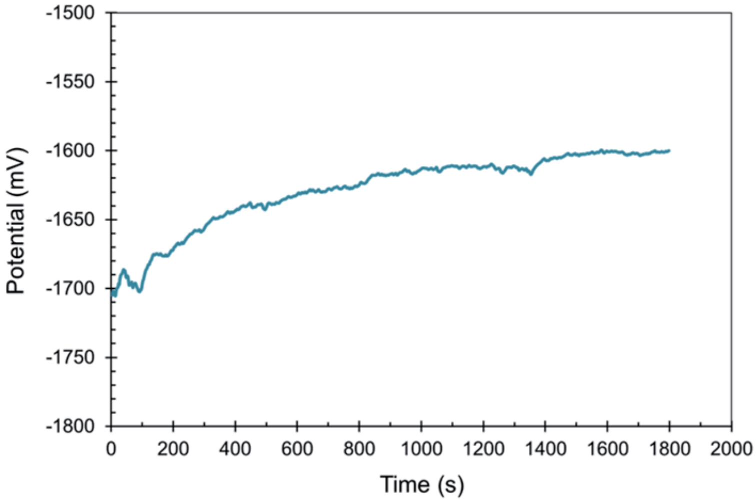

Figure 3.5 Example of OCP of a specimen measured during 1800 s exposure to a 0.5 wt. % NaCl solution

Potentiodynamic polarisation measurements

This technique is based on polarising a sample by applying an external voltage with the help of a potentiostat. Depending on the polarisation direction of the OCP occur two opposite reactions reduction and oxidation (Redox reactions). In the anodic reaction the metal atom loses *n* electrons and becomes n^+ ion, e.g. $Mg \rightarrow Mg^{2+} + 2e^-$. In the cathodic reaction the electrons produced in the oxidation reaction are used up in the reduction reaction, $2H^+ + 2e^- \rightarrow H^2$. By extrapolating the tangent (Tafel slopes) of the cathodic and anodic curves to E_{corr} the corrosion current i_{corr} is obtained by the interception of these curves, as shown in Figure 3.6. However at the corrosion potential the cathodic and anodic currents are the same, the determination of corrosion current can be made using only the cathodic slope. This is of significant importance as the anodic slope is usually non-uniform. The i_{corr} value is used to determine the corrosion rate, normally is expressed in miles per year (mpy) or mm/year. However this technique has been received several criticisms because the calculations obtained are not consistent with other techniques [147, 148, 151] due to the negative difference effect, (see 2.3 Negative Difference Effect (NDE). Nevertheless for the current work this technique was used for a semi-quantitative approximation. The potentiodynamic polarisation measurements were started at -150 mV relative to the free corrosion potential. The scan rate was 12 mV/min and the test was terminated when a current limit of 0.01 mA/cm^2 was reached.

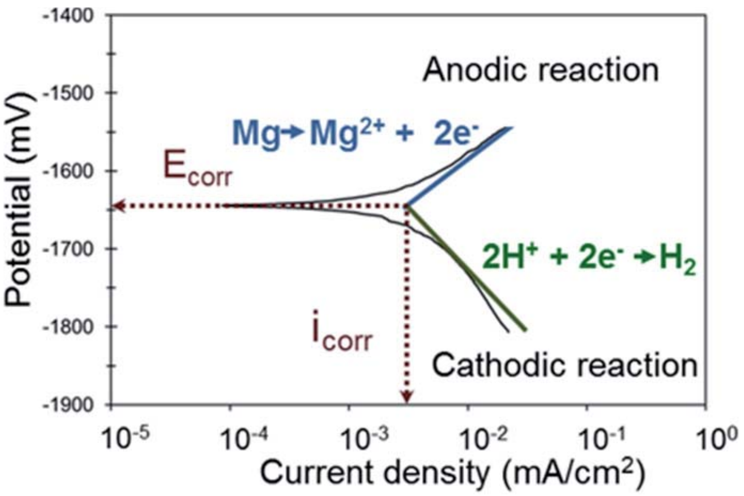

Figure 3.6 Schematic description of the determination of i_{corr} for Mg from an experimental polarisation curve (black solid curve) using Tafel slops (blue and green lines)

The corrosion rates obtained from potentiodynamic polarisation measurements (ASTM standard) [149] were calculated from the corrosion current density (i_{corr}) determined at the intersection of the Tafel slope of the cathodic branch of the polarisation curve with the vertical line through the corrosion potential using the equation.

$$Corrosion\ rate\ (mm/year) = \frac{Metal\ factor\ \times i_{corr}}{1000} \qquad (11)$$

Metal factor is calculated from:

$$Metal\ factor = \frac{t\ \times K}{\rho} \qquad (12)$$

Where

t (seconds per year) = 365.2422454*24*60*60 = 31556930 seconds

ρ is the metal density in g/cm^3

K is the electrochemical equivalent in g/coulombs, K is obtained from

$$K = \sum \frac{atomic\ \%\ of\ the\ element\ \times atomic\ weight\ of\ the\ element}{96487\ coulombs \times valency\ of\ the\ element} \qquad (13)$$

Electrochemical impedance spectroscopy (EIS)

Impedance is the opposition to the flow of alternating current (AC) in a complex system. The impedance (Z) has the same physical meaning as the resistance (R), with the difference that it varies with the frequency (ω) of the applied potential. While in direct current (DC) polarisation methods a potential is applied at a constant rate, in impedance measurements a sinusoidal potential variation is applied at different frequencies, which is generally from 10^5 to 10^{-2} Hz [150, 151]. The spectrum that correlates the real and imaginary parts of Z is called Nyquist plot Figure 3.7(a) and the spectrum which correlate total impedance and the theta angle with the applied frequency are called Bode plots Figure 3.7(b). The EIS is used to characterize the electrical behaviour of systems in which every answer is determined by several simultaneously processes which are occurring at different rates. Hence, the surfaces and generally electrochemical processes can be represented mostly with an electrical circuit. This circuit is known as an electrical equivalent circuit (EEC). Capacitors, resistors, inductors and other elements of the equivalent circuit have a physical explanation for constituting an arrangement equivalent to the electrochemical process. The description of the electrical equivalent circuit parameters can provide information about the electrochemical processes occurring at the interface or about the surface condition e.g. film formation. For example, Figure 3.8 shows the EEC used to fit the experimental impedance spectra shown in Figure 3.7 and describes two electrochemical processes; one is attributed to oxide/hydroxide film formation and the second is related to the corrosion process at the metal/electrolyte interface. These contributions are also visible in the Nyquist plot (represented by the two semicircles Figure 3.7 a) although in the Bode plots (theta vs frequency, Figure 3.7 b) they are more obvious in the two plateaus one at high frequencies (10^2) is related to the electrolyte-oxide film interface and second at low frequencies (10^{-1}) is related to the oxide film-metal interface.

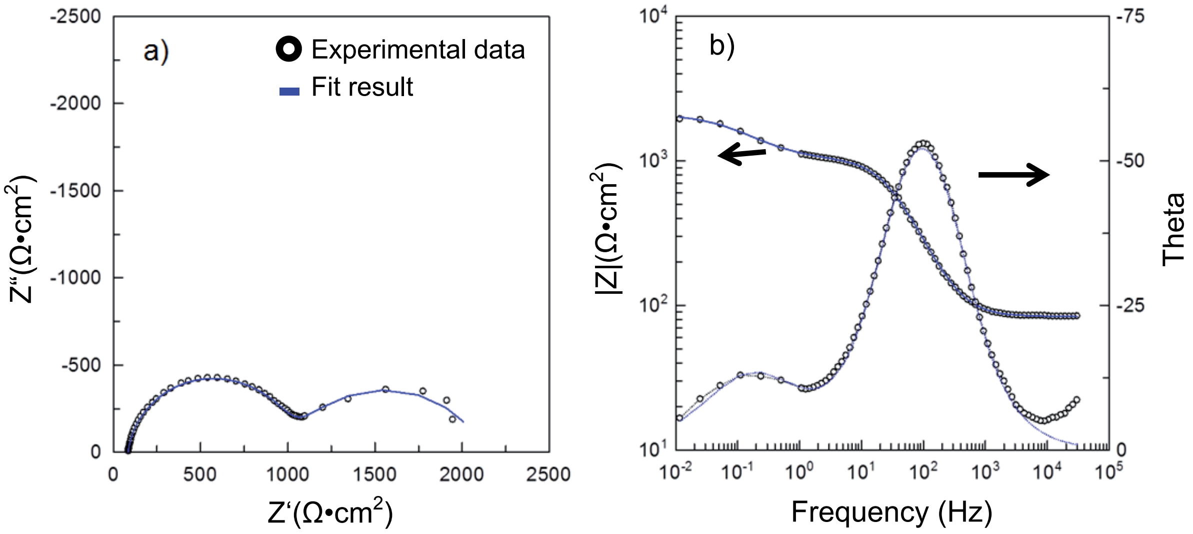

Figure 3.7 Examples of EIS spectra showing the Nyquist plot (a) and Bode plots (b) of a sample after 72 h exposure in 0.5 wt. % NaCl solution

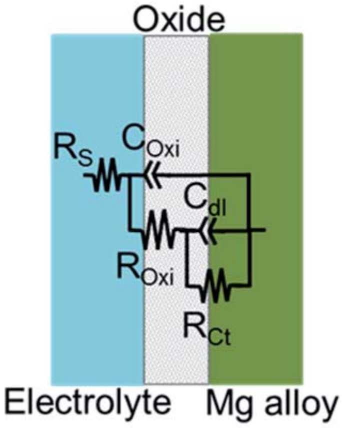

Figure 3.8 Schematic representation of the electrical equivalent circuit (EEC) used to simulate the impedance spectra of Mg sample

By fitting the impedance spectra using that EEC it is possible to follow variations in capacitance and resistance and thus variations of the surface layers with the exposure time.

Electrochemical impedance spectroscopy (EIS) measurements were performed setting up the equipment in the frequency range between 10^{-2} and 10^{4} Hz with amplitude of ± 10 mV rms. These impedance measurements were performed after different exposure periods of 1, 3, 6, 12, 24, 48, 72, 96, 120 and 144 h.

All the measurements above mentioned were performed in triplicate to guarantee the reliability of the results.

3.4.2 Hydrogen evolution and weight loss

The corrosion rate of the alloys was additionally investigated using standard eudiometer set-ups with a total volume of 400 ml and a resolution of 0.5 ml as shown in Figure 3.9 . The tests were performed in aerated 0.5 wt. % NaCl solution without agitation and a neutral starting pH value of 7. Flat specimens with dimensions 15 x 15 x 15 mm^3 or slides of 15 mm diameter x 4 mm thickness were cut using a diamond cutting disc and ground using the same procedure as described in 4.3.1. Then the coupons were immersed in the solution, the hydrogen evolution as an indicator of the corrosion rate was monitored after certain time periods. The samples were removed when the hydrogen has replaced the total volume of 400 ml water out the column. The average corrosion rate of each specimen at the end of the tests was calculated in mm per year by converting the total amount of collected hydrogen into material loss (1 ml H_2 gas = 0.001083 g dissolved Mg) and using the following equation

$$CR = \frac{8.76\,x10^4 \cdot \Delta g}{A \cdot t \cdot \rho} \qquad (14)$$

Where:

Δg: weight change in grams

A: area in contact with the solution in cm^2

t: time in hours

ρ: density of the material in g/cm^3 and

8.76x10^4: conversion factor to obtain the corrosion rate in mm/year (millimeter per year).

This corrosion rate was cross-checked by measuring the weight of the specimens before and after the corrosion test. Therefore the specimens were cleaned for 30 minutes in chromic acid solution (180 g/l) at room temperature then washed with ethanol and finally dried in hot air. With this cleaning process all the corrosion products were removed.

Figure 3.9 Eudiometer set-ups

3.4.3 Galvanic coupling

The intermetallics phases described in section 3.1 were used to determine the galvanic current between the magnesium matrix and the intermetallic phase. The schematic experimental set-up of galvanic coupling is shown in Figure 3.10. The electrochemical cell consist of two working electrodes (WE_1 and WE_2) with exposed area of approximately 0.5 cm^2 and 0.5 cm^2 respectively, and two reference electrodes of Ag/AgCl (RE_1 and RE_2) which are connected to two multimeters. The electrolyte used is a 0.5 wt. % NaCl solution at pH 11. The electrochemical cell is connected to a Gill AC Potentiostat from ACM Instruments working as zero resistance amperemeter and all the data (exchange current, mixed potential) were recorded by a computer. The experiments were carried out for 24 hours with stirring at 21.5 ±

0.5 °C. In this study pure magnesium was used as working electrode 1 (WE_1) and the different Mg-RE-intermetallics (see section 3.1 casting) were placed as working electrode 2 (WE_2). Before starting the test the potential of both materials in the electrolyte were recorded. Subsequently the working electrodes were short cut. The current density of the system is measured between two working electrodes (WE_1, WE_2) and the potential of the system also called mixed potential will be measured with the reference electrode 1 (RE_1). The purpose of these measurements is to predict the exchange current of an intermetallic in a Mg matrix. Lower exchange currents may suggest better corrosion resistance.

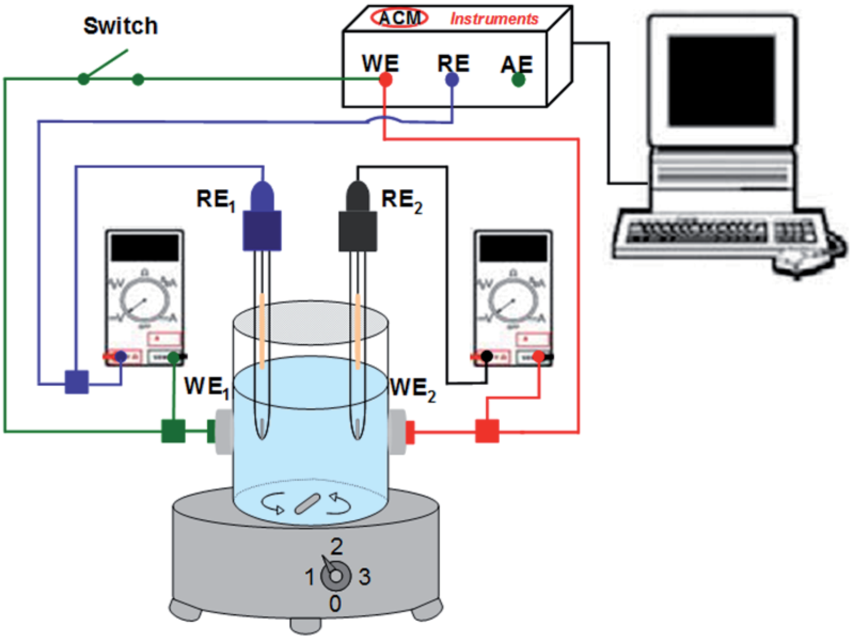

Figure 3.10 Galvanic coupling assembly, where RE_1, RE_2 are the reference electrodes and WE_1, WE_2 are the working electrodes

3.4.4 Drop / Immersion test

In order to observe more details about the starting corrosion process and the way it will carry on, a drop and immersion test was performed which consist of dropping a very small amount of 5 wt. % NaCl solution on the surface of the samples for periods between 10 to 60 s. If the samples did not present enough damage to stop the experiment, they were immersed for periods between 10 to 60 minutes or even longer in the same solution mentioned above. The chamber for this technique is shown in Figure 3.11 inside there are two glasses one is for the sample and the second contains some water to maintain humidity and prevent drying of the drop in the chamber. After exposure time, the remaining solution was removed and the surface was cleaned for 30 minutes in chromic acid solution (180 g/l) at room temperature then washed with ethanol and finally dried in hot air. The surface appearance before and after the test was controlled by scanning electron microscopy (see section 3.3.3)

Figure 3.11 Drop/immersion test chamber

4. Results

4.1 Evaluation of the corrosion behaviour of pure metals

Rare earths are extracted as a mixture of rare earth elements with various compositions. The most common misch-metal is rich in Ce, followed by La, with smaller amounts of Nd, sometimes Pr and Y [152]. When misch-metals are added to Mg alloys, it is generally assumed that all elements behave the same (in part as evidenced by the use of symbol E to denote all rare earth elements in the alloy nomenclature). However, the Mg-RE phase diagrams suggest that each individual rare earth element will have different behaviour when present as the dominant alloying element [15]. For this work the most common rare earth elements Ce, Dy, Gd, La, Nd and Y were selected based on their solid solubility in Mg and their electrochemical compatibility to Mg. The rare earth elements with lowest solid solubility are La (0.042 at. %) [84, 153-155]; Ce (0.1 at.%) [156, 157] and Nd (0.63 at.%) [84, 153]. While Dy (3.5 at.%) [158, 159] , Y (3.75 at.%) [159, 160] and Gd (4.6 at. %) [161, 162] show the highest solid solubilities. However not much is known about their electrochemical properties in chloride containing aqueous solutions. Thus in a first step the basic properties were determined.

a) Open Circuit Potential (OCP)

The variation of the open circuit potential (OCP) as a function of immersion time is used to follow the chemical stability and corrosion process of the surface layers on a sample during immersion [163]. The OCP curves of the pure metals are shown in Figure 4.1 and all results are summarised in Table 4.1. All the metals exhibited a more active potential at the beginning of the test. With increased immersion time their behaviour could be divided into three groups. In the first group including La and Ce, the OCP changed rapidly between 100-200 s to much higher values. The initial values of OCP are jumping from -1645 to -1420 mV for La and from -1668 to -1521 mV for Ce. After some time, OCP of La increased further to reach a nobler potential of -1342 mV at 2830 s and remained stable until the end of the test. For Ce, the OCP needed up to 4000 s to reach a stable potential value of -1464 mV. The second group consisted of Nd, Gd and Y, which did not show stabilization regions as the OCP continued to shift to more noble potentials. The last group contains Dy and Mg. The OCP of Dy increased initially and after 1900 s reached a nobler potential of -1316 mV; before it decreased to -1374 mV again after 2440 s and remained constant until the end of the test. Mg had a slight shift of the potential to -1614 mV after 44 s of immersion. The potential became slightly more active (-1636 mV) again between 44 and 328 s of immersion. Finally, the OCP became nobler reaching -1568 mV after 1090 s immersion and remained almost constant until the end of the test.

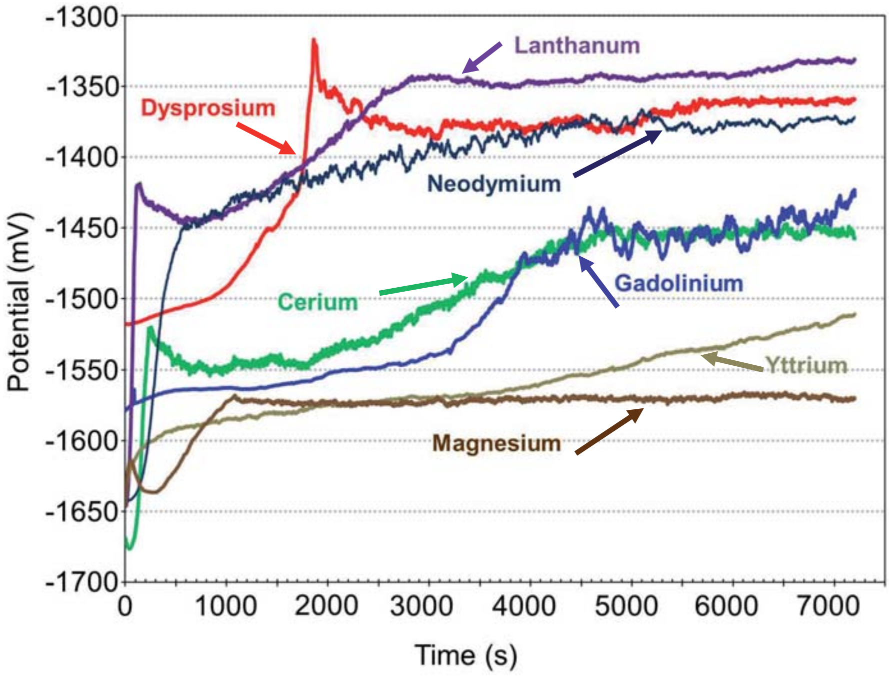

Figure 4.1 Open circuit potential (OCP) vs. time of pure metals after 2 h immersion in 0.5 wt.% NaCl solution

Table 4.1 Open circuit potential (OCP) measurements and after 2 h of pure metals in 0.5 wt.% NaCl solution

Element	OCP_{start} (mV vs. Ag/AgCl)	OCP_{final} (mV vs. Ag/AgCl) after 2 h
Ce	-1668 ± 2	-1454 ± 2
Dy	-1517 ± 1	-1360 ± 2
Gd	-1578 ± 3	-1430 ± 7
La	-1645 ± 2	-1333 ± 3
Nd	-1637 ± 2	-1370 ± 2
Y	-1641 ± 5	-1508 ± 9
Mg	-1645 ± 4	-1574 ± 5

The behaviour of all pure metals in NaCl solution could be assigned to different stages of interaction between surface and electrolyte. Regions with stable OCP reflect the formation of passive/protective film, which is in a stable equilibrium state of formation and dissolution. The region, where the OCP shifted to more active values or shows fluctuations reflect that the electrolyte and especially chloride ions penetrated the passive layer and reach the pure metal, this is the case of La, Dy, Ce, which present similar behaviour like Mg. The protective film is lost locally or gets thinner. Zones with higher fluctuations of potential such Gd and Nd could reflect that the passive layer could have some defects as pores or cracks, where the electrolyte reacted with the pure metal. If the OCP shifts into the noble direction the thickness of the passive/protective film is growing or gets denser. The fast changes at the beginning of immersion reflect a fast conversion of the air grown oxide layer most likely a hydroxide/oxide mixture.

b) Potentiodynamic polarisation measurements

Potentiodynamic polarisation measurements of the pure metals are shown in Figure 4.2. From Figure 4.2 the values of corrosion potential (E_{corr}), the corrosion current density (i_{corr}) and the corrosion rate (calculated from the intersection current density) can be derived. Corrosion potentials of the RE elements are nobler than the corrosion potential of Mg, which is consistent with the long term OCP measurements. However i_{corr} of the most of the RE elements are roughly 2 orders of magnitude higher, compared to pure Mg (see Table 4.2). However, RE metals such as Dy and Gd displayed some form of “passive range” at potentials between -987 to -809 mV for Dy and -1080 to -872 mV for Gd, where there appears to be “spontaneous passivity”. This behaviour of Dy and Gd is very interesting, since it reveals that at least some RE metals are rather resistant to corrosion in 0.5 wt. % NaCl, which is consistent with findings from Birbilis et al. [15].

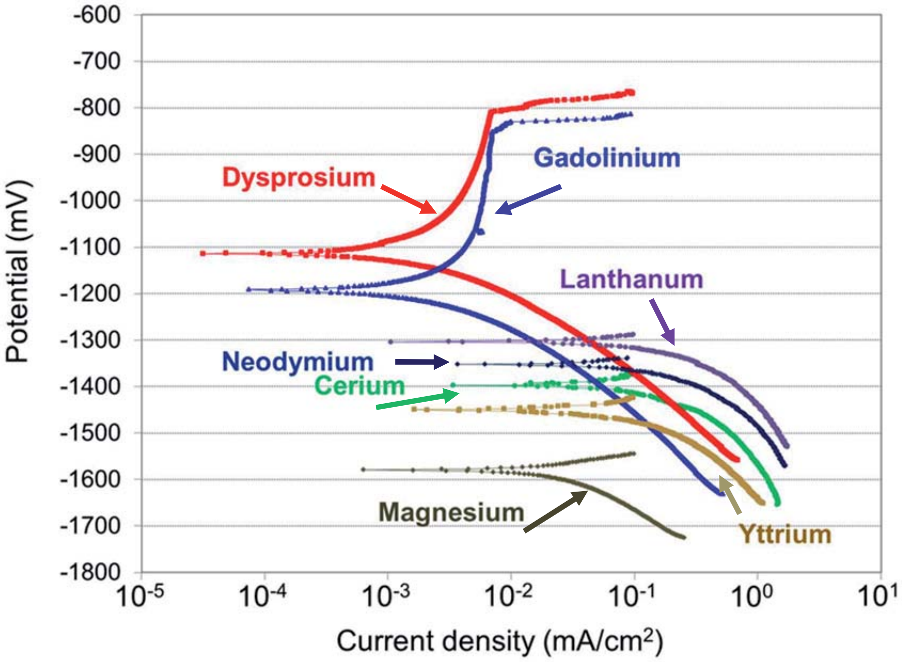

Figure 4.2 . Potentiodynamic polarisation measurements of pure elements in 0.5 wt. % NaCl solution

Table 4.2 Electrochemical data from potentiodynamic polarisation measurements of pure metals in 0.5 wt. % NaCl solution

Element	i_{corr} (mA/cm^2)	E_{corr} (mV vs. Ag/AgCl)	CR (mm/year)	Passive range (mV vs. Ag/AgCl)	E_{pit} (mV vs. Ag/AgCl)
Ce	0.13 ± 0.05	-1351 ± 58	3.00 ± 1.4	-	-
Dy	8.3×10^{-3} ± 0.004	-1110 ± 4	0.17 ± 0.08	-987 to -809	-809
Gd	0.027 ± 0.02	-1290 ± 77	0.59 ± 0.4	-1080 to -872	-861
La	0.17 ± 0.01	-1307 ± 5	4.26 ± 0.3	-	-
Nd	0.19 ± 0.003	-1350 ± 2	4.21 ± 0.06	-	-
Y	0.09 ± 0.04	-1403 ± 66	1.91 ± 0.08	-	-
Mg	4.9×10^{-3} ± 0.003	-1580 ± 13	0.11 ± 0.08	-	-

The corrosion studies of pure RE elements show that all RE elements were nobler to Mg. Based on these results it was decided to prepare Mg-RE-intermetallics with, Ce, Gd, La, Nd and Y. Only Dy was not selected because of higher price and higher exchange current in a couple with Mg compared to Gd, but similar properties e.g. passivity and solubility. Ce, La and Nd were chosen for their relatively low solid solubility in Mg which allows microstructural modifications with low amounts of RE addition. Gd was selected due to its extensive solid solubility in Mg. Additionally; Gd showed a passivation region that may suggest enhanced corrosion resistance. Y has the lowest potential difference compared to Mg [164] i.e. it is the least noble of all the RE elements tested.

4.2 Mg-RE-Intermetallics

If RE elements are added to Mg and if the solubility limit is exceeded the specific Mg rich intermetallic will form $Mg_{12}Nd$, Mg_5Gd, $Mg_{17}Ce_2$, $Mg_{17}La_2$ and $Mg_{24}Y_5$. These Mg-RE-Intermetallics as a combination of the selected RE with magnesium have a composition of Mg33Ce, Mg57Gd, Mg40La, Mg38Nd and Mg40Y, in weight percent. Alloys with intermetallic composition were casted because of two reasons:

a) To see how the combination with pure Mg affects the electrochemical properties of RE elements and vice versa; and

b) To evaluate the electrochemical data of the intermetallics to understand their interaction in the Mg matrix.

4.2.1 Microstructure

4.2.1.1 As-cast condition

a) Scanning electron microscopy (SEM) and Energy Dispersive X-ray Spectroscopy (EDS)

The SEM micrographs of the as-cast Mg-RE-intermetallics are shown in Figure 4.3. EDS point analysis were made on the selected points labelled as A, B, C, D, E, F, G, and reported in Table 4.3. Mg33Ce alloy consisted of a small volume fraction of secondary phases with different morphologies (Figure 4.3 a). Small spherical particles and a small fraction of a eutectic lamellar structure were observed. The higher magnification micrograph shown in (Figure 4.3 b) indicates the different morphologies and sizes of the phases. Both the lath like (marked as “A”) and the small spherical phases (marked as ‘B’) contained more Ce (Table 4.3) than the eutectic lamellar structure (marked as ‘C’) and the irregular shaped phase (marked as “D”). E shows compositions between (7.5-9.1 at. %) Ce and (89.6-91.4 at. %) Mg. The concentration of the ratios of Mg to Ce were around 4.4 and 20.5 for spherical/lath particles and eutectic lamellar particles, respectively, which are too far from the ideal Mg/Ce ratios of 8.5 or 8.2 for $Mg_{17}Ce_2$ or $Mg_{41}Ce_5$ phases, respectively, reported in the Mg-Ce system [100, 165]. However the ratios Mg/Ce for the matrix were between 9.8 and 12.1, which are relatively close to the above Mg-Ce phases.

Mg57Gd alloy consisted of a large volume fraction of intermetallic phases (Figure 4.3 c): mainly large particles with irregular shape and small volume fraction of cubic-spherical structure. The higher magnification micrograph (Figure 4.3 c) shows the distribution and morphologies of secondary phases. Small particles with geometrical shape (marked as “A”), lath shaped (marked as “B”) and irregular shape (marked as “C”) contained the highest amount of Gd between 33 and 72 at. % (Table 4.3). While the irregular shaped particles dark grey (marked as “D”) has a composition of 19.60 at. % Gd. While the matrix showed composition between 12.8 to 17.10 at. %. These results are consistent with Hampl et al. [161]. The ratios of Mg to Gd were around 4 and 6 for the phases marked as “C”, “D” and the matrix “E” respectively, and are relatively close to the ideal ratio of 5 for the phase Mg_5Gd, reported for the Mg-Gd system [14, 161].

The microstructure of the as-cast Mg40La alloy (Figure 4.3 e) consisted of a small volume fraction of second phases. Figure 4.3f shows the higher magnifications micrograph of the Mg40La microstructure. Several particles with different morphologies were observed: eutectic lamellar structure (marked as “A” and “C”) with La concentration of 23.4 at.% and 18.4 at.% respectively (Table 4.3); small volume fraction of bright particles marked as “B” with the lowest La concentration of 5.2 at.%; and an irregular shaped phase (marked as “D”) with approximately 19.9 at.% of La similar to “C”. While “E” showed a range concentrations between 8.1 to 10.11 at.% La. Chia et al. [152] and Birbilis et al. [15] studied the Mg/La system with additions of up to 4 wt. % La, and found the $Mg_{12}La$ intermetallic phase. In this investigation using a high concentration of La, $Mg_{17}La_2$ intermetallic phase was expected but only in the marked regions as “E” and “F” the Mg/La ratio were between 8 and 11, which are close to the 8.5 ideal ratio of $Mg_{17}La_2$ for the other positions the La/Mg ratios determined by SEM- EDS analysis were not representative of this phase.

The Mg38Nd microstructure consisted of a large volume fraction of second phases (Figure 4.3 g): mainly large particles with irregular shape (dark grey) and small volume fraction of cubic or spherical morphology (bright phases). The high magnification micrograph (Figure 4.3 h) shows the small volume fraction of the bright irregular shape microstructure marked as “A”, with 38 at.% Nd, cubic shape marked as “B” or “C” with similar concentration of Nd, at 16.8 at.% and 16.9 at.% respectively; and spherical shaped particles marked as “D” with concentration approximately of 2.7 at.% Nd. The large volume fraction of irregular phase (dark grey) marked as “E” contained the lowest concentration of Nd with 1.5 at.%, “F” contained a high concentration of Nd, around 22 at.% and "G" regions contains a wide range of concentrations of Nd (8.0 – 18.3 at%.). Birbilis et al. [15] have demonstrated that with additions of up to 4 wt.% of Nd it is possible to observe the Mg_3Nd intermetallic phase but Easton et al. [166] demonstrated that the occurrence of Mg_3Nd and $Mg_{12}Nd$ intermetallic phase formation depend upon the solidification rate and the heat treatment.

Mg40Y alloy consist of several phases as well (Figure 4.3 i): mainly large particles with irregular shape (dark grey) and small volume fraction of cubic structure (bright phases). The high magnification image (Figure 4.3 j) shows a small volume fraction of the bright cubic shaped microstructure marked as “A” and “B”, with higher Y concentrations of around 53.2 at.% and 40.9 at.% respectively. The large volume fraction of irregular phase (dark grey) marked as “C” and “D” has Y concentration of around 21.8 at.% and 4.2 at.% respectively. While the regions marked as “E” has between 11.40 to 21.60 at.% Y. Latter result is in agreement to those of Zhang et al. [108], who reported in an alloy with up to 15 wt.% Y intermetallic compound $Mg_{24}Y_5$.

The X-ray diffraction analysis reported below in conjunction with SEM-EDS composition analyses clarify the intermetallic phases expected.

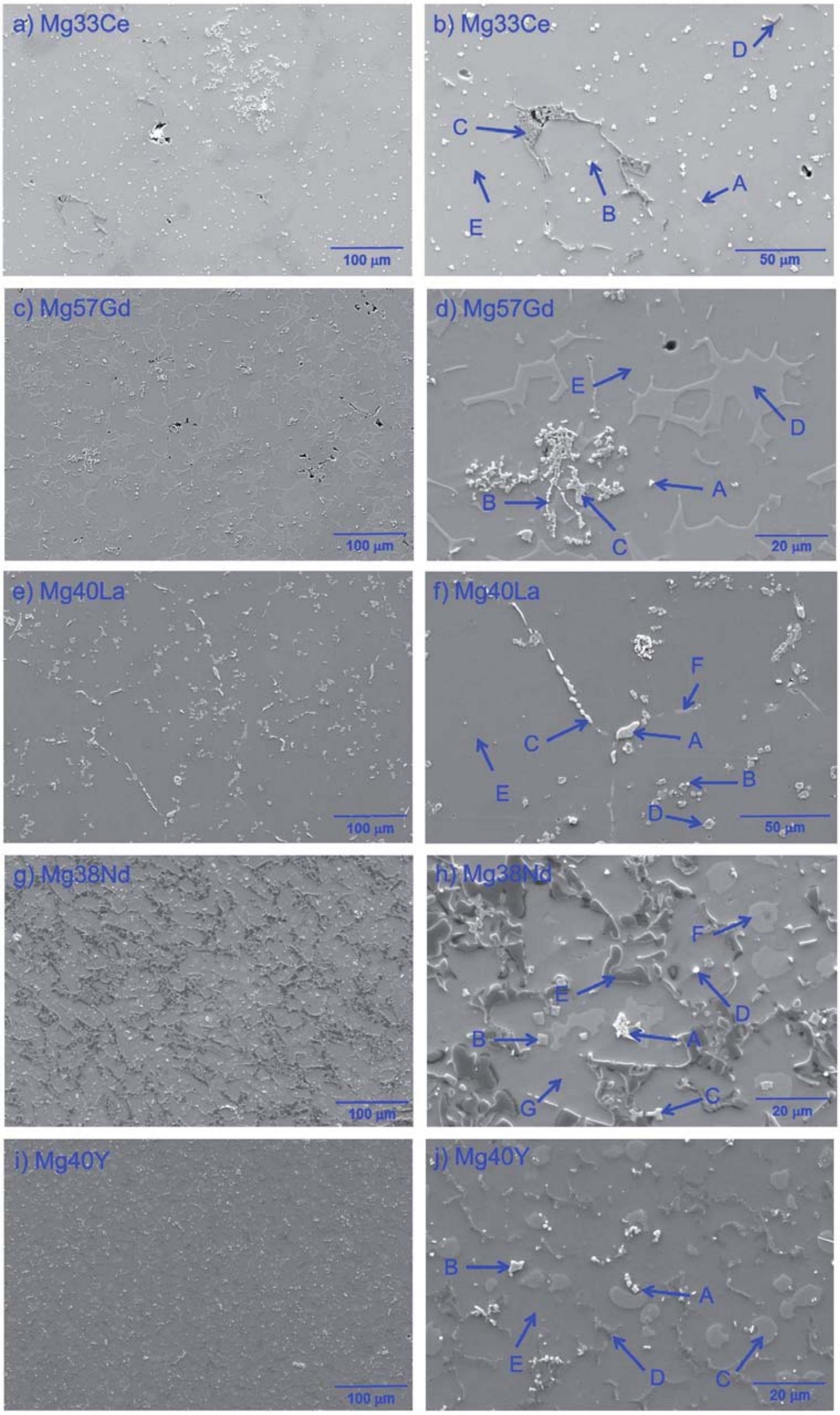

Figure 4.3 SEM micrographs of as-cast Mg-RE- Intermetallics: left side lower magnifications, right side higher magnifications showing different phases

Table 4.3 EDS analysis of the selected points of the as-cast Mg-RE-Intermetallics

Alloy	Location	Ce (at.%)	O (at.%)	Si (at.%)	Fe (at.%)	Mg (at.%)	Mg/Ce ratio
Mg33Ce	A	15.55	14.87	0.81	0.28	68.49	4.40
	B	17.49	2.59	3.05	-	76.87	4.39
	C	3.65	0.79	-	-	95.56	26.18
	D	6.10	0.82	-	-	93.08	15.25
	E	7.5-9.1	0.9-1.28	0.1-0.25	-	89.54-91.4	9.85-12.19
		Gd (at.%)	O (at.%)	Si (at.%)	Fe (at.%)	Mg (at.%)	Mg/Gd ratio
Mg57Gd	A	50.21	11.13	1.06	-	37.60	0.74
	B	32.16	1.38	1.35	-	65.11	2.02
	C	71.88	10.33	1.22	-	16.57	0.23
	D	19.60	1.17	0.06	-	79.17	4.03
	E	12.8-17.1	0.93- 7.6	0.3-0.5	-	74.9-83.41	4.38-6.22
		La (at.%)	O (at.%)	Si (at.%)	Fe (at.%)	Mg (at.%)	Mg/La ratio
Mg40La	A	23.41	15.48	0.40	-	60.71	2.59
	B	5.21	7.39	1.00	0.16	86.24	16.55
	C	18.38	12.26	-	-	69.36	3.77
	D	19.87	3.30	-	-	76.83	3.86
	E	8.1-10.11	1.33-3.03	0.1-0.2	-	86.68-90.1	8.57-11.05
	F	9.65	1.33	-	-	89.02	9.22
		Nd (at.%)	O (at.%)	Si (at.%)	Fe (at.%)	Mg (at.%)	Mg/Nd ratio
Mg38Nd	A	32.59	11.12	0.51	-	55.78	1.71
	B	16.82	2.09	1.42	-	79.67	4.73
	C	16.91	1.56	1.89	-	79.64	4.70
	D	2.73	5.72	1.04	-	90.51	33.15
	E	1.52	0.63	-	-	97.85	64.37
	F	21.99	2.05	-	-	75.96	3.45
	G	8.0-18.3	0.20-1.53	0.1-0.3	-	80.2-90.2	4.38-11.44
		Y (at.%)	O (at.%)	Si (at.%)	Fe (at.%)	Mg (at.%)	Mg/Y ratio
Mg40Y	A	53.23	14.68	0.13	-	31.96	0.60
	B	40.96	5.37	-	-	53.67	1.31
	C	21.84	2.03	-	-	76.13	3.48
	D	4.21	0.86	-	-	94.93	22.54
	E	11.4-21.6	2.1-6.7	1.0-1.60	-	70.2-87.4	3.25-7.33

b) X-Ray diffraction (XRD)

Figure 4.4 shows the X-ray diffraction patterns from the as-cast Mg-RE-Intermetallics, α-Mg peaks are present for all the casting. The diffraction pattern of Mg33Ce showed peaks that correspond to the $Mg_{17}Ce_2$ phase and weak peaks of $Mg_{41}Ce_5$ phase. For Mg38Nd, the diffraction pattern showed three intermetallic phases identified as $Mg_{12}Nd$, $Mg_{41}Nd_5$ and Mg_3Nd. Easton et al. [166] found that the intermetallics phases in this system depends on the casting parameters and non-equilibrium phases such as Mg_3Nd and $Mg_{12}Nd$ were observed in as-cast alloys. The diffraction patterns of Mg57Gd, Mg40La and Mg40Y suggested the presence of the intermetallic phases as Mg_5Gd, $Mg_{17}La_{12}$ and $Mg_{24}Y_5$ respectively.

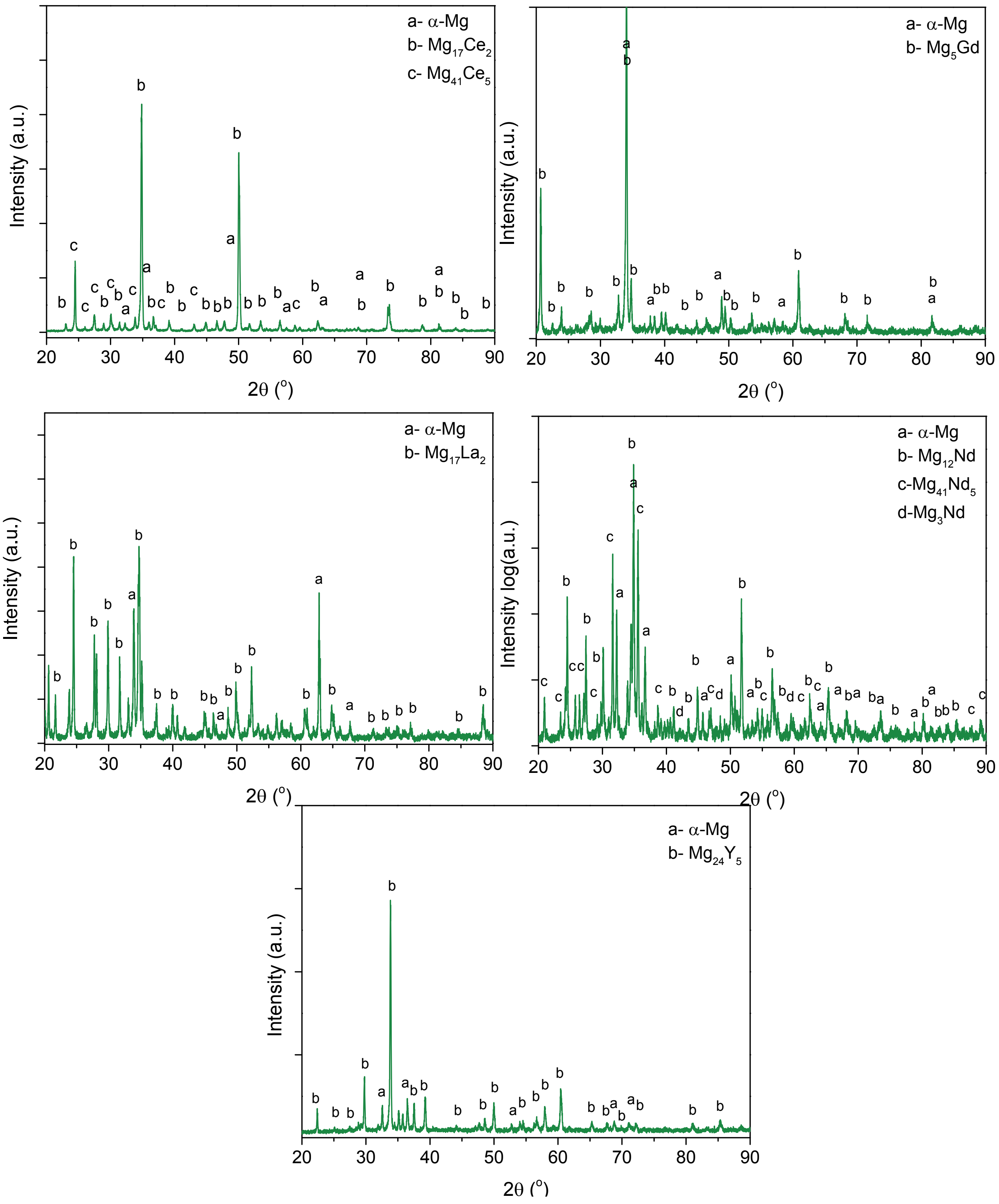

Figure 4.4 X-ray diffraction patterns of as-cast Mg-RE-Intermetallics

(λ=1.54 nm and CuKα radiation)

4.2.1.2 Effect of heat treatment

a) Scanning electron microscopy (SEM) and Energy Dispersive X-ray Spectroscopy (EDS)

Figure 4.5 shows the SEM micrographs of the Mg-RE-intermetallics after heat treatment at 540°C for 72 h. EDS point analyses were made on the selected points labelled as A, B, C and D. Mg33Ce consisted of a small volume fraction of small spherical or lath type of particles (Figure 4.5 a). There is no evidence of eutectic lamellar structure as observed in the as-cast state in Figure 4.3 (b). The EDS analysis reported similar concentration of Ce and Mg in the secondary phases (marked as “A”) and bright/ dark grey areas marked as “B”, “C” and “D” respectively. The ratio of Mg to Ce was higher than 11 for all four positions, which is not really close to the ideal Mg /Ce radio of 8.5 for $Mg_{17}Ce_2$ but suggests homogeneous composition.

Mg57Gd consisted of a large volume fraction, mainly bright particles with irregular shapes (marked as “A”) and geometrical shape (marked as “C”) (Figure 4.5 b), which contained the highest amount of Gd 29 and 87 at.% respectively, (Table 4.4) and dark grey particles with irregular shape (marked as “B”) has Gd compositions of 12 at.%, while the region marked as “D” have Gd compositions between 11.80 to 16.05 at.% respectively, which corresponds relatively good to the ideal ratio of 5 for the Mg_5Gd phase.

The microstructure of the Mg40La (Figure 4.5 c) consisted of a small volume fraction of secondary phases, bright particles (marked as “A”) with La concentration of 19 at.% (Table 4.4). SEM-EDS analysis made on the bright (marked as “B”) and dark (marked as “C”) areas show concentration of La around 9 at. %. While the areas marked as “D” show concentration between 7.4-9.1 at.% La. The ratios of Mg to La were around 3.92 for the bright particles and for the two areas 9.74 and 10, while “C” areas were 9 to 11, these values are close to the ideal Mg/La ratio of 8.5 for $Mg_{17}La_2$.

The microstructure of Mg38Nd after heat treatment showed small volume fraction of secondary phases (Figure 4.5 d): mainly irregular shape particles, marked as “A”, with 10.77 at% Nd, and Mg/Nd ratio was 8.05, which corresponds to the $Mg_{41}Nd_5$ phase. The areas marked as “B” and “C” showed Nd concentrations of 12.60 at. % and between 8.3 to 12.6 at.% respectively, the Mg/Nd ratios were around 6.73 and between 6.7 to 10.5 respectively.

The microstructure of Mg40Y showed a large volume fraction of secondary phases: mainly consisted of regular shape particles marked as “A” and irregular shape particles marked as “B” (Figure 4.5 e). The Y concentration of these regular particles was 19.70 at.% which corresponds to a composition close to $Mg_{41}Y_5$ intermetallic phase. The irregular particles “B” presented the heights concentration of Y around 36.39 at.% and the area marked as “C” contained Y concentration between 11.20 to 13.27 at.% (Table 4.4). The SEM-EDS analysis of selected particles shows that the heat treatment increased the amount of the expected intermetallic phases and homogenise distribution of RE in the intermetallics phases, but did not remove the secondary RE phases fully.

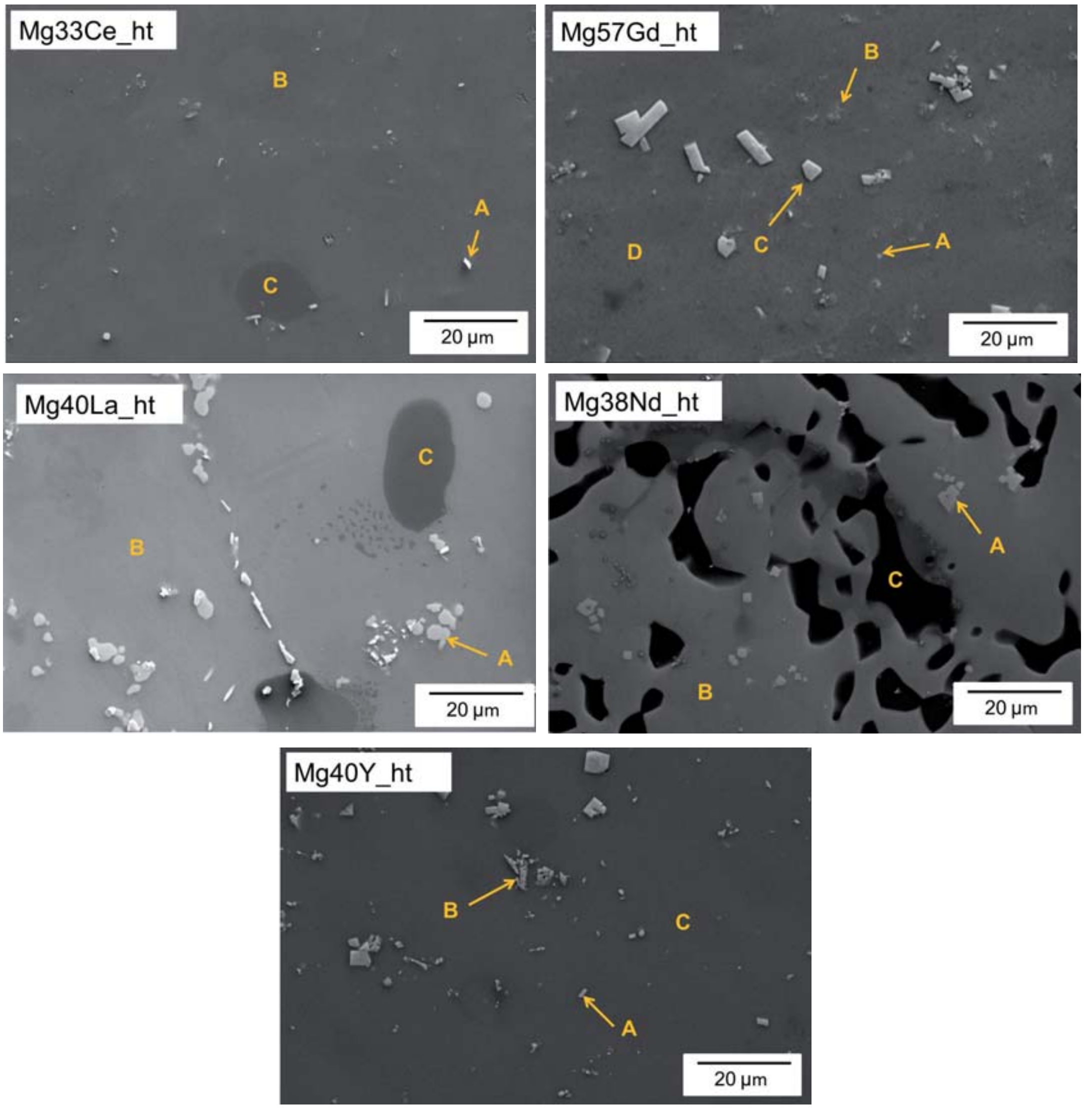

Figure 4.5 SEM micrographs of Mg-RE- Intermetallics after heat treatment at 540°C for 72 h

Table 4.4 EDS analysis of the selected points of the Mg-RE-Intermetallics after heat treatment at 540°C for 72 h

Alloy	Location	Ce (at.%)	O (at.%)	Mg (at.%)	Mg/Ce ratio
Mg33Ce_ht	A	7.96	1.43	90.61	11.38
	B	8.01	2.00	89.99	11.23
	C	6.5-8.03	1.43-4.10	89.20-90.61	11.19-13.78
		Gd (at.%)	O (at.%)	Mg (at.%)	Mg/Gd ratio
Mg57Gd_ht	A	29.67	2.22	68.11	2.30
	B	12.71	18.90	68.39	5.38
	C	87.69	4.94	7.37	0.08
	D	11.80-16.05	1.38-4.70	82.42-83.60	5.14-7.08
		La (at.%)	O (at.%)	Mg (at.%)	Mg/La ratio
Mg40La_ht	A	19.27	5.02	75.71	3.93
	B	9.18	1.38	89.44	9.74
	C	7.40-9.18	1.38-4.60	87.40-89.44	9.74-11.97
		Nd (at.%)	O (at.%)	Mg (at.%)	Mg/Nd ratio
Mg38Nd_ht	A	10.77	2.43	86.80	8.06
	B	12.60	1.27	85.54	6.79
	C	8.30-12.60	1.86-4.89	85.50-89.20	6.79-10.58
		Y (at.%)	O (at.%)	Mg (at.%)	Mg/Y ratio
Mg40Y_ht	A	19.70	-	80.30	4.08
	B	36.39	42.09	21.52	0.59
	C	11.20-13.27	2.80-3.70	82.60-85.40	6.54-7.60

b) X-Ray diffraction (XRD) after heat treatment

Figure 4.6 shows the X-ray diffraction patterns of the Mg-RE-Intermetallics after heat treatment. Except for Mg38Nd the results indicate the presence of a single intermetallic phase while some traces of α-Mg were also detected. The diffraction patterns of Mg33Ce, Mg58Gd, Mg40La and Mg40Y showed peaks with better resolution for the intermetallic phases compared with the X-ray patterns of the as-cast condition samples (Figure 4.4). The intermetallic phases of $Mg_{17}Ce_2$, Mg_5Gd, $Mg_{17}La_2$ and $Mg_{24}Y_5$ were observed for Mg33Ce, Mg58Gd, Mg40La and Mg40Y respectively, while in Mg38Nd, two intermetallic phases were identified, $Mg_{41}Nd_5$ and Mg_3Nd.

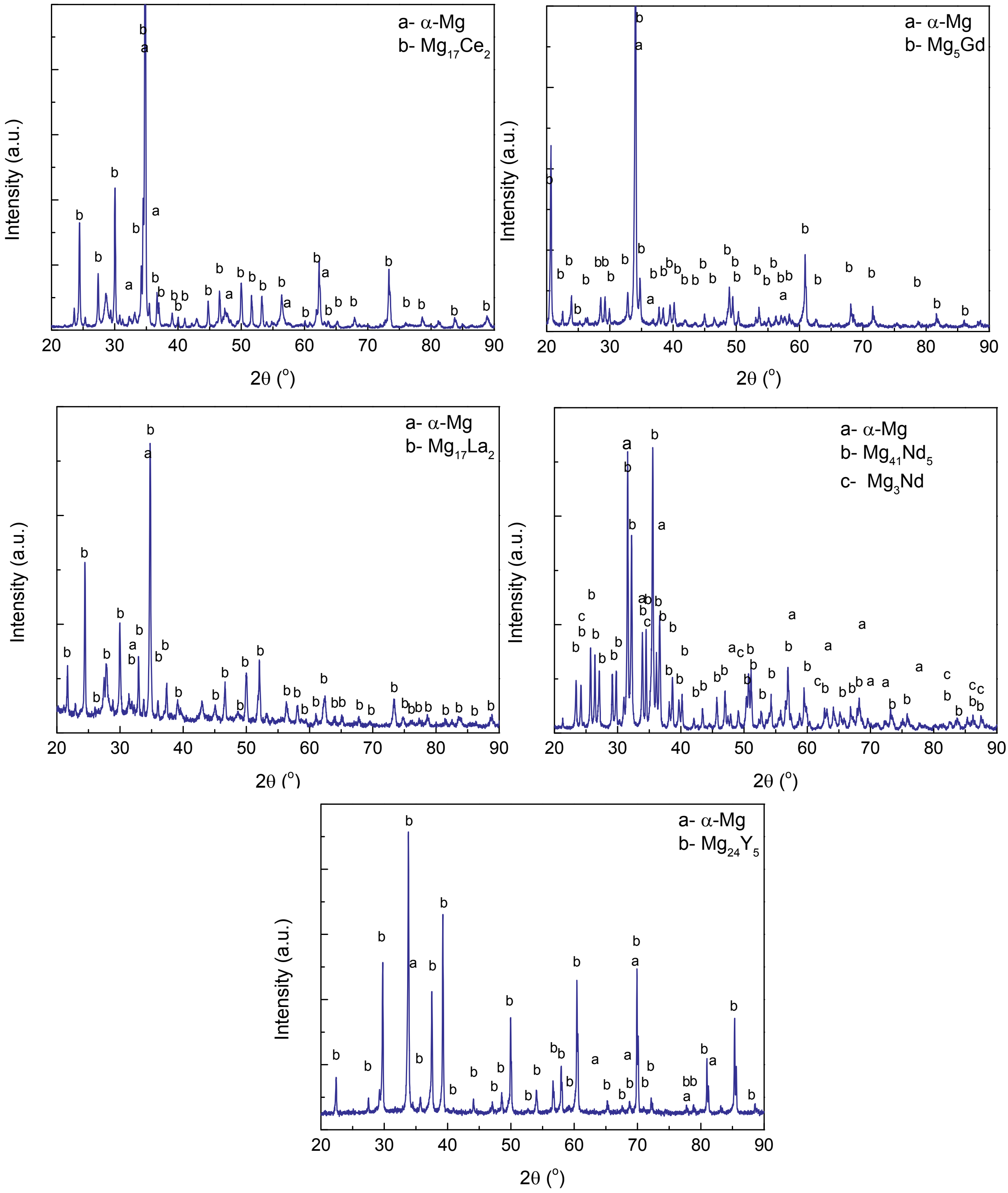

Figure 4.6 X-ray diffraction patterns of Mg-RE-Intermetallics after heat treatment at 540°C for 72 h (λ=1.54 nm and CuKα radiation)

4.2.2 Evaluation of the corrosion behaviour

4.2.2.1 As-cast condition

a) Open Circuit Potential (OCP)

Open circuit potential (OCP) of the Mg-RE-intermetallics is shown in Figure 4.7. It reveals that the OCP of the RE element has no direct influence on the potential of Mg-RE-intermetallic e.g. it cannot be used to predict their behaviour, as the order of activity (potential) is not the same anymore. The OCP values of Mg-RE-intermetallics shifted to less noble values compared with pure RE potential values (Figure 4.1), but they are still significantly less active than pure magnesium. The intermetallic castings of Mg38Nd, Mg40Y and Mg40La show stable OCP values during the test, while Mg33Ce shows stronger potential fluctuations and the final potential shifted to a value of approximately -1576 mV (see Table 4.5). On the other hand OCP of Mg57Gd shifts towards a more noble potential values during the test compared to with the other intermetallics and reached a nobler potential at -1507 mV (see Table 4.5). The OCP results might be influence by phase mixtures especially for the Mg38Nd and Mg 33Ce castings.

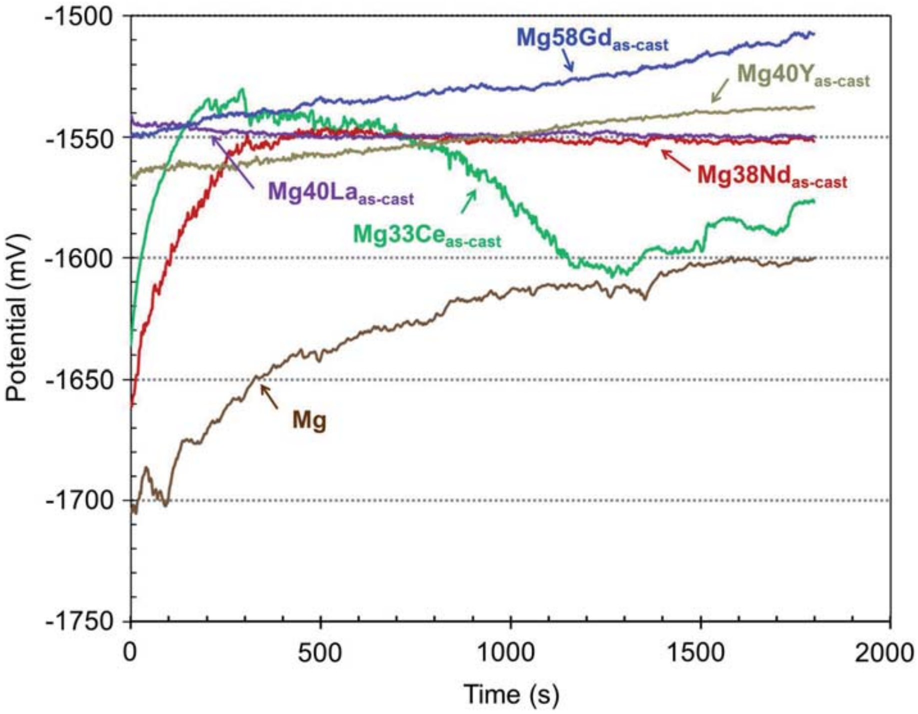

Figure 4.7 Open circuit potential (OCP) vs. time of the as-cast Mg-RE-intermetallics after 30 minutes immersion in 0.5 wt.% NaCl solution

Table 4.5 Electrochemical data from open circuit potential (OCP) measurements of the as-cast Mg-RE-intermetallics in 0.5 wt% NaCl solution

Mg-RE-int. as-cast condition	$E_{initial}$ (mV vs. Ag/AgCl)	E_{final} (mV vs. Ag/AgCl)	OCP (mV vs. Ag/AgCl) after 30 min
Mg33Ce	-1636	-1576	-1570 ± 3
Mg38Nd	-1661	-1552	-1558 ± 6
Mg40La	-1541	-1550	-1549 ± 0.4
Mg40Y	-1568	-1538	-1551 ± 15
Mg58Gd	-1550	-1507	-1529 ± 22
Mg	-1704	-1600	-1629 ± 54

b) Potentiodynamic polarisation measurements

Figure 4.8 shows the potentiodynamic polarisation measurements for the Mg-RE-intermetallics. The plot includes the response for the high purity magnesium, for comparison. These results, illustrate that combination of RE with Mg form respective intermetallic, which leads to a corrosion potential closer to Mg but which is still higher by up to 50 – 99 mV compared to pure RE and Mg (see Table 4.6). Higher corrosion rates were also observed. Mg33Ce showed the lowest corrosion rate (2.24 mm/year), while Mg40 Y has the highest corrosion rate at 15.45 mm/year. Mg38Nd, Mg40La and Mg58Gd presented intermediate values, at 7.84 mm/year, 9.93 mm/year and 10.36 mm/year, respectively.

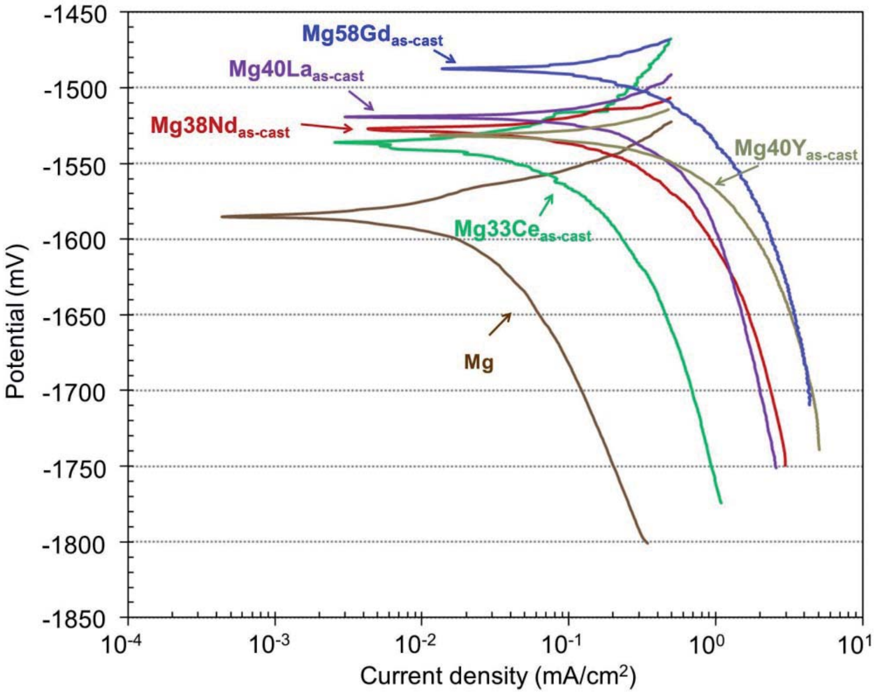

Figure 4.8 Potentiodynamic polarisation measurements of the as-cast Mg-RE-intermetallics in 0.5 wt.% NaCl solution

Table 4.6 Electrochemical data from potentiodynamic polarisation measurements of the as-cast Mg-RE-intermetallics in 0.5 wt.% NaCl solution

Mg-RE-int. as-cast condition	i_{corr} (mA/cm^2)	E_{corr} (mV vs. Ag/AgCl)	CR (mm/year)
Mg33Ce	0.10 ± 0.06	-1536 ± 1	2.24 ± 1
Mg38Nd	0.34 ± 0.05	-1527 ± 2	7.84 ± 3
Mg40La	0.43 ± 0.03	-1519 ± 3	9.93 ± 2
Mg40Y	0.68 ± 0.02	-1532 ± 3	15.45 ± 4
Mg58Gd	0.45 ± 0.04	-1487 ± 2	10.36 ± 4
Mg	0.03 ± 0.003	-1586 ± 5	0.61 ± 0.7

4.2.2.2 Effect of the heat treatment

a) Open Circuit Potential (OCP)

Figure 4.9 illustrates the open circuit potential values (OCP) of the Mg-RE-intermetallics after heat treatment at 540°C for 72 h. The OCP values of the heat treated Mg-RE-intermetallics shifted slightly to more active values compared with the as-cast intermetallics (Figure 4.7), but they are still less active than pure magnesium. The intermetallics, Mg38Nd, Mg40La and Mg40Y show unstable OCP values during the initial seconds (0 – 500 s), then their OCP values shifted to more noble potentials at -1562 mV, -1559 mV and -1540 mV, respectively. Mg33Ce shows less potential fluctuations compared with as-cast condition and the final potential shifted to a value of approximately -1584 mV (see Table 4.7). On the other hand OCP of Mg57Gd stabilised after 500 s immersion and at the end is still the noblest OCP with -1533 mV

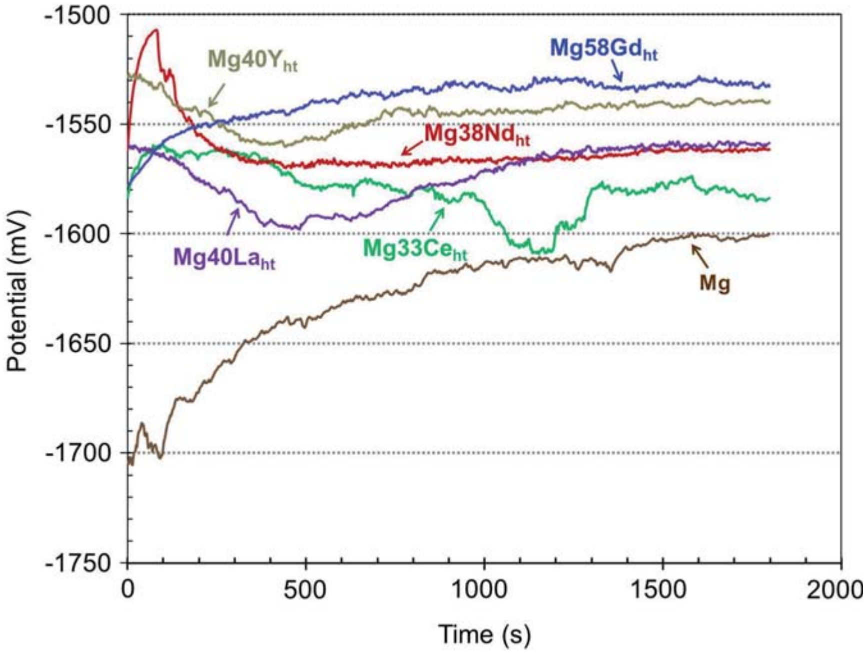

Figure 4.9 Open circuit potential (OCP) vs. time of heat treated Mg-RE-intermetallics after 30 minutes immersion in 0.5 wt.% NaCl solution

Table 4.7 Open circuit potential (OCP) measurements of the heat treated Mg-RE-intermetallics in 0.5 wt% NaCl solution

Mg-RE-int. after heat treatment	$E_{initial}$ (mV vs. Ag/AgCl)	E_{final} (mV vs. Ag/AgCl)	OCP (mV vs. Ag/AgCl) after 30 min
Mg33Ce	-1583	-1584	-1579 ± 3
Mg38Nd	-1562	-1562	-1561 ± 1
Mg40La	-1559	-1559	-1573 ± 3
Mg40Y	-1528	-1540	-1551 ± 3
Mg58Gd	-1578	-1533	-1529 ± 3
Mg	-1704	-1600	-1629 ± 54

b) Potentiodynamic polarisation measurements

Potentiodynamic polarisation curves of the Mg-RE-intermetallics after heat treatment at 540°C for 72 h are shown in Figure 4.10. After the heat treatment the corrosion potential values (E_{corr}) of the intermetallics and Mg were divided in three categories. Lower E_{corr} differences compared to Mg and the as-cast condition were observed for Mg33Ce, Mg38Nd and Mg40La with around 18 mV, 35 mV and 50 mV respectively. Mg40Y showed nearly no change and the E_{corr} difference remained at 53 mV. Mg58Gd showed the highest E_{corr} difference around 135 mV which is even higher than in the as-cast condition (see Table 4.8). The current densities were also affected by the heat treatment changing the corrosion rates compared with the values of the as-cast intermetallics (see Table 4.6). The corrosion rate increased dramatically for Mg38Nd (14.41 mm/year). The opposite was observed for Mg58Gd with a corrosion rate of 4.75 mm/year, indicating a reduction of 50% of the as-cast value. Mg33Ce, Mg40La and Mg40Y did not show remarkable changes of their corrosion rates (see Table 4.6 and Table 4.8). The Mg addition tends to produce less noble values of E_{corr} for the intermetallics, as the Mg additions are less noble than pure RE [15]. Corrosion potential values (E_{corr}) for the Mg-RE-intermetallics are clearly nobler than corrosion potential of Mg. However icorr of Mg-RE-intermetallics are considerably higher than icorr of pure Mg generating high corrosion rates. In general the intermetallic phases degraded faster than pure magnesium

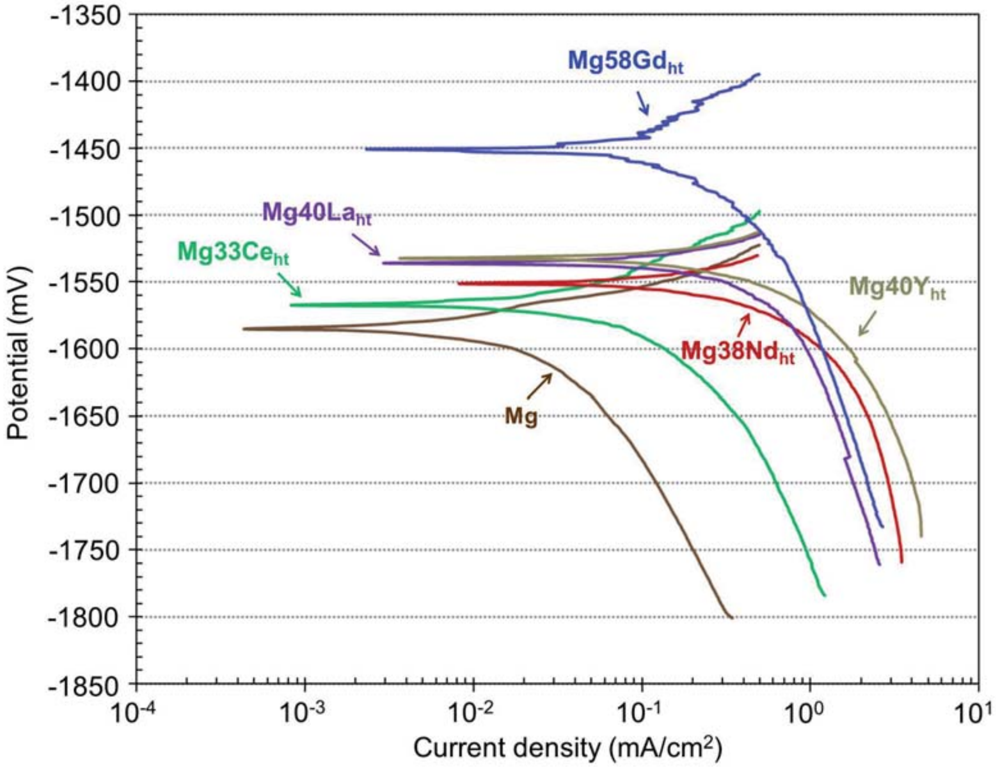

Figure 4.10 Potentiodynamic polarisation measurements of heat treated Mg-RE-intermetallics in 0.5 wt.% NaCl solution

Table 4.8 Electrochemical data from potentiodynamic polarisation measurements of the heat treated Mg-RE-intermetallics in 0.5 wt. % NaCl solution

Mg-RE-int. after heat treatment	i_{corr} (mA/cm^2)	E_{corr} (mV vs. Ag/AgCl)	CR (mm/year)
Mg33Ce	0.11 ± 0.01	-1567 ± 4.92	2.57 ± 0.19
Mg38Nd	0.63 ± 0.03	-1551 ± 1.13	14.41 ± 0.09
Mg40La	0.47 ± 0.20	-1536 ± 2.76	10.64 ± 4.16
Mg40Y	0.67 ± 0.03	-1533 ± 1.65	15.36 ± 0.97
Mg58Gd	0.21 ± 0.01	-1451 ± 2.51	4.75± 0.55
Mg	0.03 ± 0.003	-1586 ± 5.43	0.61 ± 0.7

4.2.2.3 Galvanic coupling

The galvanic current was measured between the magnesium matrix and the Mg-RE-intermetallics in the as-cast condition and following the heat treatment. The measurements were performed using an exposed area of 0.5 cm^2 for both electrodes. The galvanic coupling reveals the interaction between the intermetallic phases and the matrix when in contact with a corrosive medium. Figure 4.11 shows the resulting current density vs. time for the coupling of pure Mg with the Mg-RE-intermetallics in the as-cast condition (a) and after the heat treatment (b) in 0.5 wt.% NaCl solution. For the as- cast intermetallics the coupling between Mg and Mg57Gd show the highest current density of around 0.375 mA/cm^2, followed by Mg and Mg38Nd at 0.166

mA/cm^2, Mg and Mg33Ce with 0.107 mA/cm^2 . Mg and Mg40Y revealed large current density fluctuations during the test but the final current density was 0.032 mA/cm^2. Mg and Mg40La showed the lowest current density at 0.011 mA/cm^2. The coupling experiment following the heat treatment show changes to the current density of the galvanic couples, some show an increase while others show a decrease of current densities compared with those as-cast samples. Mg and Mg33Ce showed a slight increase in the current density (0.144 mA/cm^2), while for Mg-Mg38Nd and Mg-Mg40Y current density doubled (0.30 mA/cm^2) and 0.086 mA/cm^2 respectively. Mg and Mg40La showed the strongest relative increase six times more in the final value of the current density with 0.05 mA/cm^2.

Mg and Mg57Gd showed a 50% reduction of the current density (0.185 mA/cm^2) in the heat treated condition compared to the as-cast samples. The uniform distribution of elements, and the reduced amount of additional phases detected after the heat treatment resulted in the increase of the current density of the galvanic coupling of all intermetallics with Mg. Only the Mg57Gd showed an opposite trend. A possible explanation is the reduction of α-Mg in the intermetallic castings after heat treatment. This has removed or reduced a local self-protection effect of the cathode by incorporated sacrificial Mg anode areas reducing the external current between Mg anode and intermetallic cathodes.

The intermetallic containing Nd was the exception, as even after the heat treatment two different intermetallics phases were observed and it is difficult to judge which one of the phases is responsible for the properties.

At this point only three Mg-RE systems are of further interest: Mg-La because of the lowest exchange currents, Mg-Ce because of the lowest practical potential difference and the lowest corrosion rate of its intermetallic phase and Mg-Gd because of its high solubility offering the chance to prevent critical intermetallic precipitates. Furthermore the intermetallics in this system it present seems to be the more detrimental from the point of galvanic coupling.

The other two systems (Mg-Nd and Mg-Y) were omitted, because they did show only average properties. For the other systems binary alloy were casted with different amounts of intermetallics in the microstructure and the detailed analysis of microstructure and properties will be addressed in the following chapter.

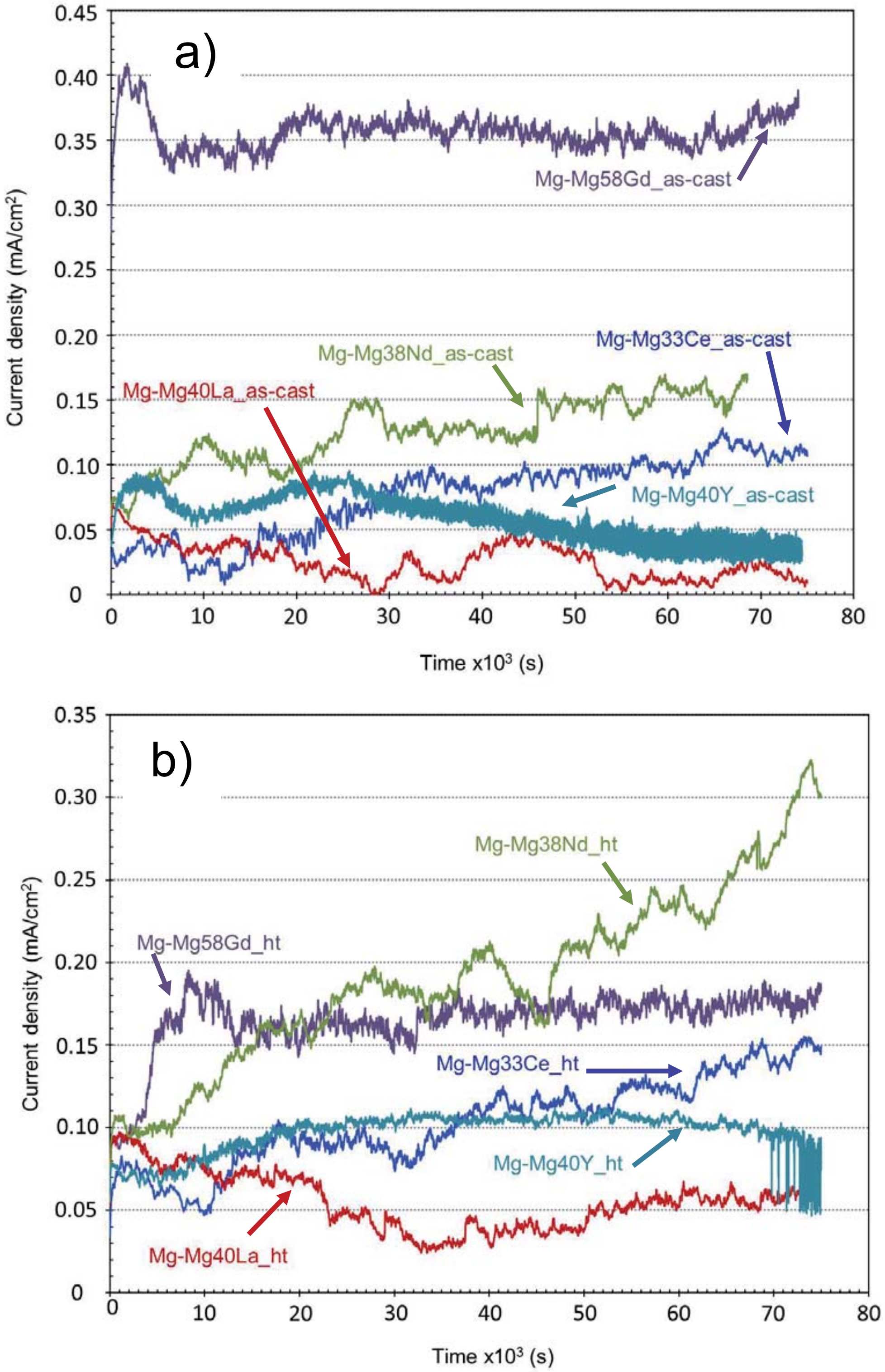

Figure 4.11 Current density vs time of the galvanic coupling Mg-Intermetallics: a) as-cast condition and b) after heat treatment

4.3 Binary alloys

4.3.1 The as-cast alloys

The Mg-Ce, Mg-La and Mg-Gd binary alloys were prepared to evaluate the influence of composition (amount of intermetallic phases) on the corrosion behaviour. Four concentrations were casted with 1, 5, 10 and 15 wt. % of Ce, La and Gd. Ce and La have low solubility, while Gd has the highest solubility of the RE elements in Mg. So the influence of different combinations of Mg matrix solubilities with different amounts of intermetallics on the corrosion behaviour can be studied.

4.3.1.1 Characterization

a) Scanning electron microscopy (SEM) and Energy Dispersive X-ray Spectroscopy (EDS)

Increase in the alloying addition increased the amount of intermetallic or eutectic phase. Figure 4.12 shows the morphology of as-cast Mg-Ce alloys with different Ce concentrations. With 1 wt. % Ce addition, the eutectic phase is fine. Increase in Ce content to 5 wt. % resulted in a continuous distribution of intermetallic phase along the grain boundaries. The bright phases in all alloys which are the intermetallics contain amounts of Ce between 1.5 and 7 at%. Which is consistent with the analysis of the casted and heat treated Mg-Ce-intermetallics and the dark phase marked as “C" is the α-Mg matrix with Ce content between 0.07 and 0.75 at%. When the Ce addition increased to 10 wt.%, the primary α-Mg dendrites (marked as “C”) decreased considerably and at an addition of 15 wt.% Ce, the eutectic phase (marked as “A” and “B”) is more abundant and the amount of α-Mg (marked as “C”) is low.

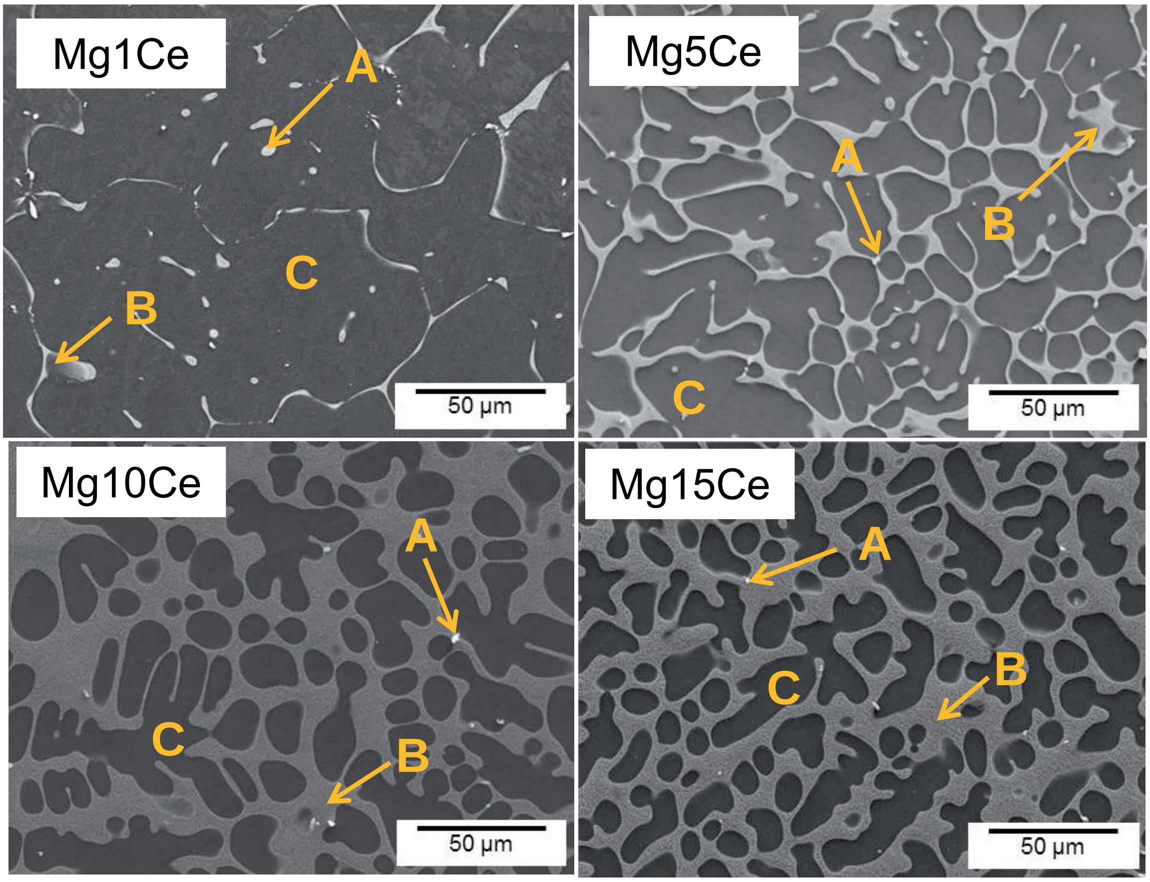

Figure 4.12 SEM micrographs of as-cast Mg-Ce alloys with 1 wt.%, 5 wt.%, 10 wt.% and 15 wt.% of Ce

A similar behaviour was also observed in Mg-La alloys. Figure 4.13 shows the microstructures of gravity die-cast Mg-La alloys with different amounts of La. The dark phases are α-Mg solid solutions (marked as "C") and the grey phases in all alloys (marked as "A" and "B") presented La content between 3 and 6 at% (see Table 4.9). This system shows an even larger amount of eutectic phases in the inter-dendrite regions compared with Mg-Ce [152].

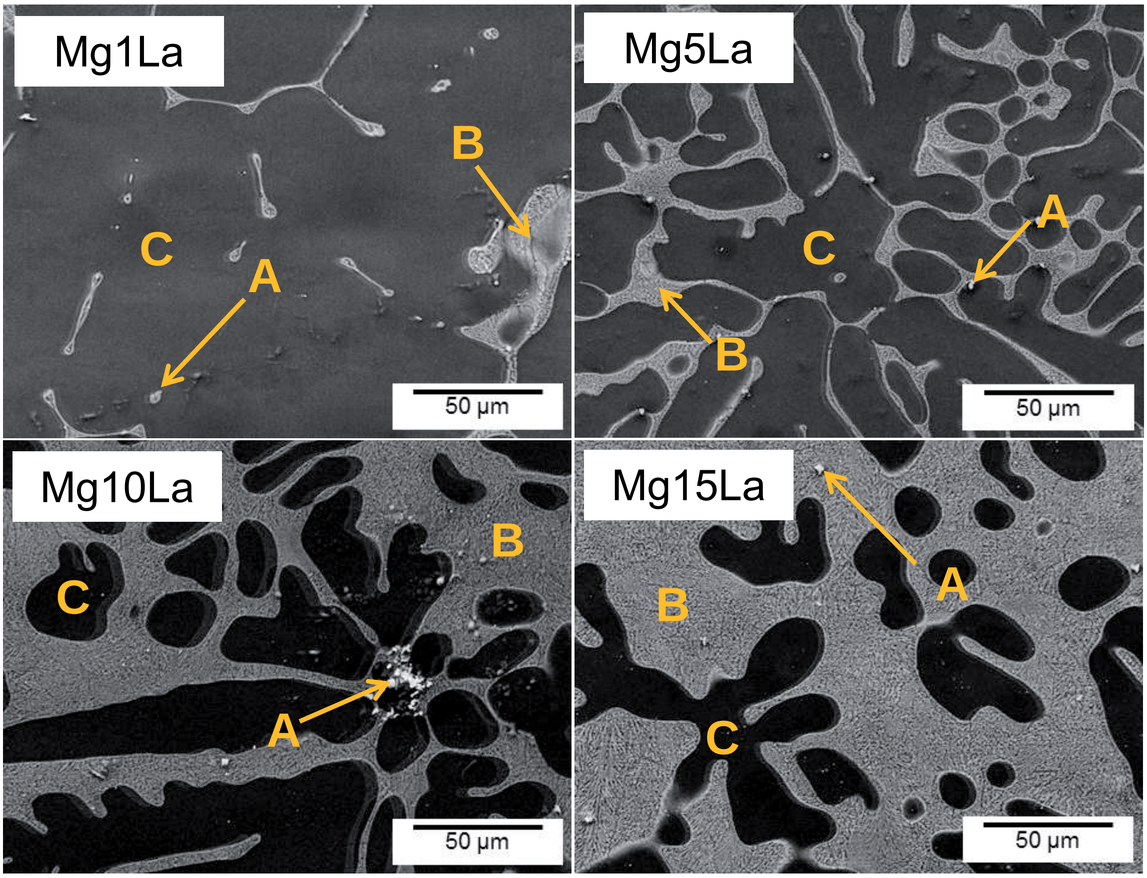

Figure 4.13 SEM micrographs of as-cast Mg-La alloys with 1 wt.%, 5 wt.%, 10 wt.% and 15 wt.% of La

The Mg-Gd alloys show a different behaviour compared with Mg-Ce and Mg-La. The typical microstructures of as-cast Mg-Gd alloys are shown in Figure 4.14. The α-Mg phase (marked as "D") and the intermetallic phases in all alloys marked as "A" and "B" do contain between 5 and 15 at.% Gd in the precipitates indicating the presence of the Mg_5Gd intermetallic phase. In addition some α-Mg zones with Gd-enrichment of up to 4 at. % were observed in all alloys and marked as "C", this Gd content is relatively higher compared to the primary α-Mg dendrites ("D"). The eutectic phases (A+B) form not only at the grain boundaries but also at intra-granularly locations in α-Mg phase. Altogether, the Mg-Gd alloys have a much lower amount of eutectic phase due to the high Gd solubility in α-Mg

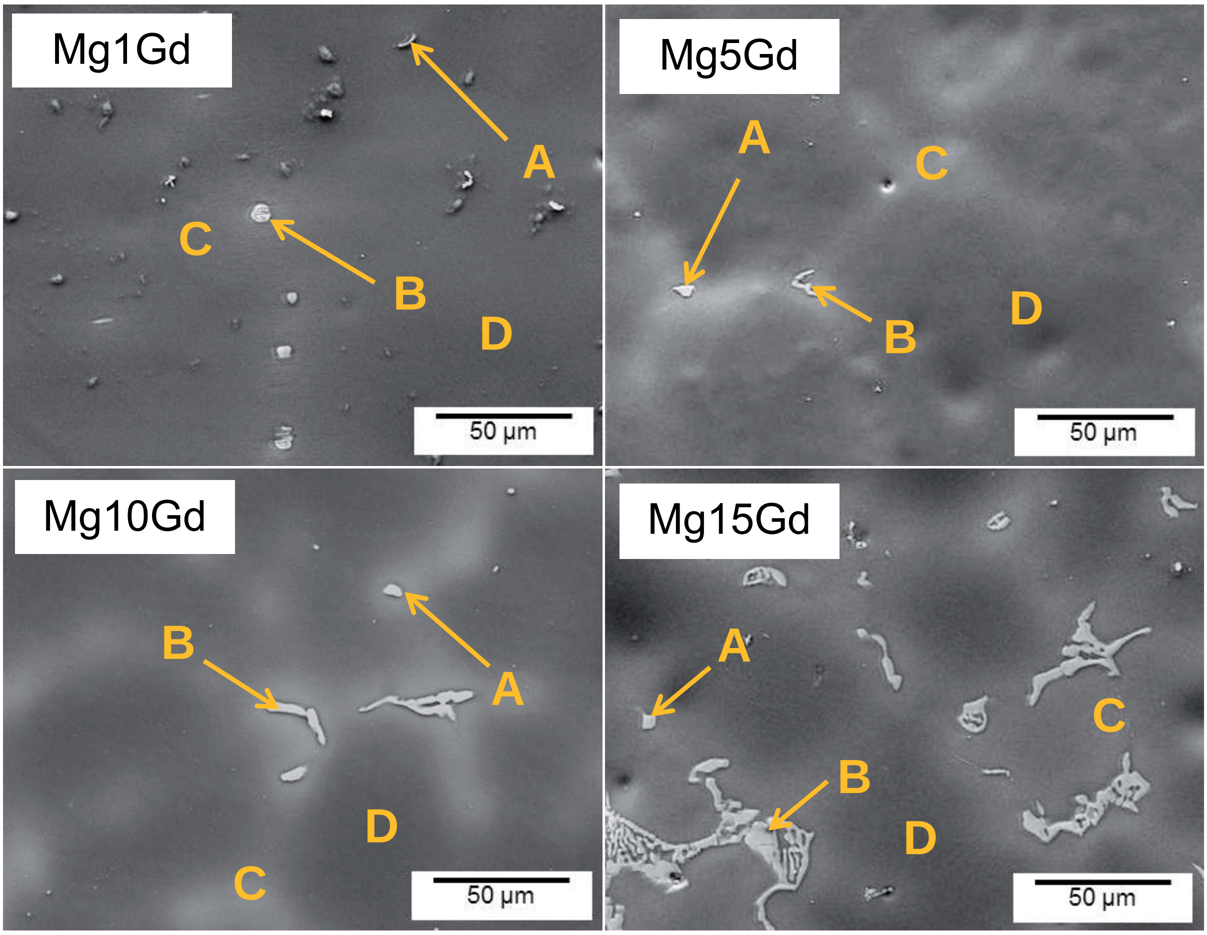

Figure 4.14 SEM micrographs of as-cast Mg-Gd alloys with 1 wt.%, 5 wt.%, 10 wt.% and 15 wt.% of Gd

In this investigation the La/Mg and Ce/Mg ratios determined by SEM- EDS analysis were not accurate for the intermetallic phase identification, due to two main factors, the size of the intermetallic and eutectic phases and the contribution of the matrix. Nevertheless the results of X-Ray diffraction analyses in the next section will use for the identification of the intermetallic phases. For Gd/Mg ideal ratio of the Mg_5Gd intermetallic phase could be observed in the four binary alloys.

Table 4.9 EDS analyses of the selected points of the as-cast Mg-Ce, Mg-La, Mg-Gd binary alloys

Alloy	Location	Ce (at.%)	O (at.%)	Si (at.%)	Ca(at.%)	Mg (at.%)
Mg1Ce	A	2.45	-	0.12	-	97.43
	B	1.44	-	1.31	-	97.25
	C	0.75	-	0.16	-	99.09
Mg5Ce	A	3.00	0.10	0.10	-	96.80
	B	3.82	1.09	0.24	-	94.86
	C	0.10	0.74	0.44	-	98.72
Mg10Ce	A	4.49	1.07	-	-	94.44
	B	5.14	1.13	-	-	93.73
	C	0.20	0.75	-	-	99.05
Mg15Ce	A	4.56	0.93	-	-	94.51
	B	6.81	1.08	-	-	92.11
	C	0.07	0.75	-	-	99.18
Alloy	Location	La (at.%)	O (at.%)	Si(at.%)	Ca(at.%)	Mg (at.%)
Mg1La	A	3.59	1.14	0.09	-	95.18
	B	3.39	1.02	0.10	-	95.50
	C	0.02	0.73	0.07	0.08	99.10
Mg5La	A	3.26	1.09	0.13	-	95.52
	B	3.03	1.02	0.13	-	95.82
	C	0.01	0.85	0.08	-	99.06
Mg10La	A	6.13	19.64	1.24	-	72.70
	B	3.29	0.78	0.12	-	95.82
	C	0.01	0.45	0.03	-	99.50
Mg15La	A	3.77	10.03	8.54	-	77.66
	B	3.21	1.07	0.12	-	95.61
	C	0.06	0.55	0.07	-	99.32
Alloy	Location	Gd (at.%)	O (at.%)	Si(at.%)	Ca(at.%)	Mg (at.%)
Mg1Gd	A	5.53	0.91	0.43	-	93.13
	B	12.52	4.55	0.72	-	82.22
	C	0.40	0.53	0.08	-	98.99
	D	0.14	0.56	0.17	-	99.13
Mg5Gd	A	13.62	2.10	0.03	-	84.26
	B	15.99	3.90	0.12	-	79.98
	C	0.86	0.61	0.03	-	98.50
	D	0.11	0.54	0.09	-	99.26
Mg10Gd	A	14.36	-	0.12	-	85.52
	B	11.23	23.86	0.09	-	64.81
	C	3.61	-	0.06	-	96.34
	D	0.76	0.02	0.06	-	99.17
Mg15Gd	A	13.71	1.11	0.14	-	85.03
	B	13.72	1.45	0.15	-	84.68
	C	2.42	0.69	0.04	0.05	96.81
	D	2.35	0.73	0.10	0.06	96.77

b) X-Ray diffraction (XRD)

Figure 4.15 shows the X-ray diffraction patterns from the as-cast Mg-Ce, Mg-La and Mg-Gd binary alloys. Four concentrations with 1, 5, 10 and 15 wt. % of Ce, La and Gd, respectively were measured in each alloy. The diffraction pattern of the four Mg-Ce alloys showed peaks that correspond to α-Mg and with additions from 5 wt. % Ce, the $Mg_{17}Ce_2$ phase was identified.

While for the Mg-La system two phases were identified α-Mg and $Mg_{17}La_2$ phase. The diffraction patterns from Mg-Gd system suggested the presence of α-Mg and the intermetallic Mg_5Gd phase. These results were consistent with analysis of the casted and heat treated Mg-RE-Intermetallics.

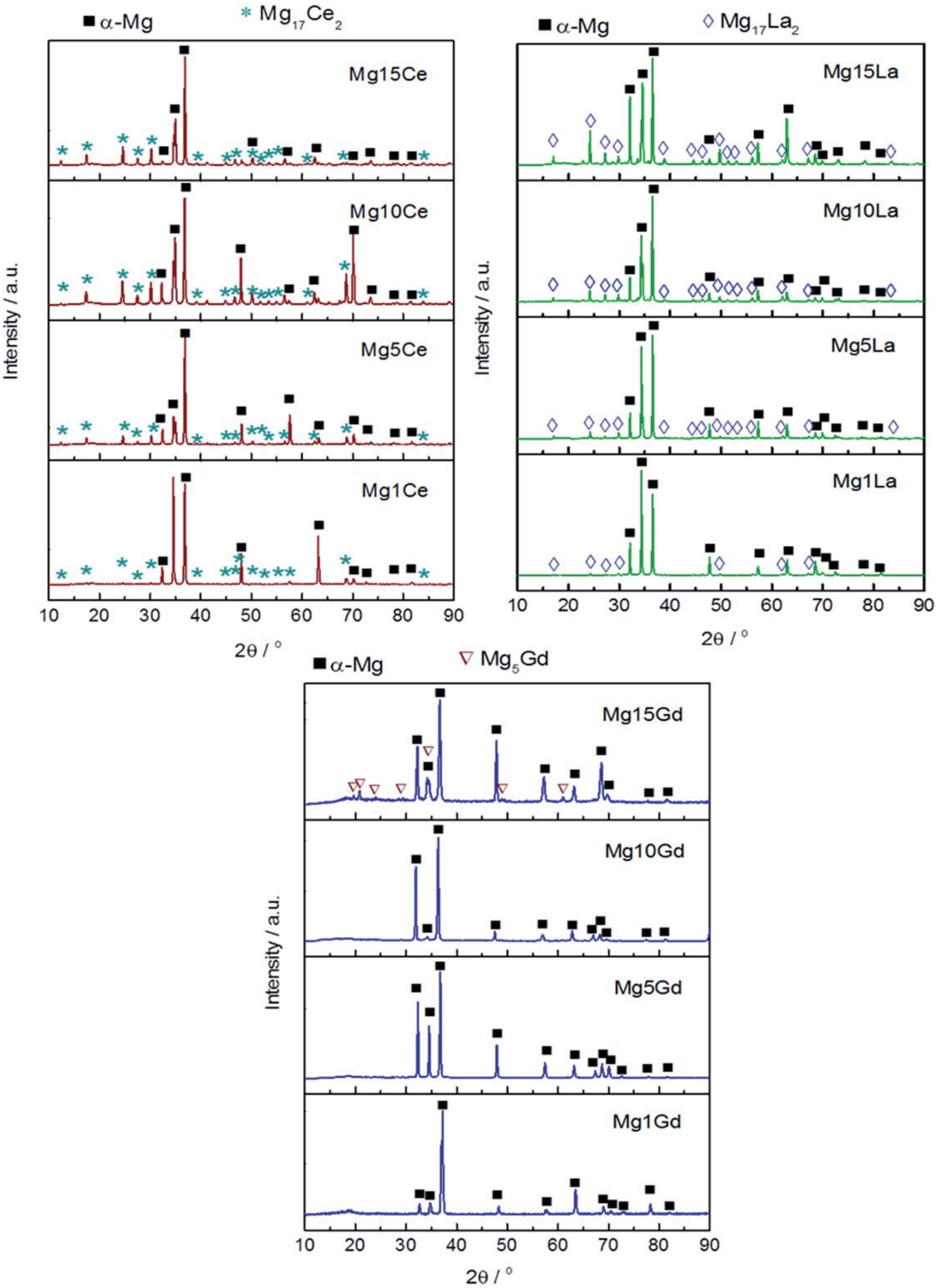

Figure 4.15 X-ray diffraction patterns of as-cast Mg binary alloys with 1 wt%, 5 wt. %, 10 wt. % and 15 wt % Ce, La and Gd, respectively (λ=1.54 nm and CuKα radiation)

4.3.1.2 Evaluation of the corrosion behaviour

a) Open circuit potential (OCP)

Increasing the amount alloying additions also modified the electrochemical properties of the binary alloys. The open circuit potential (OCP) of the binary alloys is shown in Figure 4.16. Compared to pure Mg all alloys show a relatively more active potential at the beginning of the test. The OCP measurements for Mg-Ce system is shown in Figure 4.16 (a). The OCP of Mg1Ce shifted to more stable potential value of -1667 mV after immersion of 1200 s but is increasing still slowly. Also the OCP of Mg5Ce was not stable during the test and after 30 minutes it shifted to a nobler potential of –1578 mV. The of Mg10Ce and Mg15Ce changed rapidly during the initial period of immersion (0-160 s) to more stable potentials of -1550 mV for Mg10Ce and -1562 mV for Mg15Ce and remained stable until the end of the test.

For the Mg-La system the OCP values are displayed in Figure 4.16 (b). The OCP of Mg1La shifted more rapidly towards a noble potential value within the first 1000 s of immersion afterwards the increase slowed down reaching finally -1586 mV at the end of the test. The OCP of Mg5La (-1589 mV), Mg10La (-1566 mV) and Mg15La (-1561 mV) reached nobler potentials after immersion for 200 s and remained stable during the rest of the test.

The OCP measurements for Mg-Gd system are illustrated in Figure 4.16 (c). The OCP of Mg1Gd, Mg5Gd, and Mg10Gd shifted to less active potentials of -1716 mV, -1603 mV and -1581 mV respectively after immersion for 1800 s. Only the Mg15Gd alloy reached stable conditions (after 900 s) and the potential remained at -1581 mV.

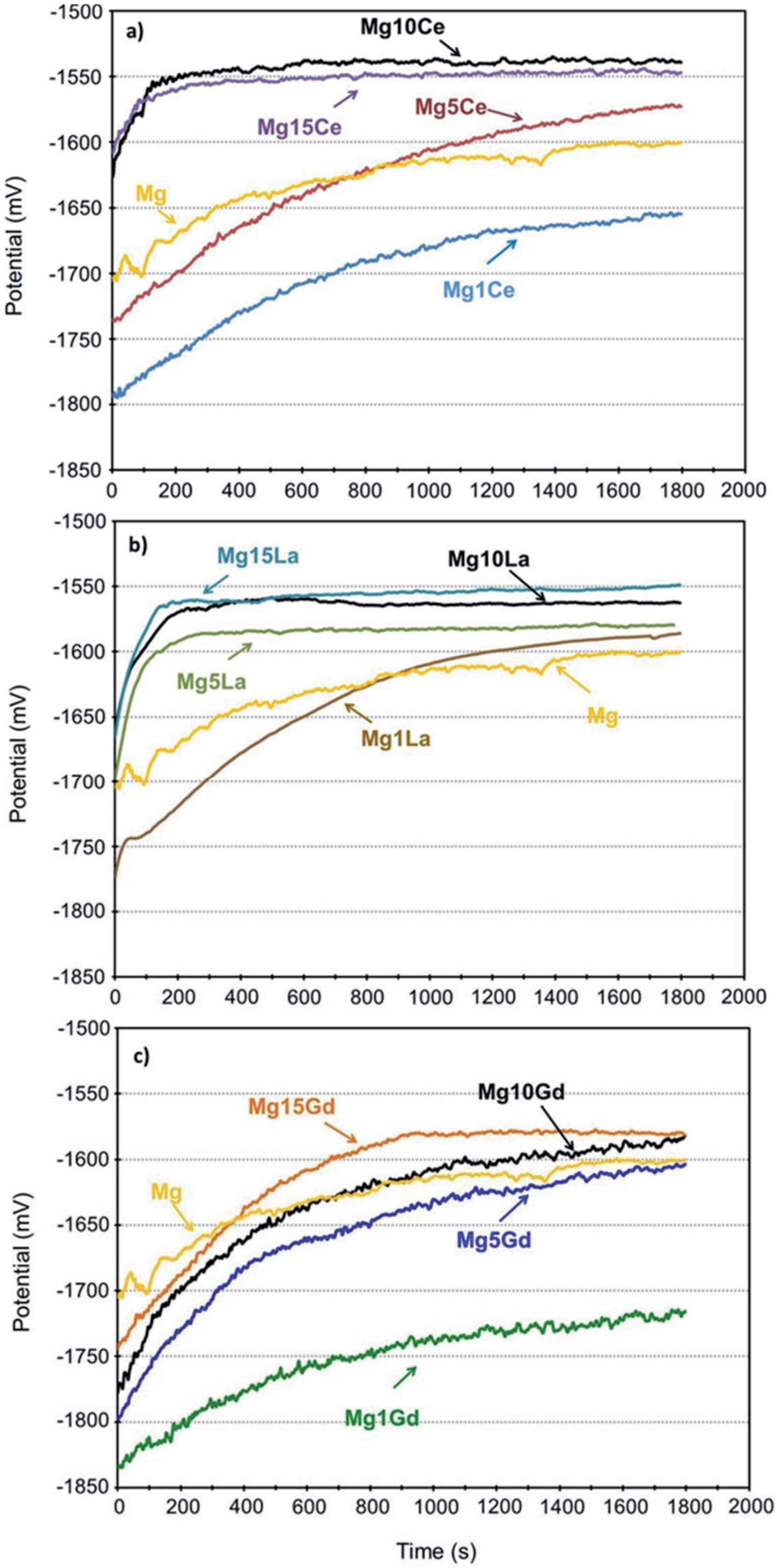

Figure 4.16 Open circuit potential (OCP) vs. time of the Mg-RE binary alloys: a) Mg-Ce alloys, b) Mg-La alloys and c) Mg-Gd alloys after 30 minutes immersion in 0.5 wt.% NaCl solution

Summarising microstructural analysis and OCP, the following trends can be observed:

- The initial potential values are lower compared to pure Mg when RE elements are added.
- The final potential values (Table 4.10) depend on the amount of intermetallics which are forming (compare chapter section 4.3.1.1).
- The more intermetallics present in the alloy the faster stable conditions are reached.
- If the intermetallics are present in larger amounts (Mg-XCe, Mg-XLa and Mg15Gd) the final potentials are more noble than pure Mg. Solid solution alloys (Mg1Gd, Mg5Gd and Mg10Gd) do reach potentials closer to Mg

In the next section the effect of increased alloying element on the corrosion rates will be reported for each of these systems.

b) Potentiodynamic polarisation measurements

Figure 4.17 illustrates the potentiodynamic polarisation measurements for the Mg-RE binary alloys. For Mg-Ce alloys (Figure 4.17 a), additions of 1 wt. % Ce shifted the corrosion potential (E_{corr}) with respect to the corrosion potential of pure Mg (-1586 mV) to less active values (ΔE=18 mV). The addition of 5 wt. % Ce generated a slightly higher potential difference (ΔE= 25 mV) and the addition of 10 and 15 wt. % resulted in the largest potential differences ΔE of 102 mV and 98 mV respectively.

For Mg-La alloys (Figure 4.17 b) the corrosion potential values shifted to nobler values as soon as the concentration of La increased and the amount of the intermetallics is increased. For this system a large displacement in the corrosion potential with respect to the corrosion potential of pure Mg was observed. The corresponding ΔE values are 4, 55, 96 and 121 mV (see Table 4.10).

For the Mg-Gd alloys (Figure 4.17 c), additions of 1 wt% Gd shifted the corrosion potential (E_{corr}) to more negative value ΔE= -58 mV with respect to the corrosion potential of pure Mg (-1586 mV). The addition of 5 wt. % and 10 wt. % Gd generated similar a positive potential difference of ΔE= 26 mV and ΔE= 19 mV respectively. Alloying additions of 15wt. % Gd resulting in precipitation of Mg_5Gd intermetallics shifted the corrosion potential from ΔE to 50 mV.

This shift of E_{corr} corresponds nicely with the OCP and the corrosion rate which will be shown in the following. The icorr values of Mg-Ce alloys became larger with the increase in the Ce amounts in the binary alloys (see Table 4.10); generating higher corrosion rates (Figure 4.18), i.e. Mg1Ce revealed a corrosion rate value of 0.45 mm/year, while Mg5Ce, Mg10Ce and Mg15Ce show corrosion rate values of 0.82 mm/year, 2.16 mm/year and 2.96 mm/year respectively. Similar tendency was observed for Mg-La alloys. Mg1La and Mg5La presented similar corrosion rate values of 0.93 mm/year and 1.14 mm/year, respectively; while for Mg10La and Mg15La higher corrosion rate values of 2.79 and 3.48 mm/year were obtained. Opposite behaviour was observed in the Mg-Gd system. Mg1Gd presented a corrosion rate of 0.59

mm/year. Additions up 5 wt. % Gd increased the corrosion rate to 1.33 mm/year, but when Gd concentration is about 10 wt. % the corrosion rate was reduced to 0.92 mm/year and also the Mg15Gd alloy had a corrosion rate value of only 1.04 mm/year. All the three are very similar which can be related to the small amount of intermetallics in all of them and the increasing matrix corrosion resistance due to Gd in solid solution. In contrast La and Ce have low solubilities in Mg and their electrochemical performances are similar. Increasing La or Ce concentrations in the binary system, results in decreased corrosion resistance. This is consistent with Südholz et al. [167], which reported that alloying addition with concentration beyond the respective solubility limits in Mg could be detrimental to corrosion resistance. There is a clear correlation visible with the volume of intermetallic phases; the higher the higher corrosion rate is. The corrosion resistance of Mg-Gd system showed a behaviour that is more or less independent of the alloy concentration because the amount of intermetallics is negligible in the selected concentration range.

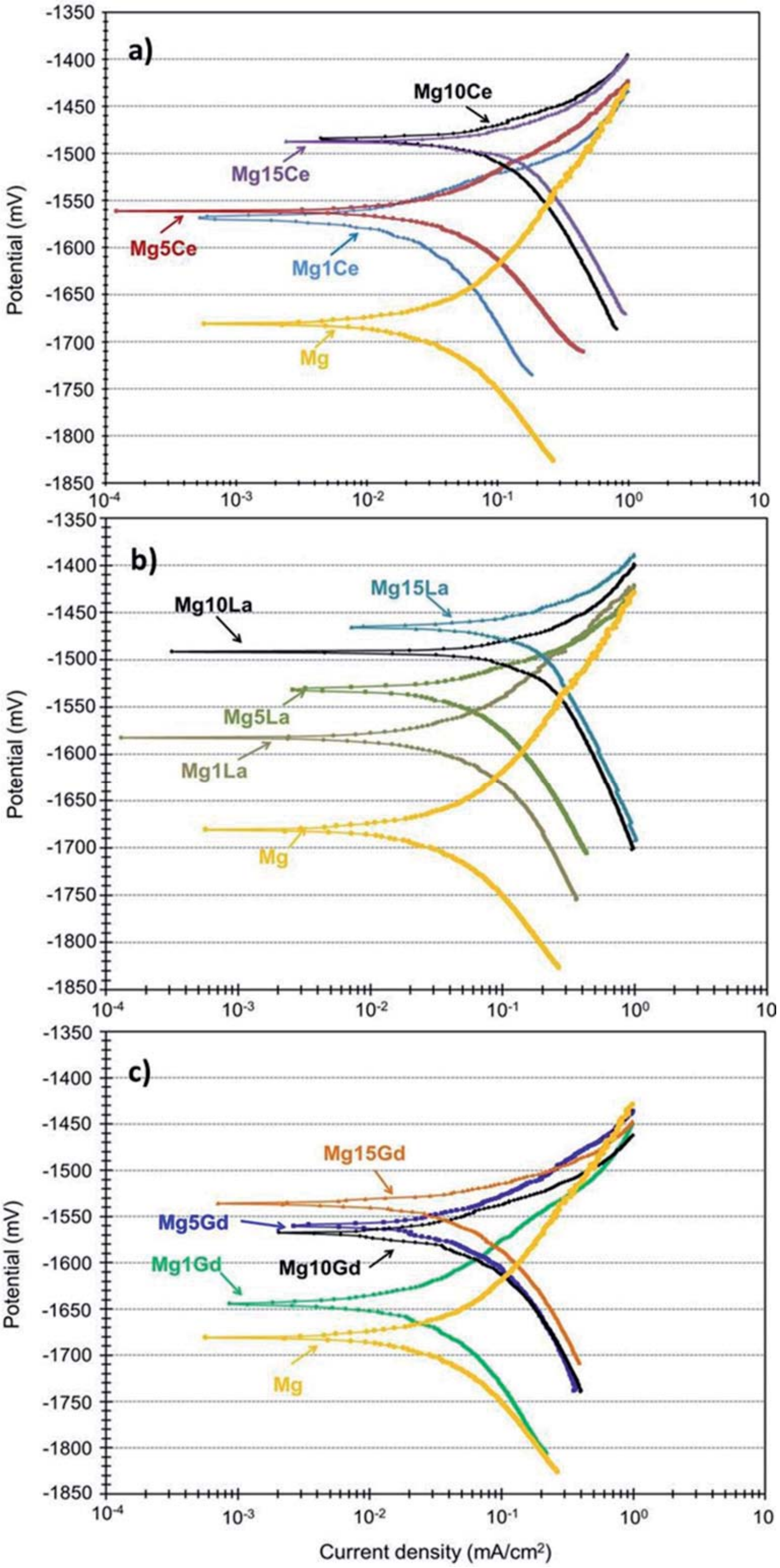

Figure 4.17 Potentiodynamic polarisation measurements of the Mg-RE binary alloys: a) Mg-Ce alloys, b) Mg-La alloys and c) Mg-Gd in 0.5 wt.% NaCl solution

Table 4.10 Electrochemical data from open circuit potential (OCP) and potentiodynamic polarisation measurements of the Mg-RE binary alloys in 0.5 wt.% NaCl solution

Alloy	OCP (mV vs. Ag/AgCl)	i_{corr} (mA/cm^2)	E_{corr} (mV vs. Ag/AgCl)	CR (mm/year)
Mg1Ce	-1654 ± 16	0.019 ± 0.005	-1568 ± 19	0.45 ± 0.1
Mg5Ce	-1572 ± 9	0.035 ± 0.005	-1561 ± 21	0.82 ± 0.1
Mg10Ce	-1539 ± 2	0.094 ± 0.05	-1484 ± 9	2.16 ± 1.1
Mg15Ce	-1546 ± 3	0.13± 0.02	-1488 ± 23	2.96 ± 0.5
Mg1Gd	-1716 ± 16	0.025 ± 0.002	-1644± 18	0.59 ± 0.05
Mg5Gd	-1604 ± 18	0.058 ± 0.02	-1560 ± 37	1.33 ± 0.4
Mg10Gd	-1582 ± 8	0.040 ± 0.004	-1567 ± 4	0.92 ± 0.1
Mg15Gd	-1579 ± 3	0.045 ± 0.005	-1536 ± 7	1.04 ± 0.1
Mg1La	-1586 ±1	0.040 ± 0.006	-1582 ± 17	0.93 ± 0.2
Mg5La	-1579 ± 7	0.050 ± 0.01	-1531 ± 10	1.14 ± 0.2
Mg10La	-1562 ± 7	0.122 ± 0.02	-1491 ± 14	2.79 ± 0.4
Mg15La	-1549 ± 5	0.152 ± 0.02	-1465 ± 12	3.48 ± 0.4
Mg	-1629 ± 6	0.030 ± 0.003	-1586 ± 5	0.61 ± 0.7

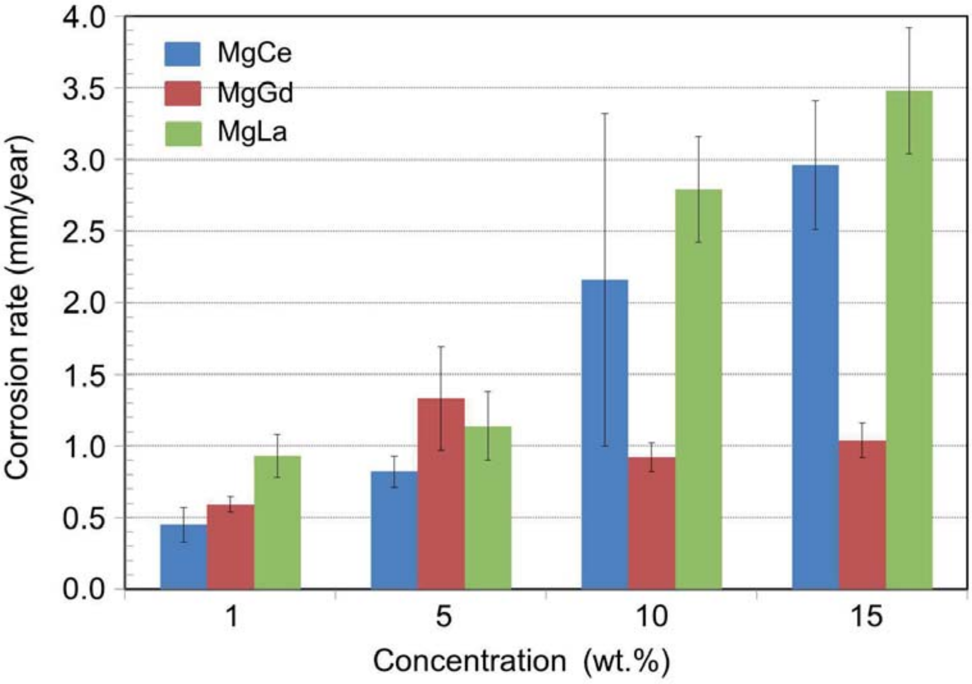

Figure 4.18 Corrosion rates diagram (calculated from the i_{corr} values) of the Mg-RE binary alloys in 0.5 wt. % NaCl solution

c) Electrochemical impedance spectroscopy measurements

The evolution of impedance spectra with time for the Mg-Ce alloys is shown in Fig. 4.19. The impedance spectra of Mg1Ce alloy showed two time constants (Figure 4.19 (a), (b)). In the equivalent circuit, R_s is the resistance of the corrosive medium, namely 0.5 wt. % NaCl solution.

The resistance R_{oxi} and capacitance C_{oxi} are the response of the oxides/hydroxides formation on the metal surface. The film is not dense and water and corrosive species can still reach the surface of magnesium. Thus the second time constant appears in the low frequency region. This is the initiation of the corrosion process and is attributed to the existence of the double-layer capacitance at the metal/electrolyte interface, C_{dl} and corresponding resistance, R_{Ct}. For the quantitative estimation of the corrosion protective properties of the oxides/hydroxides film, experimental impedance spectra were fitted with the equivalent circuit, schematic representation and physical interpretation of which are shown in Figure 4.22. Constant phase elements (CPE) instead of pure capacitances were used in all fittings presented in the work, since the CPE elements are considered for a not homogeneous surface, such as surface roughness or different thickness of the layers [168].

Figure 4.19 (c),(d) represent the evolution of the impedance spectra of Mg5Ce alloy. At the beginning of the test, the alloy shows two well defined time constants similar to Mg1Ce alloy. After 3 h immersion the high frequencies constant is shifted towards middle frequencies values, indicating that the surface film is less protective on the alloy surface. The second time constant at lower frequencies is still visible but it is not meaningful to determine it because of an active dissolution occurring locally and changing conditions during EIS measurements, see Bode-phase diagram (Figure 4.19 d). This behaviour was also observed for Mg10Ce and Mg15Ce alloys (Figure 4.19 (e),(f),(g),(h)), where the surface film is not effective anymore and the active dissolution dominate the corrosion process already as soon as the test starts. The simulated parameters from experimental EIS data of Mg-Ce alloys are listed in Appendix A1.

Note that at the beginning of the test there is a natural protective film on the magnesium alloys, which forms during sample preparation and atmosphere contact, before the test starts. As soon as the sample is immersed in NaCl solution, this film dissolves or is converted into a more hydroxide dominated film. At high frequencies EIS spectra show scattered data, indicating some other contributions of resistance possibly from the equipment. Thus those measurements were also ignored for the fitting, because there is no physical interpretation for these values.

The Nyquist and Bode plots of Mg-La alloys are presented in Figure 4.20. Mg1La shows two time-dependent processes in the first 3 hr immersion. The time constant at high frequencies relate to the capacitive response of the oxide film, C_{oxi} and the resistance R_{oxi}, previously described for the Mg-Ce alloys. After 6 hr immersion the shift of the time constant at high frequencies towards middle frequencies indicate the loss of protectiveness of the film on the alloy surface. At lower frequencies, the process contribution of the double-layer at the metal/electrolyte interface, where the corrosion process takes place is still present. Figure 4.20 (c),(d) show the EIS spectra of Mg5La alloy. At the beginning of the test two time constants are visible as observed in Mg1La. After 3 hr immersion, one time-dependent process was observed at middle frequencies, for this response one constant phase element was used to fit the experimental data, which corresponds to the contribution of the oxide layer. However a small inductive loop at lower frequencies indicates already local breakdown of the film (Figure 4.20 d). The corrosion at this point was already so severe that no stable conditions were obtained for proper EIS measurements to estimate the charge transfer resistance (R_{Ct}) and only the oxide film resistance (R_{oxi}) was determined using a simple Randles circuit as shown in Figure 4.22 b).

For Mg10La and Mg15La alloys the passive films do not offer any protection and breakdown directly after immersion (Figure 4.20 (e),(f),(g),(h)). After one hour the specimens corrode severely so that the fitting was performed only for the oxide films contributions. These values were just an estimation using a simple Randles circuit (Figure 4.22 b). All the fit results as a function of the immersion time of Mg-La alloys are listed in Appendix A2.

The EIS spectra of Mg-Gd alloys are shown in Figure 4.21. For Mg1Gd during the first 6 h immersion, the EIS spectra (Figure 4.21a, b) consist of two well defined time-constants, one at high frequencies (10^2 Hz), associated with the oxide film and the second at low frequencies (~ 10^{-1} Hz) related to the corrosion process. The experimental data was fitted using the equivalent circuit shown in Figure 4.22 (a). From 10 h immersion until the end of the test, at middle frequencies there is one dominating time constant ascribed to an oxide layer, which is partially protective. However at lower frequencies an inductive loop was visible indicating that a localised corrosion process takes place. The equivalent circuit used to fit these measurements is shown in Figure 4.22 (b).

Figure 4.21(c),(d) present the evolution of the impedance of Mg5Gd alloy during the immersion time. During the first hour two time-constant are observed. At high frequencies (~10^2 Hz) attributed to a partly protective oxide film and at lower frequencies related to the active localised corrosion. From 3 h immersion the film resistance is decreasing and the corrosion becomes more severe until the end of the test. The equivalent circuits used to fit the experimental data is simplifying the corrosion mechanisms and is focussing mainly on the dissolution process of the oxide film since the charge transfer resistance is not measurable after 1 hour immersion (Figure 4.22 a,b). The EIS spectra of Mg10Gd alloy is shown in Figure 4.21 (e),(f). At the beginning of the test two time-dependent processes are visible. The time constant at high frequencies (10^2 Hz) related to the oxide film on the surface. The second time constant is weakly defined at lower frequencies (1 Hz) and it is related to the corrosion activity. After 1 h immersion one time constant remains visible related to oxide film, while the second time constant is less visible due to a high dissolution activity. Figure 4.22 (a),(b) show the equivalent circuits used to fit the experimental data. The EIS spectra of Mg15Gd alloy is depicted in Figure 4.21 (g),(h) and exhibits the same behaviour as described for Mg10Gd alloy. However the degradation process is just faster. All the fitted parameters of the Mg-Gd alloys are listed in Appendix A3.

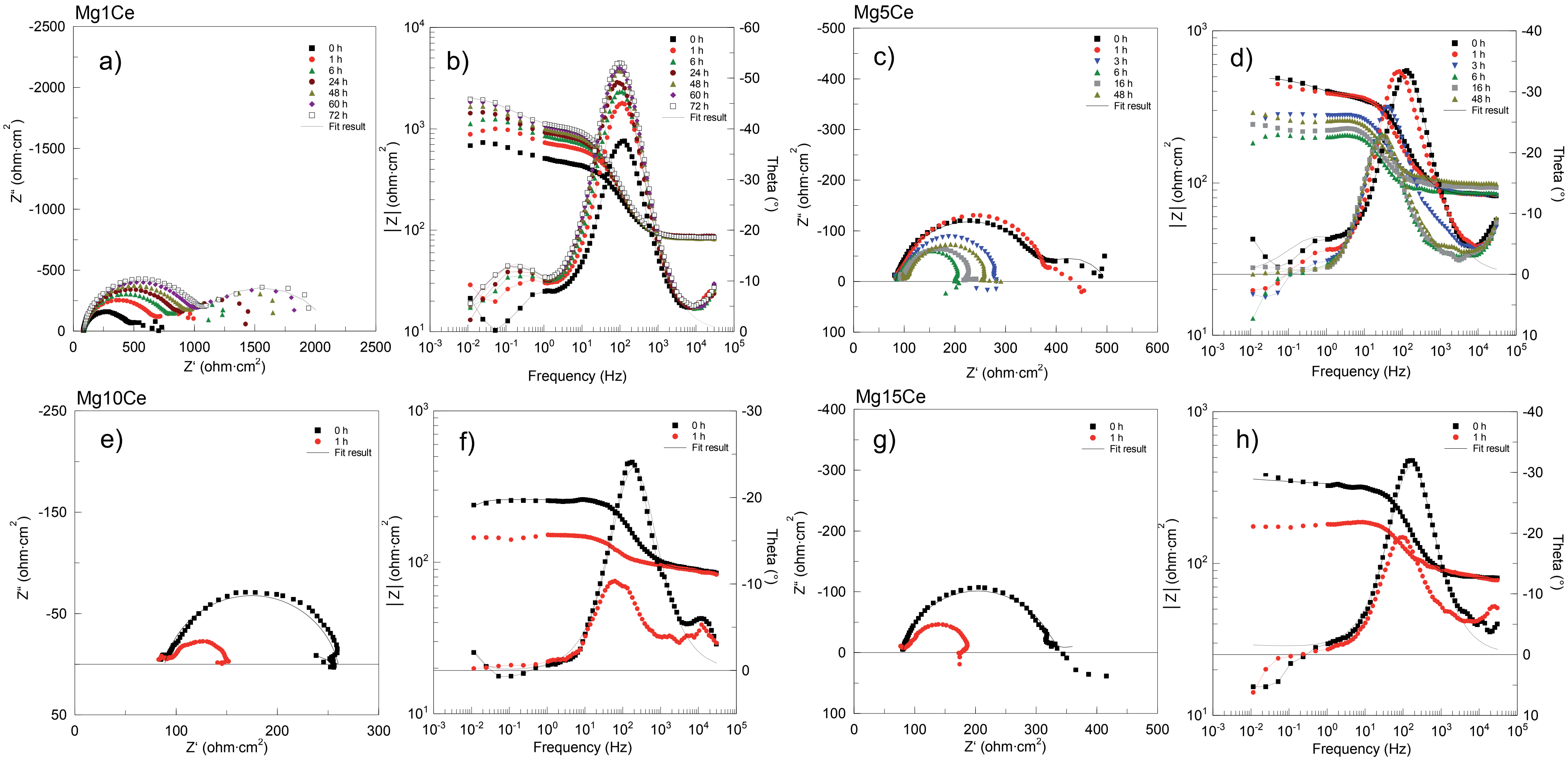

Figure 4.19 EIS spectra of Mg-Ce alloys, where (a), (b) are the Nyquist and Bode plots of Mg1Ce alloy, (c),(d) are the Nyquist and Bode plots of Mg5Ce alloy, (e), (f) are the Nyquist and Bode plots of Mg10Ce alloy, and (g), (h) are the Nyquist and Bode plots of Mg15Ce alloy, after immersion in 0.5 wt. % NaCl solution for several times

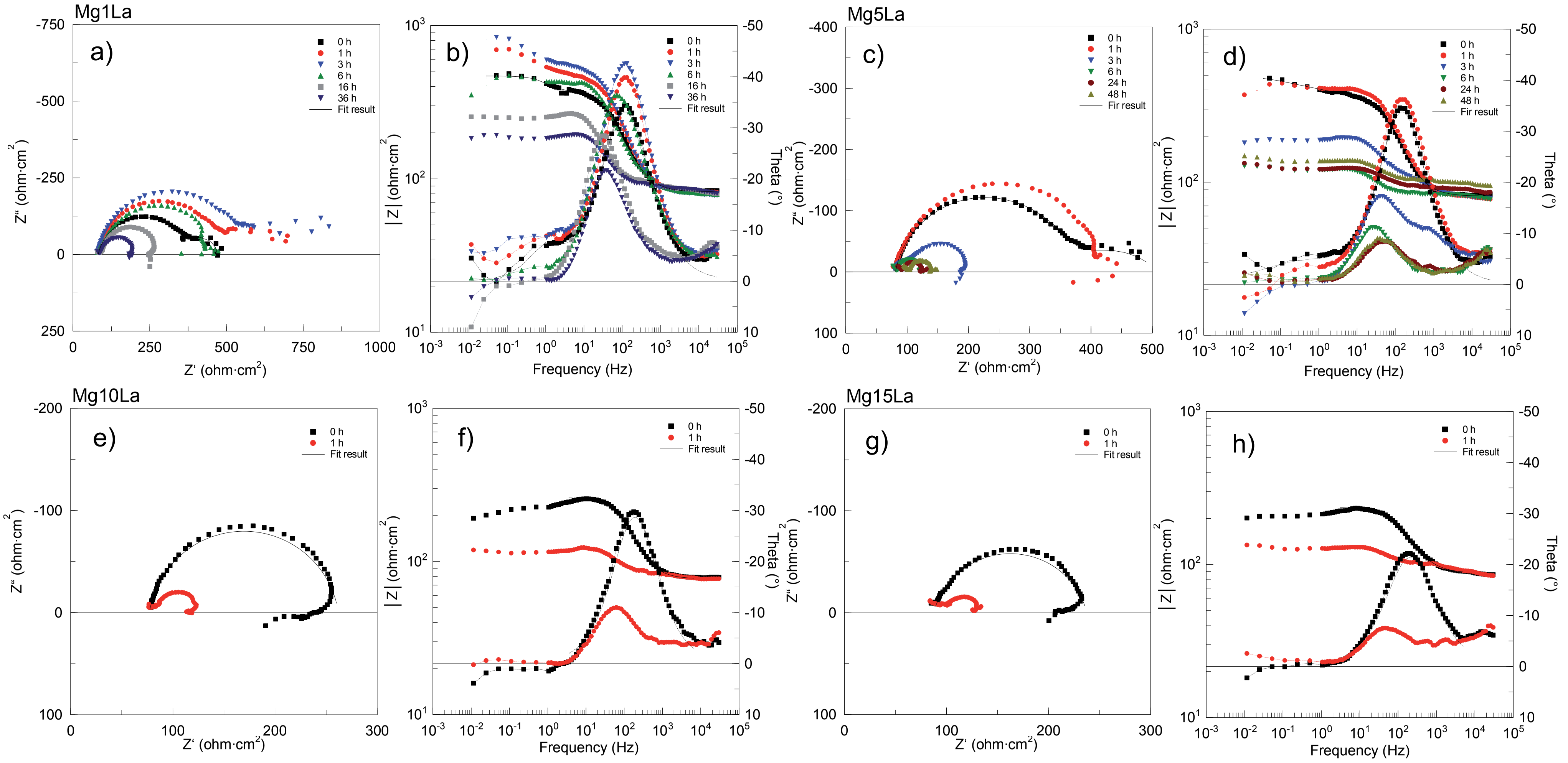

Figure 4.20 EIS spectra of Mg-La alloys, where (a), (b) are the Nyquist and Bode plots of Mg1La alloy, (c),(d) are the Nyquist and Bode plots of Mg5La alloy, (e), (f) are the Nyquist and Bode plots of Mg10La alloy, and (g), (h) are the Nyquist and Bode plots of Mg15La alloy, after immersion in 0.5 wt.% NaCl solution for several times

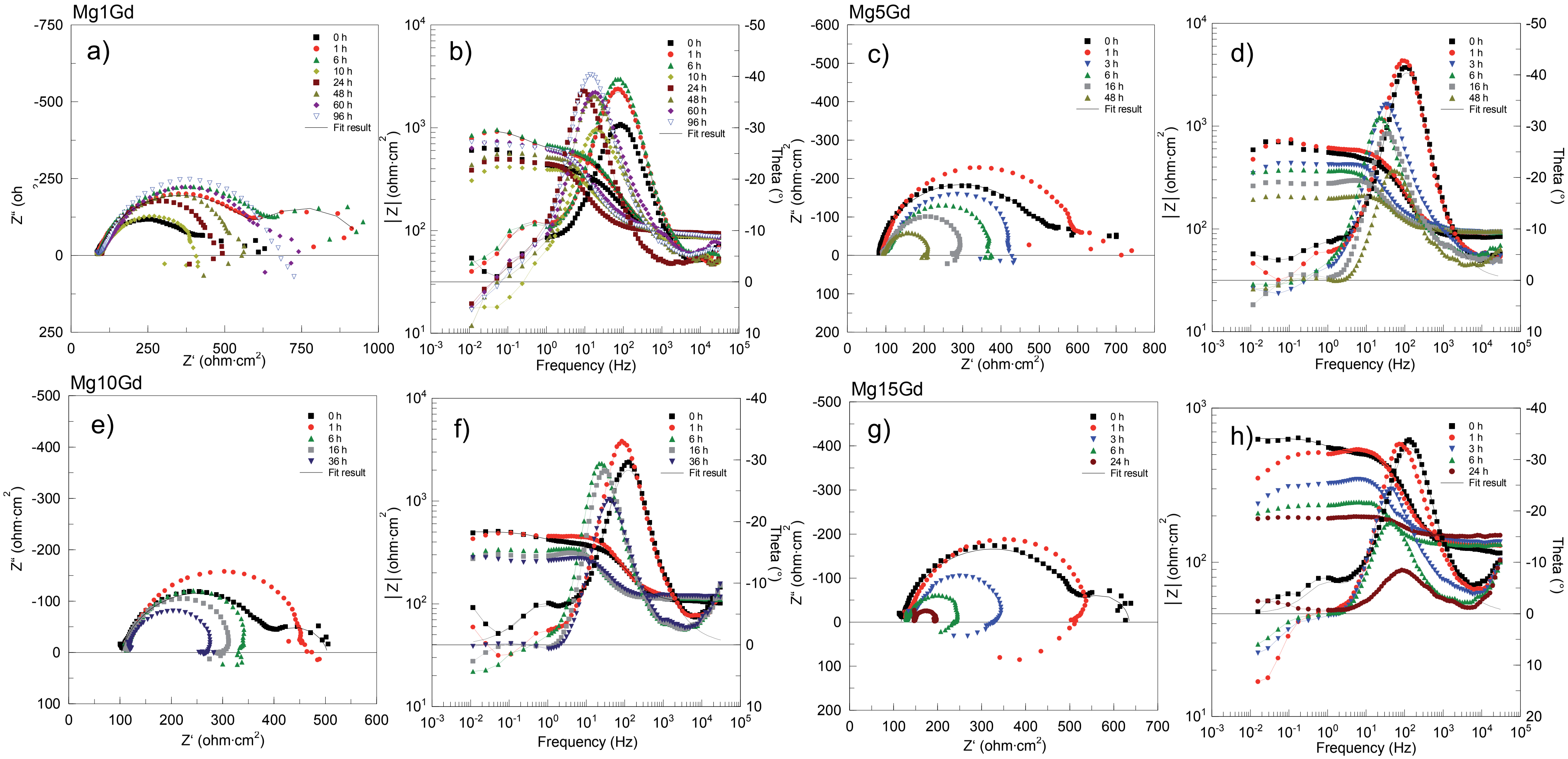

Figure 4.21 EIS spectra of Mg-Gd alloys, where (a), (b) are the Nyquist and Bode plots of Mg1Gd alloy, (c),(d) are the Nyquist and Bode plots of Mg5Gd alloy, (e), (f) are the Nyquist and Bode plots of Mg10Gd alloy, and (g), (h) are the Nyquist and Bode plots of Mg15Gd alloy, after immersion in 0.5 wt.% NaCl solution for several times

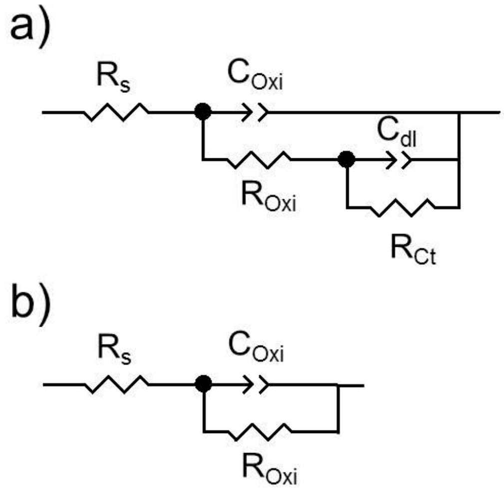

Figure 4.22 Equivalent electrical circuits used to simulate EIS spectra for the binary Mg-RE alloys during different immersion time, where R_{oxi} and C_{oxi} are the resistance and capacitance of the oxide film. R_{Ct} represents the charge transfer resistance and C_{dl} is attributed to the existence of the double-layer capacitance at the metal/electrolyte interface

Altogether the EIS results confirm the negative effect of all RE precipitates in the Mg matrix (see Figure 4.23). Good corrosion resistance is only obtained if the volume of intermetallics is kept low. For example, the Mg1Ce alloy showed excellent long term stability. But also the “solid solution alloys” Mg1Gd, Mg5Gd and Mg10Gd perform reasonable well confirming the polarisation results. All the alloys with large volume of intermetallics reveal very severe active corrosion driven by local galvanic cells. The alloy Mg10Gd is somehow in between solid solution and occurrence of intermetallic phases. Therefore the effect of (a) heat treatments and (b) ternary alloying addition will be investigated to understand their roles in modifying the corrosion behaviour of Mg10Gd alloy and to attempt further optimization for the corrosion performance.

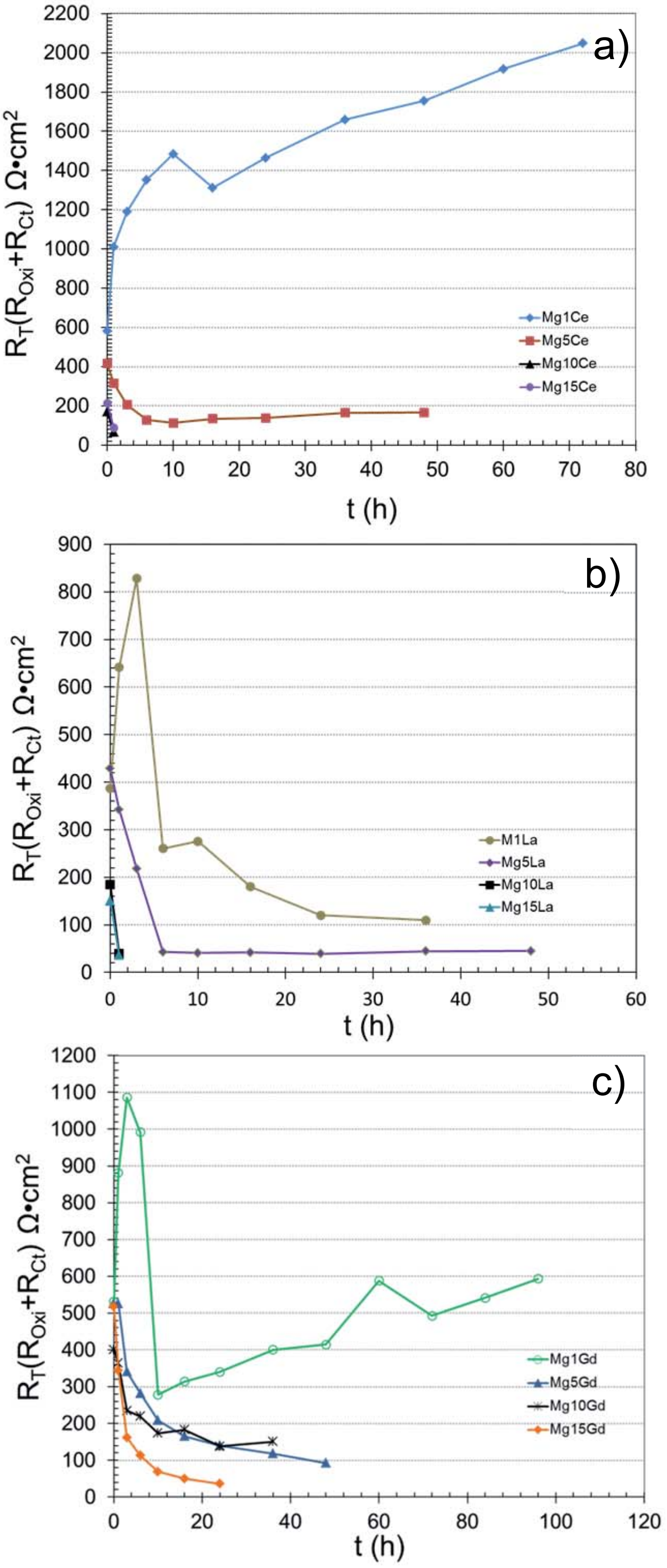

Figure 4.23 Average evolution of total resistance (R_T) values obtained after fitting EIS spectra of (a) Mg-Ce, (b) Mg-La and (c) Mg-Gd alloys during immersion time in 0.5 wt. % NaCl solution

4.3.2 Effect of heat treatments on Mg10Gd alloy

4.3.2.1. Characterization

a) Scanning electron microscopy (SEM)

Figure 4.24 shows the evolution in the microstructure of Mg10Gd alloy after solution treatment and aging for 24 h at 200°C, 300°C and 400°C and compares it with the as-cast and the homogenised conditions. Figure 4.24 (a) shows a typical dendritic microstructure of as-cast Mg10Gd alloy. Primary α-Mg dendrites "a" are visible with Gd enrichment zones "c" and Mg_5Gd "b" intermetallic phase between the dendrite arms. The EDS analysis conducted in the selected particle "b" shows that the ratio in atomic percent between Mg and Gd is about 5.7 which suggest that the particle corresponds to Mg_5Gd (see Figure 4.24 b). After homogenization treatment, the dendritic microstructure disappears and just few smaller intermetallic particles remain undissolved, the particles have relative low concentrations of Gd (4-8 at. %). These low Gd concentrations are mainly due to the size of the precipitates, which is ~1µm (see Figure 4.24 c), this could give non proper information about the real Gd content and because the higher matrix contributions. Moreover, previous studies have shown that these kind of intermetallic phases correspond to the GdH_2 phases [169]. However, from it can be assumed that these particles are free of Mg (see Figure 4.27) and most liked Gd hydride because the Mg_5Gd phase should be dissolved in the matrix. After aging at 200 °C a very small amount of the same particles are observed (see Figure 4.24 d). Other particles are not visible with SEM. These microstructures can be compared to the predicted volume fraction of intermetallic phase expected in the Mg-Gd phase diagram Figure 4.25 [162], The maximum solubility of Gd in Mg matrix is high 23.5 wt. %, which results in a relative low volume fraction of intermetallics in as-cast condition if cooling down is sufficiently fast. Water quenching is obviously sufficient to keep Gd in solid solution after the homogenisation treatment Figure 4.24(c). The maximum precipitation should be at 200 °C according to the phase diagram as the solubility is the lowest. However, after 24 h aging it is not possible to see these precipitates with SEM. There are two main reasons for this. Firstly, the size of precipitates might be very fine and cannot be resolved with SEM or XRD and the other might be that diffusion of Gd in the mg matrix is too slow and further aging at 200°C would be required to form visible precipitates. Previous investigations using TEM show that precipitates are relatively fine at 200°C [170] and the maximum hardness and maximum density of precipitates are observed after approximately 120 h aging. Figure 4.24(e) exhibits the microstructure at 300 °C with high volume fraction of the intermetallic phase Mg_5Gd. The higher magnification micrograph shown Figure 4.24(f) indicates uniformly precipitation of Mg_5Gd throughout the whole matrix and slightly stronger along the grain boundaries. However, when the aging temperature is 400 °C, the majority of the precipitates dissolve and just a few round Mg_5Gd and many cubic shaped GdH_2 particles are observed (see Figure 4.24 g).

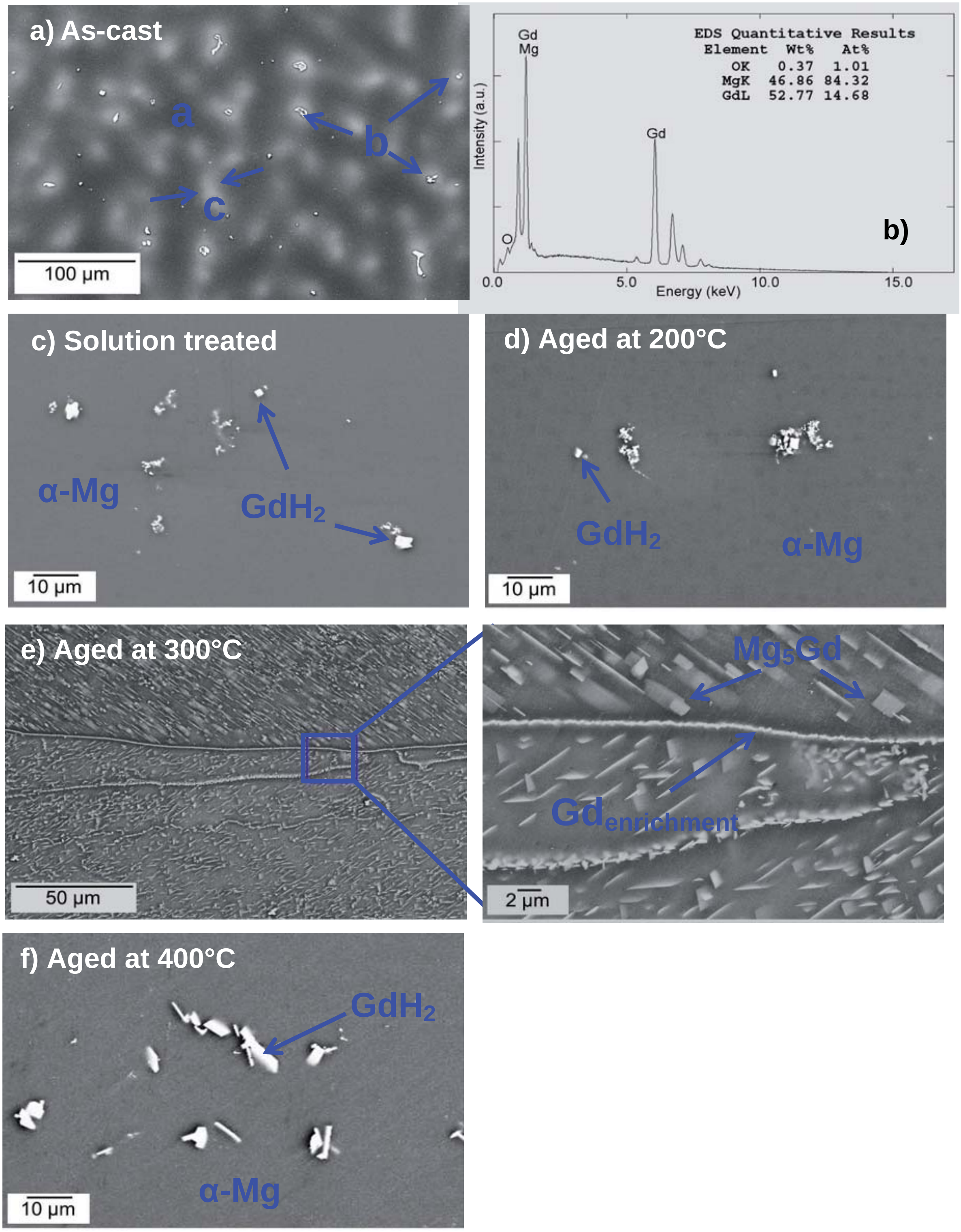

Figure 4.24 SEM micrographs of Mg10Gd alloy: (a) as-cast microstructure, letters a, b, c, corresponds to α-matrix, Mg_5Gd intermetallic phases and Gd enrichment zones, respectively, (b) typical EDS analysis of the “b” particles (c) solid solution treatment microstructure, after 24 h at 540°C, aging treatments for 24 h (d) at 200°C, (e) at 300 °C (low and high magnifications) and (f) at 400° C

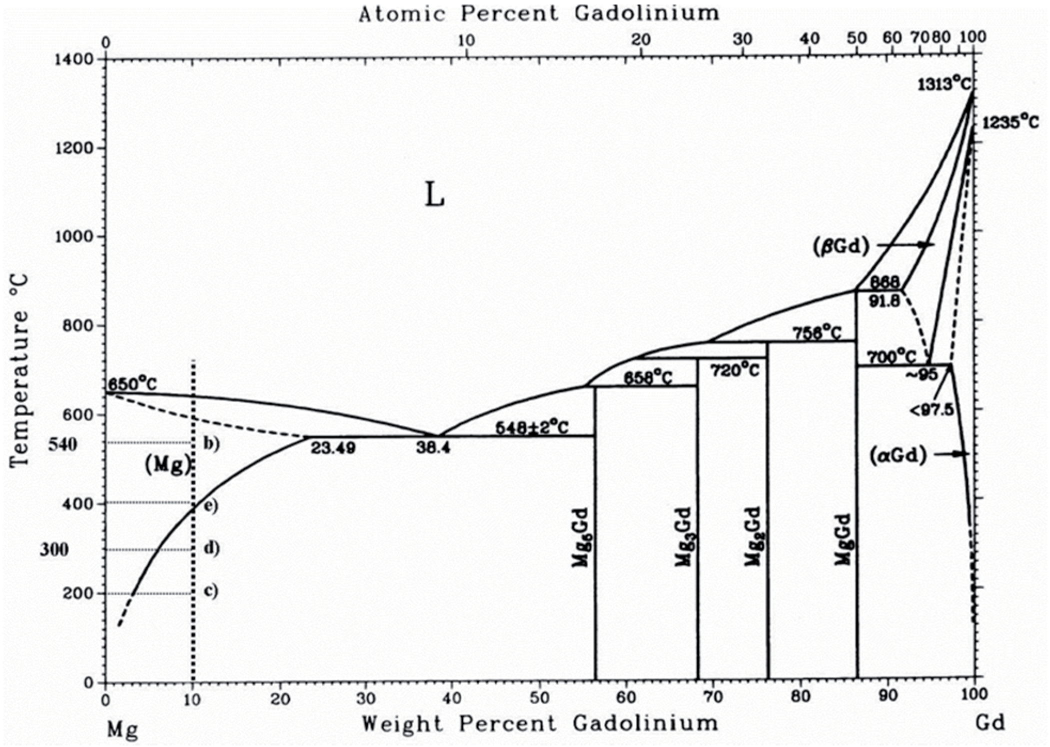

Figure 4.25 Mg-Gd phase diagram [162]

b) EDX mapping and X-Ray diffraction (XRD)

The presence of Mg_5Gd phase was further confirmed for all conditions by XRD (see Figure 4.26). At 200° C, it is impossible to distinguish the characteristic peaks of the secondary Mg_5Gd phase, whereas at 300 °C the intensities of those peaks are large enough. At 400 °C, the peak intensities are similar to the solid solution state, where the precipitates were dissolved in the matrix. In addition EDX elemental mappings were performed on selected region of the Mg10Gd alloy after the aging treatments to demonstrate the distribution of the secondary phases and the Gd-enriched zones (see Figure 4.27). Gadolinium distribution is visible in the different microstructures, but in as-cast condition and in the grain boundaries of samples heat treated at 300°C Gd-enrichment zones and Mg_5Gd precipitates can be observed. In solid solution, and 200°C heat treated alloy samples, gadolinium was mainly found in a different modification, most likely as gadolinium hydride. The Gd concentration in the precipitate is higher giving a whiter appearance in BSE mode than the Mg_5Gd phase. Furthermore Mg is nearly present looking at the mapping result. In the 400°C heat treated alloy, the intermetallic phase is partly identified as Mg_5Gd, but there are most likely GdH_2 as well.

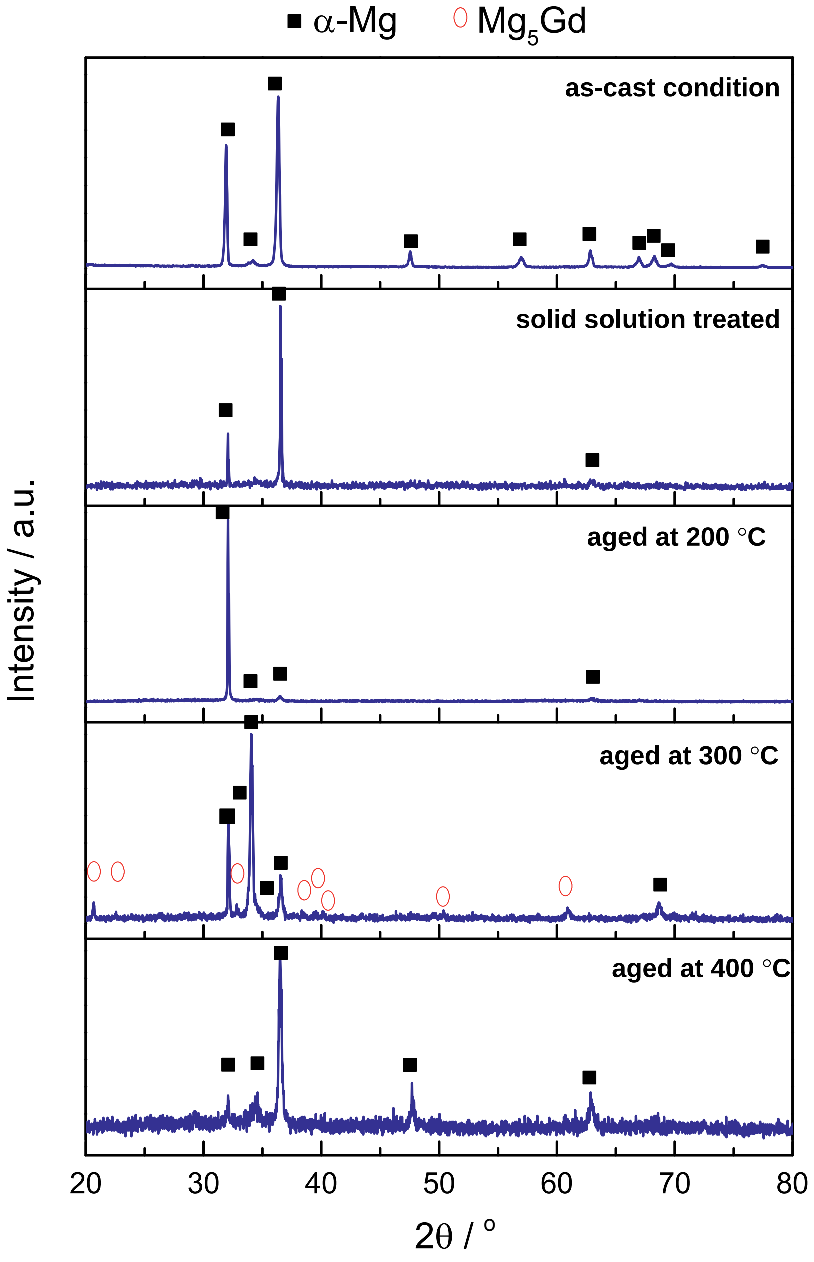

Figure 4.26 X-ray diffraction patterns of as-cast condition, solid solution treated and aging treatments at 200°C, 300°C and 400°C of Mg10Gd alloy

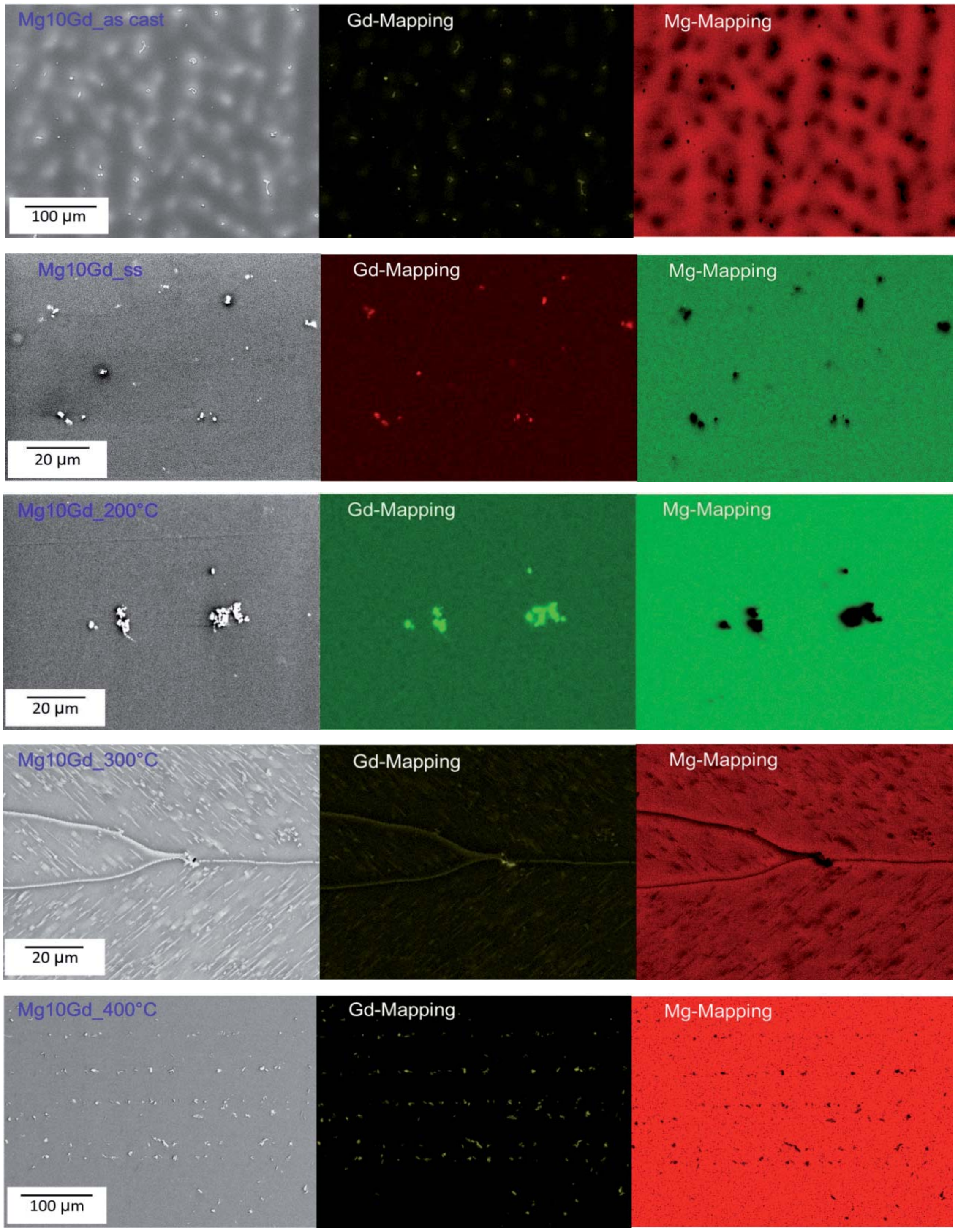

Figure 4.27 Microstructure and elemental mapping (EDX) of the elements Gd and Mg revealing the distribution of each element in the different of as-cast condition, solid solution treated and aging treatments at 200°C, 300°C and 400°C of Mg10Gd alloy

4.3.3.2 Evaluation of the corrosion behaviour

a) Hydrogen evolution and weight loss

Figure 4.28 shows the corrosion rates determined by volumetric measurements of hydrogen evolution and gravimetric measurements of the weight loss for Mg10Gd after aging treatments at 200°C, 300°C and 400° C, The plots include the response of the as-cast, and solid solution treated Mg10Gd for comparison. Both calculations show similar results. Similar corrosion rates of about 5 mm/y were observed for the samples of Mg10Gd alloy in the as-cast, heat treated at 200°C and 300°C. While the corrosion rate in the solution treated sample increased to almost twice of the rate of as-cast alloy (8.92/10.32 mm/year). The sample aged at 400 ° C showed a drastic increase in the corrosion rate, to around 31.04/25.11 mm/year, which is five to six times greater than the as-cast corrosion rate. For these two conditions solid solution treated and aged at 400°C the microstructure mainly consist of a small volume fraction of Mg_5Gd intermetallic phase and GdH_2, which were not uniformly distributed in the matrix. At a treatment of 400°C the amount of GdH_2 seems to increase. The size of the phases is small generating possibly local damage due to galvanic couples, which is detrimental to the sample. However, GdH_2 seems to be more detrimental than the Mg_5Gd phase. This statement will be corroborated in the next section, where corrosion process will be monitored. Based on the results above, aging treatments did not improve the corrosion resistance of the Mg10Gd alloy but the aging at 200°C and 300°C did not deteriorate the corrosion resistance.

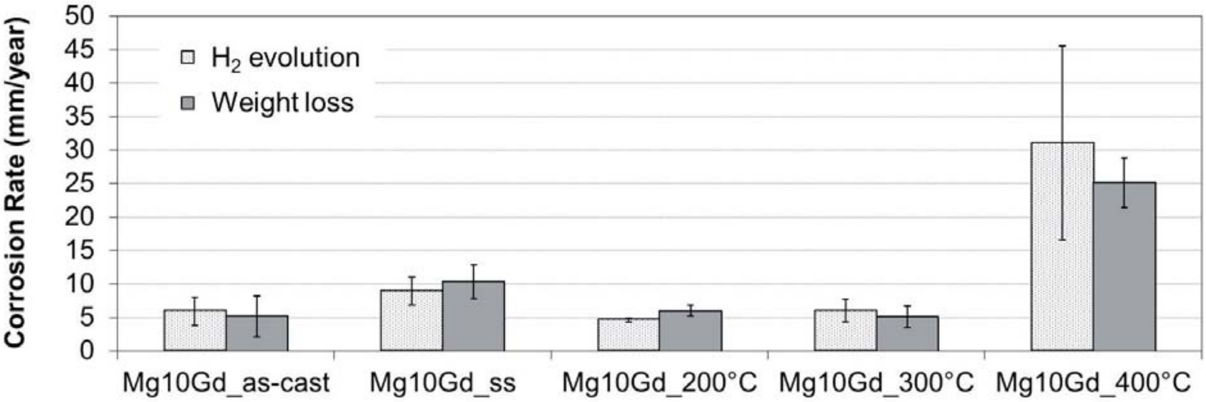

Figure 4.28 Hydrogen evolution and weight loss of as-cast condition, solid solution treated and aging treatments at 200°C, 300°C and 400°C of Mg10Gd alloy

b) Drop/Immersion test

In this section the results are divided into two groups, the first consisting of Mg10Gd as-cast condition and the second consisting of Mg10Gd after the aging treatments to observe where and how the corrosion processes start and develop over time.

- ***As-cast Mg10Gd***

Figure 4.29 shows the corrosion process of as-cast Mg10Gd after different exposure periods to 0.5 wt. % NaCl solution. After 10 minutes of exposure the sample shows slight attack on the Gd-enrichment areas (green arrows) and small sections around the secondary cubic phase (blue dotted circle), Figure 4.29 (b). From 20 minutes of immersion some small holes were generated at the base of the cubic GdH_2 and Mg_5Gd precipitates, (blue dotted circles Figure 4.29 d). Both phases are found close together so in the beginning of the corrosion process it is hard to decide which one is more detrimental. After 30 minutes immersion, the secondary phase (Mg_5Gd) remains and the cubic phase disappeared most likely by undermining Figure 4.29 (f). After one-hour immersion the matrix presented small pits (yellow dotted line Figure 4.29 h). Finally after 3 hours immersion, the deterioration could be observed in the matrix, Mg_5Gd phase and Gd enrichment zones. After 5 hours immersion, the sample presented more deterioration and filiform corrosion was also visible, Figure 4.29 (o). After 10 hours of immersion, some matrix (marked with the yellow arrow) and intermetallics areas (blue dotted circle) were dissolved due to localized attack and the progress of filiform corrosion (Figure 4.29 n).

Summarizing, the cubic phase (GdH_2) is the most detrimental phase in the as-cast alloy. It causes strong attack, but it is not sure if it is removed by undermining due to the fast dissolution of the surrounding matrix or by subsequent chromic acid cleaning. However, the much longer holes around them are good indicators for the severeness of the galvanic attack. The Mg_5Gd phase seems to be less detrimental at least in the early stages of corrosion, but it causes dissolution of the surrounding Gd-rich α-Mg.

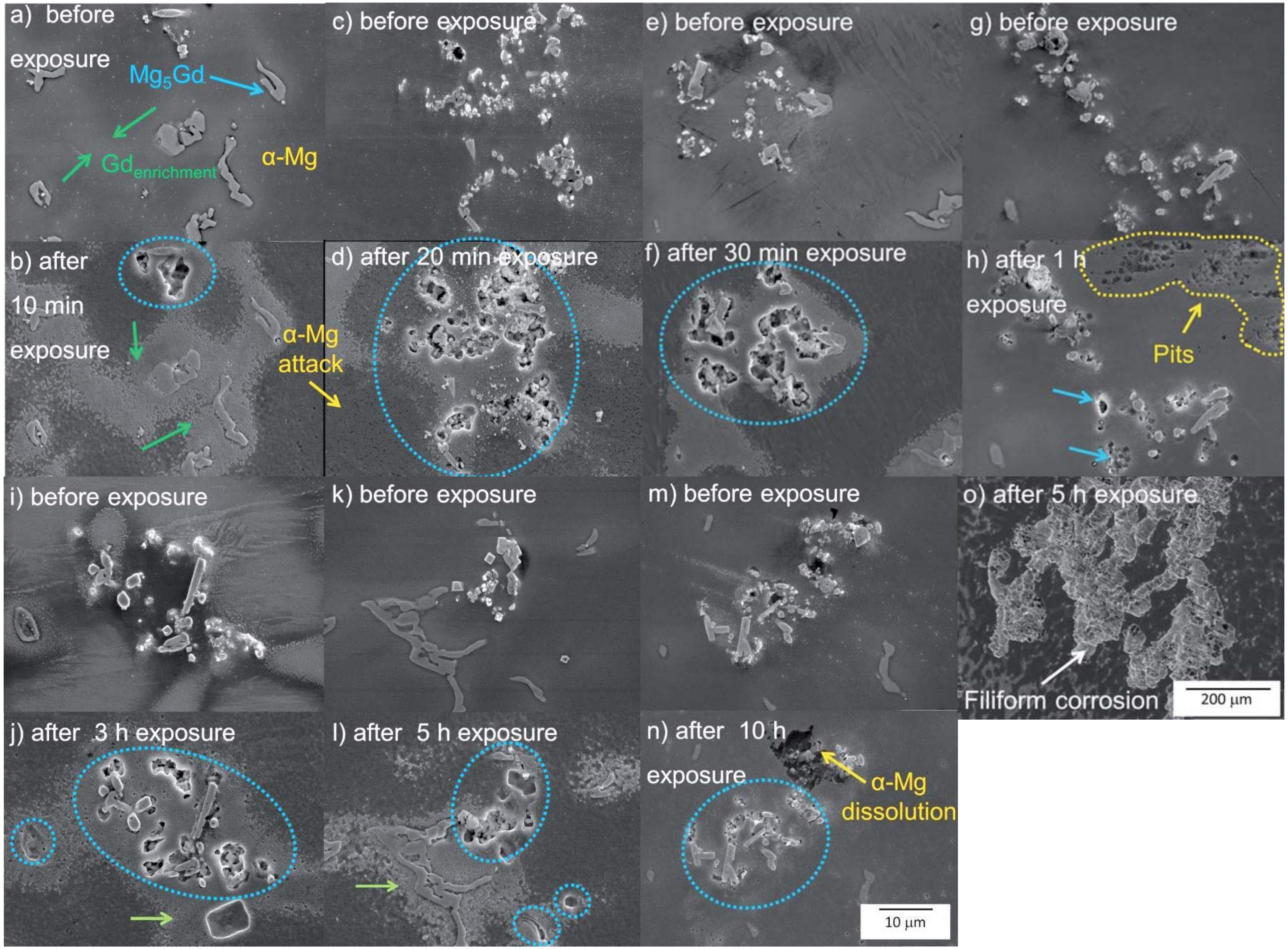

Figure 4.29 Corrosion monitoring using immersion test of as-cast Mg10Gd alloy after different exposure time in 0.5 wt.% NaCl solution. Yellow arrows/dotted areas depict the corrosion attack on the α- Mg matrix, blue arrows/dotted circles indicate corrosion process on the Mg_5Gd/GdH_2 phases and the green arrows show the corrosion degradation on the Gd enrichment areas

- ***Mg10Gd after aging treatments***

In this section three immersion periods were used at 30, 60 minutes and 3 hours as the short periods did not show any change on the samples surface. Figure 4.30 shows the corrosion process of the solid solution treated and after aging treatments at 200°C, 300°C and 400°C of Mg10Gd alloy. In the solution treated samples the attack began on α-Mg matrix areas more or less independent of the surrounding GdH_2 or Mg_5Gd particles (see blue arrow, Figure 4.30 c). First pits occur in the matrix after 60 minutes immersion, Figure 4.30 (c) and after 3 h immersion, Figure 4.30 (d), only minor changes in size and number were visible. The sample aged at 200 ° C shows the same attack as in the solution treated sample but it has a more widespread pitting attack in the matrix after exposure for 60 minutes (yellow arrows), Figure 4.30 (g) and shows more severe attack after 3 h immersion, Figure 4.30 (h). In the sample aged at 300 ° C the amount of Mg_5Gd precipitates is the highest and surprisingly there is no attack on the surface up to one hour exposure. After three hours the first pitting occurred in the selected area. However, the treatment did not prevent the advance of filiform corrosion in another area of the specimen (Figure 4.31). In the sample aged at 400 ° C the first corrosion was also observed after 60 minutes of immersion Figure 4.30 (o) and at 3 h immersion it was spread specifically in areas close to the across the Mg_5Gd/GdH_2 precipitates (blue dotted circles) generating more degradation in the matrix, Figure 4.30 (p).

It is obvious that the homogenisation of Gd distribution in the matrix has positive effects retarding the first pitting attack. For the solid solution treated, aged at 200°C and 300°C specimens the attack is relative uniform and in spite of having a large number of Mg_5Gd precipitates after 300°C aging this is not detrimental for the corrosion resistance.

In contrast aging at 400°C seems to increase the amount of GdH_2 precipitates in the matrix and if they are present they seems to influence the location of pitting. Pitting now occurs close to the agglomeration of the bright white cubic GdH_2 precipitates

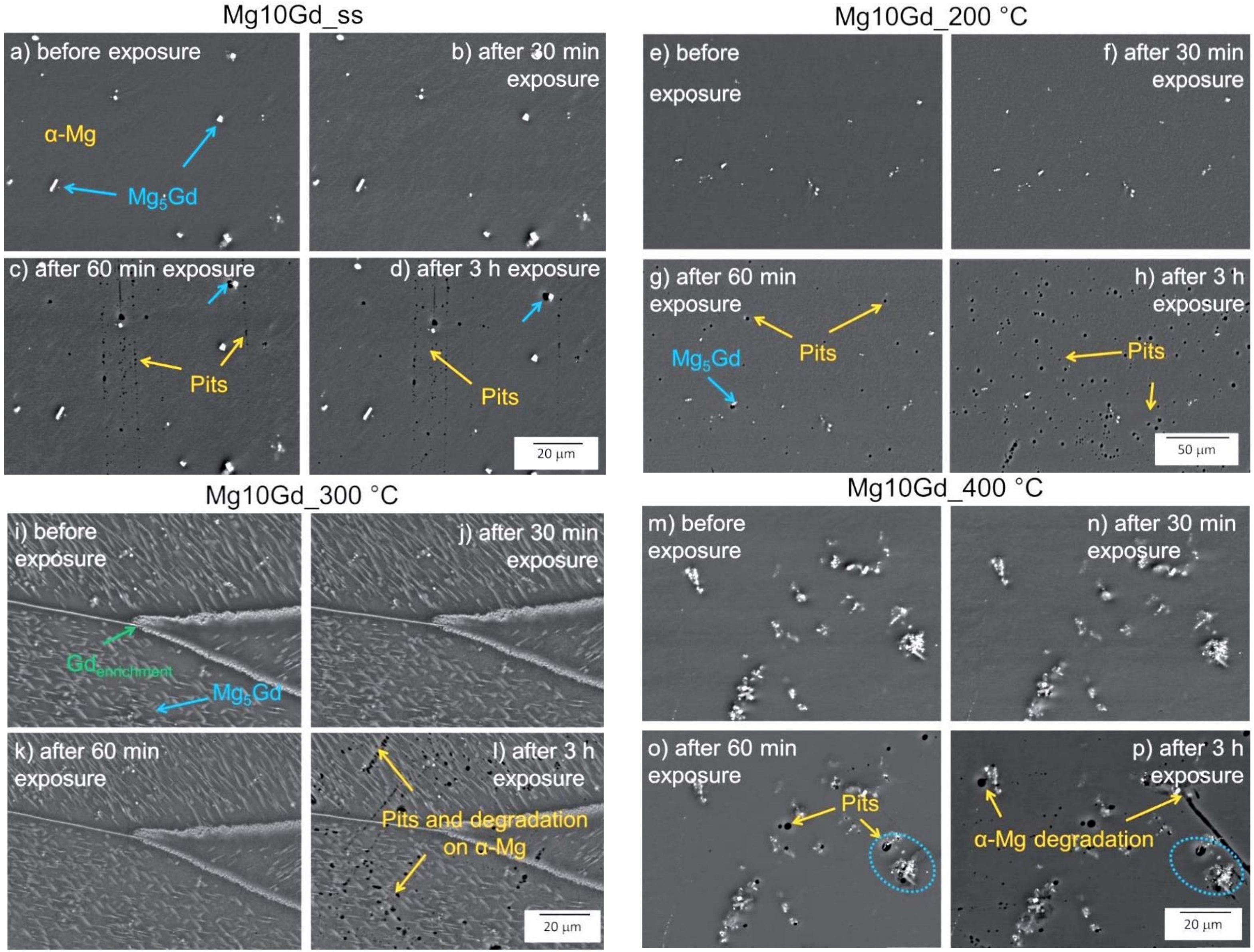

Figure 4.30 Corrosion monitoring using immersion test of as-cast condition, solid solution treated and aging treatments at 200°C, 300°C and 400°C of Mg10Gd alloy after 30, 60 minutes and 3 h time exposure in 0.5 wt.% NaCl solution Yellow arrows depict the corrosion attack on the α- Mg matrix, blue arrows/dotted circles indicate corrosion process on the Mg_5Gd/GdH_2 phases and green arrows indicate Gd enrichment areas

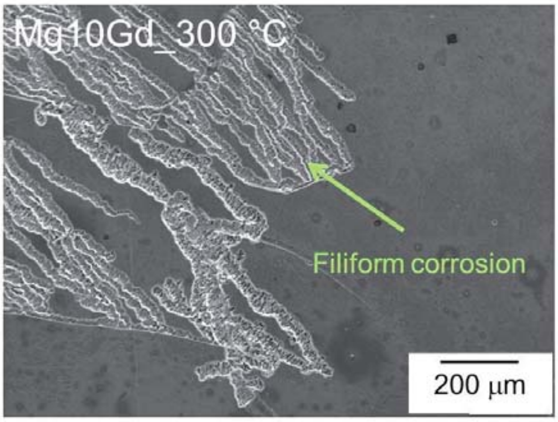

Figure 4.31 SEM micrograph of filiform corrosion of Mg10Gd aged at 300°C after 3 h immersion in 0.5 wt.% NaCl solution

4.3.3.4 Electrochemical characterization

a) Open circuit potential (OCP)

The aging treatments do not only influence the microstructure of the Mg10Gd alloy but also their electrochemical properties. The OCP curves of the Mg10Gd after aging treatments are shown in Figure 4.32. The plots include the response of the as-cast and solution treated Mg10Gd, for comparison. All samples showed a more active potential throughout the whole test compared to the as-cast condition. After 500 s only the OCP of the as-cast condition reach a stable condition and for all the other conditions the potential continues to shift to more noble potential values. This might be a result of different growth of a protective surface film [171]. The as-cast Mg10Gd alloy showed the noblest OCP of -1574 mV. The solution treated Mg10Gd alloy reached an OCP of around -1754 mV, Mg10Gd alloy aged at 200°C shifted to -1790 mV. The Mg10Gd alloy aged at 300°C reached an OCP of -1708 mV and Mg10Gd alloy aged at 400°C showed an OCP of -1717 mV. Comparison of the OCP of heat treated Mg10Gd alloys with Mg10Gd as-cast condition alloy show the potential differences ΔE after 30 min immersion as follows: 172 mV for Mg10Gd solid solution treated, 208 mV for Mg10Gd aged at 200°C, 126 mV for Mg10Gd aged at 300°C and 135 mV for Mg10Gd aged at 400°C. The open circuit potentials of Mg10Gd alloy in the five conditions decrease in the following order: Mg10Gd as-cast> Mg10Gd aged at 300°C> Mg10Gd aged at 400°C> Mg10Gd solution treated> Mg10Gd aged at 200°C. The heat treatments have a direct influence on the OCP response, in samples, where more Mg_5Gd/GdH_2 phase was found a less active potential was measured.

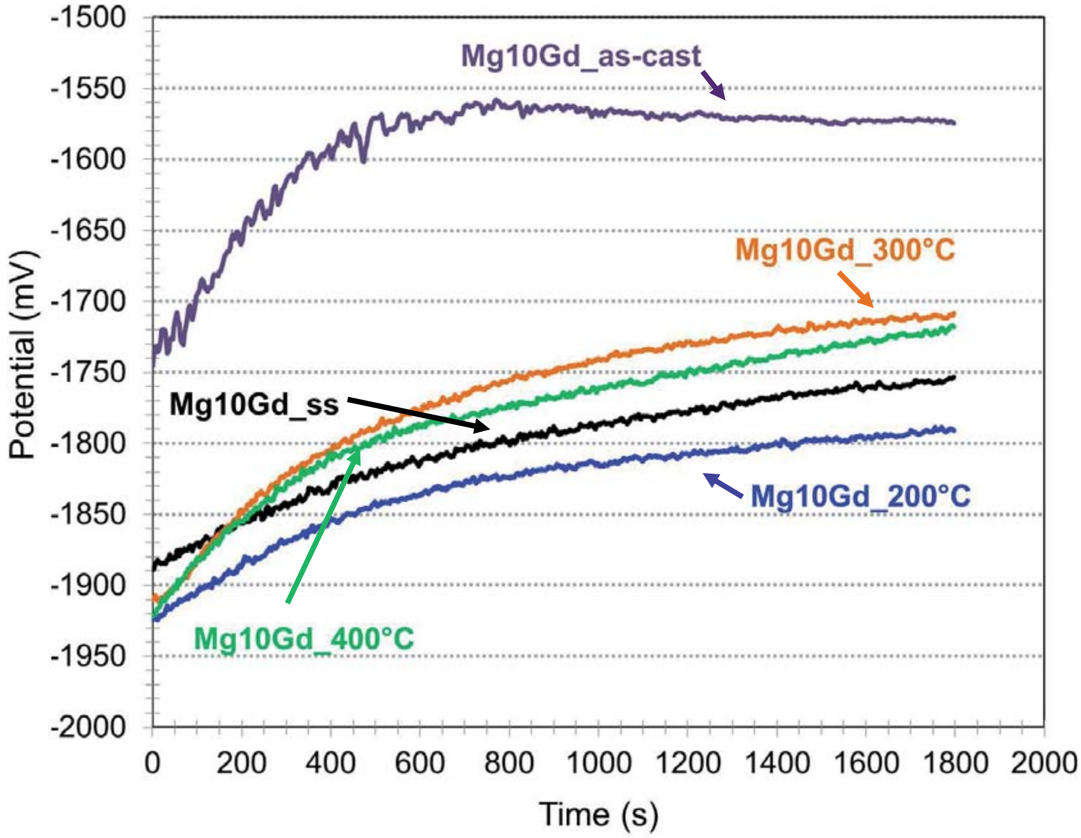

Figure 4.32 Open circuit potential vs. time of as-cast condition, solid solution treated and aging treatments at 200°C, 300°C and 400°C of Mg10Gd alloy in 0.5 wt. % NaCl solution

b) Potentiodynamic polarisation measurements

The effect of the heat treatments on the corrosion potential and current density in Mg10Gd alloys is shown in Figure 4.33. The plots include the response of as-cast Mg10Gd for comparison. Fig 5.32 shows that the values of corrosion potential (E_{corr}) of the Mg10Gd alloys after aging treatments are more active than the corrosion potential of the as-cast Mg10Gd alloy. However corrosion rates of the five alloys are similar, 0.92 mm/year for the as-cast alloy, 2.40 mm/year for the solid solution treated alloy, 1.94 mm/year for the alloy aged at 200°C, 1.91 mm/year for the alloy aged at 300°C and 2.17 mm/year for the alloy aged at 400°C (see Table 4.11). As shown before the corrosion rates still correlate with the volume of Mg_5Gd phase, but another phase appeared especially during heat treatments, which influences the corrosion performance. There is evidence of GdH_2 formation and larger amounts of this phase are found in the solution treated and the 400°C aged condition. Both specimens revealed the highest corrosion rates. Furthermore the homogenisation of Gd distribution appears to be not beneficial for the overall corrosion rate although pitting seems to be retarded (Figure 4.29 and Figure 4.30). However differences are small, but in the short term (around 20 to 60 min immersion), the heat-treatments did not improve corrosion resistance. The corrosion rate of as-cast Mg10Gd alloy is only half of the corrosion rates obtained after heat treatments

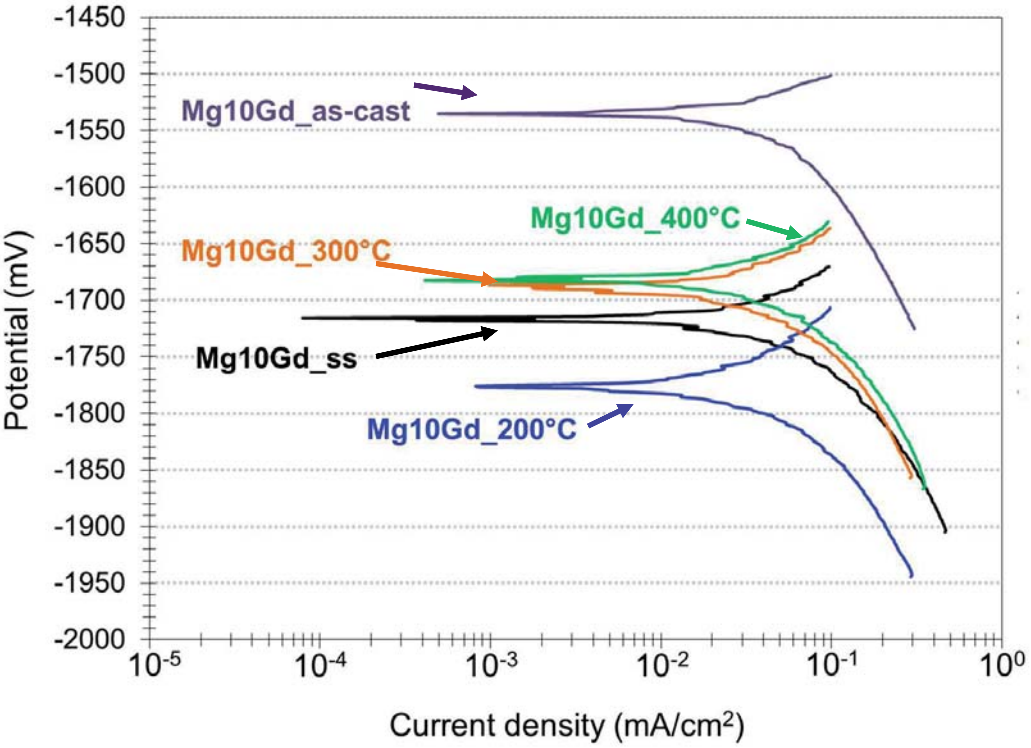

Figure 4.33 Potentiodynamic polarisation measurements of as-cast condition, solid solution treated and aging treatments at 200°C, 300°C and 400°C of Mg10Gd alloy in 0.5wt. % NaCl solution

Table 4.11 Electrochemical data from open circuit potential (OCP) and potentiodynamic polarisation measurements of as-cast condition, solid solution treated and aging treatments at 200°C, 300°C and 400°C of Mg10Gd alloy in 0.5 wt% NaCl solution

Alloy	OCP (mV vs. Ag/AgCl)	i_{corr} (mA/cm^2)	E_{corr} (mV vs. Ag/AgCl)	CR (mm/year)
Mg10Gd_as-cast	-1582 ± 8	0.04 ± 0.004	-1567 ± 4	0.92 ± 0.2
Mg10Gd_ss	-1754 ± 23	0.10 ± 0.02	-1715 ± 3	2.40 ± 0.6
Mg10Gd_200°C	-1790 ± 6	0.085 ± 0.01	-1776 ± 9	1.94 ± 0.3
Mg10Gd_300°C	-1708 ± 0.3	0.083 ± 0.009	-1686 ± 0.2	1.91± 0.2
Mg10Gd_400°C	-1717 ± 3	0.095 ± 0.005	-1682 ± 6	2.17 ± 0.1

c) Electrochemical impedance spectroscopy (EIS)

The EIS spectra of Mg10Gd alloys after heat treatments are illustrated Figure 4.34. Impedance spectra for all alloys show two well defined time constants. One time constant is related to a porous oxides/hydroxides layer formation on the alloys surface and the second time constant is attributed to the corrosion process on the interface metal/electrolyte penetrated film. After solid solution treatment this behaviour was observed during the first 10 hours of immersion (Figure 4.34 (a),(b)). The film is growing in thickness and thus the resistance is increasing. After 24 h the oxide layer is failing due to localized corrosion. The simulated parameters from EIS spectra are listed in Appendix A4. The equivalent circuits used for fitting the EIS spectra of the alloy are shown in Figure 4.35 (a) and (b). The EIS spectra of the Mg10Gd aged at 200°C is shown in Figure 4.34 (c), (d). It has two time constants during the whole test. The first time constant at high frequencies is attributed to the oxide film on the surface and the second time constant is related to the double layer. The impedance response increases with the exposure time indicating an oxide layer growing in thickness on the alloy surface. The simulated parameters from the EIS spectra are listed in Appendix A5. The EIS spectra of Mg10Gd aged at 300°C is shown in Figure 4.34 (e), (f) and a similar behaviour as describe above for the 200°C aging specimen is observed. Moreover Mg10Gd aged at 300°C shows the highest impedance response (10^3 – 10^4 $\Omega \cdot cm^2$) compared to the other differently aged specimen. The aging treatment at 300°C permits an oxide layer more stable and thicker with increasing time of exposure. The simulated parameters from EIS spectra are listed in Appendix A6. For Mg10Gd aged at 400°C the degradation of the oxide layer occurs after 1 h immersion, revealing a rapid breakdown of the oxides/hydroxides layer and the corrosion process is dominated by local active areas without protective film (see Figure 4.34 (g),(h)). Appendix A7 summarizes the corresponding fitted parameters. In the equivalent circuits used for fitting the EIS spectra of Mg10Gd alloys after heat treatments, R_s represents the resistance of the solution. The resistance R_{oxi} and capacitance C_{oxi} are the response of the oxide film due to oxides/hydroxides formation on the metal surface. The defects that form on the oxide layers generate pathways that allow the diffusion of corrosive species to the magnesium surface. Thus the second time constant appears in the low frequency region. This is the initiation of the corrosion process and is attributed to the existence of the double-layer capacitance at the metal/electrolyte interface, C_{dl} and corresponding resistance, R_{Ct}. When the specimen starts to corrode actively, the remaining areas covered by oxide layer are short-cutted and the remaining resistance can be estimated using a simple Randles model (see Figure 4.35).

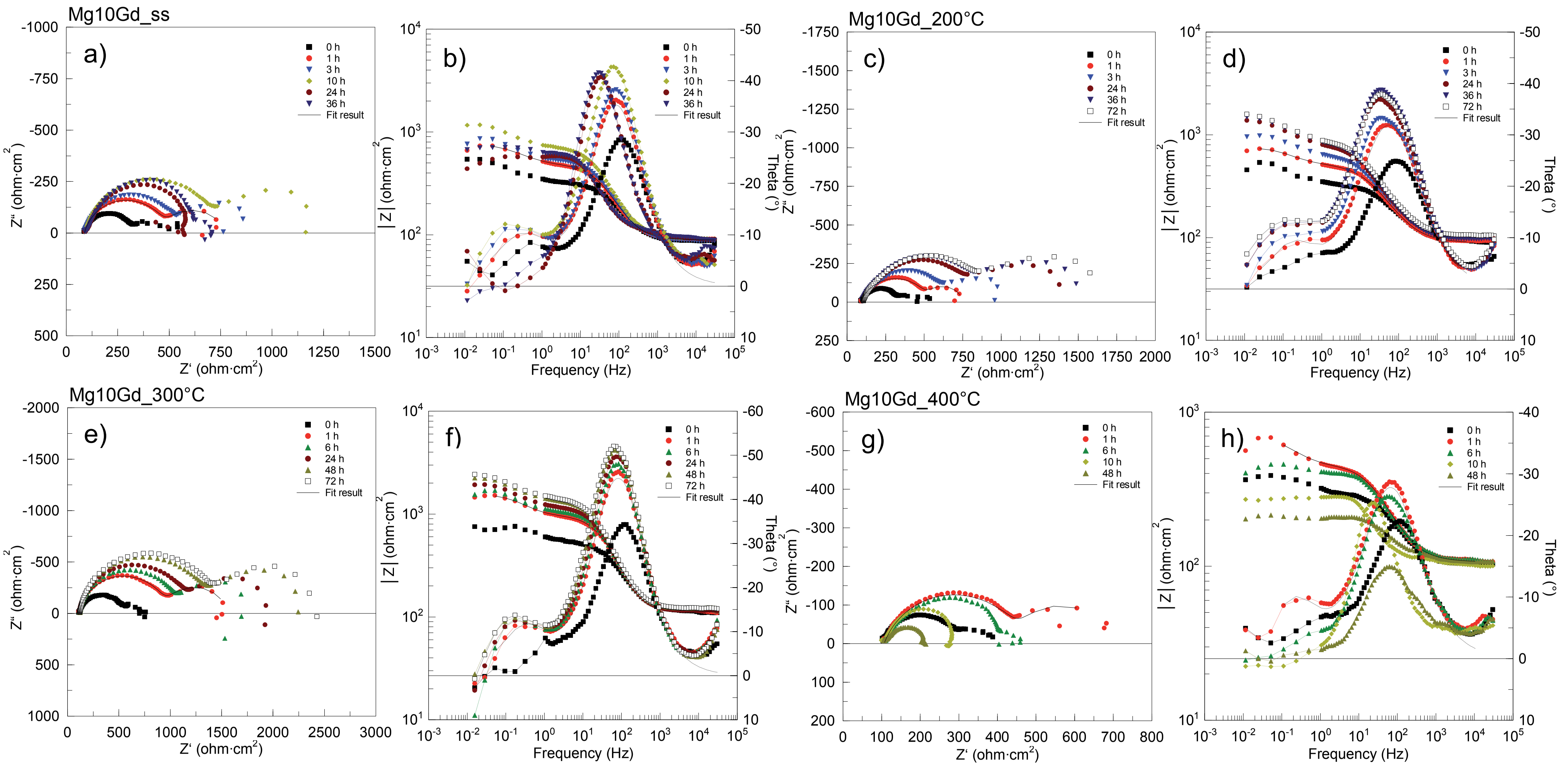

Figure 4.34 EIS spectra of Mg10Gd alloy, where (a), (b) are the Nyquist and Bode plots of Mg10Gd alloy after solid solution treatment, (c),(d) are the Nyquist and Bode plots of Mg10Gd alloy aged at 200°C, (e), (f) are the Nyquist and Bode plots of Mg10Gd alloy aged at 300°C, and (g), (h) are the Nyquist and Bode plots of Mg10Gd alloy aged at 400°C, after immersion in 0.5 wt% NaCl solution for several times

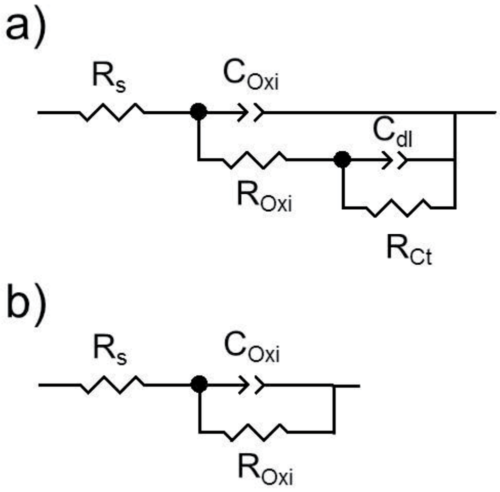

Figure 4.35 Equivalent electrical circuits used to simulate EIS spectra for as-cast condition, solid solution treated and aging treatments at 200°C, 300°C and 400°C of Mg10Gd alloy during different immersion time where R_{oxi} and C_{oxi} are the resistance and capacitance of the oxide film. R_{Ct} represents the charge transfer resistance and C_{dl} is attributed to the existence of the double-layer capacitance at the metal/electrolyte interface

The resistance of the Mg10Gd alloys after heat treatments is shown in Figure 4.36. The plots include the response of the as-cast Mg10Gd for comparison. The starting resistance values are all similar which is consistent with the polarisation results. The remarkable differences are developing with longer immersion times only. Compared to the as-cast condition all heat treatments perform better. The solid solution treatment and 400°C aging show larger amounts of the GdH_2 precipitates and do show less stable oxide film indicated by earlier film breakdown and active local corrosion spreading with time over the whole surface. The as-cast condition has large Mg_5Gd precipitates and none uniform solid solution distribution of Gd in the Mg matrix. Obviously this is detrimental for a uniform film formation. A homogenised Gd distribution in the matrix and uniformly distributed small Mg_5Gd precipitates are supporting the oxide film formation (200°C and 300°C aging)

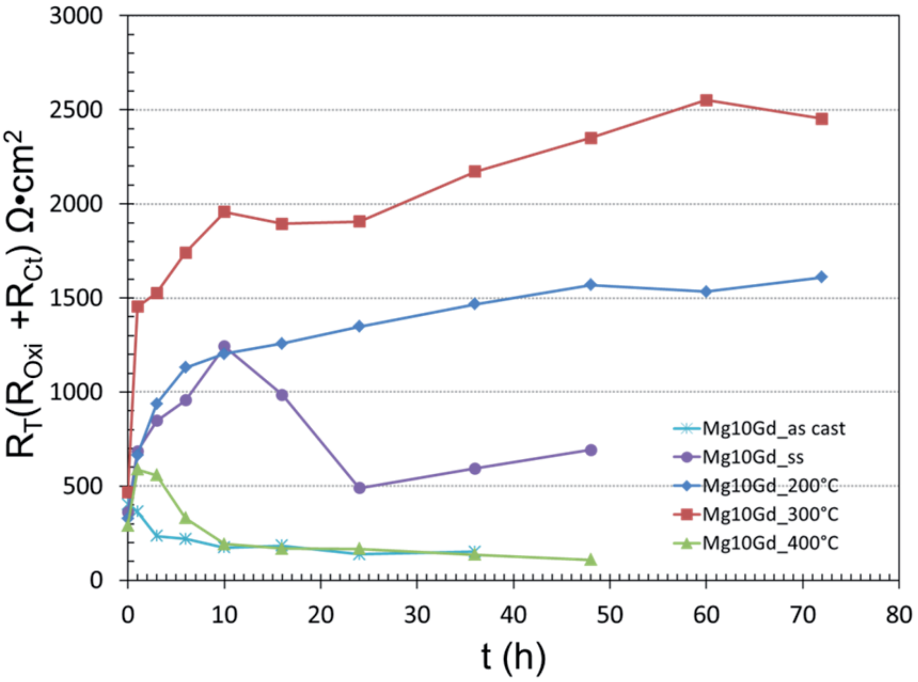

Figure 4.36 Average evolution of total resistance (RT) values obtained after fitting EIS spectra of as-cast condition, solid solution treated and aging treatments at 200°C, 300°C and 400°C of Mg10Gd alloy during immersion time in 0.5 wt.% NaCl solution

4.4 Ternary alloys

In order to evaluate the effect of additional alloying elements and to improve the corrosion resistance of the Mg10Gd alloy ternary alloying elements were considered. In this section some common alloying elements for Mg were added to Mg10Gd alloy to cast Mg10Gd5Al, Mg10Gd5Ga, Mg10Gd1Mn, Mg10Gd5Y and Mg10Gd5Zn ternary alloys. These elements are normally used in commercial Mg alloys, i.e. Al for AE alloys, Zn for ZE alloys, Y for WE alloys and Mn for ME alloys. Ga was selected because it belongs to the group IIIA in the periodic table of elements, likely to have similar behaviour as Al. The amount of alloying elements is based on their solid solubility in Mg and the possibility of forming different intermetallics phases which could change the galvanic effects

4.4.1 Characterization

a) Scanning electron microscopy (SEM)

The addition of the ternary alloying element to as-cast Mg10Gd alloy modifies the microstructure of the binary alloy as shown in Figure 4.37. EDS point analyses were made on selected points labelled as, A, B, C, D, E, etc. and reported in Table 4.12. The microstructure of Mg10Gd5Al consisted of a large volume fraction of secondary phases with different morphologies and sizes, small size of irregular shape, large geometrical shape and needle like shaped phases were observed (Figure 4.37 b). The irregular shape phases marked as “A” and “B” have a grain size of 1.69 µm and 1.29 µm, Figure 4.38 (a),(b), respectively, which ratios Mg/Gd were around 4.01 and 5.3 respectively, are close to the ideal Mg/Gd ratio of 5 for Mg_5Gd phase. The geometrical shape phases marked as “D”, “E” and “F” presented ratios of Al/Gd around 2.02, 2 and 2.13 which are consistent to Al_2Gd phase. The needle shaped phase marked as “G” and “H” represents the large volume fraction of secondary phase for this alloy. The ratios of Al/Gd were around 2.43 for “G” and 2.79 for “H”, indicating that this phase is also Al_2Gd phase.

The microstructure of Mg10Gd5Ga consisted of a large volume fraction of secondary phases with three morphologies, Figure 4.37(c). Spherical, lath and eutectic lamellar particles were observed. The eutectic lamellar structure marked as “A” and “B” contained similar concentration of Ga, Gd, and Mg, around 17.10, 13.32 and 67.70 at.% respectively for “A” and 17.36, 17.13 and 63.38 at.% respectively for “B”. These composition ratios (3/1/1) suggested the presence of Mg_3GdGa phase, which is consistent with the XRD results. However the spherical particles marked as “C” and lath particles marked as “D” showed another composition of 27.12 at. % Ga, 29,57 at.% Gd and 40.32 at. % Mg for “C” while for “D” were around 28.04 at.% Ga, 30.07 at. % Gd and 38.47 at.% Mg. Generating composition ratios of (1/1.36/1.48) for “C” and for “D” (1/1.27/1.37) which correspond to the MgGdGa phase.

The microstructure of Mg10Gd1Mn consisted of a relative low volume fraction of secondary phases compared to the other ternary alloys, Figure 4.37 (d) and the appearance is still similar to the binary Mg10Gd alloy. For this alloy an irregular shaped phase was observed (marked as “A”, “B” and “C”), which showed similar Gd content as found in as-cast Mg10Gd alloy (11 to 14.6 at. %), indicating the formation of Mg_5Gd phase. Moreover some light grey zones marked as “D” were observed. The EDS analysis indicated that these zones present Gd-enrichment compared to the dark zones (α-matrix) marked as “E” (see Table 4.12). However in the selected particles and matrix, Mn was also found. These results suggested that Mn is distributed in the secondary phase, Gd-enrichment zones and matrix.

Mg10Gd5Y consisted of low volume fraction of secondary phases with eutectic lamellar structure, (marked as “A”, “B” and “C”) and some light grey zones marked as “D” (Figure 4.37 e). The composition of “A” was 11.01 at. % Y and 12.07 at.% Gd. Similar compositions were observed in the particles “B” and “C”. The ratios of Y and Gd to Mg for “A” were 6.9/6.29. Similar ratios for the “B” (Mg/Y, 6.37 and Mg/Gd, 6.56) and “C” (Mg/Y, 6.06 and Mg/Gd, 5.76) particles were observed (see Table 4.12. The experimental ratios of Mg/Gd and Mg/Y for the three particles are relative close to the ideal 4.8, which correspond to the $Mg_{24}(Gd,Y)_5$ phase. Moreover some Gd enrichment zones (marked as “D”) were also observed, where the concentration of Gd is higher compared to the primary α-Mg matrix.

Mg10Gd5Zn contains large volume fraction of dendritic microstructure (Figure 4.37 f). The eutectic phases marked as “A” showed concentrations of 16.18 at.% Gd and 21.28 at:% Zn, while "B" the concentrations of Gd and Zn were 15.40 at.% and 20.15 at.% respectively. The ratios of Gd and Zn to Mg were around 3.84 and 2.92 for particle "A", while for particle "B" were around 3.99 and 3.05 respectively. These results are close to the ideal ratio of 3 for the $Mg_3(Gd,Zn)$ phase. The intermetallic phases were determined with reference to XRD data presented in the following section.

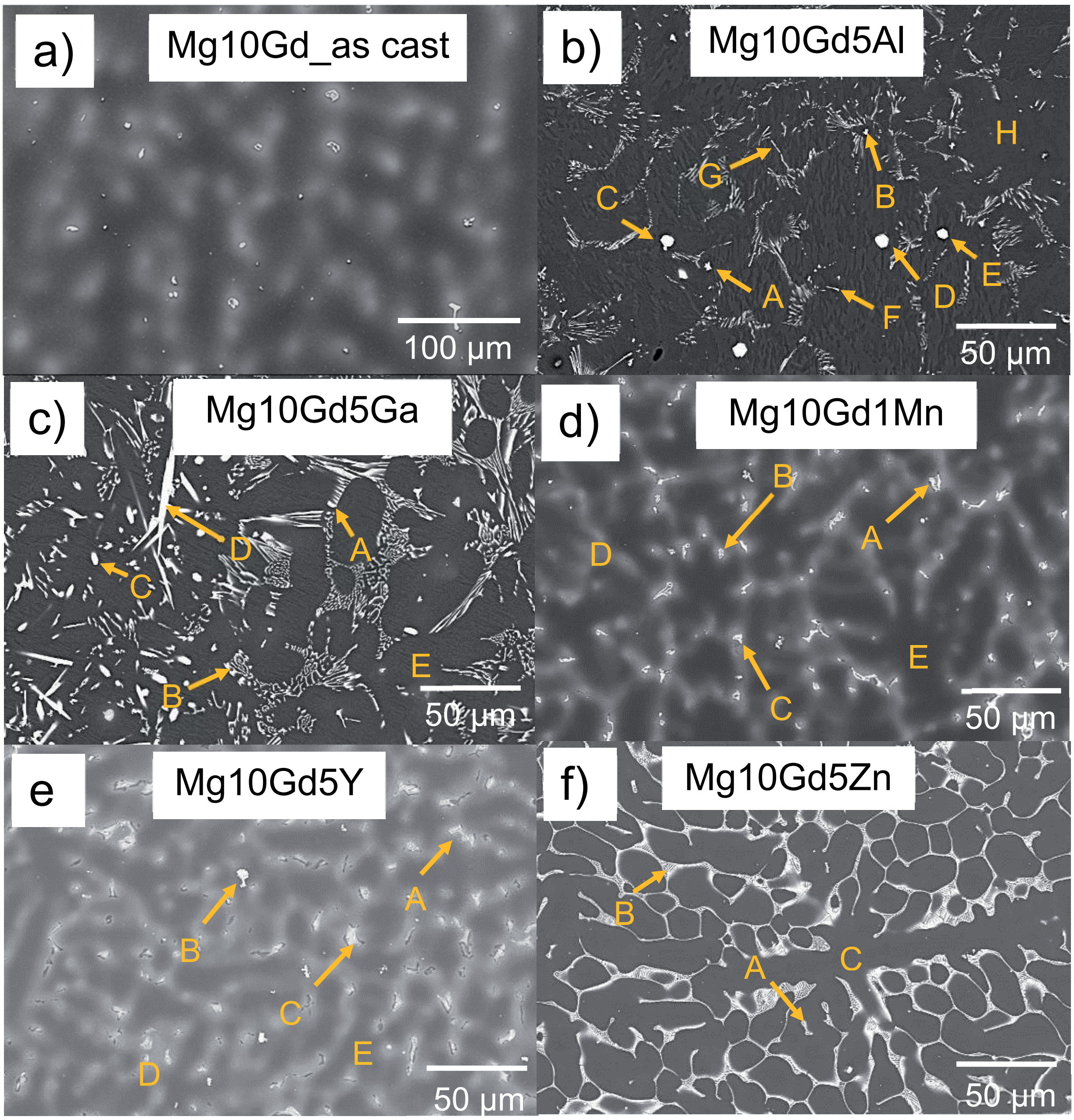

Figure 4.37 SEM micrographs of as-cast ternary alloys: a) Mg10Gd 5Al, b) Mg10Gd5Ga, c) Mg10Gd1Mn , d) Mg10Gd5Y and e) Mg10Gd5Zn

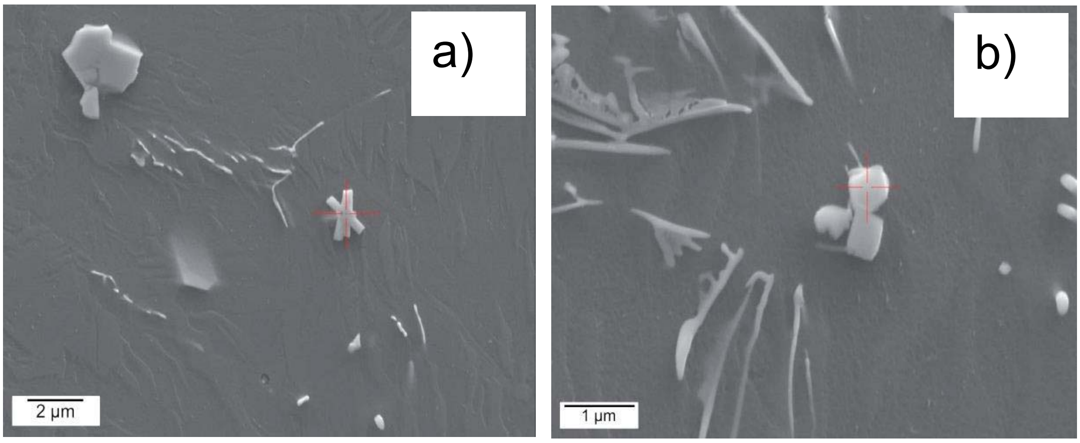

Figure 4.38 SEM micrographs of as- cast Mg10Gd5Al alloy: a) and b) show the precipitates of Mg_5Gd at higher magnifications

Table 4.12 EDS analysis of the selected points of the as-cast ternary alloys: Mg10Gd5Al, Mg10Gd5Ga, Mg10Gd1Mn, Mg10Gd5Y and Mg10Gd5Zn

Alloy	Location	Al (at.%)	Gd(at.%)	O (at.%)	Si (at.%)	Mg (at.%)
Mg10Gd5Al	A	1.86	16.52	2.34	12.87	66.4
	B	3.74	13.27	1.15	10.61	71.22
	C	62.80	30.96	0.73	-	5.51
	D	59.03	29.37	0.98	0.85	9.77
	E	61.41	28.71	0.71	-	9.16
	F	23.54	9.66	1.01	-	65.79
	G	8.43	3.02	0.68	0.03	87.84
	H	0.88	0.03	0.42	0.03	98.64
		Ga (at.%)	Gd(at.%)	O (at.%)	Si (at.%)	Mg (at.%)
Mg10Gd5Ga	A	17.10	13.32	1.88	-	67.70
	B	17.36	17.13	2.13	-	63.38
	C	27.12	29.57	2.99	-	40.32
	D	28.04	30.07	2.92	0.50	38.47
	E	0.63	0.17	0.40	-	98.80
		Mn (at.%)	Gd(at.%)	O (at.%)	Si (at.%)	Mg (at.%)
Mg10Gd1Mn	A	0.87	14.60	0.22	-	84.30
	B	3.15	11.08	0.69	-	85.08
	C	0.86	13.04	-	-	86.11
	D	0.50	3.07	0.34	-	96.09
	E	0.49	0.55	0.35	-	98.61
		Y (at.%)	Gd(at.%)	O (at.%)	Si (at.%)	Mg (at.%)
Mg10Gd5Y	A	11.01	12.07	0.88	-	76.04
	B	11.94	11.58	0.41	-	76.07
	C	12.22	12.85	0.86	-	74.07
	D	0.42	2.61	0.51	0.03	96.43
	E	0.67	0.55	0.42	-	98.36
		Zn (at.%)	Gd(at.%)	O (at.%)	Si (at.%)	Mg (at.%)
Mg10Gd5Zn	A	21.28	16.18	0.25	-	62.29
	B	20.15	15.40	2.94	-	61.51
	C	0.42	0.41	0.36	-	98.81

b) Transmission Electron Microscopy (TEM)

In order to determine the role and distribution of Mn in the Mg10Gd1Mn alloy, a TEM investigation was conducted. Figure 4.39 (a) shows that the precipitates form along the dislocation lines when the electron beam is approximately parallel to the $< 10\bar{1}0 >_{\text{Mg}}$ direction. These dislocations were found to be mainly basal dislocations by diffraction analysis with various $\tilde{g}$ vectors. The morphology of the precipitates is seen clearly in Figure 4.39 (b). The precipitates are lath shaped particles that form within the dislocation lines. The crystal structure of these precipitates was determined by electron microdiffraction, Figure 4.39 (c) and (d). The precipitate particles can be indexed according ß' phase (a c-base centred orthorhombic structure with lattice parameter a=0.64nm, b=2.22nm and c=0.52nm) with a chemistry close to Mg_5Gd. The fully indexed schematic illustrations of the electron microdiffraction patterns acquired along $< 10\bar{1}0 > \text{Mg}$ (Figure 4.39c), and $< 11\bar{2}0 >_{\text{Mg}}$, Figure 4.39 (d) are shown in Figure 4.39 (e) and (f) respectively. The TEM EDX analysis showed that Mn is found in the intermetallics and to a lesser extent in the matrix without forming any ternary intermetallic phases (see Figure 4.40).

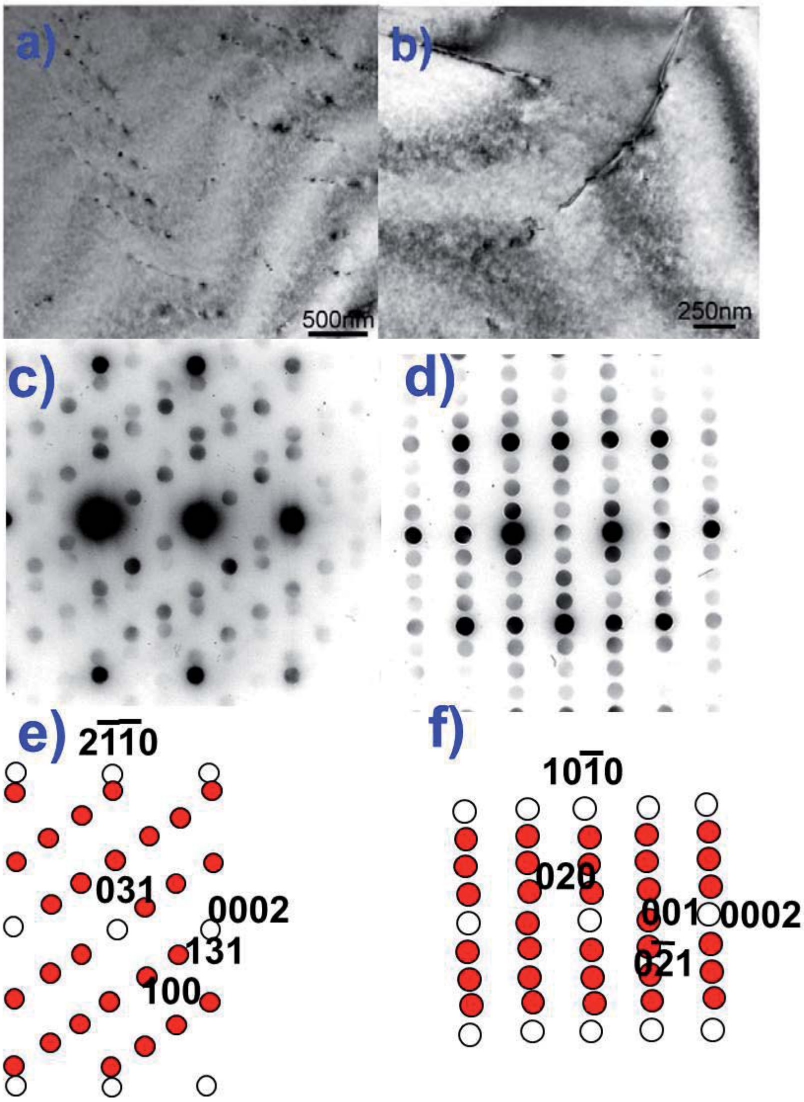

Figure 4.39 TEM micrographs of as-cast Mg10Gd1Mn alloy, a) at lower magnifications, b) at higher modifications, with associated electro microdiffraction patterns (c,d) and schematic patterns (e,f). Using an electron beam approximately parallel to $< 10\bar{1}0 >$ in (a,c) and$< 11\bar{2}0 >$ in (b,d)

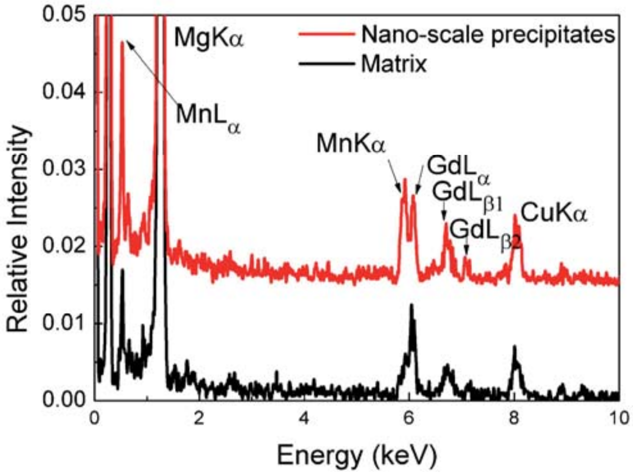

Figure 4.40 TEM EDX spectra of Mg10Gd1Mn alloy

c) X-Ray diffraction (XRD)

Figure 4.41 shows the X-ray diffraction patterns of the as-cast ternary alloys. The diffraction pattern of Mg10Gd5Al showed peaks that correspond to the Mg_5Gd phase; there is no evidence of intermetallics phases with Al, such as Al_2Gd, which were by SEM identified. Similar finding was observed for Mg10Gd1Mn alloy, diffraction pattern indicates presence of Mg_5Gd phase. While for Mg10Gd5Y, the diffraction pattern show intermetallic phase $Mg_{24}(Gd,Y)_5$ [172] as previous identified by SEM analyses. The diffraction pattern of Mg10Gd5Ga indicated peaks corresponding to Mg_3GdGa phase. While Mg10Gd5Zn diffraction pattern show the presence of Mg_3Gd phase with Zn incorporation [173-176], these results were consistent to the SEM results.

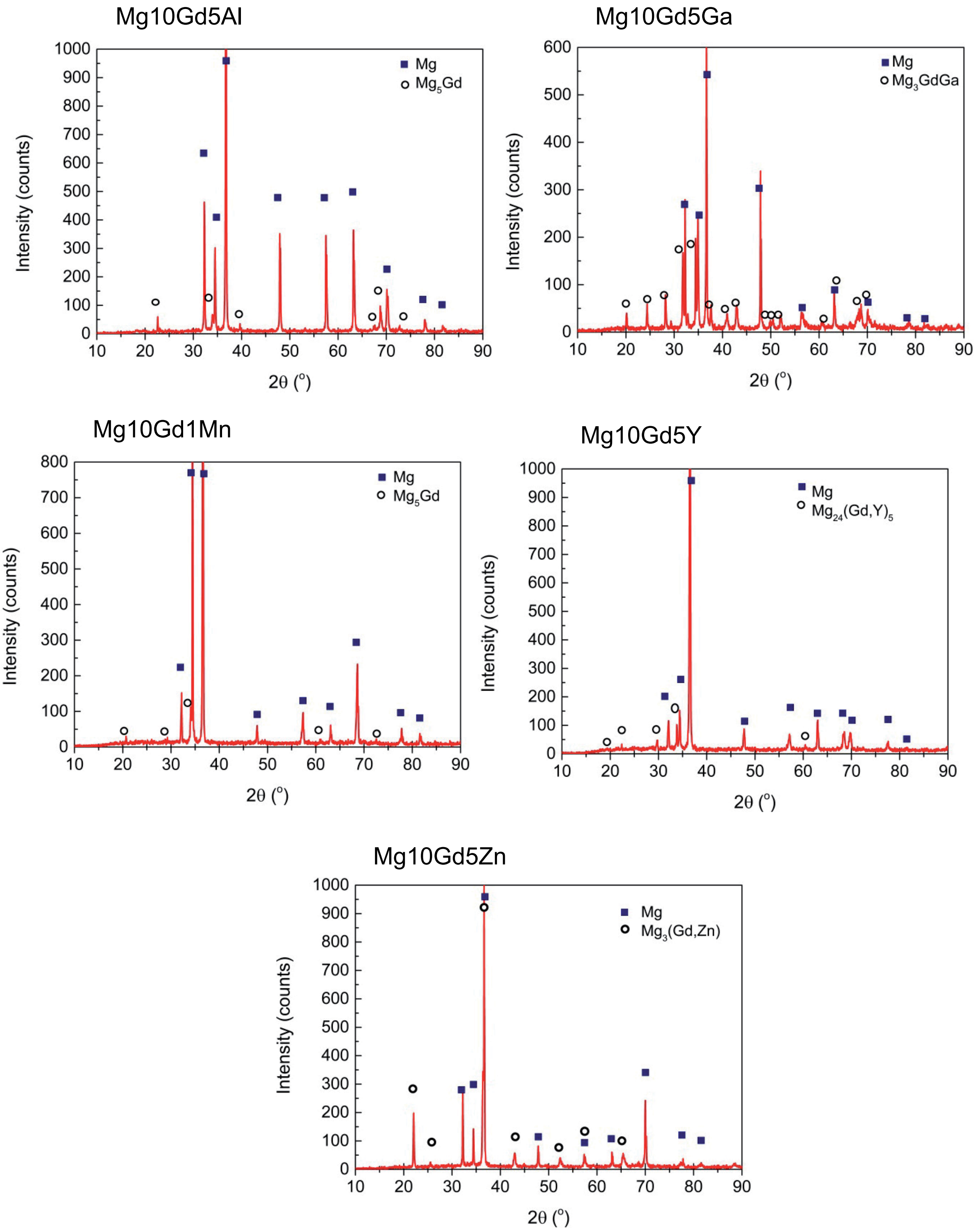

Figure 4.41 X-ray diffraction patterns of the ternary alloys: Mg10Gd 5Al, Mg10Gd5Ga, Mg10Gd1Mn, Mg10Gd5Y and Mg10Gd5Zn (λ=1.54 nm and CuKα radiation)

4.4.2 Evaluation of the corrosion behaviour

a) Hydrogen evolution and weight loss

Adding a third element to the Mg10Gd based alloy directly affect the corrosion rate of the ternary alloys. Figure 4.42 shows the corrosion rates of the ternary alloys obtained by hydrogen evolution and weight loss measurements. The lowest corrosion rates were observed for

Mg10Gd as-cast condition (5.9/5.7 mm/year), and Mg10Gd1Mn (5.8/4.2 mm/year) using both techniques. Mg10Gd5Al had corrosion rate values of 12.8 and 11.2 mm/year respectively. The highest corrosion rate values were obtained for Mg10Gd5Ga (28.5/37.2 mm/year), Mg10Gd5Y (40/41.9 mm/year) and Mg10Gd5Zn (112/117 mm/year). Thus, increased negative effect of alloying elements on corrosion was observed in the following order: Al, Ga, Y and Zn. On the other hand by adding a small amount of approximately 1 wt. % Mn, it is possible to reduce the corrosion rate of the base alloy which may give another option to increase corrosion resistance beside a heat treatment.

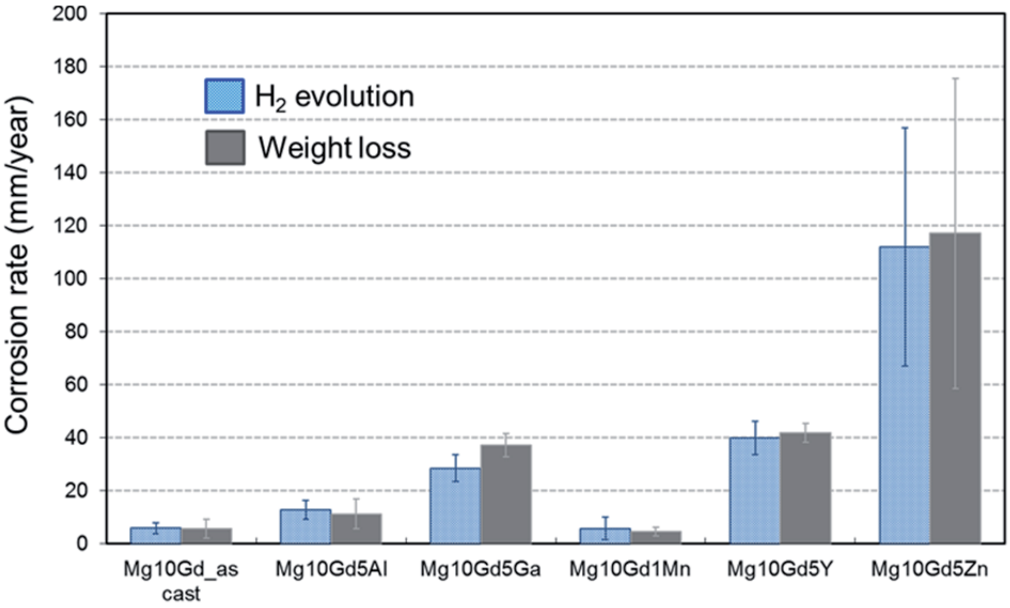

Figure 4.42 Comparison of corrosion rates using hydrogen evolution and weight loss measurements of ternary alloys: Mg10Gd5Al, Mg10Gd5Ga, Mg10Gd1Mn, Mg10Gd5Y and Mg10Gd5Zn

b) Drop/Immersion test

Based on the results of hydrogen evolution and weight loss only three of the five ternary alloys were evaluated in this section. Mg10Gd1Mn is interesting because Mn is the only alloying element which allows a reduction in corrosion rate. Mg10Gd5Al was selected because Al is the most commonly used alloying element for Mg alloys. The third selected alloy was Mg10Gd5Zn, because it can be important to understand why such fast degradation could take place and may assist in the selection of alloying elements for Mg alloys in the future.

- *Mg10Gd1Mn*

Figure 4.43 shows SEM micrographs of Mg10Gd1Mn alloy after certain exposure times in 0.5 wt. % NaCl. Three regions can be identified, α-Mg matrix, Gd enriched zones and intermetallic phase, which show different response. Colours were used to emphasize which area is damaged due to which corrosion process, thus yellow for α-Mg matrix, blue for $Mg_5Gd(Mn)$ and green for the Gd enriched zones. The composition of the matrix is mainly magnesium but also gadolinium (most of gadolinium is found in the precipitates) and manganese were present in solid solution. The precipitates which were identified as Mg_5Gd do also contain traces of manganese in solid solution, thus they are assigned as $Mg_5Gd(Mn)$ and similar cubic precipitates are present as in the Mg10Gd alloy and they are most likely GdH_2. The selected areas represent different areas on the surface, where it was possible to observe the degradation processes. During the first 30 minutes of immersion there were no remarkable changes in the microstructure; small holes at the base of the precipitates were observed (Figure 4.43 b, d) and some pits in the matrix were also visible (Figure 4.43 d, f). After 1 h immersion, these pits surrounding the intermetallic $Mg_5Gd(Mn)$ phase become small holes and some are agglomerating to larger localised attack especially in the Gd enriched areas. From 1 to 5 hours it can be observed that the localised attack is progressing and first intermetallics are lost either by dissolution or undermining After 10 hours immersion, the corrosion attack was more severe in the whole specimen. After 15 hours, filiform corrosion (see Figure 4.44) together with stronger surface material removal was observed. A typical example of material removal is shown in Figure 4.43 (q) after 28 hours of immersion where larger precipitates have disappeared along with fractions of the surrounding matrix (blue dotted circle). Summarising, the corrosion process began at the base of the smaller mostly cubic precipitates because there is a potential difference between the precipitates, Gd enrichment zones and the matrix generating galvanic corrosion. Subsequently some pits in the matrix surrounding the precipitates develop and agglomeration of them starts. This process increases and filiform corrosion can start as well. Finally, the precipitates and the neighbouring matrix regions are dissolved together or the precipitates are lost by undermining.

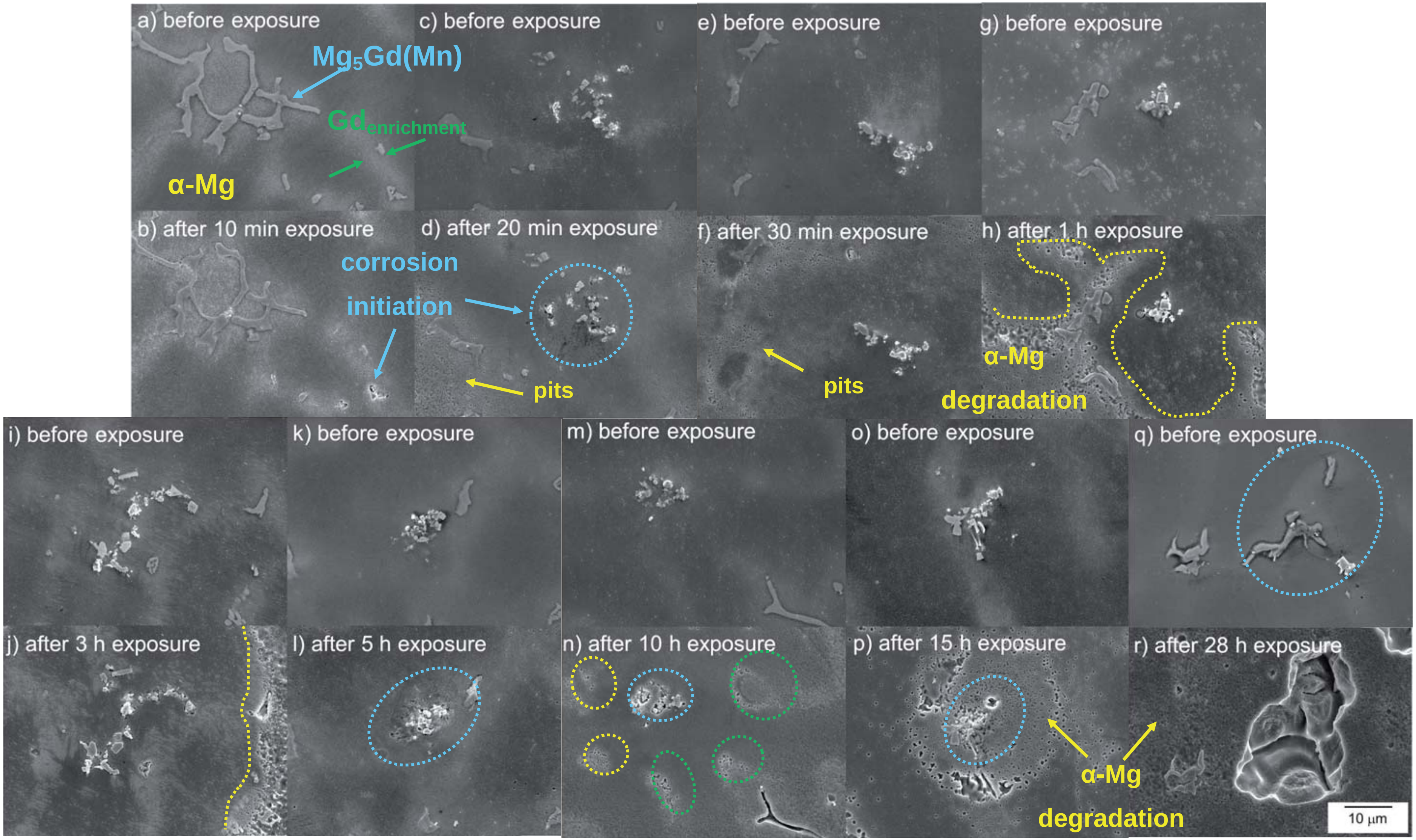

Figure 4.43 Corrosion monitoring using immersion test of as-cast Mg10Gd1Mn alloy after different exposure time in 0.5 wt.% NaCl solution. Yellow dotted circles depict the corrosion attack on the α- Mg matrix, blue dotted circles indicate corrosion process on the $Mg_5Gd(Mn)$ phases and the green dotted circles show the corrosion degradation on the Gd enrichment areas

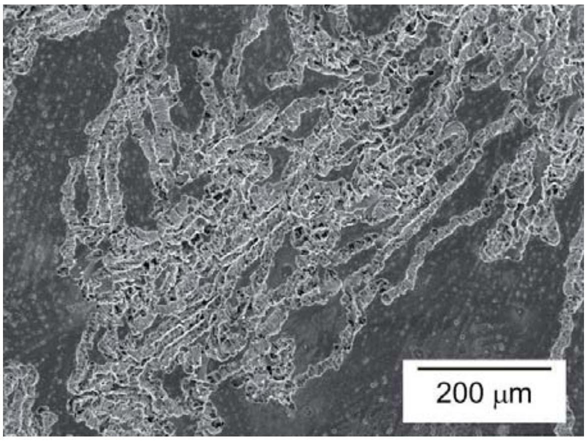

Figure 4.44 Filiform corrosion in Mg10Gd1Mn alloy after 15 h immersion in 0.5 wt.% NaCl solution

- *Mg10Gd5Al*

Figure 4.45 shows the corrosion process of Mg10Gd5Al alloy after different exposure times to 0.5 wt.% NaCl solution. In these SEM micrographs small amounts of Mg_5Gd phase can be seen and a large amount of needle shaped phase, which was identified as Al_2Gd using SEM-EDS analysis. After 10 minutes immersion, the corrosion process started at the base of the needle-shaped precipitates (Figure 4.45 b). After 20 and 30 minutes immersion, inside the yellow dotted circles slight dissolution and first pits in the α-matrix were observed Figure 4.45 d, f). After an hour immersion, the α-matrix exhibits greater roughness and dissolution of the matrix surrounding, the intermetallic phases is clearly visible (Figure 4.45h). For the Mg10Gd5Al alloy, filiform corrosion occurs after 3 h immersion (Figure 4.46). After 5 h immersion, the α-matrix show rapidly degradation due to the progress of filiform corrosion (Figure 4.45 l). The Mg_5Gd and Al_2Gd phases did not undergo any degradation. Before degradation of the matrix, a small volume fraction of Al_2Gd phase was observed (Figure 4.45 k), which consisted of small rounded and lath like particles. After immersion test, these particles were still present and more of them were not free by the dissolving matrix.

In the Mg10Gd5Al alloy the corrosion process started at the base of the smaller Al_2Gd precipitates with pitting. Subsequently some regions of α-matrix revealed degradation by uniform dissolution and pitting. The severeness is increasing together with immersion time. Thereafter filiform corrosion started and matrix regions dissolve, exposing larger volume fractions of Al_2Gd phase accelerating further the degradation.

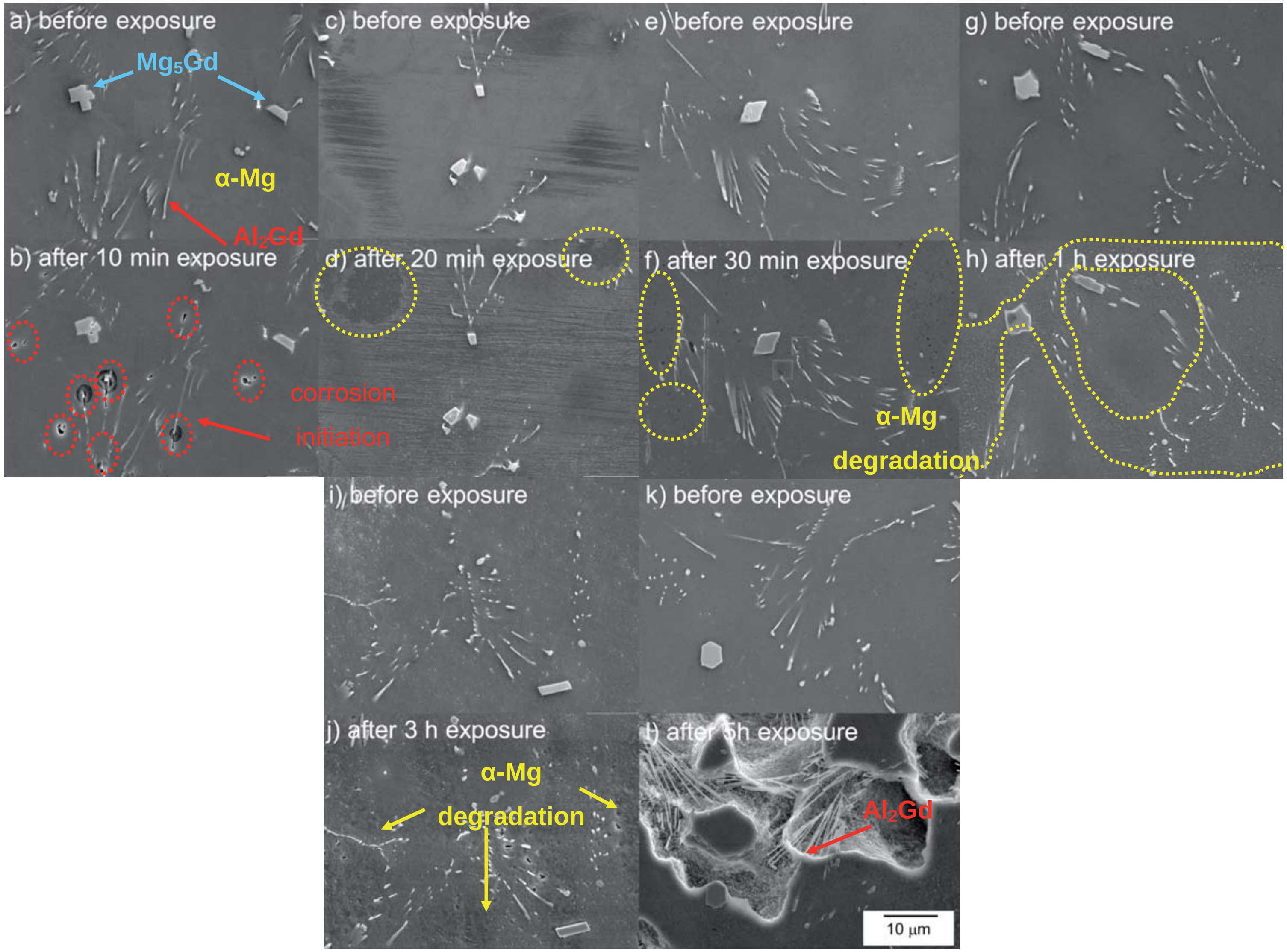

Figure 4.45 Corrosion monitoring using immersion test of as-cast Mg10Gd5Al alloy after different exposure time in 0.5 wt.% NaCl solution. Showing in yellow dotted circles the corrosion attack on the α- Mg matrix, blue dotted circles indicate corrosion process on the Mg_5Gd phases and the red dotted circles show the corrosion degradation on the Al_2Gd phases

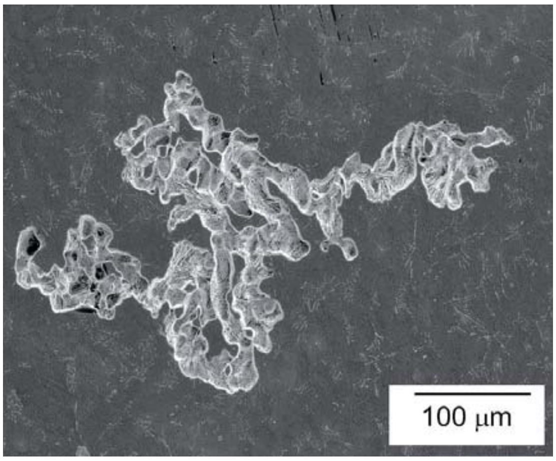

Figure 4.46 Filiform corrosion in Mg10Gd5Al alloy after 3 h immersion in 0.5 wt.% NaCl solution

- *Mg10Gd5Zn*

Figure 4.47 compares microstructure of Mg10Gd5Zn alloy before and after corrosion process of different exposure times in 0.5 wt. % NaCl solution. After polishing the sample showed some pores along the $Mg_3(Gd,Zn)$ phase. These pores could have been generated during the preparation, as punctual initiation of the detachment of the intermetallic phases or already galvanic attack during preparation. This fact has been noted and taken into account for all samples used for the drop/immersion test. Mg10Gd5Zn alloy has a large amount of $Mg_3(Gd,Zn)$ intermetallic phase, which is distributed as lamellar eutectic forming a network along the grain boundaries. During the first 10 minutes immersion no corrosion damage was observed (Figure 4.47 b). After 20 minutes immersion, some lamellar intermetallics dissolved partially (orange dotted circle) and α-matrix regions (yellow dotted circle) dissolved locally at the base of intermetallic phases (Figure 4.47 d). Some α-matrix areas show generally greater roughness and shallow pits close to the intermetallic phases after 30 minutes exposure (Figure 4.47 f). After 1 h exposure, the sample suffers already from severe corrosion; most of the α-matrix regions (yellow arrows) are dissolved and intermetallics are partially attacked (Figure 4.47 h). Severe corrosion of large areas was found after 1 h exposure (Figure 4.48). After 3 hours there are regions where the lamellar structure was exposed (orange dotted circles) after the dissolution of the matrix (Figure 4.47 j). This alloy had the worst performance in the immersion test compared to Mg10Gd5Al and Mg10Gd1Mn alloys, and has a very low corrosion resistance. After 5 hours matrix and intermetallics are severely attacked The $Mg_3(Gd,Zn)$ phase is distributed as lamellar network, and promotes a faster dissolution of the α-matrix but seems to be unstable as well. The corrosion process of Mg10Gd5Zn alloy could be described as follows: using after a short time of immersion; some α-matrix areas and certain regions of $Mg_3(Gd,Zn)$ phase were dissolved. Subsequently matrix losses became deeper exposing a large amount of skeletons of the lamellar structure of $Mg_3(Gd,Zn)$ phase; while in other regions, the intermetallic phase deteriorate as well and the selected areas were less visible. Finally only few lamellar intermetallic skeleton regions could be seen as the α-matrix severely degraded.

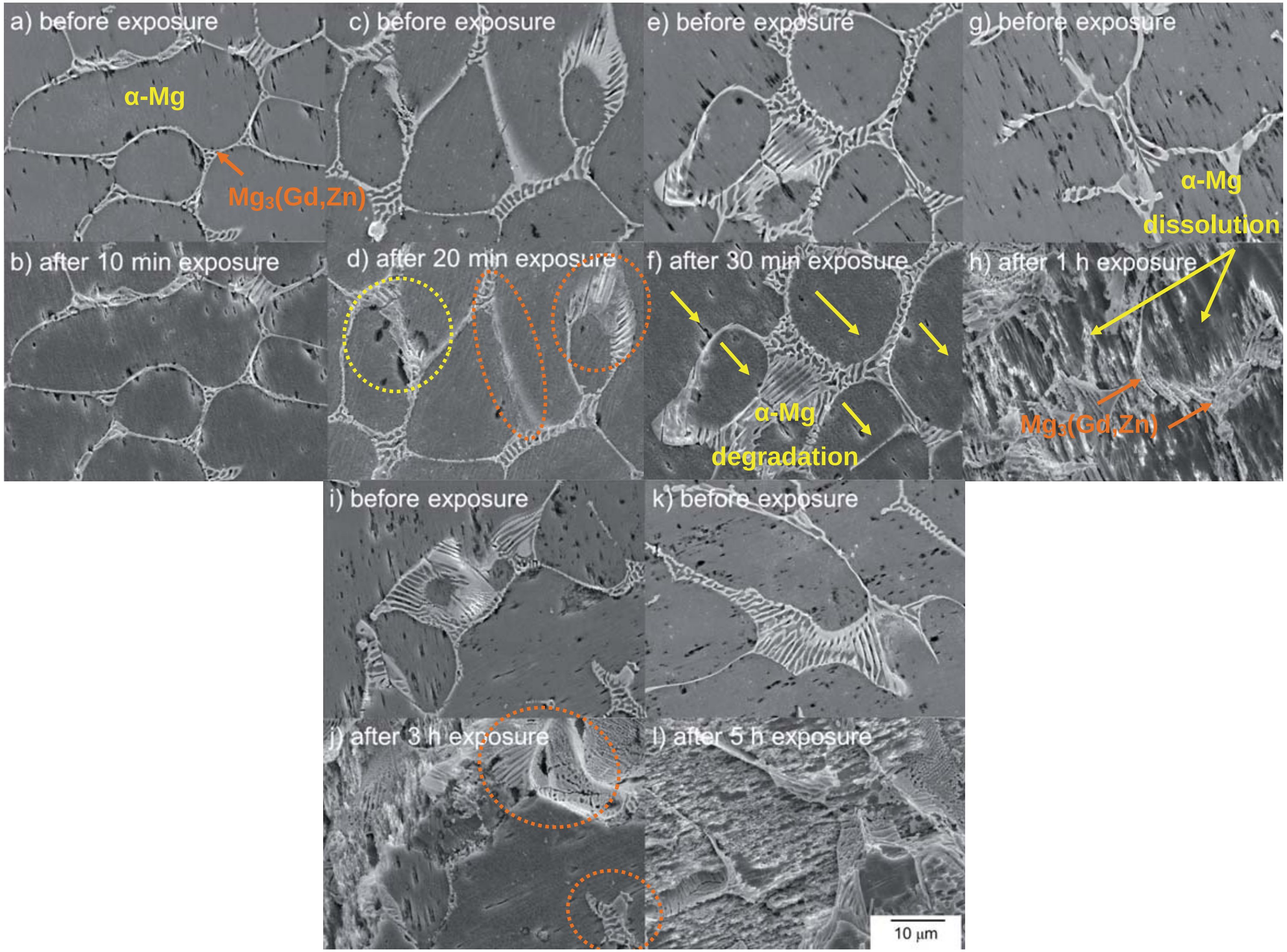

Figure 4.47 Corrosion monitoring using immersion test of as-cast Mg10Gd5Zn alloy after different exposure time in 0.5 wt.% NaCl solution. Showing in yellow arrows/dotted circles the corrosion attack on the α- Mg matrix, orange arrows/dotted circles indicate corrosion process on the $Mg_3(Gd,Zn)$ phases.

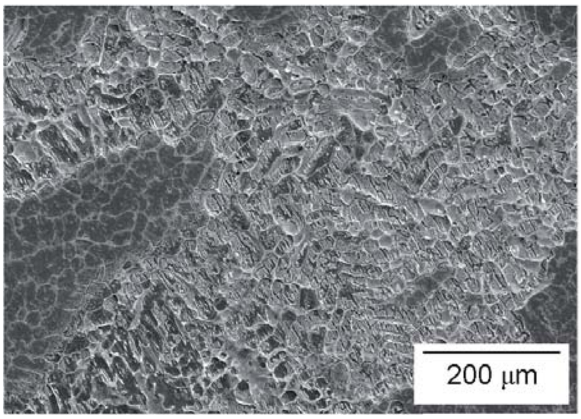

Figure 4.48 Severe large area corrosion in Mg10Gd5Zn alloy after 1h immersion in 0.5 wt.% NaCl solution

The corrosion process for Mg10Gd1Mn, Mg10Gd5Al, and Mg10Gd5Zn alloys present the typical corrosion processes of Mg base alloys. The corrosion is initiated in the matrix areas adjacent to secondary phase particles, as a result of the breakdown of passivity [3]. This creates an galvanic electrolytic cell in which the secondary phase particle is the cathode and the surrounding Mg matrix is the anode[41]. Therefore, two kinds of corrosion morphologies can occur: a) the α-matrix is preferentially dissolved and b) the secondary phases are undermined because of the dissolution of the α-matrix[4]. The dissolution of the matrix start with some pits then filiform corrosion was observed in Mg10Gd1Mn and Mg10Gd5Al alloys and a severe corrosion for Mg10Gd5Zn alloy. These results are consistent to the observations made by Lunder et al. [83, 177]

4.4.3 Electrochemical characterization

a) Open Circuit Potential (OCP)

Figure 4.49 shows the open circuit potential measurements of the ternary alloys. These curves are used to study the response of the surface of the magnesium alloys to immersion in to 0.5 wt.% NaCl solution. All curves show similar trends with increased immersion time. At the beginning, all samples show a more active potential; thereafter the potential values shift towards the noble side. This might be related to surface film formation [171]. The potential of Mg10Gd5Ga stabilised after 250 s immersion and show a noble OCP around -1554 mV. Similar behaviour was observed for Mg10Gd5Al and Mg10Gg1Mn alloys, which have reached OCP values around -1684 mV and -1683 mV, respectively. Despite M10Gd5Al and Mg10Gd1Mn showing more active potential compared to the other ternary alloys, they did not have large potential fluctuations, but it is also obvious that the potentials are still shifting towards more noble potentials. The OCP of Mg10Gd5Zn reached a more stable value of -1541 mV after 750 s immersion; while OCP of Mg10Gd5Y did not reach a stable value during the test ending at -1575 mV.

The amount, distribution and composition of the secondary phases have a direct influence on the OCP response, but the situation is more complex with the third element added. However indication of a stable OCP should not be misinterpreted assuming that this is caused by protective/passive layer formation on their surface. It seems to be the opposite, alloy with a reluctant change of potential show less corrosion attack. The following sections will discuss this aspect by determining the corrosion rates/ resistances of the alloys.

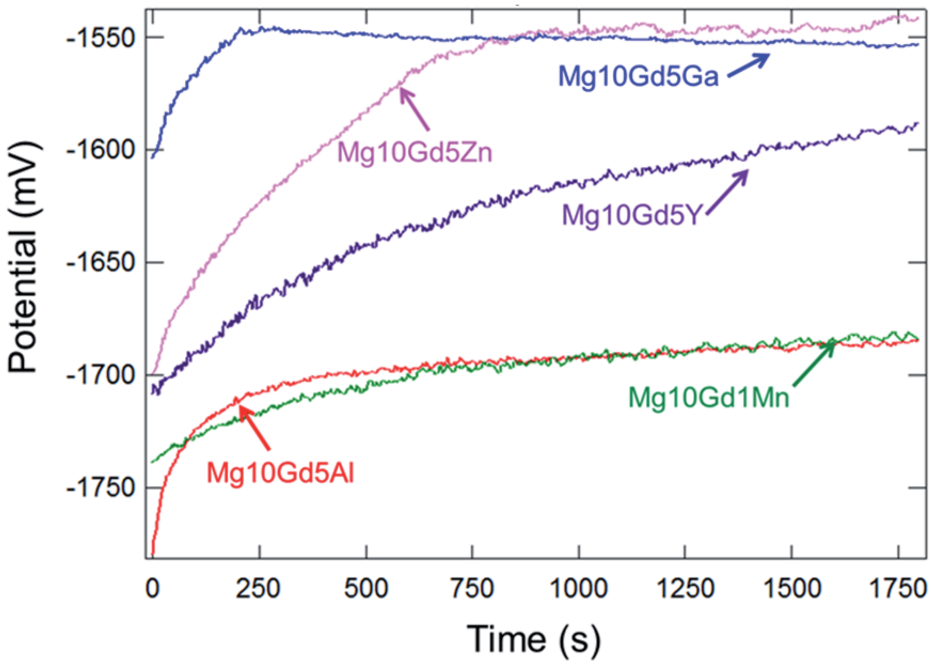

Figure 4.49 Open circuit potential (OCP) vs. time of the ternary alloys in 0.5 wt.% NaCl solution

b) Potentiodynamic polarisation measurements

Potentiodynamic polarisation curves of the ternary alloys are shown in Figure 4.50. The corrosion potential values (E_{corr}) of the ternary alloys were similar to the final OCP values. Even when the corrosion potentials (E_{corr}) of Mg10Gd5Ga, Mg10Gd5Y Mg10Gd5Zn were less active after short immersion periods in NaCl solution; their corrosion rates were higher compared to the corrosion rates of Mg10Gd5Al and Mg10Gd1Mn. The corrosion rates in ascending order are as follows, 1.38 mm/year for Mg10Gd1Mn, 2.14 mm/year for Mg10Gd5Al, 2.51 mm/year for Mg10Gd5Ga, 2.68 mm/year Mg10Gd5Y and 4.29 mm/year for Mg10Gd5Zn (Table 4.13). These results follow the same tendency as the hydrogen evolution and weight loss measurements (Figure 4.42). The higher corrosion rates in the ternary alloys result from the larger volume fraction of secondary phases observed in Mg10Gd5Ga, Mg10Gd5Y, Mg10Gd5Zn and Mg10Gd5Al, which generate severe localized corrosion generating a faster dissolution of the matrix. Similar results were observed in the AZ91 alloy. Raman et al. [144] suggested that an increase in the volume ratio of the ß-phase and surrounding α-phase results in an increasing in the localized corrosion, generating higher corrosion rates. Mg10Gd1Mn show opposite behaviour due to the lower volume fraction of the $Mg_5(Gd,Mn)$ phase and exhibits better corrosion resistance.

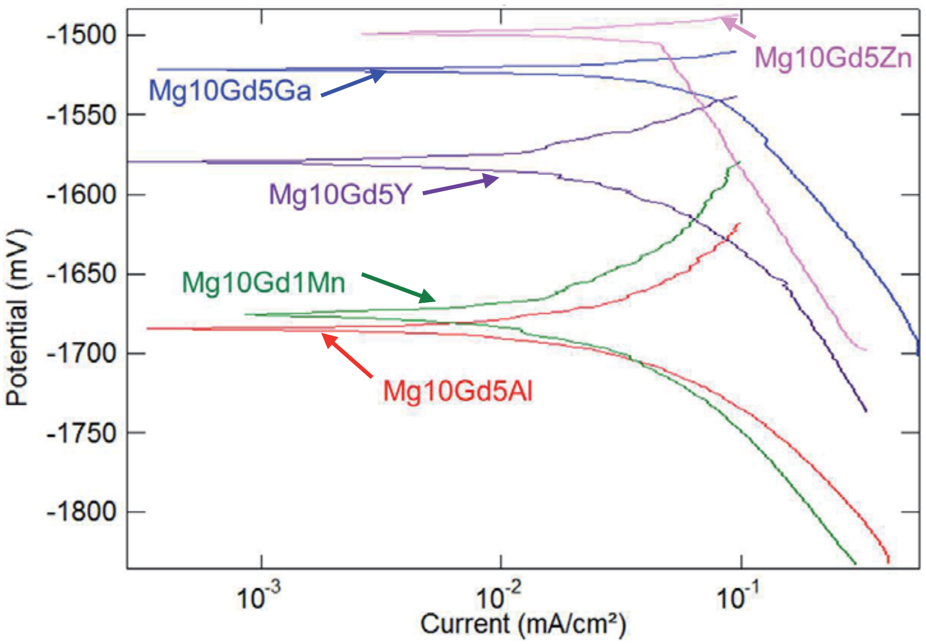

Figure 4.50 Potentiodynamic polarisation measurements of the ternary alloys in 0.5 wt.% NaCl solution

Table 4.13 Electrochemical data from the polarisation test of the ternary alloys in 0.5 wt.% NaCl solution

Alloy	E_{corr} (mV vs. Ag/AgCl)	i_{corr} (mA/cm^2)	Corrosion rate (mm/year)
Mg10Gd5Al	-1679 ± 20	0.09 ± 0.02	2.14 ± 0.7
Mg10Gd5Ga	-1520 ± 7	0.11 ± 0.01	2.51 ± 0.3
Mg10Gd1Mn	-1675 ± 14	0.06 ± 0.01	1.38 ± 0.4
Mg10Gd5Y	-1573 ± 23	0.12 ± 0.02	2.68 ± 0.5
Mg10Gd5Zn	-1486 ± 11	0.18 ± 0.06	4.29 ± 1.4

c) Electrochemical impedance spectroscopy (EIS)

- *Mg10Gd5Al*

The impedance spectra of Mg10Gd5Al alloy is shown in Figure 4.51(a),(b). At the beginning of the test two well-defined time constants are visible. The first time constant at high frequencies is related to the oxides/hydroxides formation on the metal surface and the second time constant at low frequencies is attributed to the existence of the double-layer capacitance at the metal/electrolyte interface. After 6 h immersion the time constant related to the oxide layer is shifting to middle frequencies and an inductive loop at lower frequencies indicated strong localised corrosion. From 24 h immersion, the oxide film does not offer any effective protection and the localised corrosion became more severe. For the quantitative estimation of the corrosion protection properties of the oxides/hydroxides layer, experimental impedance spectra were fitted with the equivalent circuits, the schematic representation and physical interpretation of which are shown in Figure 4.52. In the electrical equivalent circuits (EEC), R_s is the resistance of the 0.5 wt.% NaCl solution. The resistance R_{oxi} and capacitance C_{oxi} are the response of the oxide film; C_{dl} is the capacitance of the double-layer and corresponding resistance, R_{Ct}. The fitted parameters as function the immersion time are listed in Appendix A8.

- *Mg10Gd5Ga*

The impedance spectra of Mg10Gd5Ga is shown in Figure 4.51 (c),(d). The corrosion behaviour of the Mg10Gd5Ga can be described simplified with one time constant ignoring the early stage inductive loop. The resistance values of the oxide film were considerably small between $3x10^1$ – $2x10^2$ $\Omega•cm^2$ during the test, indicating that the oxide film is unstable due to the porous corrosion products and allows an active corrosion process. The impedance spectra of the Mg10Gd5Ga are simulated with the equivalent circuit shown in Figure 4.52 (b). In which R_s is the resistance of the solution, C_{oxi} is the capacitance of the oxide layer and corresponding resistance, R_{oxi}. The simulated parameters from EIS spectra are listed in Appendix A9.

- *Mg10Gd 1Mn*

The Nyquist and Bode plots for Mg10Gd1Mn alloy are shown in Figure 4.51 (e),(f). The EIS spectra for Mg10Gd1Mn were characterized by two capacitive semicircles. The high frequency semicircle corresponds to the oxide film formation on the surface and the low frequency semicircle is attributed to the double layer. The equivalent circuit applied for fitting the EIS spectra of Mg10Gd1Mn alloy is shown in Figure 4.52 (a). In which R_s, is the resistance of the electrolyte. The resistance R_{oxi} and capacitance C_{oxi} are the response of the oxide film; C_{dl} is the capacitance of the double-layer and corresponding charge transfer resistance, R_{Ct}. The fitted parameters as function of the immersion time are listed in Appendix A10. Mg10Gd1Mn has an interesting corrosion performance, which indicates importance of the formation of a protective oxide layer on the Mg alloys surface. During the test the corrosion resistance increased, due to the oxide layer thickness increase without any sign of localized corrosion. Mg10Gd1Mn has the best corrosion performance compared to the other 4 alloys. This behaviour can be related to slower and denser oxide layer formation with increasing thickness during immersion.

- *Mg10Gd5Y*

The evolution of the impedance spectra of the Mg10Gd5Y alloy with time is shown in Figure 4.51 (g),(h). In the beginning of the test, the impedance spectra showed two time constants. At high frequencies the first time constant is mainly related to the native oxide film formation on the alloy surface. At low frequencies the second time constant is attributed to the double layer. After 1 h immersion, the oxide film starts to fail indicated by the inductive loop. Latter is ignored so that the EEC is based only on one time constant related to the degradation of the oxide film.

Appendix A11 shows the fitting parameters as a function of the immersion time for Mg10Gd5Y alloy. In EIS spectra two EEC's were used to describe the corrosion process of Mg10Gd5Y. At the beginning of the test the EEC shown in Figure 4.52(a) was applicable. Figure 4.52(b) shows the EEC used after 1 h immersion until the end of the test. In the equivalent circuits, R_s is the resistance of the solution. The resistance R_{oxi} and capacitance C_{oxi} are the response of the oxide film; C_{dl} is the capacitance of the double-layer and corresponding charge transfer resistance, R_{Ct}.

- *Mg10Gd5Zn*

In Figure 4.51(i),(j) Nyquist and Bode plots of the Mg10Gd5Zn alloy are presented. At the beginning of the test the impedance spectra show two time constants. One at high frequencies (10^2-10^3 Hz) that can be attributed to the oxide film formation due to the native corrosion products formed already in air. The second time constant is associated to the corrosion process. The evolution of the corrosion process of Mg10Gd5Zn alloys was quantified by fitting the impedance spectra using the EEC shown in Figure 4.52. In the beginning of the immersion the impedance spectra can be adequately fitted by the EEC shown in Figure 4.52 (a). In which R_s, is the resistance of the electrolyte. C_{oxi}, is the capacitance and R_{oxi} is the resistance of the oxide film; C_{dl} is the capacitance of the double-layer and corresponding resistance, R_{Ct}. After 1 h immersion until the end of the test, the equivalent circuit present in Figure 4.52 (b). The corresponding fitted EIS parameters are summarised in Appendix A12.

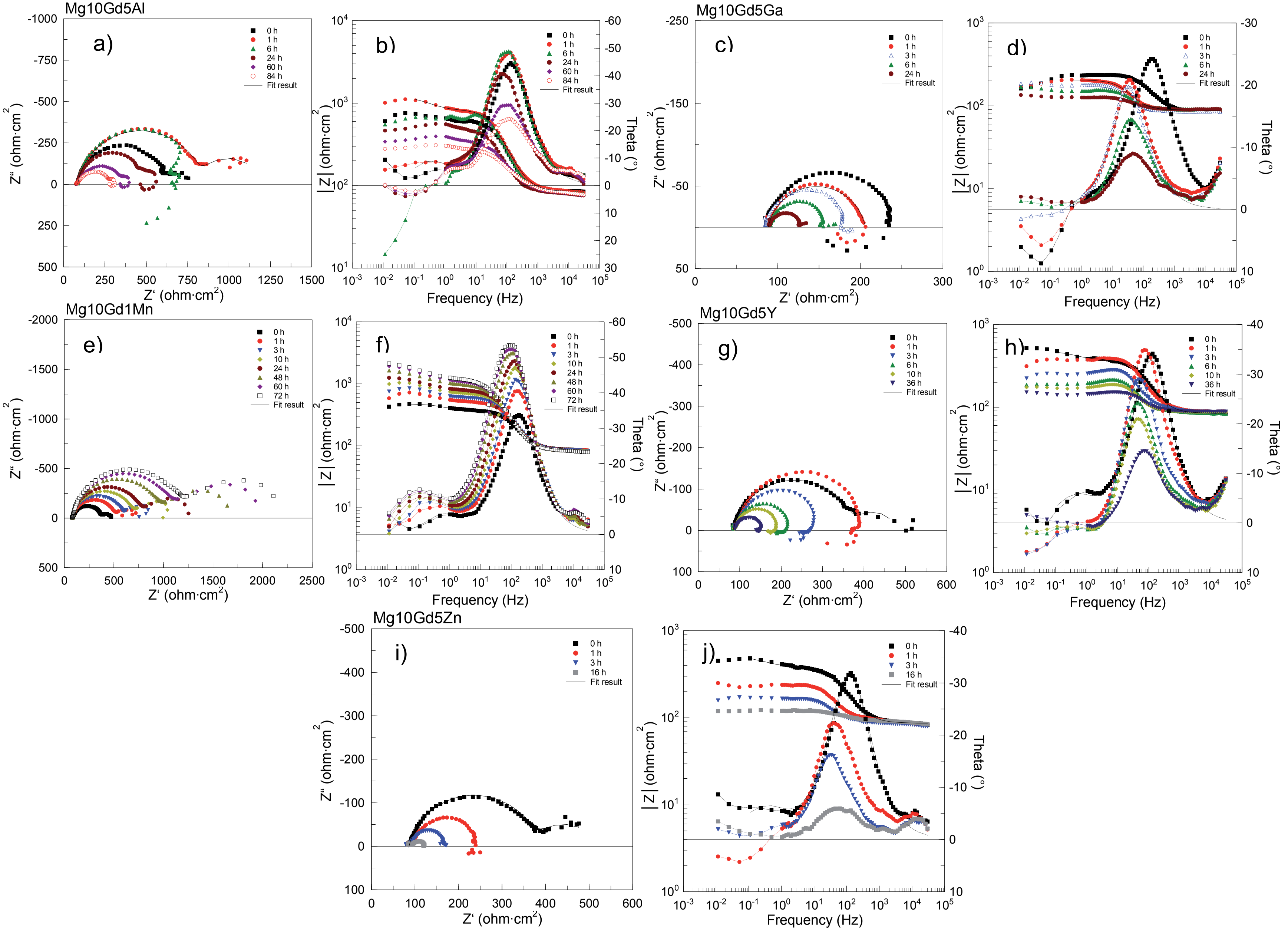

Figure 4.51 EIS spectra of ternary alloys, where (a), (b) are the Nyquist and Bode plots of Mg10Gd5Al alloy, (c),(d) are the Nyquist and Bode plots of Mg10GdGa alloy, (e), (f) are the Nyquist and Bode plots of Mg10Gd1Mn alloy, (g), (h) are the Nyquist and Bode plots of Mg10Gd5Y alloy, and (i), (j) are the Nyquist and Bode plots of Mg10Gd5Zn alloy after immersion in 0.5 wt% NaCl solution for several time.

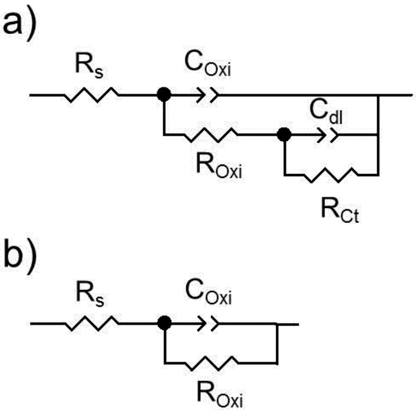

Figure 4.52 Equivalent electrical circuits used to simulate EIS spectra for the ternary alloys during different immersion time, where R_{oxi} and C_{oxi} are the resistance and capacitance of the oxide film. R_{Ct} represents the charge transfer resistance and C_{dl} is attributed to the existence of the double-layer capacitance at the metal/electrolyte interface

Figure 4.53 summarizes the determined total resistance $R_T = R_{Oxi} + R_{Ct}$ of the ternary alloys as function of immersion time. In Mg10Gd5Al alloy the resistance increased during the first 2 hours of immersion and subsequently it decreased. The native film is protective and grows in thickness at the beginning, before it starts to fail slowly. Mg10Gd5Ga, Mg10Gd5Zn and Mg10Gd5Y presented their maximum value of the corrosion resistance at the beginning of the test. Then their resistances decreased to minimum values.

The native protective film is very weak and fails easily with chloride exposure and no new film is forming. Mg10Gd1Mn presents the best corrosion resistance, its lowest value was at the beginning of the test, and then it increased over time as Mg10Gd1Mn reveal an increasingly denser or thicker oxide layer without any sign of localised corrosion.

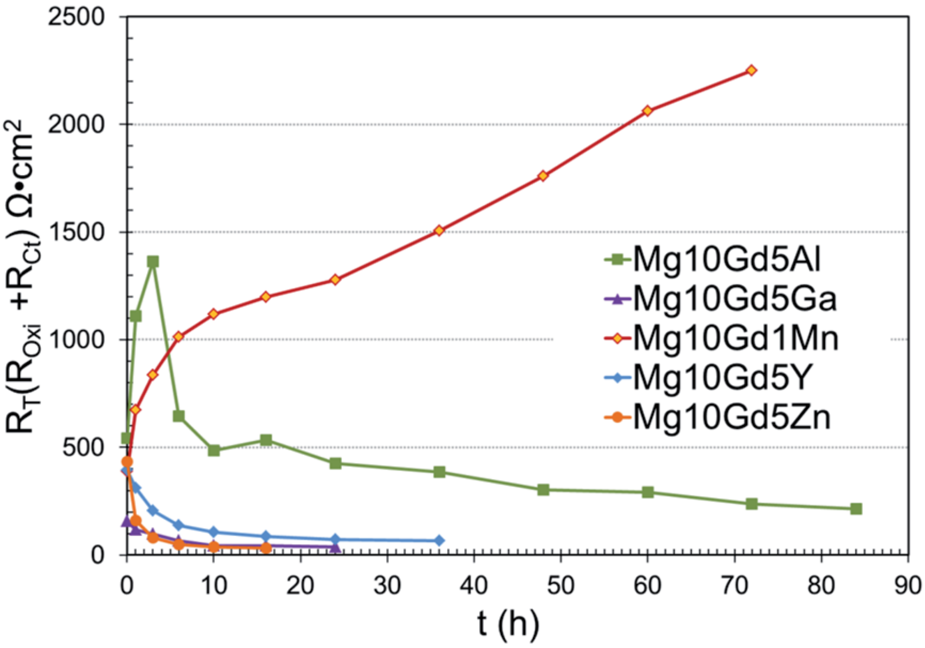

Figure 4.53 Average evolution of total resistance (RT) values obtained after fitting EIS spectra of ternary alloys during immersion time in 0.5 wt.% NaCl solution

4.4.4 Corrosion products analysis on Mg10Gd with and without Mn

4.4.4.1 Morphology and EDX composition

A detailed corrosion product analysis was performed for the Mg10Gd1Mn alloy, because this alloy provided a better corrosion resistance due to the passive film formation on the surface. The results were compared with those obtained from Mg10Gd alloy and pure Mg. The samples were immersed in 0.5 wt. % NaCl solution for 48 hours in order to observe variations in the passive/protective film. Non-destructive thickness measurements using eddy current change performed directly after the corrosion test revealed the following thicknesses for corrosion products on the surface of the specimens: pure Mg: 16 µm < Mg10Gd1Mn: 50 µm < Mg10Gd: 150 µm. Figure 4.54 illustrates the film on pure Mg surface. This film appears to be compact and dense (Figure 4.54 a) and the visible cracks are most likely a result of drying of the film after the specimens were taken out of the electrolyte (Figure 4.54 b). The adhesion of the film is nevertheless good and no flaking off can be observed. Most of the surface is covered by a flat and compact oxide layer (Figure 4.54 c) and only small regions have a needle-like appearance (Figure 4.54 d). The needles or plates are small and a compact layer seems to be located underneath. It is likely that the needles indicate accelerated dissolution and deposition of $Mg(OH)_2$/MgO while the compact modification is a result of slow dissolution and deposition.

Figure 4.55 shows the corrosion products film on the Mg10Gd alloy. The adhesion of the corrosion products is poor for the Mg10Gd alloy and the first flaking off can already be observed during thickness measurements. The poor adhesion is related to the almost 10 times thicker film compared with the pure Mg. Figure 4.55 (a) shows some film remains on the surface and a more detailed view shows the surface is completely covered by very coarse needles/plates, not forming a dense and compact film (Figure 4.55 b). The dissolution is obviously too fast, so that the compact film formation is suppressed and no protective film forms.

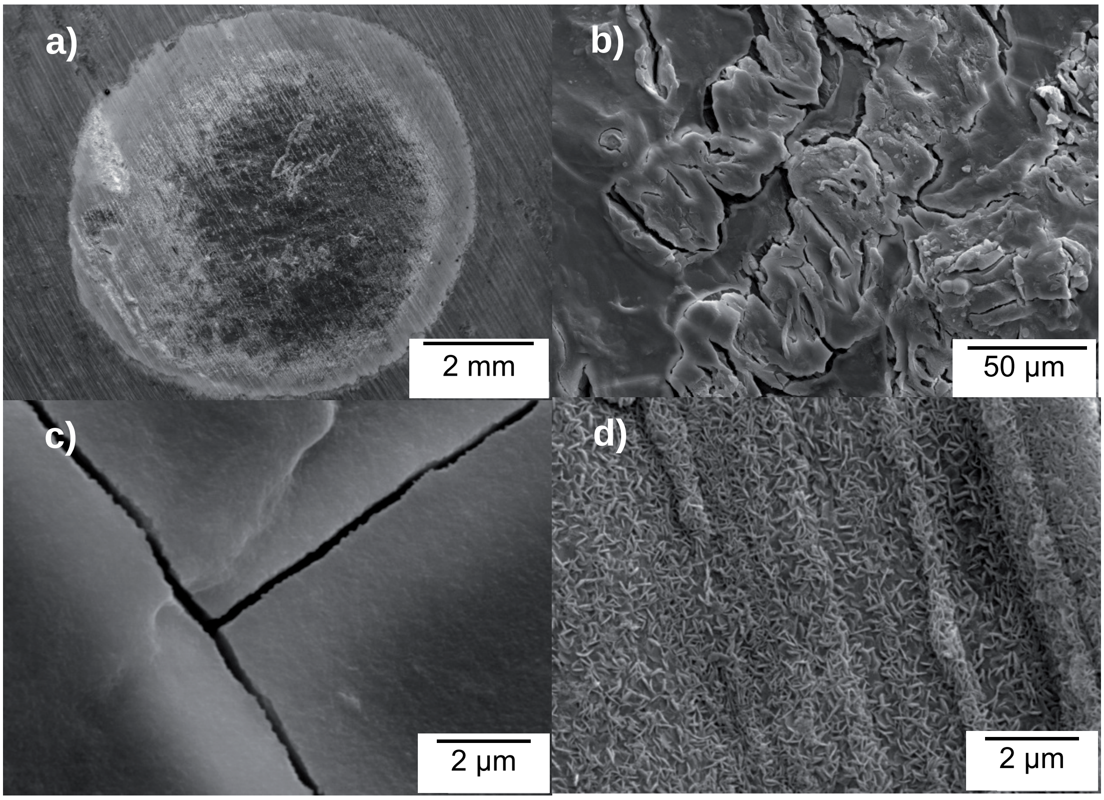

Figure 4.54 SEM micrographs of corrosion products film morphology on pure Mg surface: a) at lower magnifications, b), c) higher magnifications of the film and d) showing regions with needle-shaped corrosion products

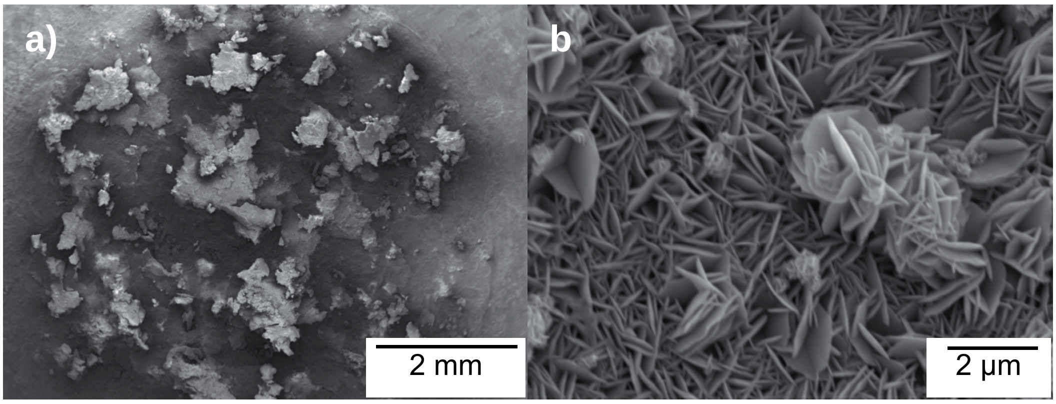

Figure 4.55 SEM micrographs of corrosion products film morphology on Mg10Gd surface: a) lower magnifications of the film and b) higher magnifications showing regions with needle-shaped corrosion products

If manganese is added to Mg10Gd, the dissolution rate is reduced and although the film is still thicker compared with pure Mg, it still has reasonable adhesion to the substrate (Figure 4.56 a). Due to the greater thickness, cracking is more severe and some flaking off can be observed (Figure 4.56 b). However, similar to pure Mg most of the film is compact (Figure 4.56 c) and in regions of higher dissolution needles are observed which have similar size to those observed on pure Mg (Figure 4.56 d). A compact film is visible underneath it EIS measurements have shown that this film is compact and protective in the electrolyte, and thus the cracks should form during drying.

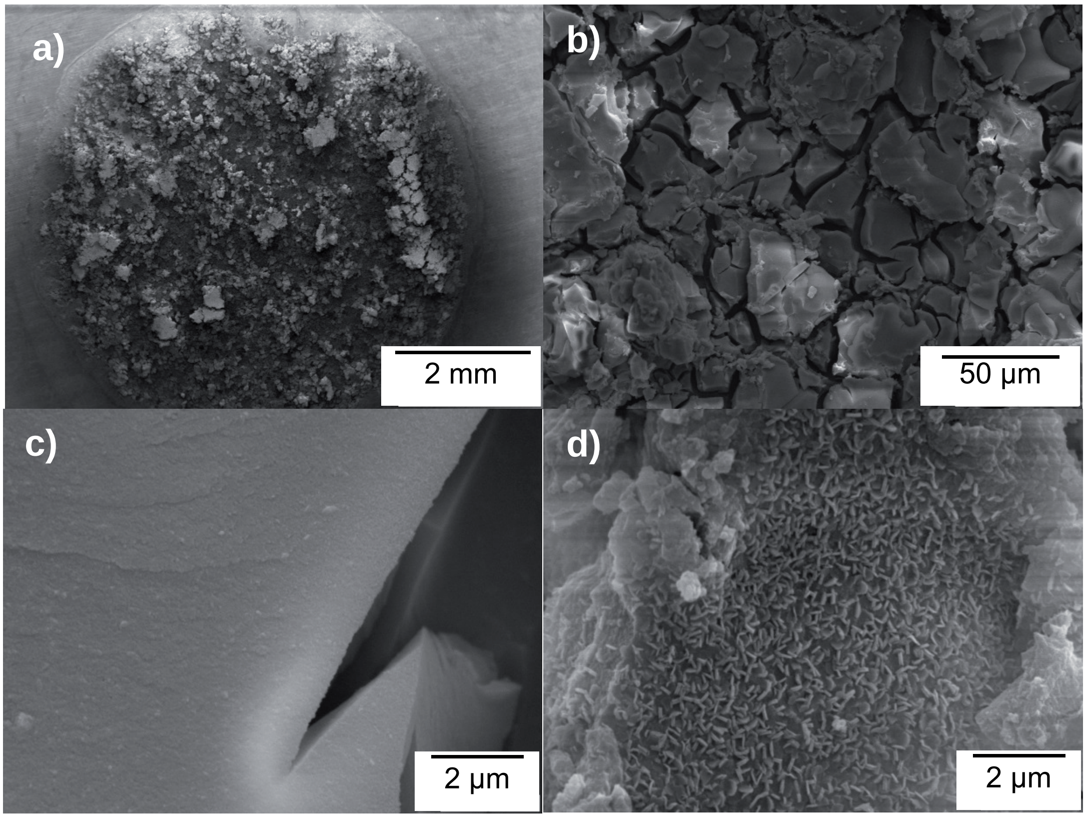

Figure 4.56 SEM micrographs of corrosion products film morphology on Mg10Gd1Mn surface: a) at lower magnifications, b), c) higher magnifications of the film and d) showing regions with needle-shaped corrosion products

The composition of the various films was determined by EDX analysis (Table 4.14). The film on pure Mg is composed of MgO/Mg$(OH)_2$ with probably some fraction of $MgCO_3$. The carbonate form from CO_2 dissolved in the aqueous electrolyte. The film on Mg10Gd has a very similar composition and Gd is not concentrated in the top corrosion product layer. Mg dominates in forming the film, indicating that it dissolves faster than the Gd which may remain in the alloy or at the interface with the corrosion product film. The carbonate fraction appears to be reduced in Mg10Gd. Adding 1 wt% of manganese completely changes the behaviour described above. There is an enrichment of Gd and Mn in the passive film, indicating that Mg dissolves slower and dissolution of Gd (intermetallics) is enhanced. However, the main components are still MgO/Mg$(OH)_2$, with an increased carbonate content (carbon concentration increases as well). From the EDX result one can speculate as to whether the Gd and Mn detected are responsible for the increased carbonate fraction or if they contribute to the oxide/hydroxide fraction.

Table 4.14 Composition of the surface oxide layer on pure Mg, Mg10Gd and Mg10Gd1Mn determined by EDX analysis

Element/Alloy	Mg (at. %)	Gd (at. %)	O (at.%)	C (at. %)	Mn (at.%)
Mg pure	31	-	53	15	-
Mg10Gd	27 - 28	0.1 - 0.2	54 - 60	10 - 11	-
Mg10GdMn	16 - 29	3 - 8	47 - 52	17 - 20	1 - 1.5

4.4.4.2 X-Ray Photoelectron Spectroscopy (XPS) characterization of the corrosion products

X-ray diffraction (XRD) and EDS give global information about the structure and phase composition; x-ray photoelectron spectroscopy (XPS) offers more detailed information about the surface and its chemical state. Because XPS is a very surface sensitive technique measuring only 5 nm in depth all absorbed molecules from the environment, like CO_2, will be detected in the surface. Therefore only after removing some nanometers of the surface by etching, the real composition could be identified.

a) Immersion in water

Figure 4.57 shows depth profiling of pure Mg, Mg10Gd and Mg10Gd1Mn samples after immersion in deionised water. The thickness of the pure Mg and Mg10Gd films formed in deionised water were thinner compared to the one observed on Mg10Gd1Mn (Figure 4.57 a, b). The oxygen concentration in Mg10Gd1Mn film decreased until 35 at.% after 9000 s etching (Figure 4.57 c) compared to 18 at.% and 9 at.% for pure Mg and Mg10Gd layers, respectively. Moreover some Gd content was observed in the layers formed on Mg10Gd and Mg10Gd1Mn surfaces with concentrations around 3 at. % and 2 at.% Gd respectively. Mn traces (~ 0.1 at.%) were visible in Mg10Gd1Mn sample. Based on depth regions spectra for pure Mg (Figure 4.58), the corrosion products on pure Mg surface consist mainly of $MgO/Mg(OH)_2$.

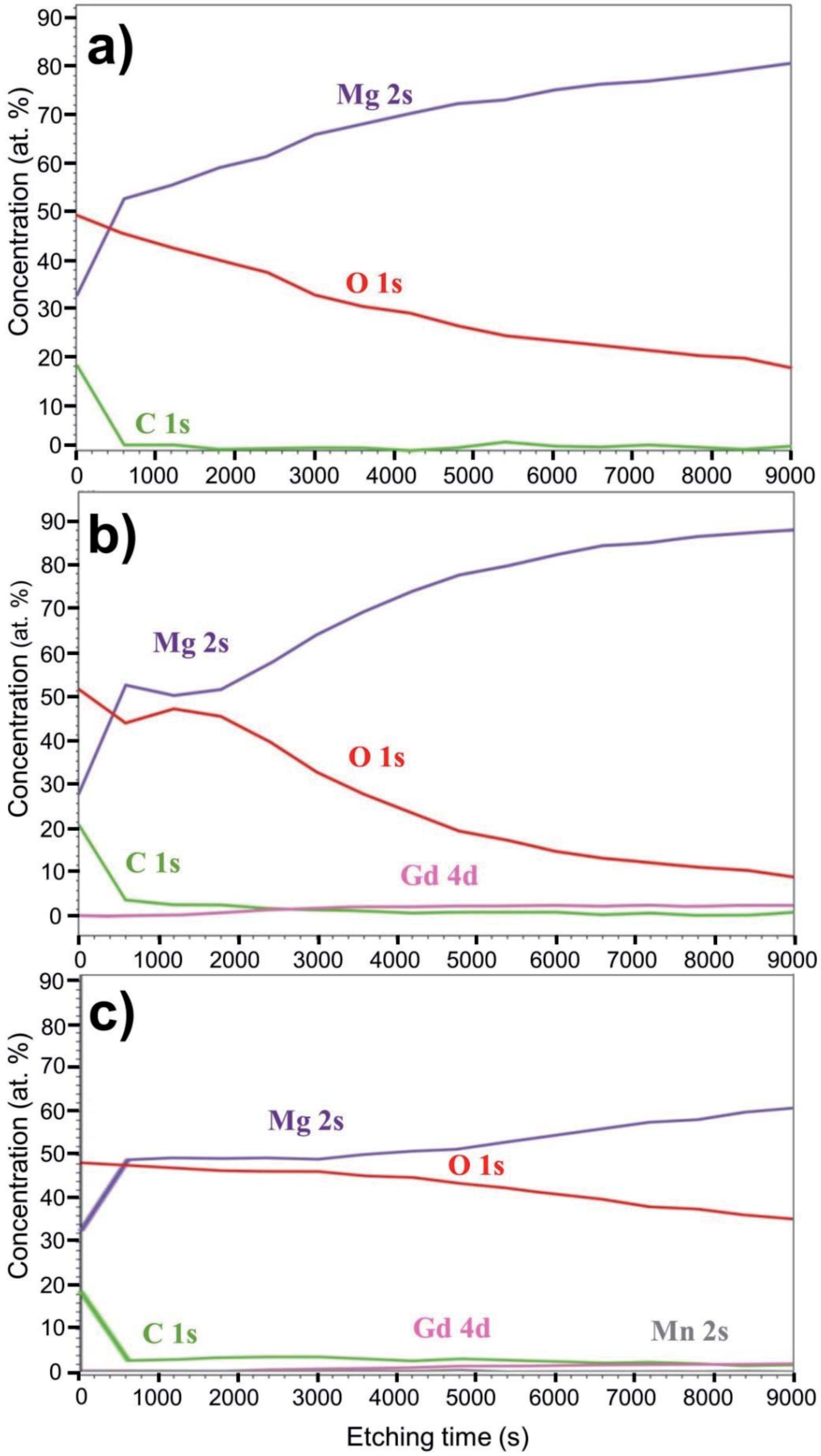

Figure 4.57 XPS depth profiling of a) pure Mg, b) Mg10Gd and c) Mg10Gd1Mn samples after immersion test in deionised water

Figure 4.58(a) shows the corresponding peaks in the profiled regions of magnesium, oxygen and carbon, after being etched these peaks shifted due to the detection of oxides, hydroxides and carbonates of magnesium subsequently (see Figure 4.58 b). This analysis also showed the existence of carbon, but with very low concentration in the film, which can be determined only in the first nanometers, due to surface contamination by CO_2 from the environment.

a) before etching

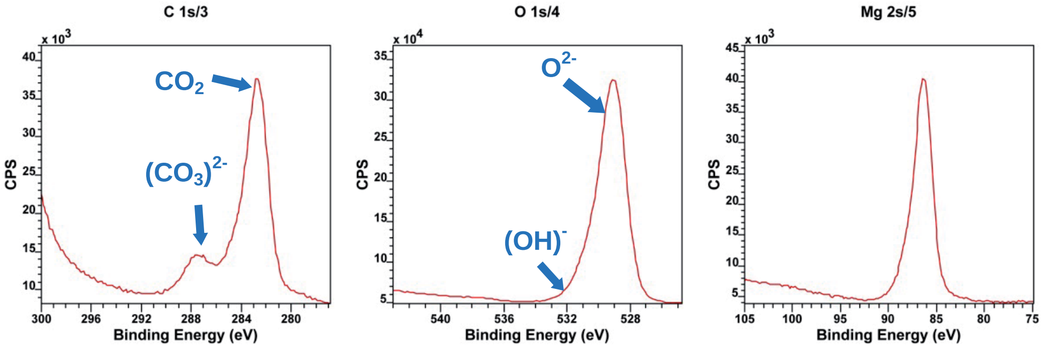

b) after etching

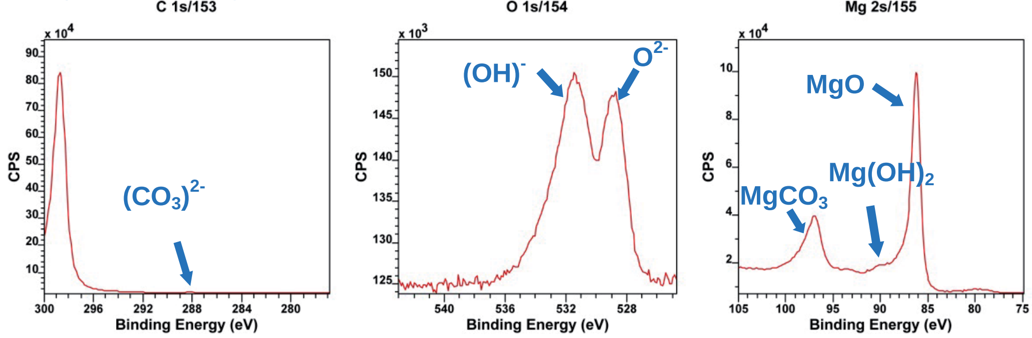

Figure 4.58 XPS depth regions of pure Mg samples, after immersion test in deionised water, (a) before and (b) after etching

Figure 4.59 shows the composition of the layer formed on Mg10Gd alloy surface after being immersed to deionised water. Before etching only contamination from CO_2 and carbonate formation could be observed, which is similar to magnesium. After etching in the oxygen region a peak related to oxide and a small protuberance approximately at 532 eV, due to the formation of a second peak generated from hydroxide can be seen. In the gadolinium region there is no well-defined peak because the concentration in the first nanometers is extremely low (Figure 4.59 a). After etching the following changes were observed: in the oxygen region the peaks related to oxides and hydroxides do not separate. Widening of the peaks is observed, and a possible explanation might be the contribution of oxides and hydroxides not only from magnesium but also from gadolinium. This assertion is based on the two peaks in the region of gadolinium, which were identified as $Gd(OH)_3$ with binding energy line of Gd at 140.97 eV and Gd_2O_3 with binding energy line at 148.10 eV (Figure 4.59 b) according to Wandelt et al. [178]

a) before etching

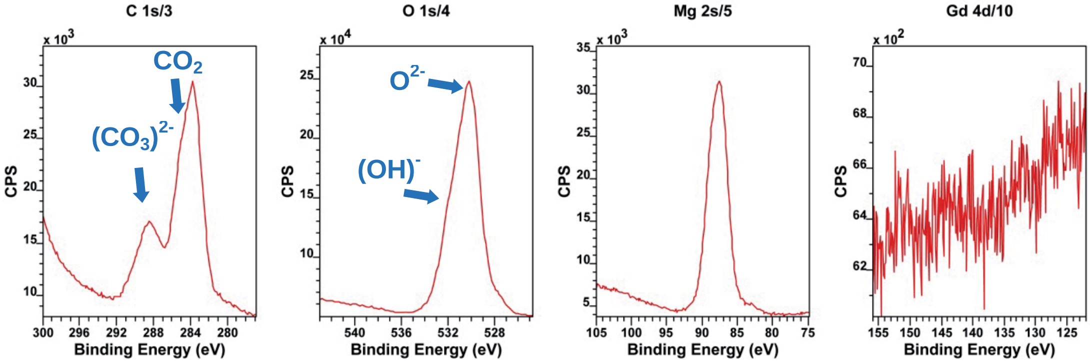

b) after etching

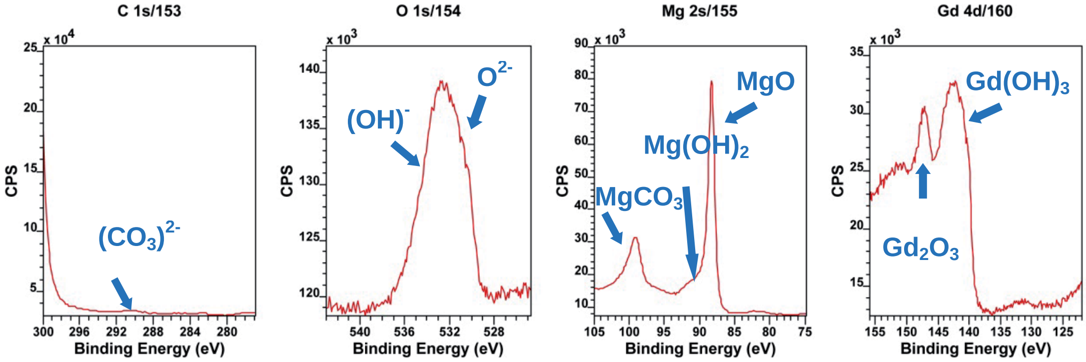

Figure 4.59 XPS depth regions of Mg10Gd samples after immersion test in deionised water, (a) before and (b) after etching

The composition of the layer formed on Mg10Gd1Mn alloy surface after being immersed in deionised water is depicted in Figure 4.60. The regions of carbon, oxygen, magnesium, manganese and gadolinium before etching are shown in Figure 4.60 (a) indicating that the layer could be composed of magnesium oxides, hydroxides and carbonates, one or more manganese oxides, as well as gadolinium oxides and hydroxides. After etching a peak appeared in the magnesium region indicating no clear separation of the magnesium oxides and hydroxides (Figure 4.60 b). Nevertheless in the gadolinium region, two peaks were observed related to gadolinium oxides and hydroxides. While in the oxygen region, the peak remained well define.

a) before etching

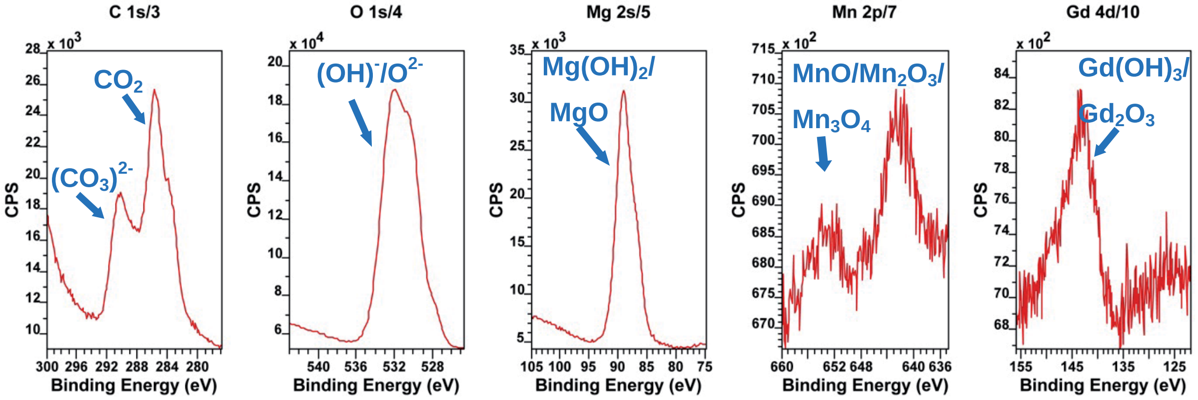

b) after etching

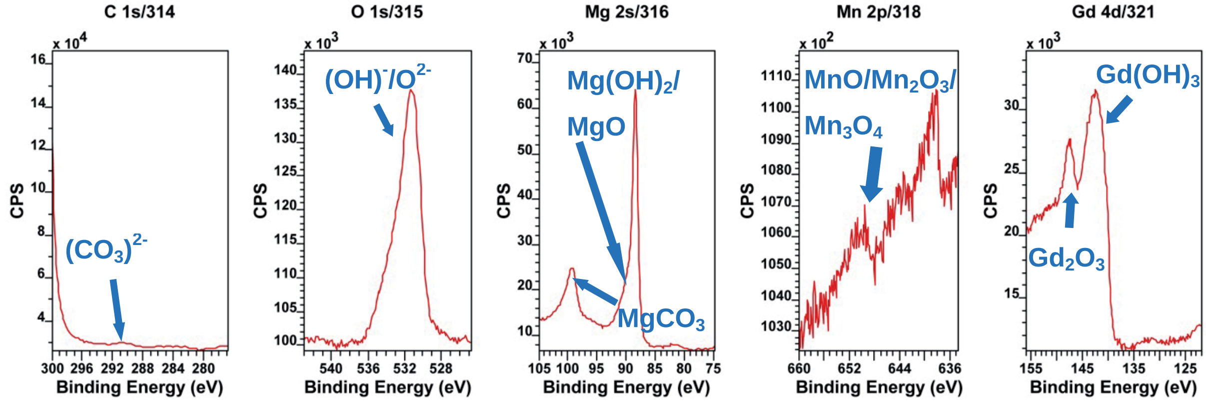

Figure 4.60 XPS depth regions of Mg10Gd1Mn samples after immersion test in deionised water, (a) before and (b) after etching

b) Immersion in 0.5 wt.% NaCl solution

The corrosion layers were also generated after immersion in 0.5 wt.% NaCl solution to compare their features to those obtained in deionised water. Figure 4.61 shows depth profiling of pure Mg, Mg10Gd and Mg10Gd1Mn samples after immersion test. The three samples showed similar composition of oxygen of approximately 42 at.% after 16000 s etching. The concentration of gadolinium in Mg10Gd alloy surface was lower than 1 at. % (see Figure 4.61 b) while in Mg10Gd1Mn alloy the increase of Gd concentration after 7000 s etching time is significant (> 4 at.%). It demonstrates an enrichment of Gd in the layer compared to the Mg10Gd layer and the Mn addition might be the reason of this change (Figure 4.61 c). Similar RE enrichment in a corrosion layer was observed when Al was added to Mg alloys [130]. The curves show some carbon in the films, due to surface contamination by CO_2 from the environment, but as etching time progresses this amount of carbon decreased in the film and the remaining amount of C might be contributed to CO_3^{2-}. In addition the presence of chlorine and sodium were also detected. This might be caused by NaCl solution residues in the film.

The composition of the corrosion product layers on pure Mg after immersion is shown in Figure 4.62. Before etching, the corresponding peaks of CO_2, $(CO_3)^{2-}$, $MgO/Mg(OH)_2$ and O^{2-}, $(OH)^-$

were observed (see Figure 4.62 a). After etching, the peaks in the carbon region disappeared while the peaks in the region of magnesium and oxygen become completely visible, indicating that the passive/protective layer is mainly formed by $MgO/Mg(OH)_2$ with some traces of $MgCO_3$ (Figure 4.62 b). The existing peaks in the sodium and chlorine regions indicated the residues from the NaCl solution as mentioned before. On the other hand the composition of the layer formed on Mg10Gd alloy surface shows two peaks in the gadolinium region before etching. These were generated from hydroxides and oxides. Also in the carbon region two contributions of CO_2 and $(CO_3)^{2-}$ were observed (Figure 4.63 a). After etching (see Figure 4.63 b) there is no separation of oxides and hydroxides in the magnesium peak, therefore both layers were overlapping. In the region of Gd, there is broadening of the peak, this indicate contributions not only of oxides and hydroxides of magnesium but also of Gd oxides and hydroxides. The sodium and chloride peaks remain unchanged indicating the existence of traces from NaCl solution even in greater depth.

Figure 4.64 shows the film composition formed on Mg10Gd1Mn after immersion in NaCl solution. Before etching in the magnesium region a thin peak was observed; this is related to the magnesium oxides. While in the manganese region peaks attributed to manganese oxides were visible and well defined. Similar behaviour was observed for the gadolinium oxides/hydroxides peaks (Figure 4.64 a)

After etching, a clear separation of peaks attributed to magnesium oxides/hydroxides and magnesium carbonates can be seen in the magnesium region (Figure 4.64 b). This can be confirmed in the oxygen and carbon regions. As in all samples immersed in a NaCl solution, there are some traces of sodium and chloride on the surface, due to residues of the solution. Nevertheless an important feature was observed for this layer, when the gadolinium and manganese were present, the passive film was composed of two layers, the outer layer consisting mainly of manganese oxides with gadolinium oxides/hydroxides. The inner layer is formed by magnesium oxide and hydroxide with traces of magnesium carbonate.

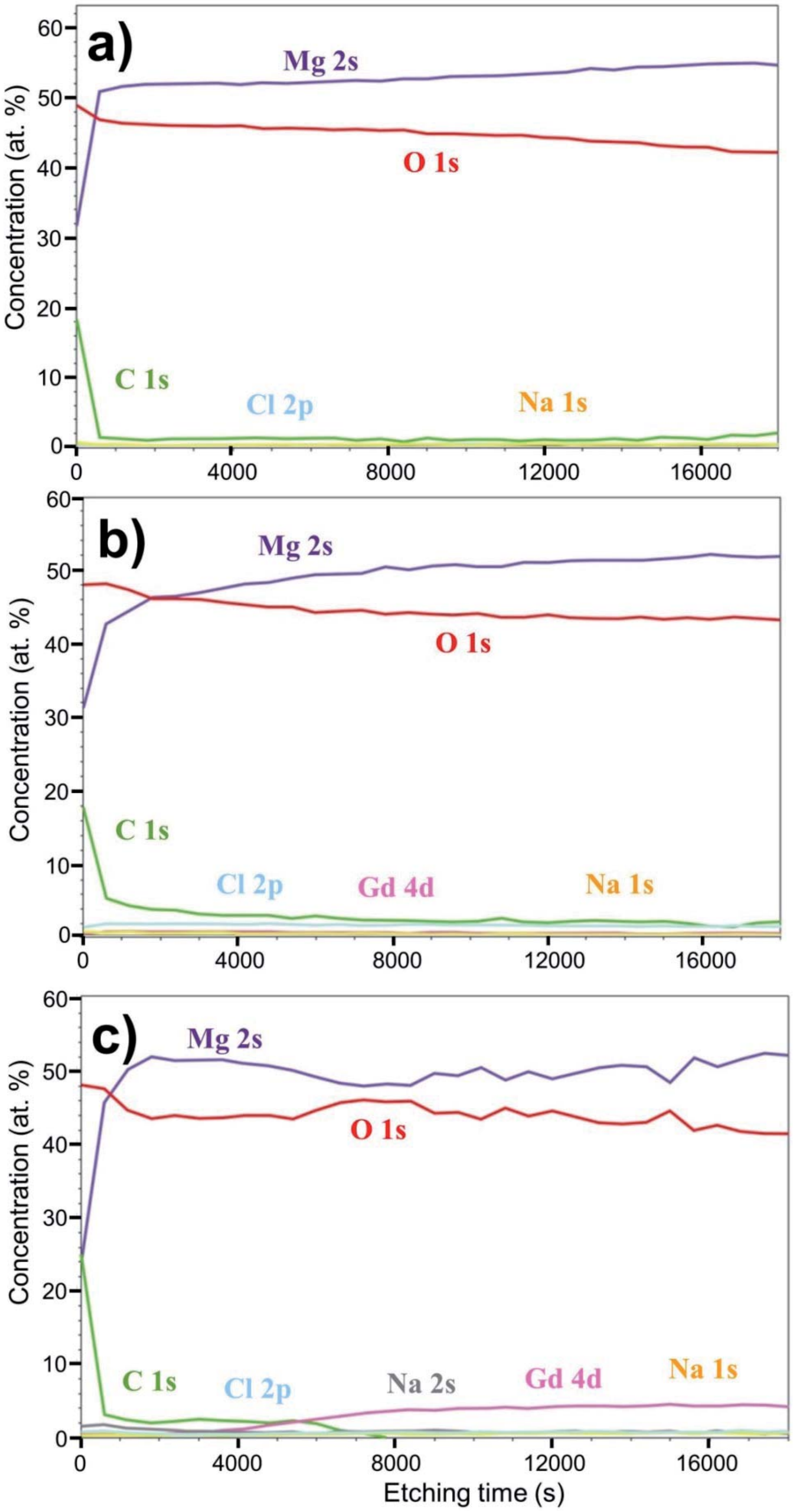

Figure 4.61 XPS depth profiling of a) pure Mg, b) Mg10Gd and c) Mg10Gd1Mn samples after immersion test in 0.5 wt.% NaCl

a) before etching

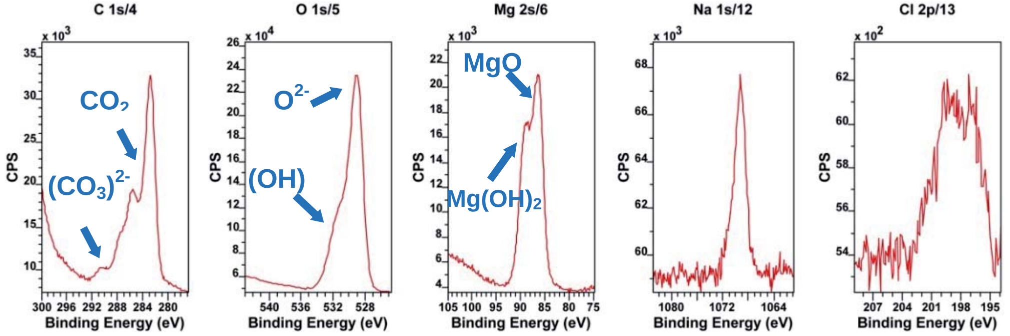

b) after etching

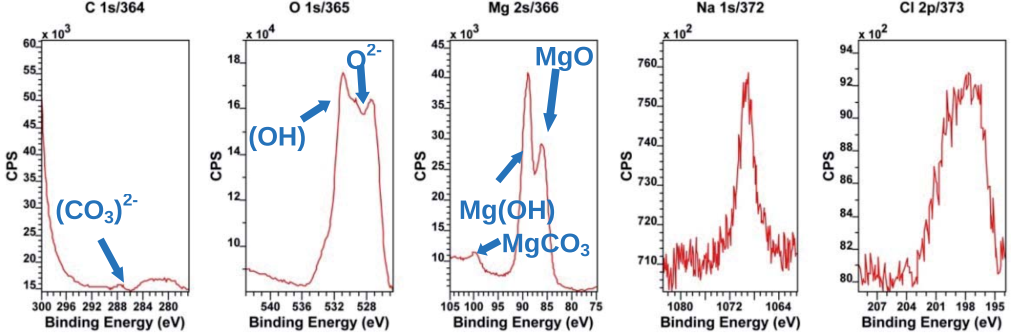

Figure 4.62 XPS depth regions of pure Mg samples after immersion test in 0.5 wt.% NaCl solution, (a) before and (b) after etching

a) before etching

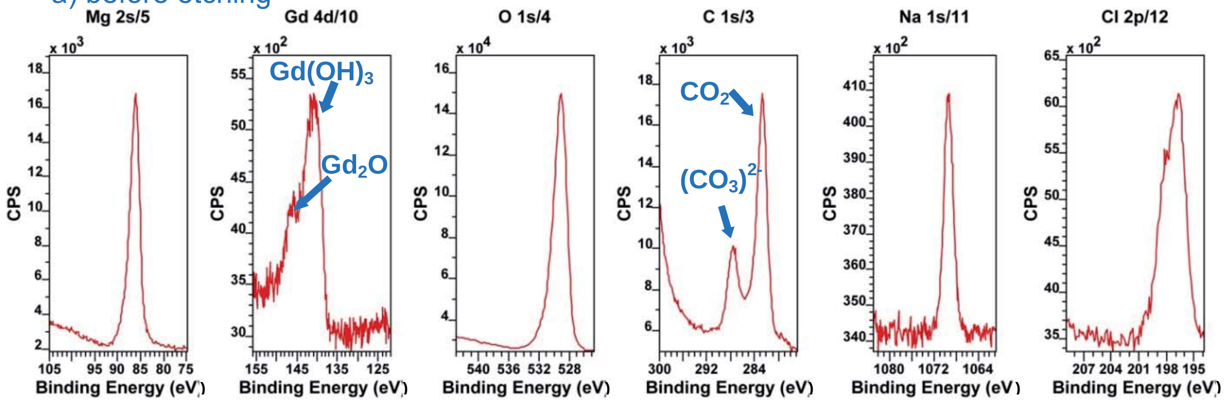

b) after etching

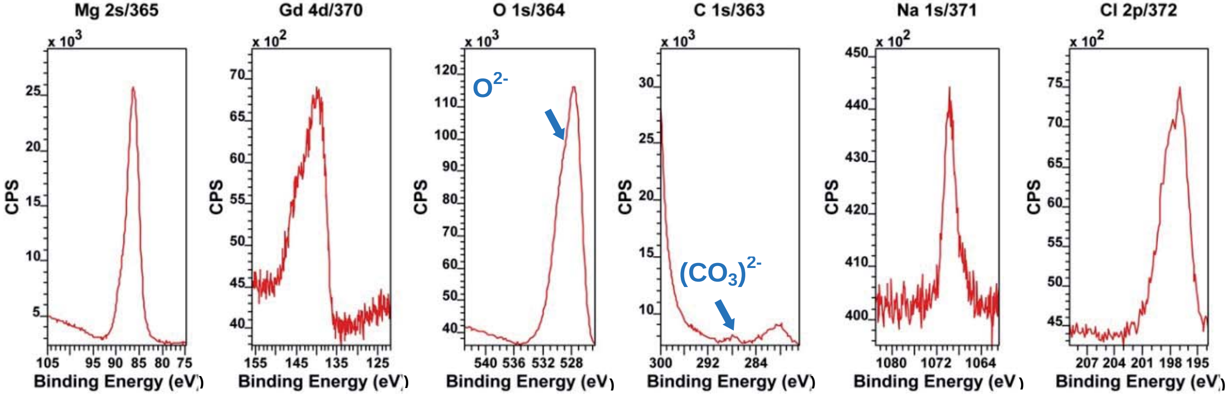

Figure 4.63 XPS depth regions of Mg10Gd samples after immersion test in 0.5 wt.% NaCl solution, (a) before and (b) after etching

a) before etching

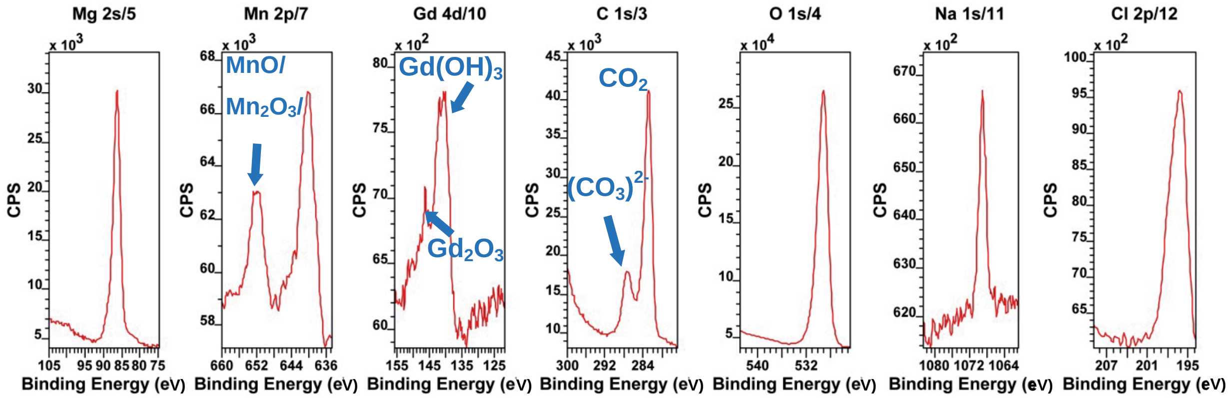

b) after etching

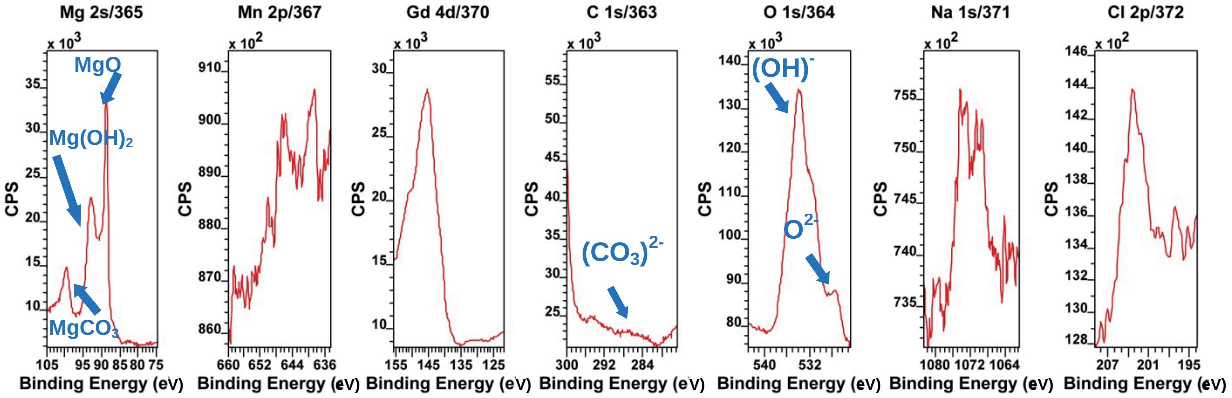

Figure 4.64 XPS depth regions of Mg10Gd1Mn samples after immersion test in 0.5 wt.% NaCl solution, (a) before and (b) after etching

4.5 Proof of concept

The results of the current studies suggested that a Gd content of 10wt.% causes some problems for the corrosion properties which might be prevent by a reduced Gd content. At the higher concentrations Mg_5Gd and GdH_2 were observed and they were identified as starting points for corrosion attack. To prevent this a reduced Gd content can be beneficial and in order to reduce those negative effects of Gd additions, Mg5Gd1Mn alloy was casted to check if lower concentrations than 10 wt.% Gd (with the same amount of Mn addition) offer even better corrosion resistance in chloride ions containing solutions as predicted. Figure 4.65 shows the impedance at 0.01 Hz frequency of Mg5Gd1Mn alloy in a long term immersion test in 0.5 wt.% NaCl solution. The impedance values increase with the exposure time and after 500 h immersion the impedance remained constant and much higher than Mg10Gd1Mn alloy (see Figure 4.51 e, f). It is obvious that Mg5Gd1Mn alloy reveals a more stable passive film formation compared to the passive film formed on Mg10Gd1Mn alloy due to a lower volume fraction of Mg_5Gd phase precipitation and possibly minimal GdH_2 formation causing less galvanic driven corrosion and weakening of the passive film. In order to know more about the corrosion behaviour of this alloy further investigations are suggested

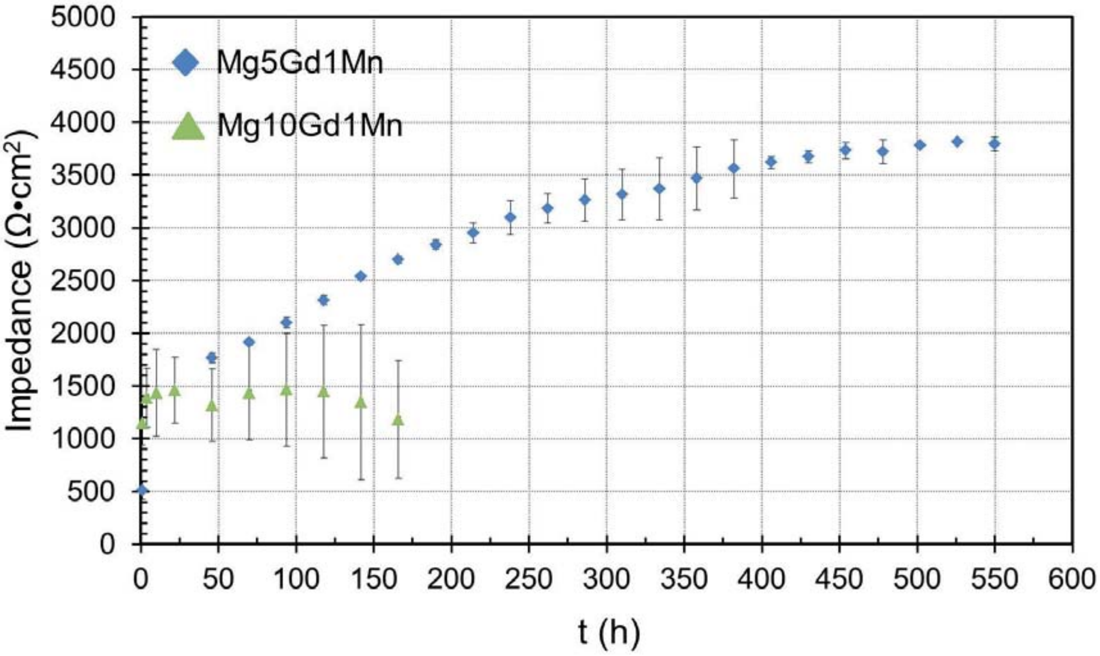

Figure 4.65 Impedance values at 0.01Hz as function of immersion time. Comparison of Mg5Gd1Mn and Mg10Gd1Mn alloys in 0.5 wt. % NaCl solution

5. Discussion

5.1 Pure metals selection

Generally RE elements are extracted as a mixture of rare earth elements with various compositions; most common is misch-metal, rich in Ce, followed by La, with smaller amounts of Nd, sometimes Pr and Y [152]. It is generally assumed that RE additions behave in a similar manner when alloyed with Mg (in part as evidenced by the use of symbol E to denote all rare earth elements in the alloy nomenclature) [15]. For this study, firstly the corrosion properties of each element in RE group were determined. Secondly, it was investigated which RE elements could be used to enhance the corrosion resistance of Mg-RE alloys. Different aspects of RE elements were important for the selection, the purity, solid solubility in Mg and the corrosion behaviour of the Mg-RE-intermetallic phase if solubility is exceeded. The RE elements have a commercial purity of 99 wt. % (see Table 3.1) and a large range of solid solubilities depending on the RE (see section 4.1 Evaluation of the corrosion behaviour of pure metals).

5.1.1 Electrochemical properties

There are only few investigations of the electrochemical properties of rare earths. However it is known that rare earth elements are among the most electrochemically active metals, with the standard potentials for RE/RE^{3+} systems between -2.6 to -2.0 V(SHE) in aqueous solutions [25, 27]. These values are outside the region of water. Accordingly, the cathodic reduction reaction for RE metals in aqueous solution is hydrogen evolution from water reduction (15), the anodic oxidation reaction is the oxidation of RE metal to RE^{3+} (16) and formation of RE(OH)$_3$ (17), as described in the following reactions [26]:

$$RE \rightarrow RE^{3+} + 3e^- \qquad (anodic\ partial\ reaction) \tag{15}$$

$$2H_2O + 2e^- \rightarrow H_2 + 2OH^- \qquad (cathodic\ partial\ reaction) \tag{16}$$

$$2RE + 6H_2O \rightarrow 2RE(OH)_2 + 3H_2 \qquad (overall\ reaction) \tag{17}$$

At the beginning of the OCP measurements the potentials of all pure metals were more active as shown in Table 5.1 After 2 h immersion in 0.5 wt.% NaCl solution, RE elements show relatively less active potential values compared with pure Mg. Nevertheless some potential fluctuations were observed indicating that the passive layer is not very stable and some electrolyte could penetrate the passive layer due to formation of defects as pores or cracks and react with the metal (see Figure 4.1). This behaviour is attributed to the oxide film formation, which act as protective layer. Lee and Greene [28, 29] suggested that RE-oxides have protective properties whereas hydroxides (form on the surface in the presence of humidity in the air) do not protect the surface of the RE- metal against further corrosion attack. Bala et al. [27] found that Nd forms an oxide layer on the surface after 10 h exposure in humid air containing 3 mgdm^{-3} SO_2 at 40°C. At the beginning, the corrosion rate was 3-4 times greater because this long initiation period was necessary to form a thick and compact oxide layer. Zhao et al.[26] indicate that the corrosion of RE metals is almost spontaneous with the dissolution of metals, without forming a passive layer on the metal surface in acidic or neutral solutions. $RE(OH)_3$ form steadily only in alkaline solution (pH > 9). They also found that the nature of surface layer depends on the electron configurations of the metal and the type of oxide. Thus the metallic ions are stable when the outmost orbit is completely full or half-full. Last conditions are associated with higher melting points of RE and the enthalpy of formation with oxygen (ΔH_f).

Table 5.2 summarizes the physicochemical properties of four RE metals. Yttrium oxides are chemically more stable than the other RE metals, while Nd oxides are the least stable. Gd3^{+} is half-full but its melting point and (ΔH_f) are lower compared to Dy. This indicate that based on ΔH_f, melting temperature and electron configuration, the best protective oxide layer forms on Y, Dy and Gd.

The potentiodynamic polarisation data reveal that the RE elements have corrosion potentials values less active than Mg (Table 5.3). This is consistent with the findings from Birbilis et al. [15] that the RE are able to ennoble their own Ecorr potential. Gd and Dy show a passive behaviour, indicating that at least these elements are more resistant to solutions which contain Cl^- ions, which is also reflected in the lower corrosion rate values. It is likely that native oxide layers survive the 30 min OCP measurement before polarisation. In contrast Zhao et al. [26] found that RE metals lack of passivation feature and their surface oxide layers are easily broken in aqueous solution.

Based on potentiodynamic polarisation measurements, elements such as Ce, Nd and La show electrochemical behaviour similar to Mg and their relatively low solid solubility in Mg this allows microstructure modifications. Yttrium showed similarities with the electrochemical behaviour of Mg and together with gadolinium offer extensive solid solubility in Mg, which could lead to enhance corrosion resistance.

Summarising, it is not possible to decide from the own screening experiments and literature which of the RE elements are the most suitable for alloying with Mg to obtain improved corrosion resistance.

Table 5.1 Electrochemical data from open circuit potential (OCP) measurements of pure metals in 0.5 wt.% NaCl solution

Element	OCP_{start} (mV vs. Ag/AgCl)	OCP_{final} (mV vs. Ag/AgCl) after 2 h
Ce	-1668 ± 2	-1454 ± 2
Dy	-1517 ± 1	-1360 ± 2
Gd	-1578 ± 3	-1430 ± 7
La	-1645 ± 2.	-1333 ± 3
Nd	-1637 ± 2	-1370 ± 2
Y	-1641 ± 5	-1508 ± 9
Mg	-1645 ± 4	-1574 ± 5

Table 5.2 Oxide structures of some RE metals and corresponding physicochemical properties [26, 179-182]

Element	Electron configuration	Atomic number	Oxide type	Oxide structure	Melting point (°C)	ΔH_f of oxide (kJ/mol)	Lattice parameters (nm)
Y	{Kr} $5s^24d^1$	39	Y_2O_3	cubic	1522	-1878	a=0.35687
Nd	{Xe} $6s^24f^4$	60	Nd_2O_3	hexagonal	1021	-1809	a= 0.38312 c= 0.60017
Gd	{Xe} $6s^24f^75d^1$	64	Gd_2O_3	cubic	1313	-1815	a= 1.080773
Dy	{Xe} $6s^24f^{10}$	66	Dy_2O_3	cubic	1413	-1869	a= 1.0672
Ce	{Xe} $6s^24f^15d^1$	58	Ce_2O_3	hexagonal	2750	-1796	a= 0.38927 c= 0.6069
La	{Xe} $6s^25d^1$	57	La_2O_3	hexagonal	2307	-1794	a= 0.03937 c= 0.6172
Mg	{Ne}$3s^2$	12	MgO	cubic	2880	-601	a= 0.42101

Table 5.3 Electrochemical data from potentiodynamic polarisation measurements of pure metals in 0.5 wt.% NaCl solution

Element	i_{corr} (mA/cm^2)	E_{corr} (mV vs. Ag/AgCl)	CR (mm/year)	Passive range (mV vs. Ag/AgCl)	E_{pit} (mV vs. Ag/AgCl)
Ce	0.13 ± 0.05	-1351 ± 58	3.00 ± 1.4	-	-
Dy	$8.3\text{x}10^{-3}$ ± 0.004	-1110 ± 4	0.17 ± 0.08	-987 to -809	-809
Gd	0.027 ± 0.02	-1290 ± 77	0.59 ± 0.4	-1080 to -872	-861
La	0.17 ± 0.01	-1307 ± 5	4.26 ± 0.3	-	-
Nd	0.19 ± 0.003	-1350 ± 2	4.21 ± 0.06	-	-
Y	0.09 ± 0.04	-1403 ± 66	1.91 ± 0.08	-	-
Mg	$4.9\ \text{x}10^{-3}$ ± 0.003	-1580 ± 13	0.11 ± 0.08	-	-

5.2 Mg-RE-Intermetallics

5.2.1 Microstructure characterization

If the solubility of RE elements in the Mg matrix is exceeded they do form intermetallic phases with Mg. Thus to understand the galvanic effects in a Mg matrix caused by the intermetallics it is important to study their electrochemical properties. Therefore it is important to produce the intermetallics as pure and single phased. However the XRD analysis indicates mixture of Mg-RE-intermetallic phases with some α–Mg matrix remains (see Figure 4.4). This means that casting cannot guarantee a pure intermetallic phase. This consideration must be taken into account when working with as- cast intermetallic alloy compositions. The XRD patterns revealed the presence of at least two intermetallic phases, $Mg_{17}Ce_2$ and $Mg_{41}Ce_5$ for the Mg-Ce system, this is in contrast with the observations from Easton et al. [166]. They suggested, $Mg_{12}Ce$ phase is more thermodynamically stable and forms in a wide variety of casting conditions due to its good crystallographic matching with Mg which facilitate its nucleation. In this case however it is likely that $Mg_{41}Ce_5$ forms from the melt and nucleation on Mg is not necessary. However in the eutectic liquid Mg and $Mg_{12}Ce$ form due to ease of co-nucleation due to lattice matching. Even three intermetallic phases, $Mg_{12}Nd$, $Mg_{41}Nd_5$ and Mg_3Nd were identified in the Mg-Nd system. Easton et al. [166] suggested that the cooling rate plays a crucial role in the Mg-Nd system. $Mg_{12}Nd$ phases could be obtained upon slow cooling while fast cooling forces the Mg_3Nd phase formation. $Mg_{41}Nd_5$ phase only forms after heat treatment at high temperature (500°C) and long period of time. Similar reasoning as for the Mg-Ce system will apply here to explain the presence of number of intermetallics. For Mg-Gd, Mg-La and Mg-Y systems, the Mg_5Gd, $Mg_{17}La_2$ and $Mg_{24}Y_5$ intermetallic phases were identified, respectively.

Hort et al. [14] found Mg_5Gd phase by XRD in the Mg15Gd alloy in F and T6 conditions. Apps et al. [183] suggested Mg_5Gd phase as the stable intermetallic phase in the Mg-Gd system but the Mg_5RE phase was not present in Mg-Dy system. Moreover, they also considered that Mg_5RE phase is stable over a significant compositional range with the exact composition determined by the local formations conditions. For this study Mg_5RE was determined only in the Mg-Gd system. Hampl et al. [161] investigated Mg-Gd system and reported that Mg_5Gd phase was observed in the alloys with Gd contents up to 20 wt. %. Peng et al. [184] observed the Mg_5Gd phase in the as-cast Mg20Gd alloy and suggested that in this system there are few metastable phases which transform into a stable Mg_5Gd phase after heat treatment for 600s at 700° K. The Mg_3Gd phase reported by Peng et al. [185] as thermally stable in the as-cast Mg-Gd alloys with Gd contents between 10 to 35 wt.% was not observed in the current investigation.

For Mg-La system there are many phases that can form, such as $Mg_{12}La$, $Mg_{17}La_2$, Mg_3La or Mg_2La [84]. There is a debate on how these phases nucleate under given solidification conditions, or which are equilibrium and metastable phases [152]. Wang et al. [186] observed with their calculation of the cohesive energies that the structure of stability of Mg-La system is higher when La content increased and it is independent of the crystal structure. Moreover, the heat of formation calculations indicates that Mg_3La, Mg_2La and MgLa are more thermodynamically stable compared to $Mg_{12}La$, $Mg_{17}La_2$. $Mg_{17}La_2$ is more stable compared with $Mg_{12}La$ [186]. Nayeb-Hashemi et al. [187] and Gou et al. [188] indicated that $Mg_{17}La_2$ phase is stable at room temperature, compared with the $Mg_{41}La_5$ phase. Giovanni et al. [155] reported that $Mg_{17}La_2$ phase is more stable at lower temperatures compared with $Mg_{41}La_5$ phase. Berche et al. [154] suggested $Mg_{17}La_2$ phase is stable at room temperature, while $Mg_{41}La_5$ phase is stable at high temperatures. On the other hand Chia et al. [152] found that $Mg_{12}La$ phase forms in the eutectic when the La concentration increases from 0.51 to 5.07 wt.%. Similar findings were observed by Birbilis et al. [15] for additions up to 6 wt.% La. In the present work $Mg_{12}La$ was not observed and only $Mg_{17}La_2$ phase was identified, possibly due to the high concentration around 40 wt.% La.

Sudholz et al. [17] studied the Mg-Y alloys using additions up to 18 wt.% Y. For all compositions the $Mg_{24}Y_5$ phase was identified. Zhang et al. [108] also reported the presence of $Mg_{24}Y_5$ phase with three different Y concentrations in Mg-Y alloys. On the other hand Rokhlin et al. [84] reported three intermetallic phases, $Mg_{24}Y_5$, Mg_2Y and MgY phases, depending of the temperatures ranges and Y concentration. In this study only $Mg_{24}Y_5$ intermetallic phase was identified.

The microstructure characterization of the as-cast Mg-RE-intermetallics using SEM-EDX analysis was not sufficient for conclusive identification of all intermetallic phases because the Mg/RE ratios are often far from the ideal Mg/RE ratios, possibly caused by the contribution from the matrix surrounding in the point analysis when the particle size is smaller than 2 µm. Furthermore there are phases which might be related to RE hydrides. Hydrides were noted in other studies as well [169].

The XRD results after heat treatment at 540 °C for 72 h (see Figure 4.6) indicate that the homogeneity of the Mg-RE-Intermetallics phases increased for the Mg-Ce, Mg-Gd, Mg-La and MgY systems. In the Mg-Nd system, $Mg_{41}Nd_5$ and Mg_3Nd phases remained and $Mg_{12}Nd$ phase transformed to either $Mg_{41}Nd_5$ or Mg_3Nd. The α-Mg was detected at lower amounts compared with the as-cast condition. The SEM-EDX analysis corroborate that heat treatment improved the distribution of the intermetallic phases and homogenise distribution of RE in the intermetallic phases, resulting Mg/RE ratios closer to the ideal Mg/RE ratios for the Mg-RE-intermetallic phases. This shows that, the intermetallics are still not perfect and internal galvanic effects may influence the corrosion measurements. However, as the discussion above has demonstrated in real Mg alloys mixtures of intermetallics can occur as well, thus corrosion properties determined from as-cast and heat treated intermetallics may reflect even better real casting conditions than 100% perfect intermetallics.

5.2.2 Corrosion behaviour

The Mg-RE- intermetallics are significantly nobler than pure Mg during immersion in NaCl solution [15, 173]. This is visible in Figure 4.7and Figure 4.9. The OCP measurements for the as-cast Mg-RE-intermetallics and heat treated Mg-RE-intermetallics were similar. The trend of potential values of each condition remained in the same order from nobler to more active, Mg-$Gd_{intermetallics}$, $Mg\text{-}Y_{intermetallics}$, $Mg\text{-}La_{intermetallics}$, $Mg\text{-}Nd_{intermetallics}$, $Mg\text{-}Ce_{intermetallics}$. The changes in OCP of the heat treated intermetallics indicate that the heat treatment modified the distribution of the intermetallic phases but the open circuit potential did not show significant changes. OCP values tend to be slightly more active compared with those obtained from the pure elements, but there is still a difference between the intermetallics and pure Mg. From the potentiodynamic curves, Figure 4.8 and Figure 4.10, the E_{corr} values for all intermetallics shifted slightly to more active values but the corrosion rates did not follow the same trend. For example, i_{corr} of Mg-Ce intermetallic did not change after heat treatment generating the lowest corrosion rate of the intermetallics. On the other hand, i_{corr} of the Mg-Gd intermetallic reduced significantly after heat treatment and has the second lowest corrosion rate. Opposite occurs for the Mg-Nd intermetallic, its i_{corr} increased dramatically after the heat treatment. I_{corr} of Mg-La and Mg-Y intermetallics increased slightly after the heat treatment, but the latter presented the highest corrosion rate before and after heat treatment. These results are possibly affected by formation of a hydroxide layer on the surface influence by RE. Moreover, the Mg-RE- intermetallics did not display any passivity in both as-cast and heat treated conditions. This is in contrast to findings by Birbilis et al. [15] for $Mg_{12}Ce$, $Mg_{12}La$ and Mg_3Nd intermetallic phases in 0.1 M NaCl solution. In the current investigation, the five Mg-RE-intermetallics have higher corrosion rates compared to the pure Mg, suggesting that they are not able to form a protective film. When these intermetallics are evaluated separately, these compounds tend to degrade faster than Mg because they are not cathodically protected by a surrounding Mg matrix. In general the electrochemical properties (OCP, E_{corr}, i_{corr} and corrosion rate) for the Mg-RE-intermetallics are significantly affected by the specific RE element addition. As described at the beginning of this chapter, RE elements have different properties in terms of corrosion and should be analysed as individual elements in alloys to understand their nature.

5.2.3 Galvanic coupling between Mg-RE-intermetallics phases and α-Mg

Galvanic coupling measurements (see section *4.2.2.3 Galvanic coupling*) estimate the compatibility between matrix and intermetallic phases of Mg by measuring the exchange current between them in a short cut. The noblest phase would be the most detrimental to the matrix during galvanic coupling with the matrix. In the literature there is information about the intermetallic phases in the AZ and AM based Mg alloys, e.g. $Mg_{17}Al_{12}$ phase. Some studies include in situ measurements, using the micro-capillary electrochemical cell method [15] or studying the micro-galvanic activity of the intermetallic phases after immersion in the NaCl solution using scanning Kelvin probe force microscopy (SKPFM) [189-191]. However, there is no literature on galvanic measurements for these Mg-RE-intermetallics. The galvanic current was measured experimentally in this investigation using the set up described in section 3.4.3 Galvanic coupling. For a better understanding these results and the theoretical galvanic current values were estimated from polarisation curves using mixed potential theory (Figure 4.8 and Figure 4.10) are plotted in Figure 5.1, and indicate the differences between the theoretical and experimental results. These differences are affected by the homogeneity of the intermetallics in the real measurements and by the corrosion products layer formation, which is different for both measurements. In the real measurements the corrosion layer forms naturally due to the oxidation–reduction reactions between the matrix and intermetallics. This layer might be relatively compact if it is growing slowly; compared to a faster growing film under polarisation thus there can be a difference in the corrosion current. In the theoretical measurements the intermetallics and the Mg are evaluated separately and the surface changes according to the overpotential applied, generating different surfaces for each measurement. Furthermore it might be possible at the cathodic polarisation of the Mg causes hydride formation changing the condition as well.

The *negative difference effect* (NDE) affects also the i_{corr} and E_{corr} in Mg alloys, which is described in the section 2.3 Negative Difference Effect (NDE). The purity of the Mg plays and important role in the theoretical evaluation, Mg with different impurities content could generated different values of current density calculated by mixed potential theory [192]. In this study both evaluations were used to estimate the compatibility between matrix and intermetallic phases in the Mg-RE alloys. It was expected that the heat treatment will result in a decrease the galvanic current values as a more homogeneous composition and distribution of the intermetallic phases was achieved. This was observed in Mg-Gd and Mg-Y intermetallics, but not for Mg-Ce, Mg-La, Mg-Nd intermetallics. The reason is likely to be that the latter group of intermetallics still contains a mixture of intermetallic phases after heat treatment, which were identified by XRD. Such mixture of phases compensates the detrimental effects of the main phases and/or the higher volume fraction of the main phases.

For the further studies Mg-Ce, Mg-La and Mg-Gd systems were selected to understand how the addition of the RE elements affect the real amount of these intermetallics and their influence in the corrosion behaviour of the Mg-RE alloys. The selection was mainly based on the galvanic exchange currents and corrosion resistance to see if separated measurements can be used to predict corrosion performance of an alloy. The Mg-Gd intermetallics have the highest galvanic exchange current with α-Mg matrix and the intermetallics do have relative low corrosion rate in NaCl solution. Mg-Ce and Mg-La intermetallics show lower galvanic differences with respect to the Mg matrix, based on the exchange current, while Ce is forming the most stable intermetallic based on corrosion rate and La is one of the most unstable intermetallics. Thus those three systems offered interesting features for the further studies.

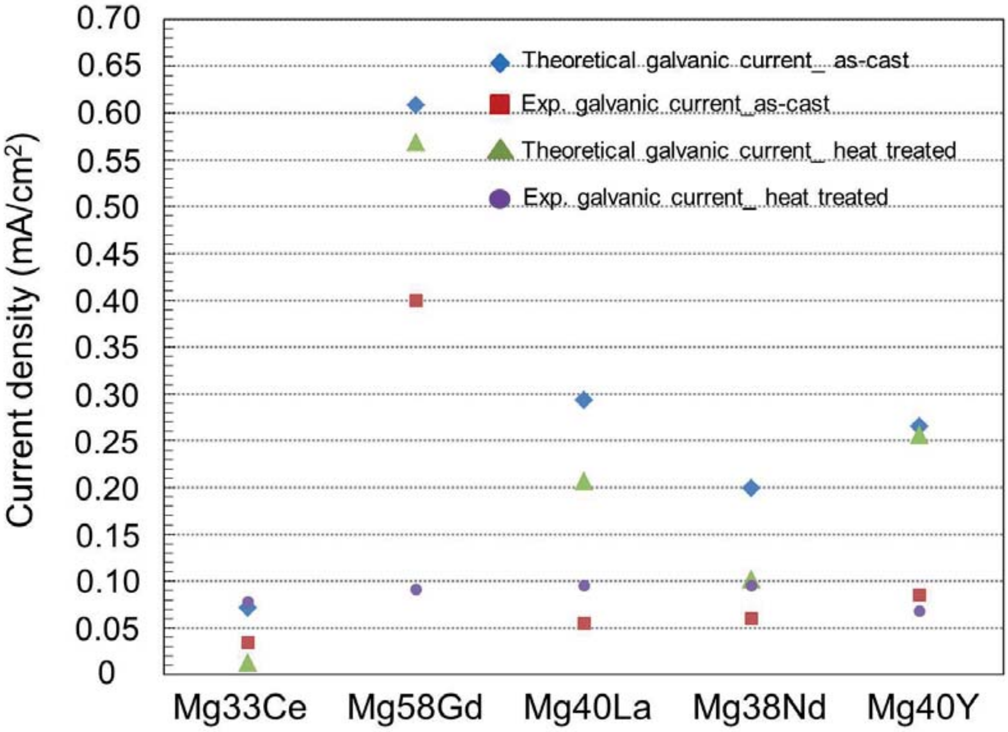

Figure 5.1 Comparison between theoretical and experimental current densities of as-cast and heat treated Mg-RE-intermetallics

5.3 Binary alloys Mg-Ce, Mg-Gd and Mg-La

5.3.1 Microstructure

The microstructures of the three binary alloys Mg-Ce, Mg-La and Mg-Gd, which are illustrated in Figure 4.12, Figure 4.13 and Figure 4.14, respectively, indicate that increased RE concentration increased the amount of the eutectic phase. Similar observations were seen by Birbilis et al. [15] for Mg-La and Mg-Ce though in this study the intermetallic phases $Mg_{17}Ce_2$ and $Mg_{17}La_2$ did not correspond with the $Mg_{12}Ce$ and $Mg_{12}La$ identified by Birbilis et al. The compositions obtained from SEM-EDS analyses of selected particles were affected by size and the contribution from the Mg matrix both being close together in the eutectic. The results from the X-ray diffraction analysis of the intermetallic phases were useful to identify intermetallics present in each Mg-RE system. These phases could be characterized using the TEM-EDX but this analysis was not performed, as it is beyond the scope of the study. The microstructure and intermetallic phase identification of Mg-Gd system was consistent with the findings of Hort et al. [14] The amount of eutectic phases decrease in the order Mg-La, Mg-Ce and Mg-Gd, due to the lower solubility of La and Ce and the higher solubility of Gd in the matrix. However especially in the Mg-Gd alloy system cubic type of precipitates were detected at the higher concentrations Peng et al. [169]

have identified them as GdH_2. They exist already after casting and can increase in number after high temperature heat treatments.

5.3.2 Corrosion behaviour

It was observed that additions of RE could ennoble the OCP value of the binary alloys [15] The change of the OCP values to more positive potentials was related to the growth of a passive layer at the surface of electrodes [18]. This was not necessarily associated with improved corrosion performance. Based on the potentiodynamic curves, the electrochemical behaviour of the Mg-Ce and Mg-La binary alloys revealed that increase in the amount of RE alloying addition systematically increased the corrosion rate of the alloy, whereas Mg-Gd binary alloys show corrosion behaviour that is relatively independent of the alloy concentrations, as seen in Figure 5.2. This is consistent with Südholz et al. [167] who reported that only alloying additions with concentrations beyond the respective solubility limits in Mg is detrimental to the corrosion resistance. Shi et al. [19] observed opposite behaviour in some as-cast Mg-RE alloys. They found that the sequence of increased corrosion rate as follows: Mg-Ce, Mg-La and Mg-Gd. The Mg-Gd alloy shows the highest corrosion rate, even when its microstructure was modified by solid solution treatment. Birbilis et al. [15] found also similar behaviour for Mg-Ce and Mg-La alloys but they did not investigate Mg-Gd alloys. On the other hand Hort et al. [14] reported similar results for all Mg-Gd alloys. This behaviour could be attributed to micro-galvanic corrosion acceleration caused by the second phase, with some phases more effective than others. Generally, Mg alloys have higher corrosion rates than pure Mg, as the typical Mg alloys are used in as-cast condition and the second phases in Mg alloys accelerate the corrosion by micro-galvanic coupling with the α-Mg matrix [19]. Thus Gd systems with the high solubility show nearly constant corrosion rates while the other two alloys show an increasing corrosion rate with increasing volume of intermetallic phase. The volume seems to be more important than the composition of the intermetallic. If one compares similar intermetallic volumes and microstructures in the different alloys e.g. Mg1Ce, Mg1La and Mg15Gd the influence of the intermetallic phase and its specific exchange current with the matrix becomes important. The best performance can be observed for the Mg1Ce system. The Mg1La alloy has a corrosion rate two times higher, which correlates well with the exchange current being nearly twice as high. The volume of intermetallic in the Mg15Gd is still lower and the morphology is more compact thus not a critical for galvanic driven corrosion but the corrosion rate is already the highest, as suggested by the highest exchange current. Summarising one can state that volume of intermetallic is the most important parameter for corrosion, followed by morphology (e.g. eutectic is critical with the different phases close to each other) and the inherent electrochemical properties of the intermetallic.

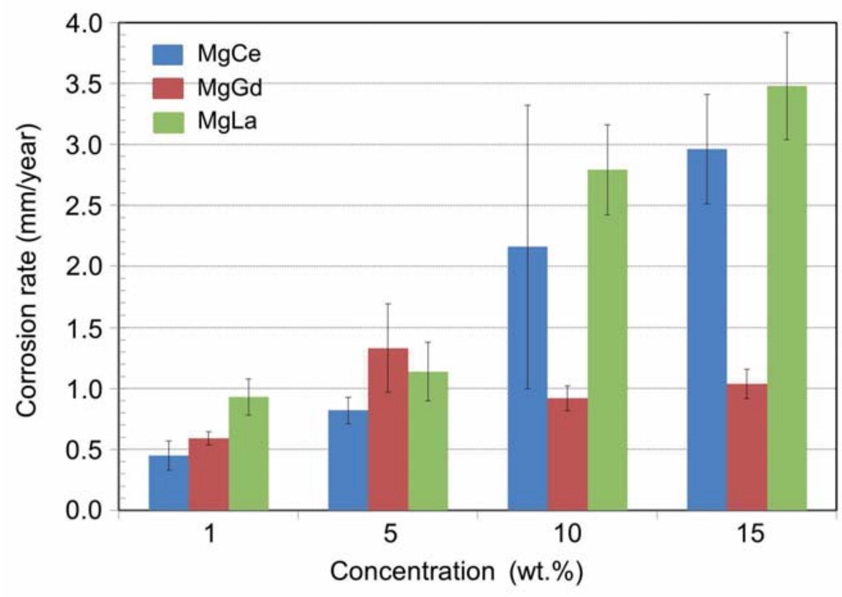

Figure 5.2 Corrosion rates diagram (calculated from the icorr values) of the Mg-RE binary alloys in 0.5 wt.% NaCl solution

5.3.3 Long term corrosion behaviour

For fitting the experimental EIS spectra, various trials were performed, using different equivalent circuits. The best fitting parameters were obtained using the electrical equivalent circuit shown in Figure 5.3 as the starting model at the earlier immersion periods. This two time constant model has been used by other researchers to describe the corrosion process of Mg alloys with or without coating. In this study no coatings were used but it is known that Mg alloys could form $Mg(OH)_2$ layers during corrosion in aqueous solutions [1], which has relative protective properties. In the electrical equivalent circuits constant phase elements (CPE) instead of pure capacitor were used for all data presented. This is because the oxide film on the surface is not completely homogeneous [168]. The first time constant is assigned to the response of the oxide film at high frequencies, whereas the second time constant at lower frequencies was correlated with the charge transfer processes and electrical double layer capacitance at the contact surface between the base metal and the oxide film which correspond with the findings of Turgoose et al. [193].

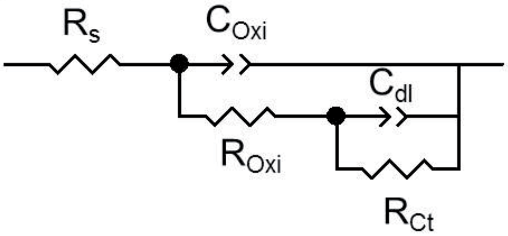

Figure 5.3. Initial equivalent electrical circuit used to fit EIS spectra for the binary Mg-RE alloys during different immersion time, where R_{oxi} and C_{oxi} are the resistance and capacitance of the oxide film. R_{Ct} represents the charge transfer resistance and C_{dl} is attributed to the existence of the double-layer capacitance at the metal/electrolyte interface

The thickness of oxide/hydroxide layers form on the Mg-Ce, Mg-La and Mg-Gd binary alloys did not increase with the immersion time because as the phase angles were smaller than 90° in the Bode plots compared with observations by Pinto et al. [194] for Mg-Zr alloys containing RE elements. However an oxide layer is observed in the Nyquist and Bode plots. The oxide layers are different based on the RE addition, indicating that additions up to 1 wt. % provide a compact and protective oxide layer. If the concentration of the RE increased the protective properties of these layers is decreasing because the resistance of the oxide film (R_{Oxi}) decreases by almost one order of magnitude and after some hours immersion one capacitive loop was observed. This behaviour was investigated by Rosalbino et al. [18], and they suggested an overlapping of the two time constants at the surface. This overlapping originated from similar values of capacitances of both the thin dielectric oxide and the double electrochemical layer in the localised areas of defects where direct contact of the electrolyte and metal is possible. They also argued that if a broadening peak on the phase angle curve is observed this could be a result of passive layer growth [18]. However, in this work broadening of peaks were not observed in the plots indicating dissolution or breakdown of the oxide film because a decrease in the R_{Oxi} values was observed. This behaviour is a direct consequence of the increment in the dissolution rate of the binary alloys, due to the polarisation of the samples [195]. Skale et al. [196] proposed an equivalent circuit with CPE element instead pure capacitor for a steel coated with an epoxy, which shows better EIS fitting quality. Furthermore it was considered not necessary to add an inductor element to the equivalent circuit to describe the severe activity of the metal interphase. Since in some cases right after immersion the R_Ct was not measurable due to the nature active degradation process of the binary alloys in the chloride ions containing solutions. The selection of appropriate equivalent circuits is important as there are circuits with very different physical significance that give data sufficiently similar to the experimental results so that no particular circuit can necessarily be selected as the best. However it is also important to determine if these values are realistic [193].

The total resistance during the corrosion process was measured with EIS indicate small RE additions (1 wt.% RE) show better corrosion performance during the first hours of immersion but not all remain stable and the resistance changes for longer immersion periods Actually the only stable oxide film was found for the Mg1Ce alloy. For higher additions of RE breakdown of the oxide film becomes faster. Although all binary alloys show a clear decrease in barrier properties, the Mg-Gd alloys demonstrate even at higher Gd content somehow higher resistance values indicating a retarded dissolution by a type of semi-protective film. The other alloys do show fast active dissolution. This is also consistent with the polarisation results. Therefore the effect of (a) heat treatments and (b) ternary alloying addition were investigated to understand their roles in modifying the corrosion behaviour of Mg10Gd alloy and to attempt further optimization of the corrosion performance. This alloy is somehow between active dissolution and passivation and therefore interesting for a study to see which measure may shift the behaviour either to passivation or dissolution.

5.4 Effect of heat treatments on Mg10Gd alloy

5.4.1. Microstructure

The microstructure in Figure 4.24 indicates that Mg10Gd alloy mainly compose of Mg_5Gd intermetallic phase and Gd enriched zones near grain boundaries are visible in as-cast condition. After solid solution treatment smaller intermetallic particles remain undissolved, Maier et al. [197] observed similar behaviour for as-cast and extruded Mg10Gd alloy. They associated this phenomenon with the formation of RE containing oxides during the casting. Hort et al. [14] reported that Gd forms Gd_2O_3, which has a higher density compared with the Mg alloy melt. During casting a filter can remove these oxides but if the oxides are finer than the filter, these particles can be incorporated into the casting. In XRD measurements no oxides were present. Information why the oxides and the intermetallic phase Mg_5Gd were not observed using XRD after different measurement is detailed in [14]. However, SEM analysis indicated the presence of GdH_2, which is not, belongs to the Gd oxide or Mg_5Gd phases. The heat treated results were consistent with the observations of Vostrý et al. [198], who proposed that decomposition of α-Mg supersaturated solid solution in Mg-9.33 wt.% Gd as: ß”($D0_{19}$) metastable phase → ß(Mg_5Gd f.c.c) stable during isochronal annealing from 20 to 500°C. Apps et al. [183, 199] suggest that decomposition of Mg supersaturated solid solution Mg(SSSS) as $\beta'' \rightarrow \beta' \rightarrow \beta_1 \rightarrow \beta$, although the compositions of the β”and β phases are uncertain due to the small size of these precipitates and their close proximity to each other. However $ß_1$ and ß phases have a stoichiometry of the eutectic phase near Mg_5RE for the Mg–7%Gd–2.25%Nd–0.6%Zr (GN72) alloy. Furthermore they observed that the presence of the Mg_5Gd phase as a stable intermetallic in the binary Mg–Gd system, where Mg_5RE phase is dependent on formation temperature. Thus ageing at 250 and 300 °C, allow a rapid formation of the $ß_1$ and ß in the GN72 alloy.

5.4.2 Corrosion behaviour

Results from hydrogen evolution and weight loss (Figure 4.28) indicate that corrosion rate of the Mg10Gd alloy is affected not only with the amount of Mg_5Gd phase presented but also its distribution. This phase is present in as-cast sample and gets almost dissolved during the solid solution treatment. However, during aging Mg_5Gd particles precipitate in solid state with largest particle size observed at 300°C. The corrosion rates are lower for the samples in as-cast condition and aged at 200°C and 300°C. These results are similar to the findings by Kainer et al. [200]. They investigated the binary Mg-Gd alloys, in the F, T4 and T6 conditions, finding that Mg10Gd in the T6 condition present the lowest corrosion rate, with nano-sized precipitates of Mg_5Gd phase which do not have an adverse influence on the corrosion rate. The above indicates that the Mg_5Gd phase has only minor negative effects on corrosion behaviour of the alloy when distributed in the following conditions: *i*) in as-cast condition with some Gd enrichment zones surrounding the larger Mg_5Gd precipitates, reducing the local damage due to galvanic couples (as-cast condition), *ii*) if most of the Gd is in solid solution in the matrix and there is only a moderate amount of Mg_5Gd phase (aged at 200°C) and *iii*) when the volume fraction of Mg_5Gd phase is larger but this phase is uniformly distributed and precipitates are small (aged at 300°C). However the most critical phases are not Mg_5Gd, but these small cubic precipitates richer in Gd are most likely GdH_2. This can be confirmed with the corrosion monitoring with SEM before and after immersion test (see Figure 4.30). Figure 5.4 presents schematically the mechanism of initiation and progress of the micro-galvanic corrosion of the as-cast, solid solution treated and aged Mg10Gd alloys. According with this mechanism once the specimen is immersed in the solution two corrosion morphologies occur depending on the Gd distribution. Firstly, formation of $Gd(OH)_3$ [25, 27] and $Mg(OH)_2$ [3, 5, 8, 25, 32] layers on the surface in as-cast condition due to degradation of Gd enrichment areas and some α-Mg matrix, as result of metal dissolution, according to the reactions (18-23), Figure 5.4 (a). These layers are normally not continuous due to the presence of the Mg_5Gd phase. The noble Mg_5Gd phase is driving this process because it is the place where the cathodic partial reaction takes place and as there is no table passive film on the intermetallic it continues as long as there is contact between Mg_5Gd and matrix. If contact is lost in the latter stages the Mg_5Gd phase is not cathodically protected anymore and starts to corrode as the phase is less stable than the matrix in NaCl solutions. However it is not necessary that contact is fully lost to start degradation. It is sufficient when the reduced contact are does not allow sufficient current flow anymore to fully protect from dissolution Figure 5.4 (b) and (c).

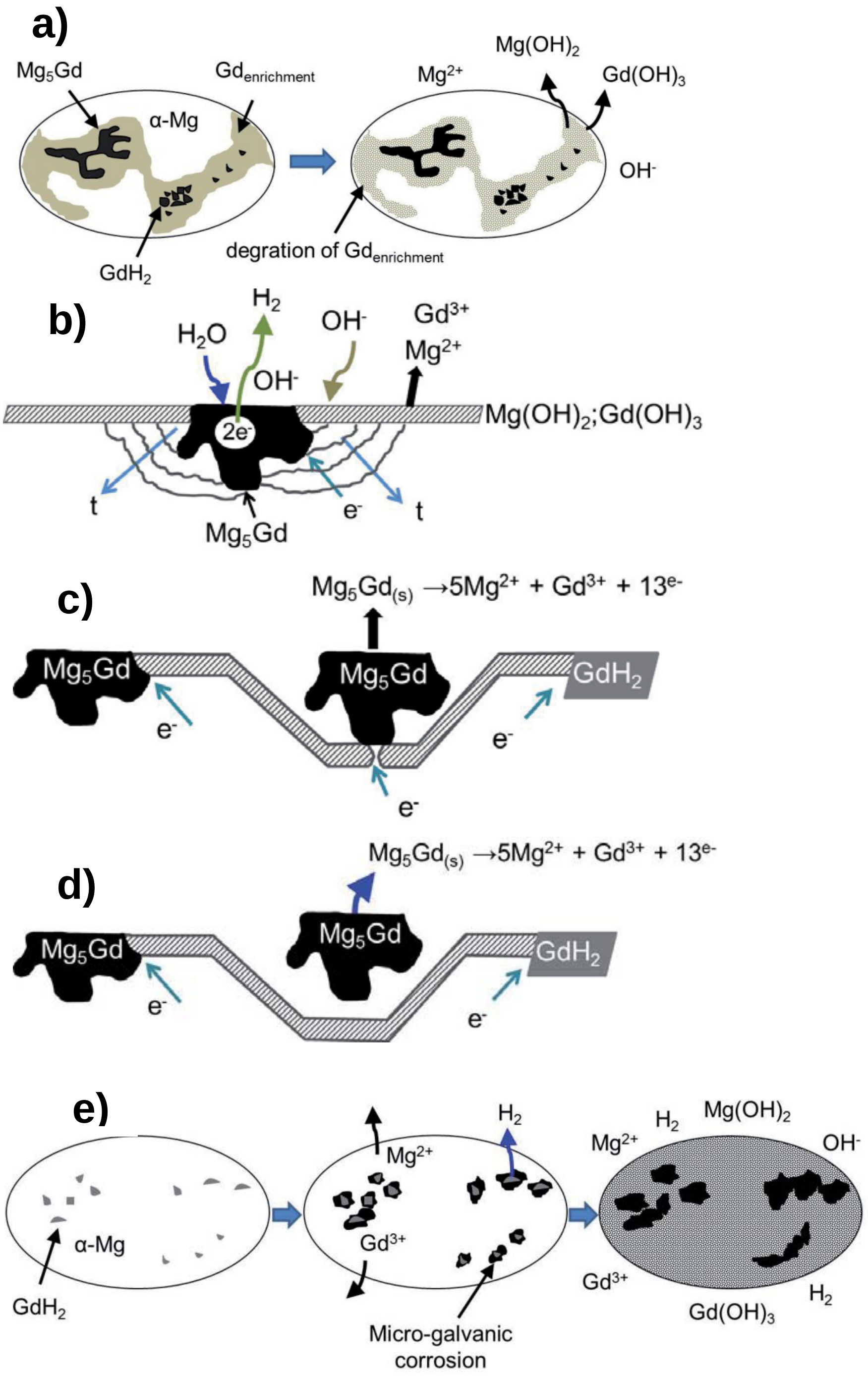

Figure 5.4 Mechanism of micro-galvanic corrosion proposed for Mg10Gd alloy: (a) formation of gadolinium and magnesium hydroxides on the surface in as-cast condition (b) starting degradation of the Mg_5Gd phase surrounding Mg matrix, c) higher dissolution of Mg matrix, exposing the Mg_5Gd phase subsequently starts the dissolution of Mg_5Gd phase due to reducing contact area d) detachment and dissolution of Mg_5Gd phase and e) localized micro-galvanic corrosion at preferential areas for samples heat treated

$$Gd \rightarrow Gd^{3+} + 3e^{-} \qquad (anodic\ partial\ reaction) \qquad (18)$$

$$2H_2O + 2e^{-} \rightarrow H_2 + 2OH^{-} \qquad (\text{cathodic partial reaction}) \qquad (19)$$

$$2Gd + 6H_2O \rightarrow 2Gd(OH)_3 + 3H_2 \qquad (overall\ reaction) \qquad (20)$$

$$Mg \rightarrow Mg^{2+} + 2e^{-} \qquad (anodic\ partial\ reaction) \qquad (21)$$

$$2H_2O + 2e^{-} \rightarrow H_2 + 2OH^{-} \qquad (cathodic\ partial\ reaction) \qquad (22)$$

$$Mg + 2H_2O \rightarrow Mg(OH)_2 + H_2 \qquad (overall\ reaction) \qquad (23)$$

Secondly, when the specimens do not contain Gd enrichment zones, galvanic corrosion begins with the hydrogen evolution (22) on the cathodic Mg_5Gd phase, while the dissolution of Mg (21) develops at the adjacent matrix areas Figure 5.4(b). In some cases the strong dissolution of these adjacent areas favours the intermetallic phase detachment (Figure 5.4 c), but also dissolution which is possible for the Mg_5Gd phase because of its poor stability if it is not cathodically protected anymore (Figure 5.4 d). Similar corrosion mechanism was proposed by Coy et al. [123] using scanning Kelvin probe force microscopy (SKPFM) for ZE41 and WE43 alloys. In this work the SKPFM was not used to measure the potential variations between the micro-constituent phases and the matrix, but the potentials were determined on the separate phases (see chapter 4.2.2 Evaluation of the corrosion behaviour). However the SEM monitoring was helpful to observe the initiation and progress of the corrosion process. For this particular case of Mg10Gd modified with heat treatments; galvanic corrosion depends of the amount and the distribution of the cathodic phases, small amount of cathodic phases (GdH_2 and impurities) without Gd enrichment zones are detrimental for corrosion resistance (in solution treated condition Figure 5.4 e), while the combination of large amount of Mg_5Gd uniformly distributed and Gd enrichment zones enhance the corrosion behaviour of this alloy. There is no negative influence of the grain boundaries as proposed in [123] if Gd is presented. Altogether the situation is relative complex with more noble but less chemically stable intermetallic phase in the magnesium matrix and depending on the situation not only matrix dissolution and particle undermining/detachment can be observed but also dissolution of the intermetallics if not enough protecting current can be provided by the dissolving matrix. Latter is obviously strongly influenced by microstructure. Fine precipitates causes a more uniform attack and they have less negative effects on passive film formation.

5.4.3 Long term corrosion behaviour

For fitting the experimental EIS spectra, the same electrical equivalent circuit showed in Figure 5.3 was used for the heat treated Mg10Gd alloys. As mentioned in the Mg-RE binary alloys, constant phase elements (CPE) instead of pure capacitor were used in all fittings presented [168]. The first time constant is assigned to the response of the oxide layer at high frequencies, whereas the second time constant at lower frequencies was correlated with the charge transfer processes and electrical double layer capacitance at the contact surface between the base metal and the passive layer [193]. For as-cast specimen, this oxide layer was only stable up to the first 60 minutes of immersion. This layer shows relatively better stability and protection after all heat treatments, but only at 200°C and 300°C stable films were observed. However the phase angles were smaller than 90° in the Bode plots, indicating these films do not offer higher protection similar, as the Mg-Zr alloys containing RE elements observed by Pinto et al. [194]. Nevertheless, the aging treatment at 200°C showed a C_{Oxi} of around 3-4x10^{-5} F/cm^2 and in the sample aged at 300°C it was 8-9x10^{-6} F/cm^2. Thus the oxide film is thicker on the 300°C specimen which correlates also with the overall higher resistance values. The resistance is increasing not only due to increasing thickness but also the layer becomes more protective (denser, less porous and other defects). The same is true for the 200°C specimens, but the layer is less protective. For aged at 400°C and solution treated specimens the oxide film is not stable. It partially dissolves or breakdown occurs and the EIS response is extremely lower compared to the other aged specimens. This behaviour also confirms the tendency observed in the hydrogen evolution and weight loss measurements. Thus the long term corrosion behaviour is governed by the oxide film formation and its breakdown.

5.5 Ternary alloys Mg10GdX

5.5.1. Microstructure

The addition of third alloying elements to Mg10Gd alloy causes severe changes not only in Mg_5Gd phase modifications, but also in the whole microstructure, as shown in Figure 4.37. The presence of Gd impedes the formation of $Mg_{17}Al_{12}$ phase which normally exist in binary Mg-Al systems, and promotes the formation of Al_2Gd phase. Pettersen et al. [201] found that increase in the RE content promotes the formation of $Al_{11}RE_3$ phases and reduce the amount of aluminium available for ß-precipitation. For a RE/Al ratio in weight above 1.4, all Al content will be bound to $Al_{11}RE_3$, and new phases may form, either RE-richer Al-RE phase or $Mg_{12}RE$ phase found in Mg-RE alloys. Arrabal et al. [92] found that when a large content of Gd was added to AZ91, Al_2Gd were the main intermetallic particles in the alloys. The explanation for Al_2Gd formation is that RE preferentially reacted with A1 to form Al-RE phases, since the difference in electronegativity between RE and Al is larger than that between RE and Mg matrix [202, 203]. In that sense Al addition to Mg10Gd should reduce the Mg_5Gd volume fraction to zero considering formation of Al_2Gd and Al is still left over for the other phase formation like

$Mg_{17}Al_{12}$. On the other hand ternary phases of MgAlGd or Al-richer binary Al_xGd_y phases are not fully excluded.

For Mg-Gd-Y system, some studies show Mg_5Gd and $Mg_{24}Y_5$ phases are the main phases for this system [172, 174, 204, 205]. Guo et al. [205] indicated that addition of Y not only decreases the solubility limit of Gd in the α-Mg matrix but also decreases the solidus and liquidus temperature. They indicated that the order of precipitation of the Mg_5Gd and $Mg_{24}Y_5$ phases depends on the concentration of Gd and Y. For lower concentrations of Gd than Y (1wt% Gd and 7 wt.% Y), the equilibrium solidification microstructure consists of α-Mg and $Mg_{24}Y_5$ and Mg_5Gd phases. For higher concentrations of Gd than Y (8 wt.% Gd and 2 wt.% Y), Mg_5Gd phase formed ahead of $Mg_{24}Y_5$. Results of the present work suggest that Y is dissolved into the Mg_5Gd. Gröbner et al. [172] found that the $GdMg_5$ intermetallic phases dissolves some Y. According with [206] Mg_5Gd phase could dissolve up to 20% Y.

There is no consent about the question which phases form in the Mg-Gd-Zn system. Balasubramani et al. found that additions of 1 wt.% Zn leads to a higher volume of Mg_5Gd phase but if 2 wt.% Zn is added a high volume of $MgZn_2$ forms and reduce the volume fraction of Mg_5Gd phase. Other studies suggested that additions of Zn promote the Mg_3Gd phase in the as-cast condition, and this phase is considered to be an equilibrium phase in the Mg-Gd-Zn system [174-176].

Srinivasan et al. [173] found $(Mg, Zn)_3$ Gd intermetallic phase as the main phase for the Mg-Gd-Zn alloys for alloys containing 2 to 6 wt.% Zn which significantly reduce the amount of Gd in solid solution. In this work XRD and SEM- EDX measurements indicated the formation of the Mg_3Gd phase with Zn incorporation.

The Mg-Gd-Ga system is new, and there is no literature related to the effects of Ga in the Mg-RE alloys. This work shows that Ga did not act similar to Al in the Mg alloys as expected because additions of 5 wt.% Ga to the Mg10Gd alloy forms the Mg_3GdGa phase as observed in the Mg-Gd-Zn system. The reason for this is not clear at present and further investigation is required.

5.5.2 Corrosion behaviour

a) Mg10Gd1Mn

The degradation mechanism of Mg10Gd1Mn is illustrated in Figure 5.5. The corrosion process starts at the base of the smaller $Mg_5Gd(Mn)$ precipitates (I), which are located in the Gd enrichment zones. There is a potential difference between the precipitates, Gd enrichment zones and the matrix generating galvanic corrosion. Subsequently some pits in the matrix surrounding the precipitates from and they agglomerate with the time (II). This process increased (III) until the precipitates and the neighbouring matrix regions dissolved (IV). The dissolution process is slow and overall passivation is not lost or the film can recover quickly after breakdown.

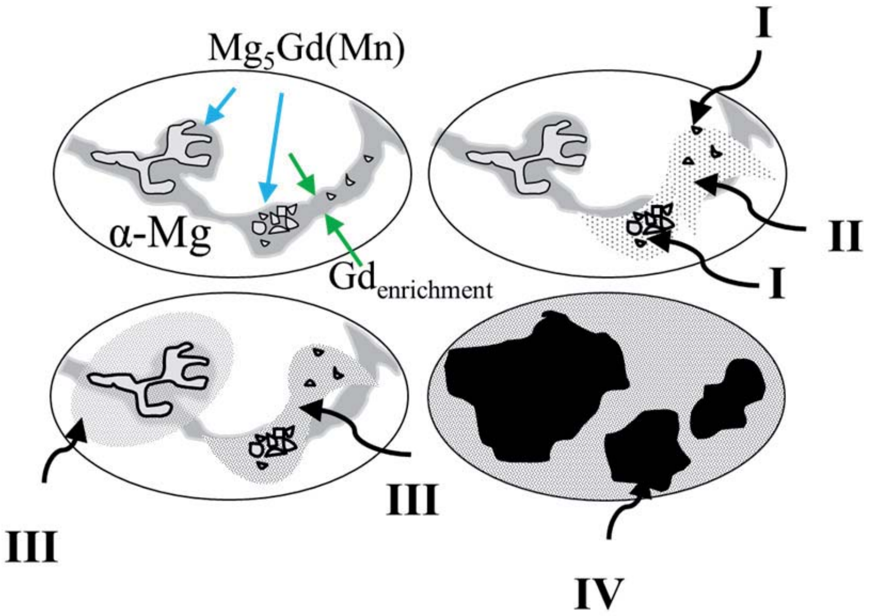

Figure 5.5 Corrosion mechanism of micro-galvanic corrosion proposed for Mg10Gd1Mn alloy. Showing in dim hatched grey areas the corrosion attack on the α- Mg matrix, blue arrows indicate corrosion process on the $Mg_5Gd(Mn)$ phases and green arrows indicate corrosion process on the Gd-enrichment zones

There are some studies on the effect of Mn in Mg alloys. Makar et al. [2] indicated that manganese itself does not improve the corrosion resistance, but reduces the harmful effects of certain impurity and alloying elements. Nelson [87] suggested that the addition of Mn improves the corrosion resistance of magnesium alloys through two mechanisms: (i) Mn combines with iron and precipitates at the bottom of the crucible melt and (ii) Mn encapsulates the iron particles that remain suspended in the metal during solidification, thereby rendering them inactive as local cathodes. Zamin [85] found that Mn incorporates in Al-Fe intermetallic phases in iron containing Al alloys and reduces the galvanic potential differences between the intermetallics and the surrounding matrix. Robinson et al. [89] showed how iron embedded in a manganese particle is less detrimental to magnesium because the galvanic activity between Mn and Mg is less than that between Fe and Mg. However, in this study there is no evidence of precipitation of Mn-rich intermetallics, but SEM and TEM examinations indicate that Mn is found in the intermetallics and to a lower extent in the matrix without forming any binary or ternary intermetallic phases, according to the recent calculations [207]. Lunder et al. [86] suggested that presence of manganese in solid solution with the matrix have a favourable effect on the corrosion behaviour of magnesium alloys. Nevertheless, Cao et al. [208] found that additions of

1 wt.% Mn to Mg alloys lead to the transition of the corrosion type from localised corrosion in the as-cast to uniform corrosion of the solution heat treated Mg1Mn alloy. The solution heat treatment is likely to have homogenised the distribution of Mn and dissolved any particles. The additions of Mn to as-cast Mg-1Mn alloy promote deep corrosion areas similar to lamellar structure, consistent with the corroded surface structure as observed by Qiao et al. [209]. The corrosion mechanism proposed for this alloy is similar to the corrosion mechanism of the as-cast Mg10Gd alloy. However, there is an extra contribution of Mn to the redox process. At the beginning $Gd(OH)_3$ layer forms due to degradation of Gd enriched areas (24-26) with some incorporation of $Mn(OH)_2$, (27-29) as Mn is very unstable in aqueous solutions and dissolves to form manganese ions (Mn^{2+}) (27) and produces hydrogen (28) [25]. Kroening et al. [210] found that Mn containing Mg alloys form an oxide film, which mainly consists of manganese hydroxides and provides surface passivity. However $Gd(OH)_3$ layers are normally not continuous due to the presence of the $Mg_5Gd(Mn)$ phase. After the degradation of the Gd enrichment areas, the adjacent α-Mg matrix dissolves according to the reactions (30) and (32) promoting formation of $Mg(OH)_2$. If the specimen has lower amount of Gd enrichment zones or no enrichment zones, the galvanic corrosion begins with the hydrogen evolution (31) on the cathodic $Mg_5Gd(Mn)$ phase, while dissolution of Mg (30) develops at the adjacent matrix areas. In some cases the fast dissolution of these adjacent areas favours the detachment of the intermetallic phases, which is attributed to the undercutting due to micro-galvanic corrosion, but also dissolution which is possible for the $Mg_5Gd(Mn)$ phase because of its poor stability if it is not cathodically protected anymore. Mn has shown to have a positive effect on the corrosion resistance of Mg10Gd alloy. The main reason seems to be the uniform Mn distribution in the alloy reducing the galvanic corrosion by reducing the potential differences and improving matrix resistance mainly by improved passive film formation. However, Mn additions cannot prevent the galvanic driven corrosion but it seems to slow it down.

$$Gd \rightarrow Gd^{3+} + 3e^- \qquad (anodic\ partial\ reaction) \qquad (24)$$

$$2H_2O + 2e^- \rightarrow H_2 + 2OH^- \qquad (cathodic\ partial\ reaction) \qquad (25)$$

$$2Gd + 6H_2O \rightarrow 2Gd(OH)_3 + 3H_2 \qquad (overall\ reaction) \qquad (26)$$

$$Mn \rightarrow Mn^{2+} + 2e^- \qquad (anodic\ partial\ reaction) \qquad (27)$$

$$2H_2O + 2e^- \rightarrow H_2 + 2OH^- \qquad (cathodic\ partial\ reaction) \qquad (28)$$

$$Mn + 2H_2O \rightarrow Mn(OH)_2 + H_2 \qquad (overall\ reaction) \qquad (29)$$

$$Mg \rightarrow Mg^{2+} + 2e^- \qquad (anodic\ partial\ reaction) \qquad (30)$$

$$2H_2O + 2e^- \rightarrow H_2 + 2OH^- \qquad (cathodic\ partial\ reaction) \qquad (31)$$

$$Mg + 2H_2O \rightarrow Mg(OH)_2 + H_2 \qquad (overall\ reaction) \qquad (32)$$

b) Mg10Gd 5Al

For Mg-Al alloys there are vast investigations focusing on the corrosion behaviour and the influence of β-phase ($Mg_{17}Al_{12}$) and magnesium matrix on it [4, 25, 83, 91-93, 144, 177, 211]. However, Das et al. [212] suggested that the absence of $Mg_{17}Al_{12}$ phase could enhance the corrosion resistance of aluminium-rich magnesium base alloys by eliminating the micro-galvanic effects, which are detrimental for Mg alloys. Since $Mg_{17}Al_{12}$ phase was not observed in the Mg10Gd5Al alloy, the corrosion process started at the adjoining area of the smaller Al_2Gd precipitates (I) Figure 5.6. Subsequently, some regions of α-matrix show degradation (II) which increases with the immersion time. After that the damaged matrix regions dissolve, Figure 5.6 (III), exposing a larger volume fraction of Al_2Gd phase Figure 5.6 (IV). The Mg_5Gd and Al_2Gd phases did not undergo any degradation. Degradation is relative fast because of the eutectic structure with cathodic and anodic regions close together. Mohedano et al. [94] reported that additions of Gd to AM50 and AZ91D alloys promote the precipitation of Al_2Gd and reduced the volume fraction of $Mg_{17}Al_{12}$ phase which increased the corrosion resistance of these alloys due to the increased surface passivity and suppression of micro-galvanic couples. Arrabal et al. [91] found that Al_2Gd phase has a cathodic behaviour with respect the Mg matrix; and the surface potential of Al_2Gd is slightly higher than $Mg_{17}Al_{12}$ phase potential in the AM50 and AZ91D alloys. During corrosion test Gd containing phases did not degrade. However, they suggested that Gd addition should not be excessive as this could be detrimental to the corrosion resistance of the Mg-Al alloys.

Based on all corrosion test including hydrogen evolution and weight loss results the addition of Al did not improve the corrosion resistance of Mg10Gd based alloy. The Mg_5Gd phase was replaced by Al_2Gd or Al_xGd_y phases which are even more detrimental and increases local galvanic corrosion. Furthermore the preferential precipitation in eutectic structure promotes the galvanic coupling effects due to short distances. Zhang et al. [213] found a dual behaviour of Al-RE intermetallic phases. A discontinuous distribution of Al-RE phases act as galvanic cathode and accelerates the micro-galvanic corrosion. While a continuously distribution with a high volume fraction of Al-RE phases act as a corrosion barrier in the Mg alloys. In this study Al_2Gd phase was discontinuously dispersed generating dissolution of the α-Mg matrix and thereafter, the volume fraction of cathodic Al_2Gd phase increased further which promotes even higher cathodic reduction rates. Since the cathodic process of Mg corrosion is mainly dominated by hydrogen/water reduction process, a higher cathodic reduction rate leads to faster anodic Mg dissolution. This is consistent with findings of Song et al. [4] where the micro-galvanic corrosion of Mg alloys is affected by two factors: i) the volume fraction and the distribution of second phase and ii) cathodic reduction rate of the second phase.

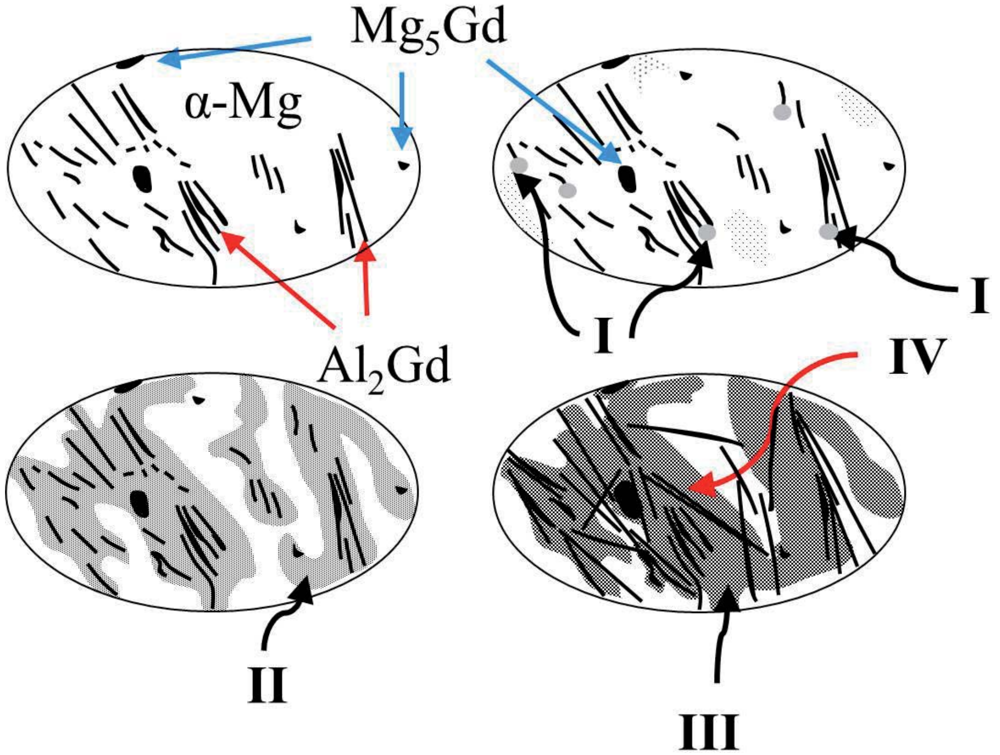

Figure 5.6 Mechanism of micro-galvanic corrosion proposed for Mg10Gd5Al alloy. Showing in grey the corrosion attack on the α- Mg matrix, blue arrows indicate corrosion process on the Mg_5Gd phases and red arrows indicate corrosion process on the Al_2Gd phases

c) Mg10Gd5Zn

The results from hydrogen evolution and weight loss indicated that Zn additions had the most detrimental effect on the corrosion resistance of Mg10Gd based alloys. Srinivasan et al. [214] suggested that lower additions of Gd (approx. 2 wt.%) promote lower corrosion rates in the Mg-2Gd-*x*Zn alloys compared with higher concentrations of Gd (around 10 wt.%) in the Mg-10Gd-*x*Zn alloys. The amount of zinc (x= 2, 6 wt.%) in the Mg-2Gd-*x*Zn alloys did not affected the corrosion rates, whilst higher amount of Zn was detrimental to the Mg-10Gd-*x*Zn. The corrosion rate values reported by Srinivasan et al. [214] were lower compared with the corrosion rates measured in this work. There might be one possibility for the above observation. The microstructural composition plays an important role in the corrosion resistance of this alloy and the casting process was different. Some studies reported presence of LPSO (Lamellar long period stacking ordered) phase and suggested that it facilitates the corrosion in these alloys [173, 215, 216]. On the other hand Zhang et al. [217] reported that the presence of lamellar LPSO phase in the Mg matrix improved the corrosion resistance of Mg-Gd-Zn alloys. However LPSO phase was not observed in this work, while it was found by Srinivasan et al. [173, 214] and possibly the absence of this phase caused the higher corrosion rates of these alloys. In the present work, the corrosion process proposed for Mg10Gd5Zn alloy is graphically described in Figure 5.7. After a short time of immersion; some α-matrix areas and some regions of

$Mg_3(Gd,Zn)$ phase dissolved, as illustrated in (I) and (II), respectively. Subsequently matrix dissolves and contains deeper pits (III) exposing large amount of the lamellar skeleton of $Mg_3(Gd,Zn)$ phase (IV); while in other regions, this phase showed also further deterioration and the selected areas were less visible (V). Finally, only few lamellar $Mg_3(Gd,Zn)$ skeleton regions could be seen (VI) as the α-matrix was severely degraded (VII).

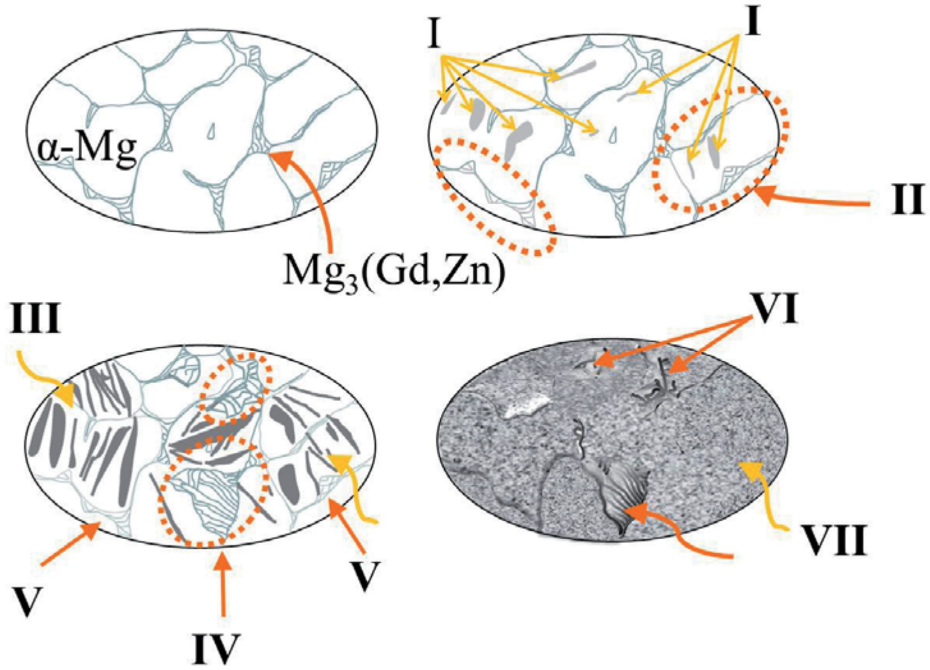

Figure 5.7 Mechanism of micro-galvanic corrosion proposed for Mg10Gd5Zn alloy. Showing in yellow arrows the corrosion attack on the α- Mg matrix, orange arrows/dotted circles indicate corrosion process on the $Mg_3(Gd,Zn)$ phases

The possible explanation of this behaviour will be discuss in two parts: i) the dissolution of the α-Mg matrix and ii) the contribution of the $Mg_3(Gd,Zn)$ phase in the corrosion mechanism. The initial dissolution of the adjacent areas to the intermetallic phases for Mg-Gd-Zn system was described by Srinivasan et al. [173, 214]based on the overall reaction of Mg in aqueous solutions, (33). It has been also described in [3, 4, 7, 211] that the volume fraction and distribution of the second phases play a significant role for the corrosion resistance of Mg alloys as described above in the Mg10Gd5Al alloy and in general for AZ alloys.

$$Mg + 2H_2O \rightarrow Mg(OH)_2 + H_2 \qquad (33)$$

Coy et al. [123] demonstrated the cathodic behaviour of the secondary phases accelerate the corrosion of α-Mg matrix for the ZE41 alloys but the potential difference of the RE-containing phases is negligible in the WE alloys. The microstructure for this alloys shows a large amount of $Mg_3(Gd,Zn)$ phase distributed as lamellar network and its higher corrosion rate indicate that a large volume fraction and the distribution of $Mg_3(Gd,Zn)$ phase induce the low corrosion resistance. This is very similar to the microstructure of the Mg10Gd5Zn alloy. Mouanga et al.

[218] studied the corrosion behaviour of zinc in NaCl solution. They reported that the corrosion mechanism of zinc proceeds via two partial reactions: *a)* the cathodic reactions corresponds to the reduction of oxygen and leads to pH increase (34) and *b)* the anodic reaction involves the dissolution of zinc and leads to weight loss (35). Furthermore formation of zinc hydroxide as result of reaction between zinc cation and the hydroxide anion (36) is expected. In presence of sodium chloride, chloride ions (Cl^-) migrate to anodic sites where zinc hydroxide chloride forms according to (37). Boshkov et al. [219] reported that (34) leads to a local increase in pH value with in the corrosion damage pits and as a result, the zinc hydroxide chloride forms in the pits and their neighbourhood areas. The corrosion layer on Zn surface in NaCl is porous and non-protective allows continuously dissolution of zinc. This can be expected to happen on the Zn rich intermetallics as well.

$$O_2 + 2H_2O + 4e^- \rightarrow 4OH^- \qquad (cathodic\ reaction) \tag{34}$$

$$Zn \rightarrow Zn^{2+} + 2e^- \qquad (anodic\ reaction) \tag{35}$$

$$Zn^{2+} + 2OH^- \rightarrow Zn(OH)_2 \qquad (corrosion\ product\ 1) \tag{36}$$

$$5Zn(OH)_2 + 2Cl^- + H_2O \rightarrow Zn_5(OH)_8Cl_2 \cdot H_2O + 2OH^- \quad (corrosion\ product\ 2) \tag{37}$$

The process is likely galvanic driven with the $Mg_3(Gd,Zn)$ phase being the cathode and the matrix the anode. However the intermetallic seems to be no stable similar like the Mg_5Gd phase and degrades as well if not enough current is provided by dissolving matrix.

Summarizing, the corrosion process of Mg10Gd5Zn is simultaneously affected by two contributions: i) the dissolution of Mg matrix due to the potential difference between the present phases and ii) degradation of $Mg_3(Gd,Zn)$ due to Zn content dissolved therein, which is susceptible to corrosion in NaCl solutions.

Note: For the following ternary systems Mg10Gd5Y and Mg10Gd5Ga the corrosion mechanisms will not be discussed in detail as the previous three as these alloys were not studied in detail. However the author would like to express some comments as possible reasons for corrosion behaviour of these alloys based on previous studies.

d) Mg10Gd5Y

In the literature there are some studies related to Y addition on the corrosion behaviour of Mg alloys [16, 17, 108, 220-223]. Rzychon et al. [220] found that as-cast samples present lower corrosion rates compared to the aged samples because aging treatments promote higher volume fraction of the intermetallic phases, which act as cathodic sites generating galvanic corrosion in the WE54 alloy. Davenport et al. [224] demonstrated that Y rich regions slow down the corrosion degradation in the as-cast WE43. Carboneras et al [222] found that heat treatment improves the corrosion resistance of the extruded WE54 alloy. The heat treatment produces a finer precipitation which decrease pitting corrosion compared to extruded alloy.

In present Mg10Gd5Zn alloy Gd allows the formation of $Mg_{24}Y_5$ phase as proposed in some studies for Mg-Y alloys [16, 17, 108] and based on XRD and SEM-EDX analysis indicate that some Y is also dissolved in the intermetallic phase forming $Mg_5(Gd,Y)$ and in the α-Mg matrix. This distribution was expected to be beneficial in terms of corrosion resistance because of Y distribution in both phases. Unfortunately this was not satisfied as Mg-Gd-Y system has a higher corrosion rate. Sudholz et al found three important features in the Mg-Y alloys: *i)* increasing Y concentration generates ennoblement of the α-Mg but the cathodic kinetics also increases generating higher current densities. *ii)* The E_{corr} of $Mg_{24}Y_5$ phase is about 40-50 mV nobler than pure Mg. The E_{corr} for the Mg-Y systems are about 200 mV more noble compared with pure Mg and iii) the Y content in solid solution combined with a stronger $Mg_{24}Y_5$ cathode placing the alloys under cathodic control. Similar effects can be expected for this alloy, because $Mg_5(Gd,Y)$ and $Mg_{24}Y_5$ phases promote higher cathodic reduction rates, which lead to faster anodic Mg dissolution.

e) Mg10Gd5Ga

Gallium is considered to be less active than Al because it forms a stable oxide film (Ga_2O_3) in aqueous solutions [25]. Kubásek et al. [140] found that additions of more than 1wt.% Ga promote high volume fraction of the secondary phase Mg_XGa and decrease the corrosion resistance in the Mg-Ga alloys. The Mg-Ga intermetallic phases are cathodic to α-Mg and generate galvanic corrosion [225]. Despite that, the corrosion process was not monitored for this alloy and the hydrogen evolution and weight loss measurements showed that Mg-Gd-Ga alloys have lower corrosion resistance as Mg-Gd-Y alloys. Probably this behaviour is related to the high volume fraction of Mg-Gd-Ga intermetallics phases which promote more corrosion sites [140] and increase its corrosion rate.

5.5.3 Long term corrosion behaviour

The OCP curves in Figure 4.49 indicate that ternary alloys reached nobler potential values after approximately 1000 s immersion, due to the quicker formation of the corrosion product layer on the surface [171]. The time for the corrosion product layers formation mainly depends on the susceptibility of the intermetallic phases, RE-rich regions and the solid solution elements within the α-Mg matrix to the chloride ions as described in the previous section. However potentiodynamic polarisation measurements show that most of these films were not stable and tend to degrade or dissolve partly or completely allowing relatively high current density values [144]. Only the alloys with Mn and Al addition shows some retarded anodic dissolution indicating the existence of a partly protective film. The EIS results of the ternary alloys are shown in Figure 4.51 and will be separately discussed for a better understanding of the passive film formation.

- *a) Mg10Gd5Al*

At the beginning of the tests two CPE's were visible. With immersion time the first CPE (at high frequencies) is shifted to relatively middle frequencies (10^2 Hz) possibly due to a pseudo inductivity influence. In the immersion test after 10 min immersion (see Figure 4.45), small pits were detected at the adjoining area of the smaller Al_2Gd precipitates corroborating this assumption. Further, the two time constants revealed the existence of an oxide layer with growing resistance up to 2 hours of immersion. Most likely the native oxide film is converted into hydroxide film. According to the immersion test during this period the Mg matrix show degradation by small pits close to the precipitates, which is related to the weaker $Mg(OH)_2$ layer close to the intermetallics [1]. It is interesting to see that the second capacitive loop shows already a distortion typical for an inductive influence, but the values are still positive at this time. This inductive influence becomes stronger with further immersion time as the small pitting is more and more replaced by localised active dissolution and filiform corrosion is spreading across the surface, removing the original protective film more and more indicated by a continues decrease in resistance.

Song et al. [8] suggested that the inductive loop is attributed mainly to the partially protective surface film. Moreover they argued the presence of Cl^- ions make the surface films more active or increase the surface area with film breakdown, and accelerate the Mg dissolution. These arguments are consistent with the observations of the immersion test for Mg-Gd-Al alloy. The Al_2Gd phases act as the cathodes and the surrounding Mg matrix is the anode. Then when the Cl- ions were absorbed the hydroxide film starts to dissolve firstly in the regions where the film is the weakest, and an electrolytic cell forms. Thus the corrosion pits initiated in the area adjacent to the secondary phases. After some time the volume fraction of the Al_2Gd phase increased, generating faster dissolution of the matrix (change from pitting to filiform corrosion) which is controlled by diffusion. This corrosion mechanism was also used by Zeng et al. [41] to describe the pitting corrosion of the AM60 alloy.

- *b) Mg10Gd5Ga*

The Nyquist plots for the Mg-Gd-Ga system revealed a capacitive loop at high and intermediate frequencies and the diameter is associated with the charge-transfer resistance. Several studies have related this loop to the metal dissolution in the corrosion process [8, 190, 226-228]. The second loop is inductive at low frequencies. Cao et al. [226] described that inductive loops at low frequencies could be caused by different processes: *i)* as a response of the rates of dissolution and formation of the outer layer of oxide film on the variation of *E. ii)* passivated metals in Cl^- containing solution during the incubation period of pitting corrosion and *iii)* when an intermediate species is absorbed in the metallic electrode surface. Song et al. [8] found that Cl^- ions are more aggressive compared to OH- ions . In NaCl solutions higher amounts of Cl^- ions would be expected to be absorbed on the surface film and on the film free surface. Moreover the Cl^- ions made the magnesium oxide/hydroxide more soluble and combined with metallic magnesium weaken the bonds among the metallic atoms and accelerate the oxidation reaction. For this alloy only one capacitive loop was visible from the beginning on and there is no evidence of oxide film formation on the surface. In contrast the Cl^- ions were quickly adsorbed in the native film and active dissolution started right from beginning. The SEM micrographs show (Figure 4.37) the volume fraction of the intermetallic phases is much higher for this alloy compared to the Mg10Gd5Al alloy generating more localised corrosion and a lower corrosion resistance. Furthermore it seems as if Ga forms less noble oxide films than Al when form mixed hydroxide layers with Mg.

- *c) Mg10Gd1Mn*

The Nyquist plot for Mg-Gd-Mn alloy is shown Figure 4.51 (e). Two capacitive loops were observed one a high frequencies and the other at lower frequencies. Turgoose et al. [193] described this impedance response as absorption of species that increase with increasing potential and in which the absorbed species reduces the corrosion rate, due to a film growth on the surface. Cao et al. [208] attributed these two capacitive loops to uniform corrosion. They also found that as-cast Mg1Mn suffered localised corrosion after immersion in 3.5 wt. % NaCl solution, however the heat-treated Mg1Mn showed a surface film which is more protective.

As similar response was observed here for Mg10Gd1Mn and the two capacitive loops indicate oxide film formation. The protective ability of this layer seems to increase with longer immersion time. For this alloy the EIS measurements were recorded only until 48 h, but in previous studies [9] the samples were measurements for longer immersion time (144 h) revealing any sign of localised corrosion. The corrosion resistance increased continuously, which can be related to an increasing thickness or density of the oxide film. The performance of the Mg10Gd1Mn alloy is much better than that the other ternary systems, which can be related to formation of a stable oxide film if the surface is exposed to chloride containing aqueous solution.

- *d) Mg10Gd5Y*

The corrosion behaviour for this alloy is similar to the Mg10Gd5Ga. At the beginning of the test two capacitive loops were observed, one at high frequencies and the other a lower frequencies, the first loop seems to be related to a possible film formation on the surface. However, from one-hour immersion localised corrosion or micro-galvanic corrosion was observed with an inductive loop at low frequencies [41, 208, 229]. For the remaining immersion time up to 12 hours the pitting is further increased and the corrosion resistance decreased for the Mg10Gd5Y alloy. Obviously the native oxide film is stronger than in the alloy with Ga addition, but weaker than the one on the Al containing alloy. The conversion of the air based oxide film into the hydroxide film is not resulting in a protective film.

- *e) Mg10Gd5Zn*

EIS measurements confirmed the poor corrosion resistance observed in other corrosion evaluations of Mg10Gd5Zn alloy. The EIS response showed at the beginning two capacitive loops at high frequencies and a very small second loop at lower frequencies, indicating the possibility of a naturally formed thin oxide film on the surface. However, it quickly gives rise to the formation of an inductive loop which is generated by localized corrosion [1, 41, 208]. The pitting corrosion is increasing rapidly changing quickly to filiform and deep localised corrosion. Thus the corrosion resistance of the Mg10Gd5Zn showed a dramatic decrease. The micro-galvanic corrosion occurred severely around the second phases and the second phases were undermined and dissolved during the corrosion as observed in the immersion test. The EIS results were also similar to the observations of Srinivasan et al. [214]. Although they argued that the secondary phases and LPSO (lamellar long period stacking ordered) phase are more detrimental for Mg-Gd-Zn alloys because LPSO facilitates the filiform corrosion. In this study the LPSO phase was not formed, but corrosion was also severe with filiform corrosion as an intermediate corrosion process between pitting and the final deep localised attack.

5.5.4 Corrosion products layer

The morphology and microstructures of the passivation layer on corroded Mg alloys surfaces have been investigated during the last decades [1, 130, 230-236]. Ghali et al. [1] show that during corrosion a relatively stable film of rather low conductivity forms on Mg even in aqueous solutions. Froats et al. [50] suggested that the oxide film on Mg offers considerable surface protection in rural and some industrial environments. However the passivity of Mg is destroyed by several anions including chloride, sulphate and nitrate. Chloride even in small amounts, usually break down the protective film on Mg [1, 237] Ghali et al. [1] reported that in aqueous solutions, Mg dissociates by electrochemical reaction with water to produce a crystalline film of $Mg(OH)_2$ and hydrogen gas (H_2), a mechanism, which is highly insensitive to oxygen concentration. In absence of oxidizing agents, the reaction is as show in (38).

$$Mg_{(s)} + 2H_2O_{(l)} \rightarrow Mg(OH)_2 + H_{2(g)} \qquad (38)$$

In this study the SEM-EDX analysis indicates that the films on pure Mg, Mg10Gd and Mg10Gd1Mn, are mainly composed of $MgO/Mg(OH)_2$ and some carbonates. These results are

consistent with previous studies. McIntyre et al. [238] found that the oxide layer is composed of $MgO•H_2O$. The film forms in air immediately after scratching the metal surface, and is initially thin, dense, amorphous, and relatively dehydrated. Ghali et al. [233] suggested that the magnesium oxide (MgO) should be hydrated to produce $Mg(OH)_2$. $Mg(OH)_2$ has a layered hexagonal crystalline structure, alternating between Mg and hydroxide ions, facilitating easy basal cleavage. Taheri et al. [239]suggested that hydration of the bulk inner MgO layer (native layer) is a necessary to cause thickening of the partial protective outer $Mg(OH)_2$ layer. Unocic et al. [240] found that the films consisted primarily of MgO, with surface regions also containing $Mg(OH)_2$ and $MgCO_3$. Lindström et al. [231] found that in presence of CO_2 and NaCl, a thick uniform corrosion layer forms that contain slightly soluble hydrated magnesium hydroxy carbonate ($Mg_5(CO_3)_4(OH)_2•5H_2O$), which provide a partial protection. More specific information of the passive layer on Mg alloys is reported by Froats et al. [50]. They suggested that an oxide film on Mg surface that forms during immersion in distilled water after 48 h is composed of a three-layered structure, consisting of an inner cellular structure with thickness of about 0.4 to 0.6 µm, a dense intermediate region (20-40 nm) and an outer layer with a platelet like morphology around 2 µm in thickness. The film formed in air showed similar hydrated inner and intermediate layers, without platelet like morphology [241]. McIntyre et al found that the oxide thickness on pure Mg after exposure for only ~10 s at ambient condition is 2.2 ±0.3 nm (approximately seven mono-layers of MgO and increases slowly, linearly with the logarithm of exposure time during a test period of 10 months. Continuing exposure to humid air or to water leads to the formation of a thicker hydrated film adjacent to the metal. Nordlien et al. [130] found that exposure to air for a period between 15 to 60 min gives a film thickness of about 20-50 nm, while exposure to humid air with approximately 65% relative humidity during 4 days leads to a thick layer of 100-150 nm.
The results of the non-destructive thickness measurements revealed the following thickness for corrosion products on the surface of the specimens: pure Mg: 16 µm < Mg10Gd1Mn: 50 µm < Mg10Gd: 150 µm. The larger layer thicknesses were due to the presence of Cl^- ions in the corrosion medium which lead to the degradation of the Mg alloys much faster generating a higher layer thickness compared with those obtained in distilled water mentioned previously. The XPS depth profile measurements have confirmed the large difference. Pure Mg and Mg10Gd1Mn layers show some cracks. Ismail et al. [242] attributed this cracking to Pilling-Bedworth ratio (PBR) effects related to the predominant formation of MgO, which has a PBR less than 1 and would not be expected to form and/or maintain a dense continuous film. Ghali et al. [233] found that the Pilling-Bedworth ratio of MgO/Mg is about 0.81, which is considered to be non-protective. However they determined that $Mg(OH)_2$ has a Pilling-Bedworth ratio about 1.77, which indicates a resistant film in compression. A combination of internal stresses and the easy basal cleavage may account for the cracking and curling of the film especially if it grows thicker.

In the corrosion testing section 5.5.2 Corrosion behaviour, it is suggested that the corrosion resistance of the binary alloy Mg10Gd is improved by the possible formation of mixed magnesium gadolinium oxides/hydroxides, while in the Mg10Gd1Mn alloy; the addition of Mn allows the formation of manganese oxides/hydroxides. XPS results verify these statements. Nakatsugawa et al. [243] demonstrated that magnesium alloys containing RE elements show a RE enrichment in the corrosion product layers. Nordlien et al. [130] reported the RE enrichment in the oxide layer in a Mg-0.15% RE alloy. Lunder et al. [10] found that corrosion resistance of AE alloys was due to the enrichment of trace amounts of solid solution RE at surface, and particularly in the oxide film. In this study $Gd_2O_3/Gd(OH)_3$ is present in the corrosion layer as observed by XPS and this corroborates with the XPS investigations made by Wandelt et al. [178] and Raiser et al. [244]. The important contribution of this work relates to the surface layer composition, when gadolinium and manganese were present. In this case, the passive film is composed of two layers, the outer layer consisting mainly of manganese and gadolinium rich compounds, and the inner layer consisted of Mg compounds. The Mn and Gd detected in the outer layer is likely to be present in the form of manganese oxides [210] and gadolinium oxides/hydroxides [178, 243, 244]. The inner layer is formed by magnesium oxide/hydroxide with traces of magnesium carbonate similar as reported in the literature [234, 236, 239, 240, 243]. Achieving a microstructure/composition that allows stable passive film formation is the key to a corrosion resistant alloy.

Relationship between microstructure and corrosion

The poor corrosion resistance of many Mg alloys is due to two general reasons: *i)* the internal galvanic corrosion caused by impurities or second phases [1] and *ii)* the quasi-passive hydroxide film on Mg is much less stable than the passive films which form on other metals such as aluminium and stainless steels [2]. Important improvements have been achieved during the last decade to increase the resistance of magnesium alloys against corrosion in the presence of chloride containing environments such as reducing the heavy metal impurity content, using diverse alloying elements and heat treatments. These advances can be understood partly in terms of increased passivity of the metal surface by incorporation of component which stabilizes the oxide formation on Mg alloys [3-11]. In NaCl solutions the Mg dissolution rate is higher, because chlorides can interfere with the formation and maintenance of the protective layer of corrosion products which decrease the severity of the attack [12]. Previous studies show that rare earth elements (RE) have a significant positive influence on the corrosion resistance of Mg alloys [13-22, 80]. The rare earth elements improve the tendency of magnesium to passivation and decrease the micro-galvanic influence of the secondary phases [6, 12, 23, 24]. The RE metals used in this work, were selected based on their solid solubility in Mg. The rare earth elements with lowest solid solubility are La (0.042 at.%), Ce (0.1 at.%) and Nd (0.63 at.%). While Dy (3.5 at.%) Y (3.75 at.%) and Gd (4.6 at.%) show the highest solid solubilities [158-162]. The RE elements and Mg are electrochemically active metals, the standard potentials for RE/RE^{3+} systems are between -2.6 to -2.0 V(SHE) [25, 26] while it is -2.4 V(SHE) for Mg/Mg^{2+} [1, 25] in aqueous solutions. However, RE elements present less active open circuit potential values compared with pure Mg in NaCl solution. The foregoing suggests the formation of an oxide layer on the surface [26, 27] which is more stable than the oxide on pure Mg and in some cases also a “passive range” was observed during polarisation e.g. for Gd and Dy, indicating that these elements are rather resistant to corrosion in NaCl solutions [15]. However, the layers on the surface of the other rare earth elements do not provide sufficient protection in solutions containing chloride ions as they show very high corrosion rates [28, 29]. As described in the beginning one of the reasons of the low corrosion resistance of the Mg alloys is due to the internal galvanic corrosion caused by second phases. The Mg-RE-intermetallics have higher corrosion rates compared with pure Mg, contradicting the theory that the intermetallic phases are nobler than Mg [15]. However in a Mg matrix they are galvanically protected and will not dissolve as long as enough cathodic current is provided by the matrix. But when they are evaluated separately, these compounds tend to degrade faster than Mg. In general the electrochemical properties (OCP, E_{corr}, i_{corr} and corrosion rate) for the Mg-RE-intermetallics are influenced by the specific RE element addition. For the galvanic coupling Mg with Mg-RE-intermetallics, the purity of intermetallic phases play an important role because it affects the system performance. Thus mishmetal additions are somehow unpredictable. This feature should be considered in the design of alloys.

The solid solution solubility is an important parameter for the corrosion resistance of the Mg-RE alloys. In this work Ce and La have a lower solid solubility in Mg matrix generating more volume fraction of the secondary phases, thus higher dissolution rates in the binary Mg-RE alloys. While Gd with higher solid solubility shows a different behaviour, additions up to 10 wt.% Gd result in similar values as obtained for 1 wt.% Gd addition. Though additions beyond 10 wt.% Gd generate higher corrosion rates which is related to increasing amount of Mg_5Gd phase. The author suggests that relatively good corrosion behaviour in as-cast Mg10Gd alloy is due to the presence of Gd enrichment zones, which reduce the local damage due to galvanic corrosion between the Mg_5Gd phase other noble phases (e.g. GdH_2) and α- Mg matrix. However when the Mg10Gd is heat treated the corrosion mechanism is positively affected if Gd is in solid solution with the matrix and the precipitates are small and uniformly distributed. Galvanic corrosion depends on the amount and the distribution of the cathodic phases, small amount of larger Mg_5Gd precipitates without Gd enrichment zones is detrimental for corrosion resistance, while the combination of large amount of fine Mg_5Gd precipitates uniformly distributed in a Gd enriched matrix enhance the corrosion behaviour of this alloy.

The main reasons are suggested for this effect:

1) Small particles can be undermined easier and if they fall out of the matrix they leave behind a uniform surface without potential differences.

2) Small particles can be covered more easily by a growing passive film. The hydroxide films have low conductivity thus they are inhibiting the water reduction reaction on the particles by reducing the exchange current.

3) Passive film formation is more uniform on the heat treated alloy; because the microstructure is more uniform and the larger amount of alloying elements in solid solution are ready for oxide/hydroxide formation.

For the ternary systems, additions of Al, Zn, Ga and Y did not show any improvement in the corrosion resistance of Mg10Gd. The reasons are all the same for the different alloying element additions. The volume fractions of critical more noble phases are increased and the microstructures are dominated by eutectic phase formation. Thus galvanic effects are becoming much stronger due to the increasing amount of cathodic phases and their precipitation closely to the α-matrix in the eutectic regions. The negative effects are increasing in the following order Al < Y < Ga < Zn. This order is not only affected by the amount of secondary phases and their distribution, but also by the possibility of the alloying element to contribute to passive film formation.

For the Mg10Gd alloy, only addition of Mn was beneficial for the corrosion. The combination of Gd and Mn did not lead to the precipitation of Mn-rich intermetallics, though Mn is found in the intermetallics and to a lesser extent in the matrix without forming any ternary intermetallic phases only the amount of Mg_5Gd phase is slightly increased. Thus no major change is expected from the galvanic coupling of the phases. The main difference was found in the passive film formation and composition.

The Mg10Gd alloy is the as-cast condition is not forming a stable film (Figure 4.21), but it requires only small modifications to get it into a condition that passive films are getting stable.

This first possibility is the change of microstructure by heat treatment. The homogenised structure shows passive film formation without changing the composition (Figure 4.34).

The second possibility is the change of composition and only Mn was suitable because of its minor effects on the microstructure. The main modification was obtained for the passive film which was stable after Mn addition. The reason was obviously a change in the film composition and structure.

It was compose about of two layers, the outer layer consisting mainly of manganese oxides with gadolinium oxides/hydroxides and the inner layer formed by magnesium oxide and hydroxide with traces of magnesium carbonate. This indicates the importance of the passive film to control the degradation of alloys and how this film depends not only on the alloy composition but also on the microstructure.

6. Conclusions

This work has shown how the presence of intermetallics can affect the overall corrosion resistance of the Mg alloys. In order to develop a RE based Mg alloy with improved corrosion resistance two aspects of RE elements were important for the selection: the solid solubility in Mg and their electrochemical properties. The solid solubility defines the amount of intermetallic phases present in the alloys and the electrochemical properties of the Mg-RE-intermetallics define the compatibility to the matrix since different types of RE elements were used and compared in this investigation, the main findings are listed below:

- Additions of RE (Ce, La, Nd, Gd and Y) elements above the solubility limit of α-Mg matrix generate at least one type of Mg-RE-intermetallic phase. At high RE contents, large volume fraction of intermetallic phases may form. They are all nobler compared to the matrix and thus they induce micro-galvanic corrosion.

- Mg-Gd system was selected from the binary alloys because Gd has a higher solubility in Mg, and because its passivation behaviour in Cl^- ions containing solutions is better. Latter might be transferred to the alloy. Furthermore the corrosion performance in the as-cast condition indicated that it might be possible to switch from active to passive states with smaller microstructural modifications, thus being a suitable demonstrator alloy.

- Mg10Gd in the as-cast condition has shown enhanced corrosion resistance, due to the presence of Gd enrichment zones, which reduce the galvanic corrosion between the Mg_5Gd phase and α- Mg matrix and thus localised corrosion attack.

- Heat treatment of Mg10Gd improves its corrosion resistance only when a uniform microstructure is obtained allowing the formation of stable oxide films.

- Addition of Mn to Mg10Gd improves the corrosion resistance. Gd and Mn act in a complementary way in terms of corrosion resistance as no new phases are formed, which generate micro-galvanic corrosion and moreover Mn improves the passive film formation on the surface decreasing the negative effect of Gd addition.

- The presence of Mn in the $Mg_5Gd(Mn)$ is beneficial because the electrochemical properties of this phase indicate that this phase is more active and degrades even faster than the Mg matrix and as soon as it dissolves the galvanic effects are minimizing and the matrix is already protected.

- Passive layers on Mg10Gd1Mn were composed mainly of two layers, the outer layer consisting of manganese oxides with gadolinium oxides/hydroxides and the inner layer based on magnesium oxide and hydroxide with traces of magnesium carbonate. The passive layer has good adhesion, is compact and dense. Gd content in the surface layer increases with the Mn addition.

With these studies a tool box was generated offering some general alloying design rules:

- Prevent excessive formation of RE intermetallics
- Prevent eutectic microstructure
- Create an uniform microstructure and small precipitates
- Selection of the intermetallics with similar electrochemical properties compared to the matrix if not, possible intermetallics with higher dissolution rate that permit to degrade faster enough to allow to matrix to protect itself
- Use alloying elements that promote protective oxide formation without changing microstructure.

Following these design rules for the Mg-Gd system this would imply to reduce the Gd content and maintain the Mn addition. To demonstrate that this improves the corrosion performance Mg5Gd1Mn alloy was casted and tested by EIS. As demonstrated in Figure 4.65 a much better corrosion performance was observed, suggesting that the same principles can be transferred to more Mg-RE alloy systems to improve their corrosion resistance.

7. Bibliography

1. E. Ghali, W. Dietzel, K.U. Kainer, *General and localized corrosion of magnesium alloys: A critical review,* Journal of Materials Engineering and Performance, 2004,. **13**(1): p. 7-23.
2. G.L. Makar, J. Kruger, *Corrosion of magnesium,* International Materials Reviews, 1993, **38**(3): p. 138-153.
3. G.L. Song, A. Atrens, *Corrosion Mechanisms of Magnesium Alloys,* Advanced Engineering Materials, 1999, **1**(1): p. 11-33.
4. G.L. Song, A. Atrens, *Understanding Magnesium Corrosion—A Framework for Improved Alloy Performance,* Advanced Engineering Materials, 2003, **5**(12): p. 837-858.
5. G.L. Song, A. Atrens, D. St. John, J. Nairn, Y. Li, *The electrochemical corrosion of pure magnesium in 1 N NaCl,* Corrosion Science, 1997, **39**(5): p. 855-875.
6. K.N. Reichek, K.J. Clark, J.E. Hillis, *Controlling the Salt Water Corrosion Performance of Magnesium AZ91 Alloy*, 1985, SAE.
7. G. Song, A. Atrens, M. Dargusch, *Influence of microstructure on the corrosion of diecast AZ91D,* Corrosion Science, 1998, **41**(2): p. 249-273.
8. G. Song, A. Atrens, D. St. John, X. Wu, J. Nairn, *The anodic dissolution of magnesium in chloride and sulphate solutions,* Corrosion Science, 1997, **39**(10–11): p. 1981-2004.
9. M.d.R. Silva Campos, N. Scharnagl, C. Blawert, K.U. Kainer, *Improving Corrosion Resistance of Mg10Gd Alloy*, *Materials Science Forum*, 2013, **765**: p.673-677.
10. O. Lunder, K. Nisancioglu, R.S. Hansen, *Corrosion of die cast magnesium-aluminum alloys*, 1993, SAE Technical Paper.
11. S.J. Splinter, N.S. McIntyre, *The initial interaction of water vapour with Mg-Al alloy surfaces at room temperature,* Surface Science, 1994, **314**(2): p. 157-171.
12. F. Zucchi, V. Grassi, A. Frignani, C. Monticelli, G. Trabanelli, *Electrochemical behaviour of a magnesium alloy containing rare earth elements,* Journal of Applied Electrochemistry, 2005, **36**(2): p. 195-204.
13. R. Silva Campos, D. Höche, C. Blawert, K.U. Kainer, *Influence of Lanthanum Concentration on the Corrosion Behaviour of Binary Mg-La Alloys*, in *Magnesium Technology 2011*, John Wiley & Sons, Inc. p. 507-511.
14. N. Hort, Y. Huang, D. Fechner, M. Störmer, C. Blawert, F. Witte, C. Vogt, H. Drücker, R. Willumeit, K.U. Kainer, F. Feyerabend, *Magnesium alloys as implant materials – Principles of property design for Mg–RE alloys,* Acta Biomaterialia, 2010, **6**(5): p. 1714-1725.
15. N. Birbilis, M.A. Easton, A.D. Sudholz, S.M. Zhu, M.A. Gibson, *On the corrosion of binary magnesium-rare earth alloys,* Corrosion Science, 2009, **51**(3): p. 683-689.
16. M. Liu, P. Schumtz, P.J. Uggowitzer, G. Song, A. Atrens, *The influence of yttrium (Y) on the corrosion of Mg–Y binary alloys,* Corrosion Science, 2010, **52**(11): p. 3687-3701.

17. A.D. Sudholz, K. Gusieva, X.B. Chen, B.C. Muddle, M.A. Gibson, N. Birbilis, *Electrochemical behaviour and corrosion of Mg–Y alloys,* Corrosion Science, 2011. **53**(6): p. 2277-2282.
18. F. Rosalbino, E. Angelini, S. De Negri, A. Saccone, S. Delfino, *Electrochemical behaviour assessment of novel Mg-rich Mg–Al–RE alloys (RE=Ce, Er),* Intermetallics, 2006, **14**(12): p. 1487-1492.
19. Z. Shi, F. Cao, G.L. Song, M. Liu, A. Atrens, *Corrosion behaviour in salt spray and in 3.5% NaCl solution saturated with Mg(OH)2 of as-cast and solution heat-treated binary Mg–RE alloys: RE=Ce, La, Nd, Y, Gd.* Corrosion Science, 2013. **76**(0): p. 98-118.
20. T. Takenaka, T. Ono, Y. Narazaki, Y. Naka, M. Kawakami, *Improvement of corrosion resistance of magnesium metal by rare earth elements,* Electrochimica Acta, 2007, **53**(1): p. 117-121.
21. E.D. Morales, E. Ghali, N. Hort, W. Dietzel, K.U. Kainer, *Corrosion Behaviour of Magnesium Alloys with RE Additions in Sodium Chloride Solutions,* Materials Science Forum, 2003, **419-422**: p. 867-872.
22. M.J. Nayyeri, F. Khomamizadeh, *Effect of RE elements on the microstructural evolution of as cast and SIMA processed Mg–4Al alloy,* Journal of Alloys and Compounds, 2011, **509**(5): p. 1567-1572.
23. W.Unsworth, *The role of rare earth elements in the development of magnesium base alloys,* International Journal of Materials and Product Technology, 1989, **4**(4): p. 359-378.
24. W. Liu, F. Cao, L. Zhong, L. Zheng, B. Jia, Z. Zhang, J. Zhang, *Influence of rare earth element Ce and La addition on corrosion behavior of AZ91 magnesium alloy.* Materials and Corrosion, 2009, **60**(10): p. 795-803.
25. M. Pourbaix, *Atlas of electrochemical equilibria in aqueous solutions*, 1974: National Association of Corrosion Engineers.
26. X. Zhao, L.L. Shi, J. Xu, *A Comparison of Corrosion Behavior in Saline Environment: Rare Earth Metals (Y, Nd, Gd, Dy) for Alloying of Biodegradable Magnesium Alloys,* Journal of Materials Science & Technology, 2013, **29**(9): p. 781-787.
27. H. Bala, S. Szymura, G. Pawlowska, *Effect of impurities on the corrosion behaviour of neodymium,* Journal of Applied Electrochemistry, 1993, **23**(10): p. 1017-1024.
28. L. Lee, N.D. Greene, *Corrosion Characteristics Of the Rare Earth and Yttrium Metals,* Corrosion, 1964, **20**(5): p. 145t-149t.
29. N.D. Greene, F.G. Hodge, *Oxidation Characteristics of the Lanthanide Metals,* Corrosion, 1966, **22**(7): p. 206-213.
30. L.L. Shreir, R.A. Jarman, G.T. Burstein, *Corrosion: Metal/environment reactions*. 1994: Butterworth-Heinemann.

31. R.W. Murray, J.E. Hillis, *Magnesium finishing: chemical treatment and coating practices*, 1990, SAE Technical Paper.

32. K.U. Kainer, P.B. Srinivasan, C. Blawert, W. Dietzel, *Corrosion of Magnesium and its Alloys*, in *Shreir's Corrosion*, 2010, Elsevier Oxford, p. 2011-2041.

33. J.E. Gray, B. Luan, *Protective coatings on magnesium and its alloys_a critical review,* Journal of Alloys and Compounds, 18 April 2002, **336**(1-2): p. 88-113.

34. H.H. Uhlig, R.W. Revie, *Corrosion and corrosion control: an introduction to corrosion science and engineering*, 1985, Ed. John Wiley & Sons Inc..

35. F. Habashi, *Alloys: preparation, properties, applications*, Ed. Wiley-VCH, 1998.

36. J.D. Hanawalt, C. E. Nelson, J. A. Peloubet, *Corrosion studies of magnesium and its alloys*, 1942.

37. G.L. Makar, J. Kruger, *Corrosion studies of rapidly solidified magnesium alloys,* Journal of the Electrochemical Society, 1990, **137**(2): p. 414-421.

38. R. Ambat, , N.N. Aung, W. Zhou, *Studies on the influence of chloride ion and pH on the corrosion and electrochemical behaviour of AZ91D magnesium alloy,* Journal of Applied Electrochemistry, 2000, **30**(7): p. 865-874.

39. A. Pardo, M.C. Merino, A.E. Coy, R. Arrabal, F. Viejo, E. Matykina, *Corrosion behaviour of magnesium/aluminium alloys in 3.5wt.% NaCl,* Corrosion Science, 2008, **50**(3): p. 823-834.

40. A. Atrens, R. Coade, J. Allison, H. Kohl, G. Hochoertler, G. Krist, Mater. Forum, 1993, **17**: p. 263.

41. R.C. Zeng, J. Zhang, W.J. Huang, W. Dietzel, K.U. Kainer, C. Blawert, W. Ke,, *Review of studies on corrosion of magnesium alloys,* Transactions of Nonferrous Metals Society of China, 2006, **16, Supplement 2**(0): p. s763-s771.

42. D. Thirumalaikumarasamy, K. Shanmugam, V. Balasubramanian, *Influence of pH, chloride ion concentration and exposure time on the electrochemical corrosion behaviour of AZ31B,* International Journal of Emerging Technology and Advanced Engineering, 2013, **3**(2): p. 308-320.

43. D. Thirumalaikumarasamy, K. Shanmugam, V. Balasubramanian, *Developing an Empirical Relationship to Predict Corrosion Rate of AZ31B Magnesium Alloy under Sodium Chloride Environment.* Transactions of the Indian Institute of Metals, 2014. **67**(1): p. 19-32.

44. W.S. Loose, *Method of protecting magnesium and its alloys from corrosion*, 1943, US Patent 2, 313, 754.

45. H. Hu, X. Nie, Y. Ma, *Corrosion and Surface Treatment of Magnesium Alloys, Intech* 2014, DOI: 10.5772/58929

46. A.J. Bard, J. Faulkner, R. Larry, *Electrochemical methods: fundamentals and applications*, Vol. 2, 1980, Wiley New York.

47. R. Chang, *Physical chemistry for the chemical and biological sciences*, 2000, University Science Books.

48. R. Tunold, H. Holtan, M-B. Hägg Berge, A. Lasson, R. Steen-Hansen, *The corrosion of magnesium in aqueous solution containing chloride ions,* Corrosion Science, 1977, **17**(4): p. 353-365.

49. G.L. Song, *Corrosion of Magnesium Alloys*, 2011, Woodhead Publishing Limited.

50. A. Froats, T. Kr. Aune, D. Hawke, W. Unsworth, J. Hillis, *Corrosion of magnesium and magnesium alloys,* ASM Handbook, 1987, **13**: p. 740-754.

51. D.L. Albright, C. Suman, *Understanding Corrosion in Magnesium Die Casting Alloys*, Society of Automotive Engineers 1988.

52. NACE, *Localized corrosion*, 1974.

53. E. Ghali, *Corrosion and Protection of Magnesium Alloys,* Materials Science Forum, 2000, **350-351**: p. 261-272.

54. E.F. Emley, *Principles of Magnesium Technology*, 1966, Pergamon Press Ltd.

55. R.P. Wei, *Subcritical Crack Growth: Stress Corrosion Cracking and Fatigue Crack Growth (Phenomenology),* 2010, Cambridge University Press.

56. S. Lebouil, A. Duboin, F. Monti, P. Tabeling, P. Volovitch, K. Ogle, *A novel approach to on-line measurement of gas evolution kinetics: Application to the negative difference effect of Mg in chloride solution,* Electrochimica Acta, 2014, **124**: p. 176-182.

57. G.G. Perrault, *Potentiostatic study of the magnesium electrode in aqueous solutio,.* Journal of Electroanalytical Chemistry and Interfacial Electrochemistry, 1970, **27**(1): p. 47-58.

58. L.M. Petrova, V.V. Krasnoyarskii, *Anodic dissolution of magnesium in river water.* Prot. Met. (Engl. Transl. United States) **22:4**; Translated from Zashch. Met.; 22: No. 4, 578-581(Jul-Aug 1986), 1987: p. 463-465.

59. C.H. Brun, J. Pagetti, J. Talbot, *Investigation of the Corrosion of Magnesium in Aqueous Solutions of 3 wt% Sodium Chloride at Room Temperatur,* Mem Sci Rev Metall, 1976, **73**(10): p. 659-668.

60. O. Fruhwirth, G. W. Herzog, I. Hollerer, A. Rachetti, *Dissolution and hydration kinetics of MgO,* Surface Technology, 1985, **24**(3): p. 301-317.

61. G.G. Perrault, *The potential-pH diagram of the magnesium-water system,* Journal of Electroanalytical Chemistry and Interfacial Electrochemistry, 1974, **51**(1): p. 107-119.

62. J. Kruger, G.L. Makar, K. Sieradzki, *A Fundamental Understanding of the Effect of Alloying Elements on the Corrosion Resistance of Rapidly Solidified Mg Alloys*. 1989, Report, Airforce office of scientific reseach.

63. J. Przyļuski, E. Paļka, *Untersuchung der Kinetik der anodischen oxydation des magnesiums in einer ammoniumchloridlösung,* Electrochimica Acta, 1970, **15**(5): p. 853-864.

64. P. Brouillet, I. Epelboin, M. Formet, *Détermination de la valence des ions métalliques au cours du polissage électrolytique en présence d'ions ClO4,* Comptes rendus hebdomadaires des séances de l'Académie des sciences, 1954, **39**: p. 1795-1797.

65. R.L. Petty, A.W. Davidson, J. Kleinberg, *The Anodic Oxidation of Magnesium Metal: Evidence for the Existence of Unipositive Magnesium1,2,* Journal of the American Chemical Society, 1954, **76**(2): p. 363-366.

66. E. Gulbrandsen, J. Taftø, A. Olsen, *The passive behaviour of Mg in alkaline fluoride solutions. Electrochemical and electron microscopical investigations,* Corrosion Science, 1993, **34**(9): p. 1423-1440.

67. E. Gulbrandsen, *Anodic behaviour of Mg in HCO−3/CO2−3 buffer solutions. Quasi-steady measurements,* Electrochimica Acta, 1992, **37**(8): p. 1403-1412.

68. D. Höche, C. Blawert, S.V. Lamaka, N. Scharnagl, C.L. Mendis, M.L. Zheludkevich, *Effect of iron re-deposition on corrosion of impurity-containing magnesium,* Physical Chemistry Chemical Physics, 2015.

69. M.R. Gennero de Chialvo, A.C. Chialvo, *Kinetics of hydrogen evolution reaction with Frumkin adsorption: re-examination of the Volmer–Heyrovsky and Volmer–Tafel routes,* Electrochimica Acta, 1998, **44**(5): p. 841-851.

70. J.E. Hillis, *The Effects of Heavy Metal Contamination on Magnesium Corrosion Performance*,1998, SAE.

71. J.E. Hillis, R.W. Murray. *Finishing alternatives for high purity magnesium alloys*, in *SDCE 14 th International Die Casting Congress and Exposition*, 1987.

72. K. Bühler, *Korrosion und Korrosionsschutz von Magnesiumlegierungen.* Metalwissenschaft and Technik, 1990, **8**: p. 749.

73. F. Habashi, *Alloys: Preparation, Properties, Applications*. 2008, Wiley-Vch.

74. ASM Handbook*, Volume 02 - Properties and Selection: Nonferrous Alloys and Special-Purpose Materials*. 1990, ASM International Handbook Committee.

75. B.L. Mordike, T. Ebert, *Magnesium: Properties — applications — potential.* Materials Science and Engineering: A, 2001, **302**(1): p. 37-45.

76. A. Luo, M.O. Pekguleryuz, *Cast magnesium alloys for elevated temperature applications.* Journal of Materials Science, 1994 **29**(20): p. 5259-5271.

77. J. Victoria-Hernandez, D. Hernandez-Silva, J. Bohlen, S.B. Yi, D. Letzig, *Low Temperature Superplasticity of Hydrostatically Extruded Mg-Al-Zn alloys*, *Materials Science Forum*, 2013 **735**: p. 307-315.

78. T. Zhang, Y. Li, F. Wang, *Roles of β phase in the corrosion process of AZ91D magnesium alloy,* Corrosion Science, 2006 **48**(5): p. 1249-1264.

79. H. Cao, M. Wessén, *Effect of microstructure on mechanical properties of as-cast Mg-Al alloys,* Metallurgical and Materials Transactions A, 2004 **35**(1): p. 309-319.

80. N.D. Nam, W.C. Kim, J.G. Kim, K.S. Shin, H.C. Jung, *Corrosion resistance of Mg–5Al–xSr alloys,* Journal of Alloys and Compounds, 2011 **509**(14): p. 4839-4847.
81. J.E. Hillis, S.O. Shook, Engineers, *Composition and Performance of an Improved Magnesium AS41 Alloy*, 1989, SAE.
82. E.M. García, *Influence of alloying elements on the microstructure and mechanical properties of extruded Mg-Zn based alloys*, Doctoral thesis, Technische Universität Berlin, 2010.
83. O. Lunder, J.E. Lein, T. Kr. Aune, K. Nisancloglu, *The Role of Mg17Al12 Phase in the Corrosion of Mg Alloy AZ91,* Corrosion, 1989 **45**(9): p. 741-748.
84. L.L. Rokhlin, *Magnesium Alloys Containing Rare Earth Metals: Structure and Properties*, 2003,Taylor & Francis.
85. M. Zamin, *The Role of Mn in the Corrosion Behavior of Al-Mn Alloys,* Corrosion 1981 **37**(11): p. 627-632.
86. O. Lunder, T.K. Aune, K. Nisancioglu, *Effect of Mn Additions on the Corrosion Behavior of Mould-Cast Magnesium ASTM AZ91,* Corrosion, 1987 **43**(5): p. 291-295.
87. C.E. Nelson, *The melting and refining of magnesium,*Transactions of the American Institute of Mining and Metallurgical Enginners, 1944 **159**: p. 16.
88. I.J. Polmear, *Physical metallurgy of magnesium alloys.* Magnesium Alloys and Their Applications, 1992: p. 201-212.
89. H.A. Robinson, P.F. George, *Effect of Alloying and Impurity Elements In Magnesium Alloy Cast Anodes,* Corrosion, 1954 **10**(6): p. 182-188.
90. D.S. Tawil, *Protection of magnesium componentes for the military environment*, in Proceedings of the 1989 Tri-Service Conference on Corrosion, 1989. Atlantic City, Naval Air Deveolpment Center.
91. R. Arrabal, A. Pardo, M.C. Merino, K. Paucar, M. Mohedano, P. Casajus, G. Garces, *Influence of Gd on the Corrosion Behavior of AM50 and AZ91D Magnesium Alloys.* Corrosion, 2012 **68**(5): p. 398-410.
92. R. Arrabal, E. Matykina, A. Pardo, M.C. Merino, K. Paucar, M. Mohedano, P. Casajus, *Corrosion behaviour of AZ91D and AM50 magnesium alloys with Nd and Gd additions in humid environments.* Corrosion Science, 2012 **55**: p. 351-362.
93. R. Arrabal, A. Pardo, M.C. Merino, M. Mohedano, P. Casajus, K. Paucar, E. Matykina, *Oxidation Behavior of AZ91D Magnesium Alloy Containing Nd or Gd.* Oxidation of Metals, 2011 **76**(5-6): p. 433-450.
94. M. Mohedano, R. Arrabal, A. Pardo, K. Paucar, M.C. Merino, E. Matykina, B. Mingo, G. Garces, *Galvanic corrosion of rare earth modified AM50 and AZ91D magnesium alloys coupled to steel and aluminium alloys,* Revista De Metalurgia, 2014 **50**(1): p. e002.

95. Y. Ding, C. Wen, P. Hodgson, Y. Li, *Effects of alloying elements on the corrosion behavior and biocompatibility of biodegradable magnesium alloys: a review,* Journal of Materials Chemistry B, 2014, **2**(14): p. 1912-1933.

96. Y. Fan, G. Wu, H. Gao, G. Li, C. Zhai, *Influence of lanthanum on the microstructure, mechanical property and corrosion resistance of magnesium alloy,* Journal of materials science, 2006 **41**(17): p. 5409-5416.

97. J. Zhang, D. Zhang, Z. Tian, J. Wang, K. Liu, H. Lu, D. Tang, J. Meng, *Microstructures, tensile properties and corrosion behavior of die-cast Mg–4Al-based alloys containing La and/or Ce,* Materials Science and Engineering: A, 2008 **489**(1–2): p. 113-119.

98. M. Yamasaki, N. Hayashi, S. Izumi, Y. Kawamura, *Corrosion behavior of rapidly solidified Mg–Zn–rare earth element alloys in NaCl solution,* Corrosion Science, 2007 **49**(1): p. 255-262.

99. Q. Peng, J. Wang, Y. Wu, J. Meng, L. Wang, *The effect of La or Ce on ageing response and mechanical properties of cast Mg–Gd–Zr alloys,* Materials Characterization, 2008 **59**(4): p. 435-439.

100. X. Zhang, D. Kevorkov, M. Pekguleryuz, *Stoichiometry study on the binary compounds in the Mg–Ce system—Part I,* Journal of Alloys and Compounds, 2009 **475**(1–2): p. 361-367.

101. A.-r. Wu, C.-q. Xia, *Study of the microstructure and mechanical properties of Mg-rare earth alloys,* Materials & Design, 2007 **28**(6): p. 1963-1967.

102. F. Mert, C. Blawert, K.U. Kainer, N. Hort, *Influence of cerium additions on the corrosion behaviour of high pressure die cast AM50 alloy,* Corrosion Science, 2012 **65**(0): p. 145-151.

103. M. Heilig, D. Zander, D. Olson, B. Mishra, N. Hort, G. Klaus, A. Buehrig-Polaczek, J. Gröbner, R. Schmid-Fetzer, *Microstructure and Corrosion of AZ91D with Small Amounts of Cerium*, *Magnesium Technology 2010,* Seattle, TMS 2010.

104. H.F. Gao, H.Q. Tan, Y. Q. Wang, J.Q. Xun, *Synergistic effect of cerium conversion coating and phytic acid conversion coating on AZ31B magnesium alloy,* Surface and Coatings Technology, 2012 **212**(0): p. 32-36.

105. W. Liu, F. Cao, L. Chang, Z. Zhang, J. Zhang, *Effect of rare earth element Ce and La on corrosion behavior of AM60 magnesium alloy,* Corrosion Science, 2009 **51**(6): p. 1334-1343.

106. W. Liu, F. Cao, A. Chen, L. Chang, J. Zhang, C. Cao, *Corrosion behaviour of AM60 magnesium alloys containing Ce or La under thin electrolyte layers. Part 1. Microstructural characterization and electrochemical behaviour.* Corrosion Science, 2010 **52**: p. 627-638.

107. W. Steurer, *Crystal structure of the metallic elements,* Physical metallurgy, 1996 **4**: p. 1-46.

108. X. Zhang, Y.J. Li, K. Zhang, C.S. Wang, H.W. Li, M.L. Ma, B.D. Zhang, *Corrosion and electrochemical behavior of Mg–Y alloys in 3.5% NaCl solution,* Transactions of Nonferrous Metals Society of China, 2013, **23**(5): p. 1226-1236.

109. Xu, D.K., et al., *The influence of element Y on the mechanical properties of the as-extruded Mg–Zn–Y–Zr alloys.* Journal of Alloys and Compounds, 2006. **426**(1–2): p. 155-161.

110. D.K. Xu, W.N. Tang, L. Liu, Y.B. Xu, E.H. Han, *Effect of Y concentration on the microstructure and mechanical properties of as-cast Mg–Zn–Y–Zr alloys,* Journal of Alloys and Compounds, 2007 **432**(1–2): p. 129-134.

111. X. Zhang, K. Zhang, X. Deng, H. Li, Y. Li, M. Ma, N. Li, Y. Wang, *Corrosion behavior of Mg–Y alloy in NaCl aqueous solution,* Progress in Natural Science: Materials International, 2012 **22**(2): p. 169-174.

112. A.C. Hänzi, P. Gunde, M. Schinhammer, P. J. Uggowitzer, *On the biodegradation performance of an Mg–Y–RE alloy with various surface conditions in simulated body fluid,* Acta Biomaterialia, 2009 **5**(1): p. 162-171.

113. Magnesium Elektron Ltd., *Elektron 21 Datasheet 455,* 2014; Available from: http://www.magnesium-elektron.com/sites/default/files/Elektron%2021.pdf.

114. Standard AMS4429, *Magnesium Alloy Castings, Sand 2.8Nd 1.4Gd 0.4Zn 0.6Zr, Solution and Precipitation Heat Treated*, 2004, SAE International.

115. J. Nicholas, *High-performance magnesium, J.* Advanced Materials and Processes, 2005 **163**(9): p. 65-67.

116. B.E. Placzankis, J.P. Labukas, E. Charleton, C.E. Miller, *Corrosion Screening of EV31A Magnesium and Other Magnesium Alloys using Laboratory-Based Accelerated Corrosion and Electro-Chemical Methods*, 2014, DTIC Document.

117. A.S. Hamdy, I. Doench, H. Möhwald, *The effect of vanadia surface treatment on the corrosion inhibition characteristics of an advanced magnesium Elektron 21 alloy in chloride media,* International Journal of Electrochemical Science, 2012 **7**(9): p. 7751-7761.

118. K.C. Tekin, U. Malayoğlu, S. Shrestha, *Electrochemical behavior of plasma electrolytic oxide coatings on rare earth element containing Mg alloys,* Surface and Coatings Technology, 2013 **236**: p. 540-549.

119. Magnesium Elektron Ltd., *Elektron WE54 Datasheet 466*, 2014; Available from: http://www.magnesium-elektron.com/sites/default/files/Elektron%20WE54.pdf.

120. O. Kazum, M. Bobby Kannan, N. Scharnagl, C. Blawert, Y. He, *Electrochemical corrosion behaviour of WE54 magnesium alloy*, *Materials Science Forum*, 2013. **765**: p. 644-647

121. L.B. Duffy, *The development of magnesium sand casting alloys,* Foundry Trade Journal, 1991 **165**(3432): p. 319-321.

122. ASTM, *B117-90 Standard Test Method of Salt Spray (Fog) testing*.
123. A.E. Coy, F. Viejo, P. Skeldon, G. E. Thompson, *Susceptibility of rare-earth-magnesium alloys to micro-galvanic corrosion,* Corrosion Science, 2010 **52**(12): p. 3896-3906.
124. G.L. Song, *Corrosion prevention of magnesium alloys*, Woodhead Publishing Ltd., 2013.
125. AZOMaterials. *Grade ZE41 magnesium alloy*, 2013; Available from: http://www.azom.com/article.aspx?ArticleID=9966#6.
126. W.C. Neil, M. Forsyth, P.C. Howlett, C.R. Hutchinson, B.R.W. Hinton, *Corrosion of magnesium alloy ZE41 – The role of microstructural features* Corrosion Science, 2009 **51**(2): p. 387-394.
127. J. Chang, X. Guo, S. He, P. Fu, L. Peng, W. Ding, *Investigation of the corrosion for Mg–xGd–3Y–0.4Zr (x = 6, 8, 10, 12 wt%) alloys in a peak-aged condition,* Corrosion Science, 2008 **50**(1): p. 166-177.
128. G. Ben-Hamu, D. Eliezer, K. S. Shin, S. Cohen, *The relation between microstructure and corrosion behavior of Mg–Y–RE–Zr alloys.* Journal of Alloys and Compounds, 2007 **431**(1–2): p. 269-276.
129. M. Bobby Kannan, C. Blawert, W. Dietzel, *Electrochemical corrosion behaviour of ZE41 and QE22 magnesium alloys*, *Materials Science Forum*, 2011 **670**: p. 385-388.
130. J.H. Nordlien, K. Nisancioglu, S. Ono, N. Masuko, *Morphology and Structure of Water-Formed Oxides on Ternary MgAl Alloys,* Journal of The Electrochemical Society, 1997 **144**(2): p. 461-466.
131. S. Krishnamurthy, M. Khobaib, E. Robertson, F.H. Froes, *Corrosion behavior of rapidly solidified Mg-Nd and Mg-Y alloys,* Materials Science and Engineering, 1988 **99**(1): p. 507-511.
132. Magnesium Elektron Ltd., *Elektron RZ5/ZE41 Datasheet 452,* 2015; Available from: http://www.magnesium-elektron.com/sites/default/files/Elektron%20RZ5.pdf.
133. J.C. Mcdonald, *Magnesium base alloy*, 1942, Dow Chemical Co., U.S.A.
134. Y. Feng, R. Wang, H. Liu, Z. Jin, *Thermodynamic reassessment of the magnesium–gallium system,* Journal of Alloys and Compounds, 2009 **486**(1–2): p. 581-585.
135. D.O. Flamini, S.B. Saidman, J.B. Bessone, *Aluminium activation produced by gallium,* Corrosion Science, 2006 **48**(6): p. 1413-1425.
136. Y. Feng, R.-c. Wang, C.-q. Peng, *Influence of freezing rate on microstructure and electrochemical properties of Mg-2%Ga alloys,*Transactions of Nonferrous Metals Society of China, 2011 **21**(5): p. 1047-1051.
137. Y. Feng, R. C. Wang, K. Yu, C. Q. Peng, W. X. Li, *Influence of Ga content on electrochemical behavior of Mg-5 at%Hg anode materials,* Materials Transactions, 2008 **49**(5): p. 1077-1080.

138. H.B. Liu, G.H. Qi, Y.T. Ma, H. Hao, F. Jia, S.H. Ji, H.Y. Zhang, X.G. Zhang, *Microstructure and mechanical property of Mg–2.0Ga alloys,* Materials Science and Engineering: A, 2009 **526**(1–2): p. 7-10.
139. L.R. Bernstein, *Mechanisms of Therapeutic Activity for Galliu,* Pharmacological Reviews, 1998 **50**(4): p. 665-682.
140. J. Kubásek, D. Vojtěch, *Structure, mechanical properties, corrosion behavior and cytotoxicity of biodegradable Mg–X (X=Sn, Ga, In) alloys,* Materials Science and Engineering: C, 2013 **33**(4): p. 2421-2432.
141. Y. Song, D. Shan, R. Chen, E.-H. Han, *Corrosion characterization of Mg–8Li alloy in NaCl solution,* Corrosion Science, 2009 **51**(5): p. 1087-1094.
142. F. Witte, J. Fischer, J. Nellesen, C. Vogt, J. Vogt, T. Donath, F. Beckmann, *In vivo corrosion and corrosion protection of magnesium alloy LAE442,* Acta Biomaterialia, 2010 **6**(5): p. 1792-1799.
143. T.-C. Chang, J.-Y. Wang, C.-L. Chu, S. Lee, *Mechanical properties and microstructures of various Mg–Li alloys,* Materials Letters, 2006, **60**(27): p. 3272-3276.
144. R.K. Singh Raman, *The role of microstructure in localized corrosion of magnesium alloys,* Metallurgical and Materials Transactions A, 2004 **35**(8): p. 2525-2531.
145. D. Hawke, L. Hillis, E. James, W. Unsworth, *Preventive practice for controlling the galvanic corrosion of magnesium alloys*, 1988, McLean, International Magnesium Association.
146. T.K. Aune, *Minimizing base metal corrosion on magnesium products. The effect of element distribution (structure) on corrosion behavior*, in *Proceedings of the 40th World Magnesium Conference*, 1983, Toronto
147. Z. Shi, M. Liu, A. Atrens, *Measurement of the corrosion rate of magnesium alloys using Tafel extrapolation,* Corrosion Science, 2010 **52**(2): p. 579-588.
148. Z. Shi, A. Atrens, *An innovative specimen configuration for the study of Mg corrosion,* Corrosion Science, 2011 **53**(1): p. 226-246.
149. G102-89 A, *Standard Practice for Calculation of Corrosion Rates and Related Information from Electrochemical Measurements*, 1999, ASTM International West Conshohocken, Pa.
150. R. Baboian, *Electrochemical techniques for corrosion engineering,* 1987, NACE.
151. T. Ferreira da Conceicao, *Corrosion protection of magnesium AZ31 alloy sheets by polymer coatings,* Doctoral thesis, Technische Universität Berlin, 2011.
152. T.L. Chia, M. A. Easton, S. M. Zhu, M. A. Gibson, N. Birbilis, J. F Nie, *The effect of alloy composition on the microstructure and tensile properties of binary Mg-rare earth alloys,* Intermetallics, 2009 **17**(7): p. 481-490.

153. L.L. Rokhlin, *Regularities of the Mg sides of the Mg-RE (magnesium-rare earth metal) phase diagrams: Comments on evaluations,* Journal of Phase Equilibria, 1995 **16**(6): p. 504-507.

154. A. Berche, P. Benigni, J. Rogez, M.-C. Record, *Re-investigation of the La–Mg phase diagram,* Journal of Thermal Analysis and Calorimetry, 2012 **107**(2): p. 797-807.

155. M. Giovannini, A. Saccone, R. Marazza, R. Ferro, *The isothermal section at 500 °C of the Y-La-Mg ternary system,* Metallurgical and Materials Transactions A, 1995 **26**(1): p. 5-10.

156. H. Baker, *Magnesium and Magnesium Alloys*, 1999, ASM International.

157. K.C. Park, B. H. Kim, Y. H. Park, I. M. Park, *Evaluation of microstructure and mechanical properties of Mg-xCe-0.5Zn alloys by nano-indentation,* Transactions of Nonferrous Metals Society of China, 2010 **20**(7): p. 1240-1243.

158. H. Okamoto, *Dy-Mg (dysprosium-magnesium),* Journal of Phase Equilibria, 1992 **13**(2): p. 214-216.

159. Y. Wu, W. Hu, *Comparison of the Solid Solution Properties of Mg-RE (Gd, Dy, Y) Alloys with Atomistic Simulation,* Research Letters in Physics, 2008 **2008**: p. 4.

160. H. Okamoto, *Mg-Y (magnesium-yttrium),* Journal of Phase Equilibria, 1992 **13**(1): p. 105-106.

161. M. Hampl, C. Blawert, M. R. Silva Campos, N. Hort, Q. Peng, K. U. Kainer, R. Schmid-Fetzer, *Thermodynamic assessment and experimental study of Mg–Gd alloys,* Journal of Alloys and Compounds, 2013 **581**(0): p. 166-177.

162. H. Okamoto, *Gd-Mg (Gadolinium-Magnesium),* Journal of Phase Equilibria, 1993 **14**(4): p. 534-535.

163. J. Liang, P. Bala Srinivasan, C. Blawert, W. Dietzel, *Comparison of electrochemical corrosion behaviour of MgO and ZrO2 coatings on AM50 magnesium alloy formed by plasma electrolytic oxidation,* Corrosion Science, 2009 **51**(10): p. 2483-2492.

164. K. Zhang, X. Zhang, X. Deng, X. Li, M. Ma, *Relationship between extrusion, Y and corrosion behavior of Mg–Y alloy in NaCl aqueous solution,* Journal of Magnesium and Alloys, 2013 **1**(2): p. 134-138.

165. M. Zhang, W. Han, M. Zhang, F. Zhu, Y. Xue, Z. Zhang, *Electrochemical formation process and phase control of Mg-Li-Ce alloys in molten chlorides,* Journal of Rare Earths, 2013 **31**(6): p. 609-615.

166. M.A. Easton, M.A.Gibson, D. Qiu, S.M. Zhu, J. Gröbner, R. Schmid-Fetzer, J. F. Nie, M.X. Zhang, *The role of crystallography and thermodynamics on phase selection in binary magnesium–rare earth (Ce or Nd) alloys,* Acta Materialia, 2012 **60**(11): p. 4420-4430.

167. A.D. Südholz, N. Birbilis, C. J. Bettles, M.A. Gibson, *Corrosion behaviour of Mg-alloy AZ91E with atypical alloying additions,* Journal of Alloys and Compounds, 2009 **471**(1–2): p. 109-115.

168. C.H. Hsu, F. Mansfeld, *Technical Note: Concerning the Conversion of the Constant Phase Element Parameter Y0 into a Capacitance.*

169. Q. Peng, Y.Huang, J. Meng, Y. Li, K.U. Kainer, *Strain induced GdH2 precipitate in Mg–Gd based alloys,* Intermetallics, 2011, **19**(3): p. 382-389.

170. L. Yang, Y. Huang, Q. Peng, F. Feyerabend, K.U. Kainer, R. Willumeit, N. Hort, *Mechanical and corrosion properties of binary Mg–Dy alloys for medical applications,* Materials Science and Engineering: B, 2011 **176**(20): p. 1827-1834.

171. H.-z. Li, H.-t. Liu, F.-f. Guo, H.-j. Wang, X-p. Liang, C-m. Liu, *Effect of ageing time on corrosion behavior of Mg-10Gd-4.8Y-0.6Zr extruded-alloy,* Transactions of Nonferrous Metals Society of China, 2011 **21**(7): p. 1498-1505.

172. J. Gröbner, R. Schmid-Fetzer, *Thermodynamic modeling of the Mg–Ce–Gd–Y system,* Scripta Materialia, 2010 **63**(7): p. 674-679.

173. A. Srinivasan, Y. Huang, C. L. Mendis, C. Blawert, K. U. Kainer, N. Hort, *Investigations on microstructures, mechanical and corrosion properties of Mg–Gd–Zn alloys,* Materials Science and Engineering: A, 2014 **595**(0): p. 224-234.

174. R. Schmid-Fetzer, J. Gröbner, *Thermodynamic Database for Mg Alloys—Progress in Multicomponent Modeling,* Metals, 2012 **2**(3): p. 377-398.

175. J. Gröbner, A. Kozlov, X.-Y. Fang, S. Zhu, J.-F. Nie, M. A. Gibson, R. Schmid-Fetzer, *Phase equilibria and transformations in ternary Mg–Gd–Zn alloys,* Acta Materialia, 2015 **90**(0): p. 400-416.

176. M. Yamasaki, M. Sasaki, M. Nishijima, K. Hiraga, Y. Kawamura, *Formation of 14H long period stacking ordered structure and profuse stacking faults in Mg–Zn–Gd alloys during isothermal aging at high temperature,* Acta Materialia, 2007 **55**(20): p. 6798-6805.

177. O. Lunder, J. E. Lein, S. M. Hesjevik, T. Kr. Aune, K. Nişancioğlu, *Corrosion morphologies on magnesium alloy AZ91,* Materials and Corrosion, 1994 **45**(6): p. 331-340.

178. K. Wandelt, C.R. Brundle, *The interaction of oxygen with gadolinium: UPS and XPS studies,* Surface Science, 1985 **157**(1): p. 162-182.

179. A. Mortensen, *Concise encyclopedia of composite materials*, 2006, Elsevier.

180. G.-y. Adachi, N. Imanaka, *The binary rare earth oxides,* Chemical reviews, 1998 **98**(4): p. 1479-1514.

181. A.R. Bunsell, M.-H. Berger, A. Kelly, *Fine ceramic fibers,* Fine Ceramic Fibers, S, 1999: p. 1-62.

182. M.W. Chase, *NIST-JANAF thermochemical tables,* Journal of Physical and Chemical Reference Data, 1998.

183. P.J. Apps, H. Karimzadeh, J.F. King, G.W. Lorimer, *Phase compositions in magnesium-rare earth alloys containing yttrium, gadolinium or dysprosium,* Scripta Materialia, 2003 **48**(5): p. 475-481.

184. Q. Peng, Y. Wu, D. Fang, J. Meng, L. Wang, *Microstructures and Properties of Melt-Spun and As-Cast Mg-20Gd Binary Alloy,* Journal of Rare Earths, 2006 **24**(4): p. 466-470.

185. Q. Peng, N. Ma, H. Li, *Gadolinium solubility and precipitate identification in Mg-Gd binary alloy,* Journal of Rare Earths, 2012 **30**(10): p. 1064-1068.

186. Y.-F. Wang, W.-B. Zhang, Z.-Z. Wang, Y.-H. Deng, N. Yu, B.-Y. Tang, X.-Q. Zeng, W.-J. Ding, *First-principles study of structural stabilities and electronic characteristics of Mg–La intermetallic compounds,* Computational Materials Science, 2007 **41**(1): p. 78-85.

187. A.A. Nayeb-Hashemi, J.B. Clark, *La-Mg phase diagram,* Bulletin of Alloy Phase Diagrams, 1988 **9**(2): p. 197-198.

188. C. Guo, Z. Du, *Thermodynamic assessment of the La–Mg system,* Journal of Alloys and Compounds, 2004 **385**(1–2): p. 109-113.

189. I. Apachitei, L.E. Fratila-Apachitei, J. Duszczyk, *Microgalvanic activity of an Mg–Al–Ca-based alloy studied by scanning Kelvin probe force microscopy,* Scripta Materialia, 2007 **57**(11): p. 1012-1015.

190. A. Pardo, M.C. Merino, A.E. Coy, F. Viejo, R. Arrabal, S. Feliú, *Influence of microstructure and composition on the corrosion behaviour of Mg/Al alloys in chloride media,* Electrochimica Acta, 2008 **53**(27): p. 7890-7902.

191. M. Jönsson, D. Thierry, N. LeBozec, *The influence of microstructure on the corrosion behaviour of AZ91D studied by scanning Kelvin probe force microscopy and scanning Kelvin probe.* Corrosion Science, 2006. **48**(5): p. 1193-1208.

192. N. Perez, *Mixed Potential Theory*, in *Electrochemistry and Corrosion Science*, 2004, Springer US, p. 155-166.

193. S. Turgoose, R. Cottis, *Corrosion Testing Made Easy: Electrochemical Impedance and Noise.* Houston, TX), NACE International, 2000.

194. R. Pinto, M.G.S. Ferreira, M.J. Carmezim, M. F. Montemor, *Passive behavior of magnesium alloys (Mg–Zr) containing rare-earth elements in alkaline media,* Electrochimica Acta, 2010 **55**(7): p. 2482-2489.

195. F. Guadarrama-Muñoz, J. Mendoza-Flores, R. Duran-Romero, J. Genesca, *Electrochemical study on magnesium anodes in NaCl and CaSO4–Mg(OH)2 aqueous solutions,* Electrochimica Acta, 2006 **51**(8–9): p. 1820-1830.

196. S. Skale, V. Doleček, M. Slemnik, *Substitution of the constant phase element by Warburg impedance for protective coatings,* Corrosion Science, 2007 **49**(3): p. 1045-1055.

197. P. Maier, S. Müller, H. Dieringa, N. Hort, *Mechanical and corrosion properties of as-cast and extruded MG10GD alloy for biomedical application*, in *Magnesium Technology*, 2012.

198. P. Vostrý, B.Smola, I. Stulíková, F. von Buch, B.L. Mordike, *Microstructure Evolution in Isochronally Heat Treated Mg–Gd Alloys,* Physica Status Solidi (a), 1999 **175**(2): p. 491-500.

199. P.J. Apps, H.Karimzadeh, J. F. King, G.W. Lorimer, *Precipitation reactions in Magnesium-rare earth alloys containing Yttrium, Gadolinium or Dysprosium,* Scripta Materialia, 2003 **48**(8): p. 1023-1028.

200. K.U. Kainer, N. Hort, R. Willumeit, F. Feyerabend, *Magnesium Alloys for the Design of Medical Implants*, in *18th International Symposium on Processing and Fabrication of Advanced Materials*. 2009, Sendai, Japan.

201. G. Pettersen, H. Westengen, R. Høier, O. Lohne, *Microstructure of a pressure die cast magnesium—4wt.% aluminium alloy modified with rare earth additions,* Materials Science and Engineering: A, 1996 **207**(1): p. 115-120.

202. S. Li, W. Zheng, B. Tang, D. Zeng, X. Guo, *Grain Coarsening Behavior of Mg-Al Alloys with Mischmetal Addition,* Journal of Rare Earths, 2007 **25**(2): p. 227-232.

203. S.C. Zhang, B. K. Wei, Q. Z. Cai, L.S. Wang, *Effect of mischmetal and yttrium on microstructures and mechanical properties of Mg-Al alloy,* Transactions of Nonferrous Metals Society of China (English Edition), 2003 **13**(1): p. 83-87.

204. C. Guo, Z. Du, C. Li, *A thermodynamic description of the Gd–Mg–Y system,* Calphad, 2007 **31**(1): p. 75-88.

205. Y. Guo, J. Li, J. Li, Z. Yang, J. Zhao, F. Xia, M. Liang, *Mg–Gd–Y system phase diagram calculation and experimental clarification,* Journal of Alloys and Compounds, 2008 **450**(1–2): p. 446-451.

206. *Panda Software for Multicomponent phase diagram calculations and Materials Properties Simulation* 2014, Using Pan Mg 2014 database version 2014.2.

207. F. Zhang, B. Hu, H. Xu, S. Liu, T. Zhou, Z. Jin, *Experimental Investigation and Thermodynamic Calculation of the Phase Equilibria in the Mg-Gd-Mn Ternary System,* Metallurgical and Materials Transactions A, 2015 **46**(10): p. 4804-4811.

208. F. Cao, Z. Shi, G.-L. Song, M. Liu, A. Atrens, *Corrosion behaviour in salt spray and in 3.5% NaCl solution saturated with Mg(OH)2 of as-cast and solution heat-treated binary Mg–X alloys: X=Mn, Sn, Ca, Zn, Al, Zr, Si, Sr,* Corrosion Science, 2013 **76**(0): p. 60-97.

209. Z. Qiao, Z. Shi, N. Hort, N. I. Zainal Abidin, A. Atrens, *Corrosion behaviour of a nominally high purity Mg ingot produced by permanent mould direct chill casting,* Corrosion Science, 2012 **61**(0): p. 185-207.

210. W.O. Kroenig, S.E. Pawlow, *Korrosion und Metallschutz*, 1934.

211. G. Song, A. Atrens, X. Wu, B. Zhang, *Corrosion behaviour of AZ21, AZ501 and AZ91 in sodium chloride,* Corrosion Science, 1998 **40**(10): p. 1769-1791.

212. S.K. Das, L.A. Davis, *High performance aerospace alloys via rapid solidification processing,* Materials Science and Engineering, 1988 **98**(0): p. 1-12.

213. T. Zhang, Y. Shao, G. Meng, Z. Cui, F. Wang, *Corrosion of hot extrusion AZ91 magnesium alloy. Part II: Effect of rare earth element neodymium (Nd) on the corrosion behavior of extruded alloy,* Corrosion Science, 2011 **53**(9): p. 2934-2942.

214. A. Srinivasan, C. Blawert, Y. Huang, C.L. Mendis, K.U. Kainer, N. Hort, *Corrosion behavior of Mg–Gd–Zn based alloys in aqueous NaCl solution,* Journal of Magnesium and Alloys, 2014 **2**(3): p. 245-256.

215. S. Izumi, M. Yamasaki, Y. Kawamura, *Relation between corrosion behavior and microstructure of Mg–Zn–Y alloys prepared by rapid solidification at various cooling rates,* Corrosion Science, 2009 **51**(2): p. 395-402.

216. J. Zhang, J. Xu, W. Cheng, C. Chen, J. Kang, *Corrosion Behavior of Mg–Zn–Y Alloy with Long-period Stacking Ordered Structures,* Journal of Materials Science & Technology, 2012 **28**(12): p. 1157-1162.

217. X. Zhang, Y. Wu, Y. Xue, Z. Wang, L. Yang, *Biocorrosion behavior and cytotoxicity of a Mg–Gd–Zn–Zr alloy with long period stacking ordered structure,* Materials Letters, 2012 **86**(0): p. 42-45.

218. M. Mouanga, P. Berçot, J.Y. Rauch, *Comparison of corrosion behaviour of zinc in NaCl and in NaOH solutions. Part I: Corrosion layer characterization,* Corrosion Science, 2010 **52**(12): p. 3984-3992.

219. N. Boshkov, K. Petrov, S. Vitkova, S. Nemska, G. Raichevsky, *Composition of the corrosion products of galvanic alloys Zn–Co and their influence on the protective ability,* Surface and Coatings Technology, 2002 **157**(2–3): p. 171-178.

220. T. Rzychoń, J. Michalska, A. Kiełbus, *Effect of heat treatment on corrosion resistance of WE54 alloy,* Journal of Achievements in Materials and Manufacturing Engineering, 2007 **20**(1-2): p. 191-194.

221. T. Valente, *Grain boundary effects on the behavior of WE43 magnesium castings in simulated marine environment,* Journal of Materials Science Letters, 2001 **20**(1): p. 67-69.

222. M. Carboneras, C. J. Munez, P. Rodrigo, M.D. Escalera, M.D. Lopez, E.Otero, *Effect of Heat Treatment on the Corrosion Behaviour of a Mg-Y Alloy in Chloride Medium*, Vol. 636-37 2010, Stafa-Zurich, SUISSE: Trans Tech. 6.

223. P.L. Miller, B.A. Shaw, R.G. Wendt, W.C. Moshier, *Assessing the Corrosion Resistance of Nonequilibrium Magnesium-Yttrium Alloys,* Corrosion, 1995 **51**(12): p. 922-931.

224. A.J. Davenport, C. Padovani, B.J. Connolly, N.P.C. Stevens, T.A.W. Beale, A. Groso, M. Stampanoni, *Synchrotron X-Ray Microtomography Study of the Role of Y in Corrosion of Magnesium Alloy WE43,* Electrochemical and Solid-State Letters, 2007 **10**(2): p. C5-C8.

225. S.G. Bratsch, *Standard Electrode Potentials and Temperature Coefficients in Water at 298.15 K,* Journal of Physical and Chemical Reference Data, 1989 **18**(1): p. 1-21.

226. C.-n. Cao, *On the impedance plane displays for irreversible electrode reactions based on the stability conditions of the steady-state—I. One state variable besides electrode potential,* Electrochimica Acta, 1990 **35**(5): p. 831-836.

227. C.-n. Cao, *On the impedance plane displays for irreversible electrode reactions based on the stability conditions of the steady-state—II. Two state variables besides electrode potentia,* Electrochimica Acta, 1990 **35**(5): p. 837-844.

228. N. Pebere, C. Riera, F. Dabosi, *Investigation of magnesium corrosion in aerated sodium sulfate solution by electrochemical impedance spectroscopy,* Electrochimica Acta, 1990 **35**(2): p. 555-561.

229. E. Ghali, *General, Galvanic, and Localized Corrosion of Magnesium and Its Alloys*, in *Corrosion Resistance of Aluminum and Magnesium Alloys*, 2010, John Wiley & Sons, Inc. p. 348-379.

230. J.H. Nordlien, K. NişancioĞlu, S. Ono, N. Masuko, *Morphology and structure of oxide films formed on MgAl alloys by exposure to air and water,* Journal of the Electrochemical Society, 1996 **143**(8): p. 2564-2572.

231. R. Lindström, J.E. Svensson, L.G. Johansson, *The Influence of Carbon Dioxide on the Atmospheric Corrosion of Some Magnesium Alloys in the Presence of NaCl,* Journal of The Electrochemical Society, 2002 **149**(4): p. B103.

232. R. Lindström, L.G. Johansson, J.E. Svensson, *The influence of NaCl and CO2 on the atmospheric corrosion of magnesium alloy AZ91,* Materials and Corrosion, 2003 **54**(8): p. 587-594.

233. E. Ghali, *Magnesium and Magnesium Alloys*, in Uhlig's Corrosion Handbook, 2011, John Wiley & Sons, Inc. p. 809-836.

234. N. Hara, D. Kagaya, N. Akao, *Ellipsometric Analysis of Growth Process of Oxidation Films on Magnesium and its Alloys in Neutral Aqueous Solutions*, in Passivation of Metals and Semiconductors, and Properties of Thin Oxide Layers, P. Marcus and V. Maurice, Editors. 2006, Elsevier Science, Amsterdam. p. 217-223.

235. M. Liu, S. Zanna, H. Ardelean, I. Frateur, P. Schmutz, G. Song, A. Atrens, P. Marcus, *A first quantitative XPS study of the surface films formed, by exposure to water, on Mg and on the Mg–Al intermetallics: Al3Mg2 and Mg17Al12,* Corrosion Science, 2009 **51**(5): p. 1115-1127.

236. L. Wang, T. Shinohara, B.-P. Zhang, *XPS study of the surface chemistry on AZ31 and AZ91 magnesium alloys in dilute NaCl solution,* Applied Surface Science, 2010 **256**(20): p. 5807-5812.

237. D.L. Hawke, J.E. Hillis, M. Pekguleryuz, I. Nakatsugawa, *Corrosion behavior,* ASM Specialty Handbook: Magnesium and Magnesium Alloys, 1999: p. 194-210.

238. N.S. McIntyre, C. Chen, *Role of impurities on Mg surfaces under ambient exposure conditions,* Corrosion Science, 1998 **40**(10): p. 1697-1709.

239. M. Taheri, R.C. Phillips, J.R. Kish, G. A. Botton, *Analysis of the surface film formed on Mg by exposure to water using a FIB cross-section and STEM–EDS,* Corrosion Science, 2012, **59**(0): p. 222-228.

240. K.A. Unocic, H.H. Elsentriecy, M.P. Brady, H.M. Meyer, G.L. Song, M. Fayek, R.A. Meisner, B. Davis, *Transmission Electron Microscopy Study of Aqueous Film Formation and Evolution on Magnesium Alloys,* Journal of The Electrochemical Society, 2014 **161**(6): p. C302-C311.

241. J.H. Nordlien, S. Ono, N. Masuko, K. NişancioĞlu, *Morphology and Structure of Oxide Films Formed on Magnesium by Exposure to Air and Water,* Journal of The Electrochemical Society, 1995 **142**(10): p. 3320-3322.

242. K.M. Ismail, S. Virtanen, *Electrochemical Behavior of Magnesium Alloy AZ31 in 0.5 M KOH Solution,* Electrochemical and Solid-State Letters, 2007 **10**(3): p. C9-C11.

243. I. Nakatsugawa, S. Kamado, Y. Kojima, R. Ninomiya, K. Kubota, *Corrosion of Magnesium Alloys Containing Rare Earth Elements*, in *Corrosion Reviews*, 1998 p. 139.

244. D. Raiser, J. Deville, *Study of XPS photoemission of some gadolinium compounds,* Journal of electron spectroscopy and related phenomena, 1991 **57**(1): p. 91-97.

Appendix A1 Circuit parameters for the Mg-Ce alloys

Alloy	Time (h)	R_s (Ω•cm^2)	C_{oxi} (F/cm^2)	n_1	R_{oxi} (Ω•cm^2)	C_{dl} (F/cm^2)	n_2	R_{Ct} (Ω•cm^2)	Chi-squared
Mg1Ce	0	84.05	8.95E-06	0.88	379.70	2.68E-03	0.79	202.20	7.23E-04
	1	84.22	9.42E-06	0.90	581.60	2.28E-03	0.73	428.40	1.15E-04
	3	83.39	9.04E-06	0.90	660.70	2.07E-03	0.74	529.70	1.51E-04
	6	86.27	9.25E-06	0.90	692.10	2.92E-03	0.69	660.70	5.06E-04
	10	86.37	9.42E-06	0.90	713.50	2.99E-03	0.69	771.00	6.34E-04
	16	87.43	9.69E-06	0.90	729.50	2.47E-03	0.76	581.80	5.82E-04
	24	85.96	9.58E-06	0.91	765.40	3.35E-03	0.71	698.30	5.10E-04
	36	83.61	8.95E-06	0.91	822.90	2.95E-03	0.72	835.30	5.65E-04
	48	81.80	8.61E-06	0.92	832.90	3.14E-03	0.70	922.30	5.26E-04
	60	84.50	8.31E-06	0.91	897.90	2.81E-03	0.71	1019.00	5.61E-04
	72	83.70	8.03E-06	0.92	952.40	2.65E-03	0.71	1095.00	5.80E-04
Mg5Ce	0	82.69	1.32E-05	0.86	291.10	5.94E-03	0.73	124.60	7.19E-04
	1	83.20	1.92E-05	0.83	315.30				8.24E-04
	3	85.23	4.28E-05	0.83	205.00				1.43E-03
	6	86.09	8.28E-05	0.88	128.60				6.01E-04
	10	87.00	7.52E-05	0.95	112.80				6.73E-04
	16	95.00	5.79E-05	0.96	134.00				1.16E-03
	24	96.57	6.22E-05	0.90	138.80				1.28E-03
	36	100.20	6.15E-05	0.87	165.00				1.29E-03
	48	100.60	5.95E-05	0.86	166.60				1.22E-03
Mg10Ce	0	88.65	1.18E-05	0.85	171.5				6.08E-04
	1	87.09	7.47E-05	0.69	65.8				7.39E-04
Mg15Ce	0	80.05	1.07E-05	0.88	213				8.67E-04
	1	82.01	2.32E-05	0.89	88.36				2.05E-03

Appendix A2 Circuit parameters for the Mg-La alloys

	Time (h)	**R_s (Ω•cm^2)**	**C_{oxi} (F/cm^2)**	**n_1**	**R_{oxi} (Ω•cm^2)**	**C_{dl} (F/cm^2)**	**n_2**	**R_{Ct} (Ω•cm^2)**	**Chi-squared**
M1La	0	82.12	1.36E-05	0.87	301.30	2.42E-03	0.55	85.68	7.69E-04
	1	80.71	1.02E-05	0.89	405.40	2.33E-03	0.80	236.2	9.32E-05
	3	79.34	1.00E-05	0.89	468.60	3.40E-03	0.74	359.4	1.20E-04
	6	79.08	9.82E-06	0.90	260.60				9.36E-04
	10	82.71	3.33E-05	0.85	275.50				2.84E-04
	16	89.73	4.69E-05	0.94	180.20				4.29E-04
	24	88.54	5.28E-05	0.95	120.30				2.80E-04
	36	87.82	5.46E-05	0.94	109.70				2.43E-04
Mg5La	0	81.06	1.06E-05	0.89	282.90	1.02E-02	0.52	145.60	2.69E-03
	1	78.21	1.03E-05	0.86	342.60				6.74E-03
	3	73.61	1.30E-04	0.49	218.30				8.58E-03
	6	81.21	1.84E-04	0.86	43.12				1.02E-03
	10	86.04	1.56E-04	0.77	41.00				1.11E-03
	16	89.34	1.57E-04	0.72	41.77				9.68E-04
	24	87.52	1.57E-04	0.70	39.37				9.50E-04
	36	97.17	1.64E-04	0.68	44.42				1.18E-03
	48	97.93	1.51E-04	0.74	44.90				9.84E-04
Mg10La	0	77.19	1.07E-05	0.91	184.80				4.14E-04
	1	82.85	7.56E-05	0.97	39.78				2.24E-04
Mg15La	0	87.43	1.32E-05	0.84	150.20				1.85E-03
	1	96.30	1.16E-04	0.86	36.21				8.49E-05

Appendix A3 Circuit parameters for the Mg-Gd alloys

Alloy	**Time (h)**	**R_s (Ω•cm^2)**	**C_{oxi} (F/cm^2)**	**n_1**	**R_{oxi} (Ω•cm^2)**	**C_{dl} (F/cm^2)**	**n_2**	**R_{Ct} (Ω•cm^2)**	**Chi-squared**
Mg1Gd	0	83.79	2.54E-05	0.79	324.10	4.69E-03	0.72	207.60	5.60E-04
	1	85.69	2.07E-05	0.80	529.20	2.66E-03	0.83	352.50	8.14E-05
	3	84.88	1.90E-05	0.82	580.40	3.82E-03	0.75	505.70	3.39E-04
	6	86.66	1.93E-05	0.81	583.50	3.35E-03	0.79	407.90	4.70E-03
	10	82.34	4.87E-05	0.87	277.90				1.49E-03
	16	90.70	1.26E-04	0.71	313.70				1.65E-03
	24	96.14	1.13E-04	0.86	340.00				1.62E-03
	36	92.96	8.87E-05	0.85	400.00				1.81E-03
	48	91.48	6.94E-05	0.80	414.60				2.32E-03
	60	89.00	7.62E-05	0.72	588.20				1.95E-03
	72	84.60	5.14E-05	0.89	492.50				5.25E-04
	84	99.88	6.37E-05	0.77	541.10				2.03E-03
	96	91.72	7.77E-05	0.80	593.50				2.10E-03
Mg5Gd	0	81.71	1.11E-05	0.91	422.40	1.46E-03	0.83	103.50	3.26E-04
	1	90.29	1.16E-05	0.89	526.40				1.60E-03
	3	95.84	3.33E-05	0.85	340.80				2.52E-03
	6	96.20	3.73E-05	0.64	282.00				2.14E-03
	10	96.84	4.07E-05	0.88	208.70				1.70E-03
	16	94.43	3.37E-05	0.92	165.50				1.56E-03
	24	92.81	2.71E-05	0.92	139.90				1.32E-03
	36	100.00	3.41E-05	1.00	118.00				1.14E-03
	48	94.70	3.08E-05	0.98	92.54				8.67E-04

Appendix A3 Circuit parameters for the Mg-Gd alloys (continued)

Alloy	**Time (h)**	**R_s (Ω•cm^2)**	**C_{oxi} (F/cm^2)**	**n_1**	**R_{oxi} (Ω•cm^2)**	**C_{dl} (F/cm^2)**	**n_2**	**R_{Ct} (Ω•cm^2)**	**Chi-squared**
Mg10Gd	0	102.90	1.33E-05	0.84	297.00	4.04E-03	0.86	104.00	8.37E-04
	1	100.00	1.48E-05	0.80	363.80				2.60E-03
	3	112.30	3.26E-05	0.90	234.90				1.94E-03
	6	114.10	4.24E-05	0.99	219.20				1.89E-03
	10	119.00	5.51E-05	0.93	173.50				2.06E-03
	16	110.00	4.16E-05	0.96	182.80				1.87E-03
	24	114.50	3.49E-05	0.93	137.40				1.96E-03
	36	117.50	3.65E-05	0.96	150.40				1.47E-03
Mg15Gd	0	116.90	9.32E-06	0.86	415.70	2.30E-03	0.96	102.70	1.08E-03
	1	128.10	1.08E-05	0.89	344.00				5.34E-03
	3	136.40	2.31E-05	0.92	161.90				4.19E-03
	6	128.70	4.16E-05	0.91	112.50				1.78E-03
	10	134.00	5.01E-05	0.96	68.83				1.16E-03
	16	141.30	3.84E-05	0.98	49.66				8.65E-04
	24	146.50	3.82E-05	0.93	35.49				7.98E-04

Appendix A4 Circuit parameters for the Mg10Gd alloy after solid solution treatment

Alloy	Time (h)	R_s (Ω•cm^2)	C_{oxi} (F/cm^2)	n_1	R_{oxi} (Ω•cm^2)	C_{dl} (F/cm^2)	n_2	R_{Ct} (Ω•cm^2)	Chi-squared
Mg10Gd_ss	0	85.29	1.81E-05	0.82	244.00	4.47E-03	0.86	115.80	5.01E-04
	1	88.73	1.78E-05	0.85	397.50	4.02E-03	0.78	287.50	4.33E-04
	3	86.30	1.69E-05	0.85	456.70	5.04E-03	0.79	390.50	3.32E-04
	6	90.21	1.62E-05	0.84	538.40	4.59E-03	0.81	418.40	4.83E-04
	10	90.54	1.56E-05	0.85	640.10	5.05E-03	0.74	601.60	4.52E-04
	16	89.12	1.43E-05	0.86	626.10	6.95E-03	0.81	359.30	7.04E-04
	24	94.39	2.72E-05	0.88	490.60				3.29E-03
	36	94.04	3.32E-05	0.84	593.70				2.14E-03
	48	93.76	2.36E-05	0.82	693.10				6.08E-03

Appendix A5 Circuit parameters for the Mg10Gd alloy after aging treatment at 200°C

Alloy	Time (h)	R_s (Ω•cm^2)	C_{oxi} (F/cm^2)	n_1	R_{oxi} (Ω•cm^2)	C_{dl} (F/cm^2)	n_2	R_{Ct} (Ω•cm^2)	Chi-squared
Mg10Gd_200°C	0	88.81	3.05E-05	0.74	258.20	4.59E-03	1.00	68.02	3.95E-04
	1	88.75	3.55E-05	0.76	443.30	6.20E-03	0.85	221.90	1.41E-04
	3	96.06	4.02E-05	0.73	589.90	5.56E-03	0.85	346.90	1.41E-04
	6	96.10	4.22E-05	0.73	702.40	4.78E-03	0.88	428.20	1.49E-04
	10	99.68	4.27E-05	0.72	723.20	4.97E-03	0.85	479.40	2.77E-04
	16	99.06	3.78E-05	0.74	751.80	4.72E-03	0.85	505.00	3.35E-03
	24	97.23	3.75E-05	0.74	777.60	4.74E-03	0.82	570.70	3.47E-03
	36	94.21	3.42E-05	0.76	828.30	4.40E-03	0.81	637.90	3.08E-03
	48	101.80	3.36E-05	0.75	856.80	4.70E-03	0.77	713.00	3.33E-03
	60	104.20	3.28E-05	0.75	802.50	4.72E-03	0.76	730.60	3.54E-03
	72	101.90	3.24E-05	0.75	841.40	4.66E-03	0.77	768.50	3.59E-03

Appendix A6 Circuit parameters for the Mg10Gd alloy after aging treatment at 300°C

Alloy	**Time (h)**	**R_s (Ω•cm^2)**	**Coxi(F/cm^2)**	**n_1**	**Roxi (Ω•cm^2)**	**C_{dl}(F/cm^2)**	**n_2**	**R_{Ct}(Ω•cm^2)**	**Chi-squared**
Mg10Gd_300°C	0	109.20	1.16E-05	0.82	466.30				7.49E-04
	1	113.20	9.33E-06	0.89	857.80	1.49E-03	0.84	594.80	1.17E-03
	3	117.20	9.01E-06	0.90	871.20	1.96E-03	0.80	656.00	9.26E-04
	6	117.30	8.88E-06	0.90	959.90	2.02E-03	0.80	781.20	1.18E-03
	10	121.80	8.67E-06	0.90	1053.00	2.05E-03	0.78	903.60	1.22E-03
	16	114.90	8.31E-06	0.91	1023.00	1.83E-03	0.78	870.90	7.84E-04
	24	113.20	8.39E-06	0.91	1058.00	1.71E-03	0.79	848.40	1.01E-03
	36	116.60	8.25E-06	0.91	1168.00	1.85E-03	0.77	1003.00	1.02E-03
	48	119.70	8.11E-06	0.91	1225.00	1.97E-03	0.73	1126.00	7.50E-04
	60	121.50	8.14E-06	0.91	1304.00	1.92E-03	0.73	1248.00	9.64E-04
	72	119.60	8.24E-06	0.91	1311.00	1.76E-03	0.77	1141.00	9.49E-04

Appendix A7 Circuit parameters for the Mg10Gd alloy after aging treatment at 400°C

Alloy	**Time (h)**	**R_s (Ω•cm^2)**	**C_{oxi} (F/cm^2)**	**n_1**	**R_{oxi} (Ω•cm^2)**	**C_{dl} (F/cm^2)**	**n_2**	**R_{Ct} (Ω•cm^2)**	**Chi-squared**
Mg10Gd_400°C	0	100.70	2.28E-05	0.78	202.30	4.80E-03	0.86	85.98	1.51E-04
	1	106.70	2.73E-05	0.78	357.70	5.35E-03	0.84	230.80	3.04E-04
	3	104.30	2.85E-05	0.77	364.00	5.74E-03	0.88	193.60	2.88E-04
	6	107.00	3.10E-05	0.75	330.70				6.53E-03
	10	105.10	6.64E-05	0.87	191.90				1.14E-03
	16	107.10	6.75E-05	0.87	168.20				1.45E-03
	24	108.50	7.97E-05	0.83	166.20				8.73E-04
	36	109.80	5.60E-05	0.78	136.60				1.04E-03
	48	106.00	5.06E-05	0.74	109.20				8.40E-04

Appendix A8 Circuit parameters for the Mg10Gd5Al alloy

Alloy	Time (h)	R_s (Ω•cm^2)	C_{Oxi} (F/cm^2)	n_1	R_{Oxi} (Ω•cm^2)	C_{dl} (F/cm^2)	n_2	R_{Ct} (Ω•cm^2)	Chi-squared
Mg10Gd5Al	0	84.83	8.33E-06	0.91	541.90				1.98E-04
	1	85.23	8.05E-06	0.90	753.60	2.37E-03	0.86	356.40	4.14E-04
	3	80.48	7.82E-06	0.91	790.20	2.33E-03	0.83	572.60	3.51E-04
	6	82.97	8.25E-06	0.94	645.70				1.68E-03
	10	84.20	1.31E-05	0.94	486.10				8.61E-04
	16	85.16	1.79E-05	0.92	533.80				6.67E-04
	24	79.96	1.56E-05	0.90	425.60				9.73E-04
	36	80.72	1.69E-05	0.85	386.20				8.64E-04
	48	75.68	1.87E-05	0.82	301.50				8.15E-04
	60	79.74	2.04E-05	0.79	290.10				6.40E-04
	72	77.43	2.14E-05	0.77	236.40				5.60E-04
	84	79.49	2.40E-05	0.74	215.40				4.84E-04

Appendix A9 Circuit parameters for the Mg10Gd5Ga alloy

Alloy	Time (h)	R_s (Ω•cm^2)	C_{Oxi} (F/cm^2)	n_1	R_{Oxi} (Ω•cm^2)	C_{dl} (F/cm^2)	n_2	R_{Ct} (Ω•cm^2)	Chi-squared
Mg10Gd5Ga	0	84.12	1.30E-05	0.85	157.40				5.21E-04
	1	88.65	6.80E-05	0.89	117.40				6.37E-04
	3	85.24	8.38E-05	0.92	97.69				5.35E-04
	6	90.63	8.02E-05	0.93	65.60				5.06E-04
	10	87.30	9.45E-05	0.89	44.20				4.91E-04
	16	90.40	1.13E-04	0.86	42.38				4.79E-04
	24	89.45	1.32E-04	0.84	39.12				4.66E-04

Appendix A10 Circuit parameters for the Mg10Gd1Mn alloy

Alloy	**Time (h)**	**R_s (Ω•cm^2)**	**C_{Oxi} (F/cm^2)**	**n_1**	**R_{Oxi} (Ω•cm^2)**	**C_{dl} (F/cm^2)**	**n_2**	**R_{Ct} (Ω•cm^2)**	**Chi-squared**
Mg10Gd1Mn	0	85.01	9.16E-06	0.88	297.00	9.38E-04	0.89	92.27	1.72E-04
	1	84.87	7.69E-06	0.90	430.10	4.68E-03	0.76	244.30	1.31E-04
	3	83.43	7.44E-06	0.91	511.10	4.12E-03	0.77	325.90	1.19E-04
	6	81.82	7.40E-06	0.91	581.50	5.44E-03	0.73	432.00	1.33E-04
	10	82.44	7.39E-06	0.92	613.80	5.68E-03	0.70	503.00	1.12E-04
	16	81.53	7.79E-06	0.91	665.00	5.22E-03	0.73	531.50	4.06E-04
	24	81.74	7.88E-06	0.91	707.60	5.28E-03	0.71	571.00	2.30E-04
	36	81.75	8.19E-06	0.91	800.60	5.09E-03	0.70	704.00	3.56E-04
	48	83.02	8.32E-06	0.91	892.00	4.74E-03	0.68	866.80	1.99E-04
	60	82.68	8.67E-06	0.91	1018.00	3.84E-03	0.70	1043.00	4.50E-04
	72	81.58	8.65E-06	0.91	1110.00	3.56E-03	0.70	1139.00	4.01E-04

Appendix A11 Circuit parameters for the Mg10Gd5Y alloy

Alloy	**Time (h)**	**R_s (Ω•cm^2)**	**C_{Oxi} (F/cm^2)**	**n_1**	**R_{Oxi} (Ω•cm^2)**	**C_{dl} (F/cm^2)**	**n_2**	**R_{Ct} (Ω•cm^2)**	**Chi-squared**
Mg10Gd5Y	0	84.14	1.37E-05	0.87	295.50	5.69E-03	0.84	98.80	7.55E-04
	1	89.66	1.70E-05	0.90	311.60				6.41E-04
	3	89.07	3.07E-05	0.91	205.80				9.69E-04
	6	86.17	4.23E-05	0.93	136.50				6.96E-04
	10	87.86	4.77E-05	0.95	104.80				4.75E-04
	16	88.48	5.34E-05	0.94	84.95				3.93E-04
	24	89.40	5.50E-05	0.92	71.38				2.89E-04
	36	88.14	5.03E-05	0.91	66.58				2.79E-04

Appendix A12 Circuit parameters for the Mg10Gd5Zn alloy

Alloy	**Time (h)**	**R_s (Ω•cm^2)**	**C_{Oxi} (F/cm^2)**	**n_1**	**R_{Oxi} (Ω•cm^2)**	**C_{dl} (F/cm^2)**	**n_2**	**R_{Ct} (Ω•cm^2)**	**Chi-squared**
Mg10Gd5Zn	0	86.20	1.41E-05	0.85	295.60	8.26E-03	0.75	137.70	3.74E-04
	1	88.13	5.22E-05	0.82	159.80				9.01E-04
	3	87.14	9.36E-05	0.89	81.60				1.45E-04
	6	87.52	9.27E-05	0.85	48.35				9.02E-05
	10	89.37	1.06E-04	0.82	38.52				1.24E-04
	16	90.84	1.26E-04	0.79	31.15				6.20E-05

Curriculum Vitae

Surname: Silva Campos
Name: Maria del Rosario
Date of birth: May 10, 1977
Place of birth: Mexico, Distrito Federal

Education

1996 - 2000
Bachelor of Science, Industrial Chemical Engineering
Escuela Superior de Ingenieria Quimica e Industrias Extractivas (ESIQIE) – IPN

2002 - 2005
Master of Science with Major in Metallurgical Engineering
Escuela Superior de Ingeniería Química e Industrias Extractivas (ESIQIE)–IPN

2009 - 2016
PhD study at Helmholtz-Zentrum Geesthacht, Centre for Materials and Coastal Research
Magnesium Innovation Centre (MagIC)
Corrosion and Surface Technology Department

Additional Trainning

"Risk-Based Management of Pipeline Integrity & Safety Course"- Clarion Technical Conferences- 12/2006 Calgary, Canada.
"Pipeline Risk Management Course" – Clarion Technical Conferences- 03/2007 Houston, U.S.A.

Languages

Spanish – Mother tongue
English – Fluent
German – Intermediate Level